Synthesis and optical properties of self-assembled 2D layered organic-inorganic perovskites for optoelectronics

Yi Wei

ECOLE NORMALE SUPERIEURE DE CACHAN

Synthesis and optical properties of self-assembled 2D layered organic-inorganic perovskites for optoelectronics

by

Yi WEI

A thesis submitted for the degree of
Doctor of Physics and Chemistry

in the

Laboratoire de photonique quantique et moléculaire

July 2012

Acknowledgements

Contents

List of Figures

List of Tables

Introduction

The innovation of advanced technology and the requirement of electronic market are always focusing on low cost electronics, easy processing, having enhanced performance. Take as an example the improvement of flat panel display. It has experienced three periods: CRT (Cathode Ray Tube), LCD (Liquid Crystal Display) and OLED (Organic Electronic-luminescence Display). CRT has been replaced by LCD and OLED because the depth and weight of CRTs are not appropriate for portable applications. The organic materials are more and more widely used due to their various advantages: low temperature processing, flexibility of organic chemistry to form molecules, good luminescent properties. However, organic compounds generally have a number of disadvantages, including poor thermal and mechanical stability, as well as a limited mobility at room temperature.

Besides the inorganic semiconductors and the organic materials, an interesting class of materials is intensively studied: the hybrid materials, which are expected to combine the attractive features of organic materials and inorganic materials within a single molecular-scale composite, and can be synergistically exploited to overcome the limitations when the two kinds of materials are used separately. In the past two decades, the organic-inorganic hybrid perovskites have arisen as a new functional material and have drawn great attention and research effort. When deposited by spin-costing, these compounds are self-assembled systems, they form a multi-quantum well structure spontaneously and exhibit excellent optical and electronic properties at room temperature. Their optical properties can be finely tuned thanks to molecular enginering on the organic part or on the inroganic part. Furthermore, spin-coating is a very simple method, compared to the deposition techniques for inorganic semiconductors, such as MBE (Molecular Beam Epitaxy), MOCVD (Metalorganic Chemical Vapor Deposition) and PECVD (Plasma Enhanced Chemical Vapour Deposition).

Recently, organic-inorganic hybrid perovskites have been used in many research and practical fields such as surface plasmons, Symonds et al. (2007, 2008) LEDs, Era et al. (1994) solar cells Kojima et al. (2009); Li et al. (2010); Koutselas et al. (2011) as well as microcavities. Bréhier et al. (2006); Lanty et al. (2008b); Wei et al. (2012) Especially the use of this hybrid semiconductor inside microcavities could open the way to realize

polariton laser at room temperature. The team "Optical Properties of Hybrid Nanostructures" of LPQM ENS Cachan has successfully realized microcavities containing two-dimensional layered organic-inorganic perovskites, working in the strong coupling regime at room temperature, and emitting in the green, blue and mear UV range. Additionally, some hybrid vertical microcavities containing a layer of inorganic semiconductors such as GaN or ZnO and a perovskite layer have been performed, and the strong coupling regime between the photon mode and the two excitons has been demonstrated at room temperature. Although perovskites show stronger excitonic properties and brighter luminescence than inorganic semiconductors, and stronger thermal- and photo-stability than most organic semiconductors, it is still quite urgent to work on optical optimization of perovskite layers, especially the long time photo-stability, in order to support higher requirements of technological and scientific applications.

These important issues bring about the research subject of this thesis. The objectives are to synthesize, characterize and optimize new functionalized organic-inorganic hybrid perovskites for the application of microcavities, and further scientific and practical requirements. In this manuscript, we focus our attention on the group of two-dimensional (2D) layered lead halide perovskites and emphatically make research efforts in several aspects:

- Improvement of optical properties

- Study on photostability

- Application of perovskite layers in microcavities

Thus, this manuscript is developed in five chapters as follows:

In **Chapter 1**, we talk about the general organic-inorganic hybrid materials and introduce the chemical composition and crystal structure of perovskites compounds. We present the particular optical and electronic properties of two-dimensional perovskites which will be mainly studied in this manuscript. We also present the possible deposition techniques for preparing 2D layered perovskites crystals. As a promising opto-electronic material, some examples of devices realized with perovskites are given in the last part of chapter.

Chapter 2 presents the experimental methods we use to characterize the structural and optical properties of perovskites. Besides, we detail the synthesis process of perovskites compounds, and different methods of fabrication which allow to obtain perovskites in various crystal forms: 2D layered films, bulks, and nanoparticles.

Chapter 3 presents the high flexibility regarding optical properties of 2D layered perovskites such as $(R-NH_3)_2PbX_4$ and $(NH_3-R-NH_3)PbX_4$, where R is an organic ammonium cation and X is an halide ion. We systematically modify the organic cations by

changing the chemical structure of R group, and find that "spatial encumbrance" of R is a crutial factor which greatly affects the filmability and the photoluminescence efficiency. Moreover, we prepare some mixed perovskites: mixing in the organic part and mixing in the inorganic part, and study the optical properties of the excitons in such systems. We show that it is possible to tune easily and continously the excitonic transitions energies from 520 nm to 340 nm.

In **Chapter 4**, the photo-stability of perovskites is studied. From the experimental results, some important factors which cause the degradation of perovskites under laser illumination are discussed and summarized. We synthesize a group of fluorinated perovskites and develop the layer deposition by including perovskite crystals in a polymer (PMMA) matrix. We show that a great improvement of the photo-stability is achieved in this new material.

Finally, **Chapter 5** is devoted to microcavities containing organic-inorganic perovskites. After introducing some basic knowledge about planar microcavities, the protocol of fabrication and experimental characterization methods are described. A λ-cavity containing fluorinated perovskite crystals included in a polymer (PPMA) matrix is produced, and the strong coupling regime at room temperature is evidenced.

Chapter 1

Hybrid organic-inorganic semiconductors

In the first chapter, we will discuss a new kind of semiconductor for optoelectronics: 2D layered organic-inorganic hybrid perovskites. First, we will talk about the general properties of some organic-inorganic hybrid materials, specifically focusing our attention on the hybrid perovskites semiconductors. Different deposition methods will be briefly described. Finally, some applications of perovskites in optoelectronic devices will be introduced.

1.1 Organic-inorganic hybrid materials

For the past sixty years, the electronic industry is mainly built on the basis of traditional inorganic semiconductors, such as silicon and gallium arsenide semiconductors, silicon dioxide insulators, and metals such as aluminum and copper. These inorganic materials, typically characterized by covalent and ionic interactions, offer the potential for high electrical mobility, a wide range of band gaps (enabling the design of insulators, semiconductors, metals, and superconductors), interesting magnetic interactions, a range of dielectric properties, substantial mechanical hardness, and thermal stability and are backbone of electronic field. Mitzi (1999b) Parallelly and more recently, a lot of progress has been made in producing devices based on organic materials such as OLEDs and OFETs because organic materials are less expensive alternatives to inorganic counterparts, present convenient processing as well as fine light emitting properties. Generally, organic-inorganic hybrid research focuses on employing the range of interactions found within organic and inorganic chemistry to create a composite combining the desirable properties of both the organic and the inorganic materials and overcoming their limitations when used separately. It is believed that combinations of organic and

inorganic materials could lead to new exploration in both physical effects and technological applications. Mitzi et al. (2001b); Agranovich (2011) An example of success is the organic-inorganic hybrid optoelectronic material realized by J. Takada Takada et al. (1992). They fabricated a heteromultilayer consisting of alternating amorphous organic layers of copper phthalocyanine (CuPc) and inorganic TiO_x, with an artificial period greater than 40 Å. This hybrid multilayer shows enhanced performance in photoconductivity which is found to be 40 times higher than that of an organic CuPc single layer. The CuPc layers have an energy gap of approximately 2.0 eV and absorb light in the visible region to generate electrons and holes. The TiO_x layers have a large energy gap and therefore exhibit no photoconductive sensitivity over most of the visible spectrum, but, they have a larger electron affinity and a substantially larger mobility. The combination of the two specific layers enables the electrons generated in the CuPc layers to transfer to the TiO_x layers, the photoconductivity is thus greatly enhanced.

In the studies of organic-inorganic hybrid perovskites, the research group of David B. Mitzi has done a lot of remarkable contributions to this field. Their work concerns structure studies, deposition techniques, optical properties, and development of opto-electronic devices... Mitzi (2001a); Mitzi et al. (1999); Mitzi and Liang (1997); Mitzi (2001b); Mitzi et al. (2001a); Mitzi (1996); Mitzi et al. (2002); Mitzi (1999a) Their previous results have provided a fruitful source of references for other researchers and have been an important basis for our work.

1.1.1 Organic-inorganic hybrid perovskites

1.1.1.1 Composition and spatial structure

The name of "perovskites" comes from a kind of mine: calcium titanate ($CaTiO_3$) which was discovered by a German mineralogist Gustav Rose in 1839. He gave the name "perovskites" in honor of a Russian mineralogist Lev Alekseevich von Perovski(1792-1856).

The basic structure of the organic-inorganic perovskites family is AMX_3. It consists of corner-sharing MX_6^{4-} octahedra, where X is typically an anion: O^{2-}, Cl^-, Br^- or S^{2-}, and the M atom is generally a divalent metal that can adopt an octahedral anion coordination, such as Ge^{2+}, Sn^{2+}, Pb^{2+}, Co^{2+}, Fe^{2+}, Cu^{2+}, Ni^{2+}, Mn^{2+}, Cr^{2+}, Pd^{2+}, Cd^{2+}, Eu^{2+}, or Yb^{2+}; Papavassiliou et al. (1999); Papavassiliou and Koutselas (1995); Papavassiliou (1997); Mitzi et al. (2001b); Ishihara et al. (1990) this family has recently been extended to include some trivalent metals such as Bi^{3+} and Sb^{3+}. Mitzi (2000) The A cations fill the large 12-fold coordinated holes between the octahedra, as shown in Figure 1.1.

Based on the geometric constraints imposed by a rigid sphere model, the size of A cation influences a lot the perovskites structures. Here we define t as the tolerance factor
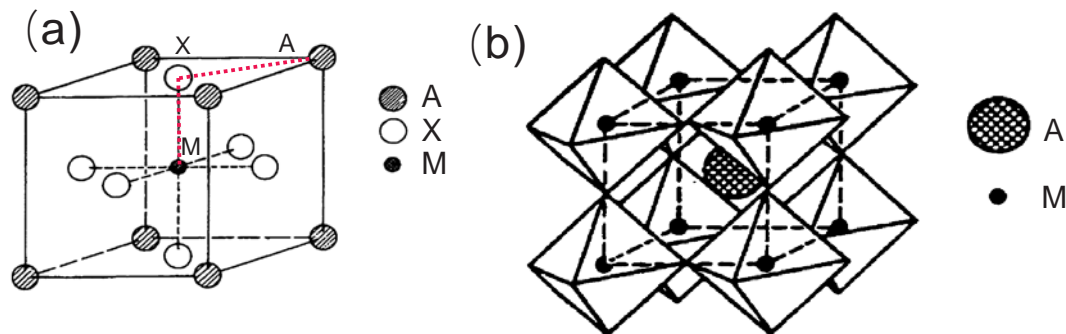
FIGURE 1.1: (a) Basic AMX_3 perovskite structure. (b) Sketch of a perovskite unit cell seen in three dimension(3D).

which satisfies the relation:

$$(R_A + R_X) = t\sqrt{2}(R_M + R_X), \tag{1.1}$$

where R_A, R_M, and R_X are the corresponding ionic radii of A, M and X ions. We suppose the values of $R_A + R_X$ and $R_M + R_X$ are approximately the distances A-X and M-X respectively. For a perfectly packed cubic perovskite structure, t is equal to 1. If the tolerance factor $t > 1$, the structure tends to distort towards a tetragonal structure; if tolerance factor $t < 1$, there is a tendency to distort towards buckling of octahedra.

3-dimensional networks:

Although the t value is theoretically regarded to be 1 for perfect 3D perovskite networks, it is empirically found that $0.8 < t < 0.9$ for most cubic perovskite structures. We take the system with M = Pb and X = I for example, the ionic radii $R_{pb} = 1.19$ Å and $R_I = 2.20$ Å , and using t =1, we find that R_A should not exceed approximately 2.6 Å. Considering that C-C or C-N bond lengths are of the order of 1.4 Å, only very small organic molecules, consisting of two or three atoms (excluding hydrogens), could fit into the structure. An example is the typical 3-dimensional perovskite compound $CH_3NH_3PbX_3$, which has one C atom and one N atom in its organic cation: the cubic lattice constants are found to be a = 5.657(2) Å (X = Cl), a = 5.901(1) Å (X = Br), and a = 6.3285(4) Å (X = I). Poglitsch and Weber (1987); Knop et al. (1990)

2-dimensional networks:

Besides the 3D network mentioned above, 2-dimensional network is also a quite common structure for organic-inorganic hybrid perovskites. It happens when the group A is too large to fit into the space provided by the nearest-neighbors X within the inorganic sheet, the organic group A then causes distortion of cubic structure and in this situation the tolerance factor t is much larger than 1. In such cases, the organic group

needs to be held away from the inorganic sheets by a spacer, such as an alkyl chain, in order to grow 2D perovskites layered structures.

The 2D layered perovskites systems include two typical groups of compounds: $(R-NH_3)_2MX_4$ and $(NH_3-R-NH_3)MX_4$, where R is an aliphatic or aromatic ammonium cation, M is a divalent metal that can adopt an octahedral coordination, and X is a halogen: Cl, Br or I. In $(R-NH_3)_2MX_4$ systems shown in Figure 1.2(a), the perovskites

$(R-NH_3)_2MX_4$

(a)

$(NH_3-R-NH_3)MX_4$

(b)
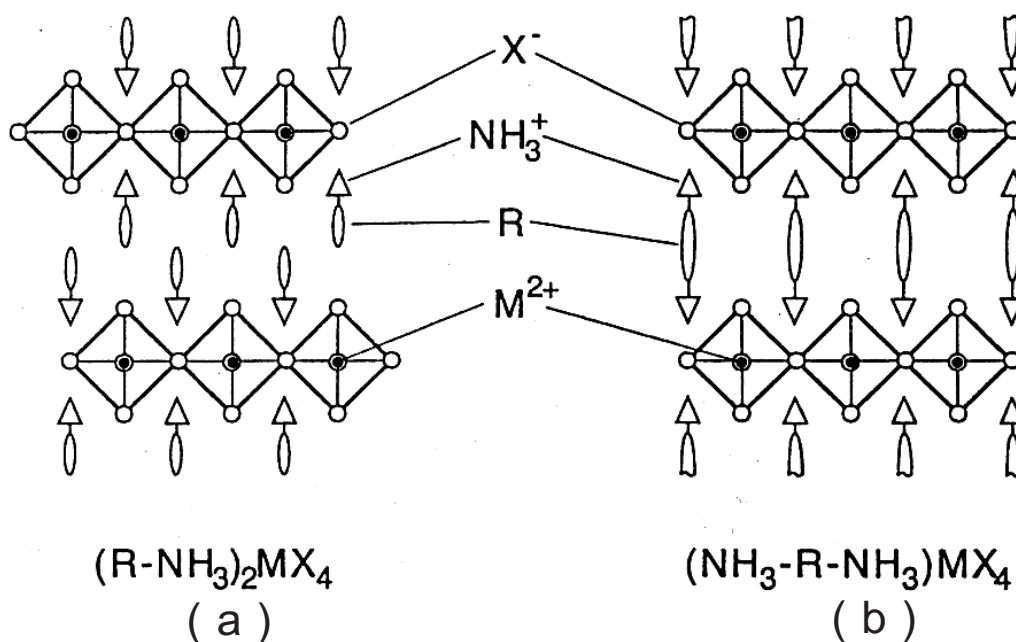
FIGURE 1.2: 2D-layered perovskites with (a) organic monoammonium cations and (b) diammonium cations. Mitzi (1999b)

consist of single layers of oriented inorganic sheets separated by bilayers of organic ammonium cations, where the organic groups R self-assemble via "π - π" interaction (when the organic group contains aromatic groups) or through Van der Waals force (when the organic group contains alkyl chains). In $(NH_3-R-NH_3)MX_4$ systems, shown in Figure 1.2(b), the organic cations make hydrogen bonds with the inorganic sheets at both ends rather than only at one end, thereby weakening the Van der Waals interaction between the layers. The inorganic sheets connect to organic sheets by hydrogen bonding, provided by the $N-H\cdots X$ interactions between the ammonium heads of the $R-NH_3^+$ or $^+NH_3-R-NH_3^+$ cations and two bridging halogens and one terminal halogen (bridging halogen configuration) or to two terminal halogens and one bridging halogen (terminal halogen configuration), Mitzi (1999b) as shown in Figure 1.3 for a $(R-NH_3)_2MX_4$ system.

Contrary to the 3D perovskite structure AMX_3, where the organic cation A must fit into a rigidly defined hole, in the 2D layered systems the distance between the inorganic sheets can vary with the length of the organic cation. Consequently, larger and more complex functional organic cations R can be incorporated, which surely enlarges the
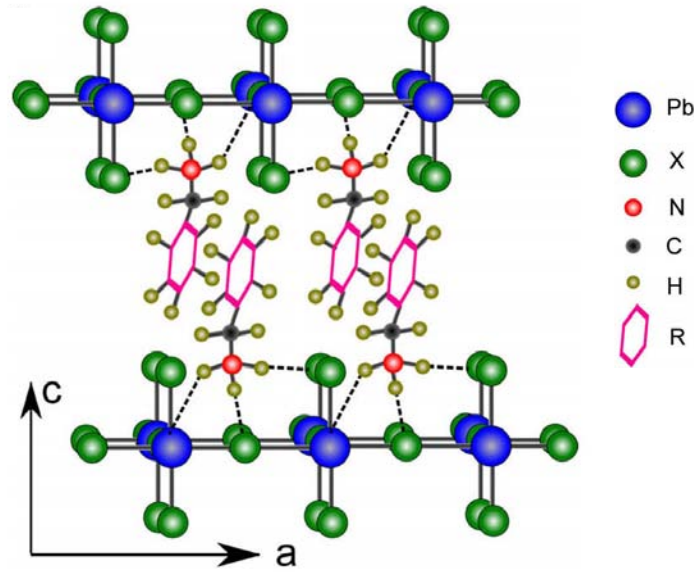
FIGURE 1.3: Sketch of 2D organic-inorganic lead halide semiconductors $(R-NH_3)_2MX_4$. The $R-NH_3^+$ head binds to the inorganic sheet by two terminal halogens and one bridging halogen.

research field and leads to more interesting and diverse properties. The 2D organic-inorganic hybrid perovskites are thus the subject we intensively study in this thesis.

1.1.1.2 Electronic structure of 2D layered perovskites

The structure of the 2D layered perovskites consists of an alternation of inorganic layers around 0.6 nm thick and of organic layers around 1 nm thick. This unique configuration provides interesting and potentially useful physical properties. Generally, the HOMO-LUMO (Highest Occupied Molecular Orbital and Lowest Unoccupied Molecular Orbital) energy gap of the organic layers is higher than the band gap of the inorganic layers (at least by 3 eV). Tanaka et al. (2002) The organic ammonium groups form a layer with a low relative dielectric constant of about 2.4 while the metal halide layers possess a high relative dielectric constant of about 6.1. Hong et al. (1992) These two kinds of layers play as barriers and wells alternating with each other, inorganic layers are wells and the organic layers are barriers for the carriers. The electronic structure of 2D layered organic-inorganic perovskites can thus be regarded as a self-organized multiple-quantum-well structure, consisting of organic barriers and inorganic wells, as shown in Figure 1.4.

For the mostly used 2D layered $(R-NH_3)_2MX_4$ perovskites, the organic barrier is optically inert and the optical transition energy is mainly decided by the band gap of wells (inorganic sheets). The width of the wells is mainly controlled by the M-X bond length, their depth is controlled by M and X species, and the width of the barrier is controlled by the organic radical R. It is thus possible to tune the sharp resonant emission wavelength
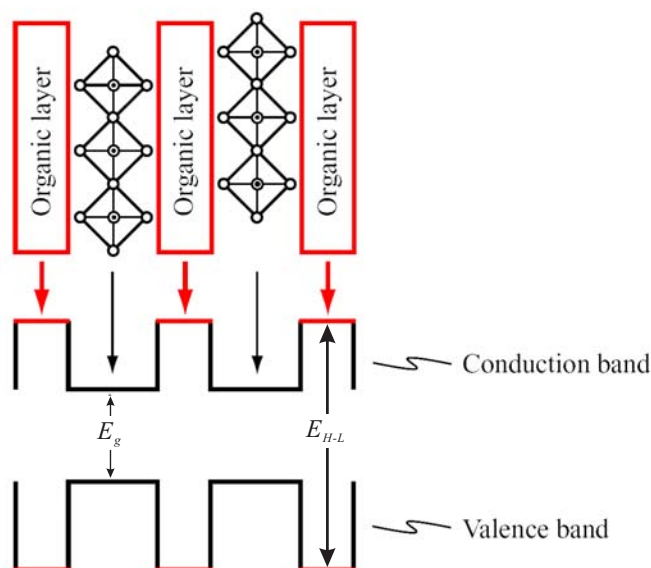
FIGURE 1.4: Schematic electronic structure of 2D layered organic-inorganic perovskites. The thickness of inorganic and organic layers are around 0.6 nm and 1 nm respectively. The HOMO-LUMO energy gap E_{H-L} of organic barriers is larger than the energy gap of inorganic wells E_g. Mitzi et al. (2001b)

in a large range from 320 to 800 nm by substituting different organic parts R, metal cations M or halides X. Papavassiliou and Koutselas (1995); Mitzi (1999b). For example, the perovskites containing Ge and Sn emit in the infrared range, perovskites containing Pb emit in the visible range. Figure 1.5(A) shows the effect, on the luminescent properties, of varying M from germanium(II) to lead(II) in IVB group. The organic amine is $C_4H_9NH_2$. For $(C_4H_9NH_3)_2PbI_4$, the luminescence spectrum consists of a strong peak with a primary maximum at 525 nm and a Full Width at Half-Maximum (FWHM) of approximately 22 nm, while the tin(II) compound shows a significant red-shift, peaking at 625 nm with a larger FWHM of 38 nm. The spectrum of $(C_4H_9NH_3)_2GeI_4$ shows a significantly smaller peak intensity, a much larger FWHM (= 180 nm), and a further red shift, with a peak centered around 690 nm. The photoluminescence spectra show the luminescence peak intensity qualitatively decreasing in the order M= Pb(II) > Sn(II) > Ge(II), while the peak width increases and the peak shifts towards longer wavelength.

Figure 1.5(B) presents the case for which the organic group and M are fixed as $C_4H_9NH_2$ and Pb respectively, while the halogen atom changes from I to Br or Cl. Absorption spectra show that the band gap increases from I to Cl. This change in the electronic transition energy, which is directly related to the halogen species, indicates that the valence band of the underlying electronic structure corresponds to a hybridization of metal and halogen states.

(A)

(B)
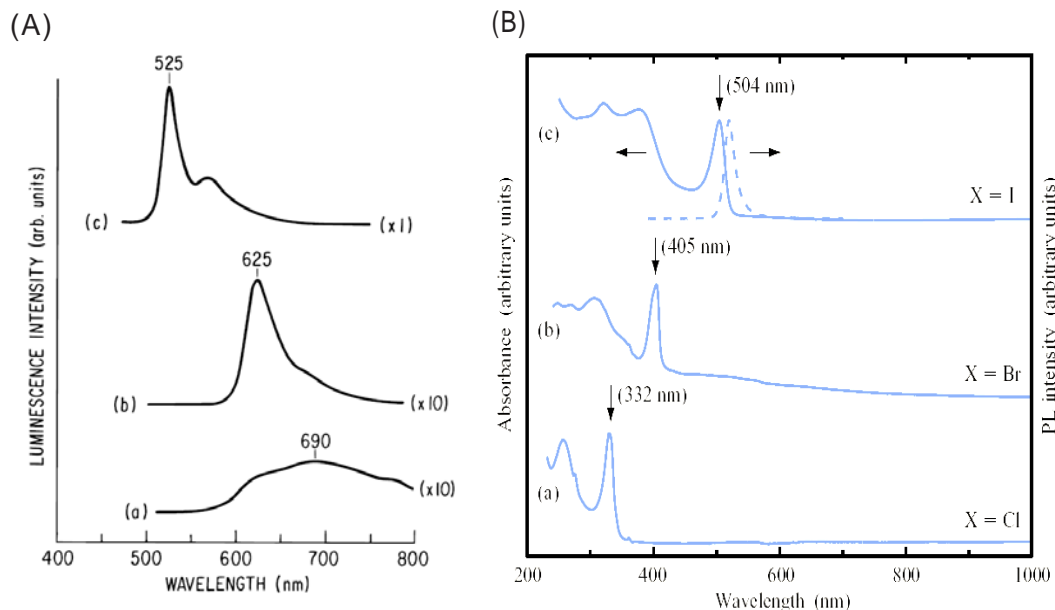
FIGURE 1.5: (A)Photoluminescence spectra for $(C_4H_9\text{-}NH_3)_2MI_4$ crystals with (a) M = Ge, (b) M = Sn, and (c) M = Pb, demonstrating a shift in the photoluminescence peak as a function of group IVB element. Intensities for the M = Ge and Sn spectra have been multiplied by 10 to enable a more convenient comparison with the M = Pb spectrum. The photoluminescence spectra were excited by 457.9 nm light from an argon ion laser. Mitzi (1996) (B) Room-temperature UV-vis absorption spectra for thin films of $(C_4H_9NH_3)_2PbX_4$ with (a) X = Cl, (b) X = Br, (c) X = I. In each spectrum, the arrow indicates the position of the exciton absorption peak (with the wavelength in parentheses). In (c), the corresponding photoluminescence (PL) spectrum (λ_{ex}= 370 nm) is indicated by the dashed curve. Note the small (~15 nm) Stokes shift between the absorption and emission peaks for the excitonic transition.

1.1.1.3 Excitonic effects

An exciton is a bound pair of an electron in conduction band (LUMO band) and a hole in valence band (HOMO band). The exciton, existing in semiconductors or insulators, is created after absorbing a photon by interband transition and the electron and hole attract each other by Coulomb interaction. There are two basic types of excitons: **Wannier-Mott excitons**, which are also called free excitons; and **Frenkel excitons**, which are also called tightly bound excitons.

The Wannier-Mott excitons are generally observed in inorganic semiconductors, in which the dielectric constant is relatively large. Consequently the electric field screening tends to reduce the Coulomb interaction between electrons and holes. As a result, the Wannier-Mott type excitons have a large Bohr radius that encompasses many atoms, and they are delocalized states that can move freely throughout the crystal, as illustrated in Figure 1.6(a), hence they get the other name of "free" excitons. The binding energy E_b is usually small, and the Bohr radius a_B large: E_b and a_B are of the order of 5 meV -100 Å in GaAs, 10 meV - 70 Å in CdTe, 30 meV -30 Å in GaN, 60 meV - 10 Å in ZnO.

(a) Free exciton   (b) Tightly bound exciton
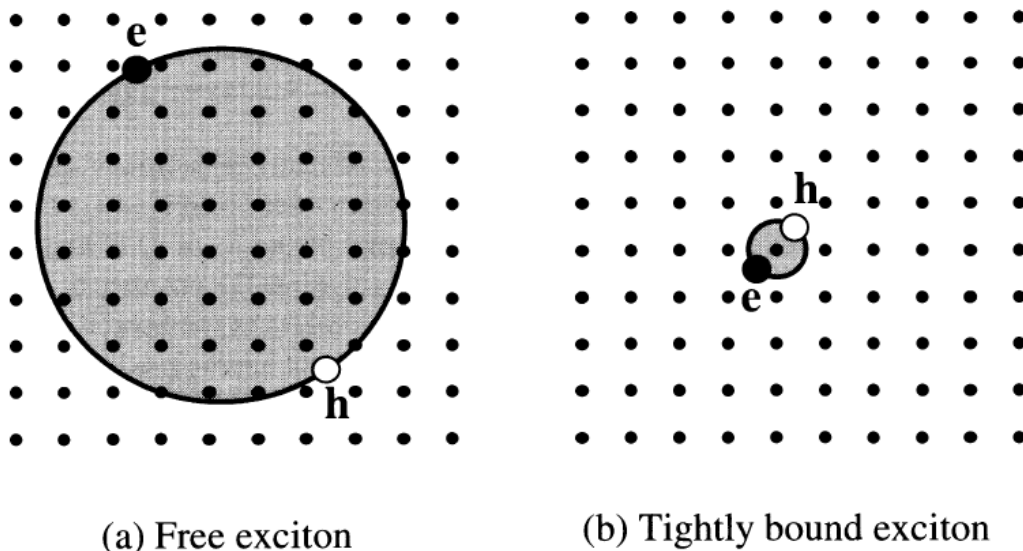
FIGURE 1.6: Schematic diagram of: (a) a free exciton, called Wannier-Mott exciton, and (b) a tightly bound exciton, called Frenkel exciton. Fox (2001)

By contrast, the Frenkel excitons have a much smaller Bohr radius which is comparable to the size of the unit cell, as shown in 1.6(b). This makes them localized states which are tightly bound to specific atoms or molecules; hence they are given the name of "tightly bound" excitons. Tightly bound excitons possess larger binding energy, on the order of 100 meV to 1000 meV, and are much less mobile than free excitons. They have to move through the crystal by hopping from one atom site to another. Fox (2001)

In our perovskites structures, because of the organic barriers, the excitons are confined in inorganic sheets. Because of the quantum confinement effect in the very thin inorganic layers (a fraction of nm), Coulomb interaction between an electron and a hole is strongly enhanced in such kind of molecules. Additionally, by virtue of the high contrast in dielectric constants between the organic layers and the PbX_4^{2-} layers, the Coulomb interaction in the well is hardly screened by the presence of the barrier. Therefore, in 2D layered perovskites, the interaction between an electron and a hole is strengthened resulting in very large binding energies of several hundreds of meV (300-400 meV for $(C_6H_5CH_2CH_4NH_3)_2PbI_4$) and small Bohr radii a_B of the order of the Angstroem (1.7 Å for $(C_6H_5CH_2CH_4NH_3)_2PbI_4$). Ishihara et al. (1992); Hong et al. (1992); Gauthron et al. (2010) . The exciton binding energy depends on the nature of the metal cation: It has been established, for example, in the related $(C_6H_5CH_2CH_4NH_3)_2MI_4$ system, that the exciton binding energy decreases from > 230 meV for M = Pb to 160 - 190 meV for M = Sn.

In this thesis, we will focus our attention on the Pb based perovskites group which has superior optical properties.

1.2 Deposition technique

The deposition technique is a quite important issue for perovskites studies, because many scientific researches and potential applications involving the organic-inorganic hybrids greatly depend on the availability of simple and reliable thin film fabrication techniques. However, deposition of hybrid materials often faces some challenges. A first one is to find an appropriate solvent to adapt the solution based deposition method, because different physical and chemical character of the organic and inorganic components, and also, adverse wetting characteristics of some substrates, make deposition inhomogeneous. Another difficulty is the decomposition or dissociation of the organic component which limits the thermal related methods to a relatively low temperature range (typically below 300 °C). Despite these difficulties, there are still a number of important opportunities for thin film deposition or crystal growth of organic-inorganic hybrids perovskites, such as two-step dipping technique, spin coating, stamping, Langmuir-Blodgett (LB), two-source thermal evaporation, solution evaporation and so on, which make possible the applications of perovskites as organic-inorganic electronic or photonic devices. Here we briefly introduce several simple deposition techniques in following paragraphs.

1.2.1 Two-step dip-processing

In this method, a metal halide film is previously deposited by vacuum evaporation or solution deposition, this film is then dipped into a solution containing the organic cation. The solvent for the dipping solution is selected so that the organic salt is soluble in it, but the starting metal halide and the final organic-inorganic hybrid are not soluble. In this case, the organic cations in solution intercalate into and rapidly react with the metal halide on the substrate and form a crystalline film of the desired hybrid, as it is described in Figure 1.7.

For the perovskite family, $(R-NH_3)_2(CH_3NH_3)_{n-1} MnI_{3n+1}$ (R = butyl or phenethyl; M = Pb or Sn; n = 1 or 2), toluene/2-propanol mixture is a suitable solvent for the organic salt. The dipping times are relatively short: several seconds to several minutes, depending on the system. For example, a film of $(C_4H_9NH_3)_2PbI_4$ was formed from a vacuum deposited film of PbI_2 (See Figure 1.7(a)) by dipping it into a butylammonium iodide solution, the dipping time for the reaction was 1-3 min, which depends on the thickness of the PbI_2 film (2000-3000 Å). After dipping, the films were immediately immersed in a rinse solution of the same solvent ratio as the initial dipping solution (but with no organic salt) and dried in vacuum. As seen in Figure 1.7(b), the resulting films exhibit the characteristic XRD $(0\,0\,l)$ reflections of the organic-inorganic perovskite (and sometimes weak off-axis reflections), as well as the characteristic photoluminescence spectrum (Figure 1.7(c)) of the $(C_4H_9NH_3)_2PbI_4$ perovskite.
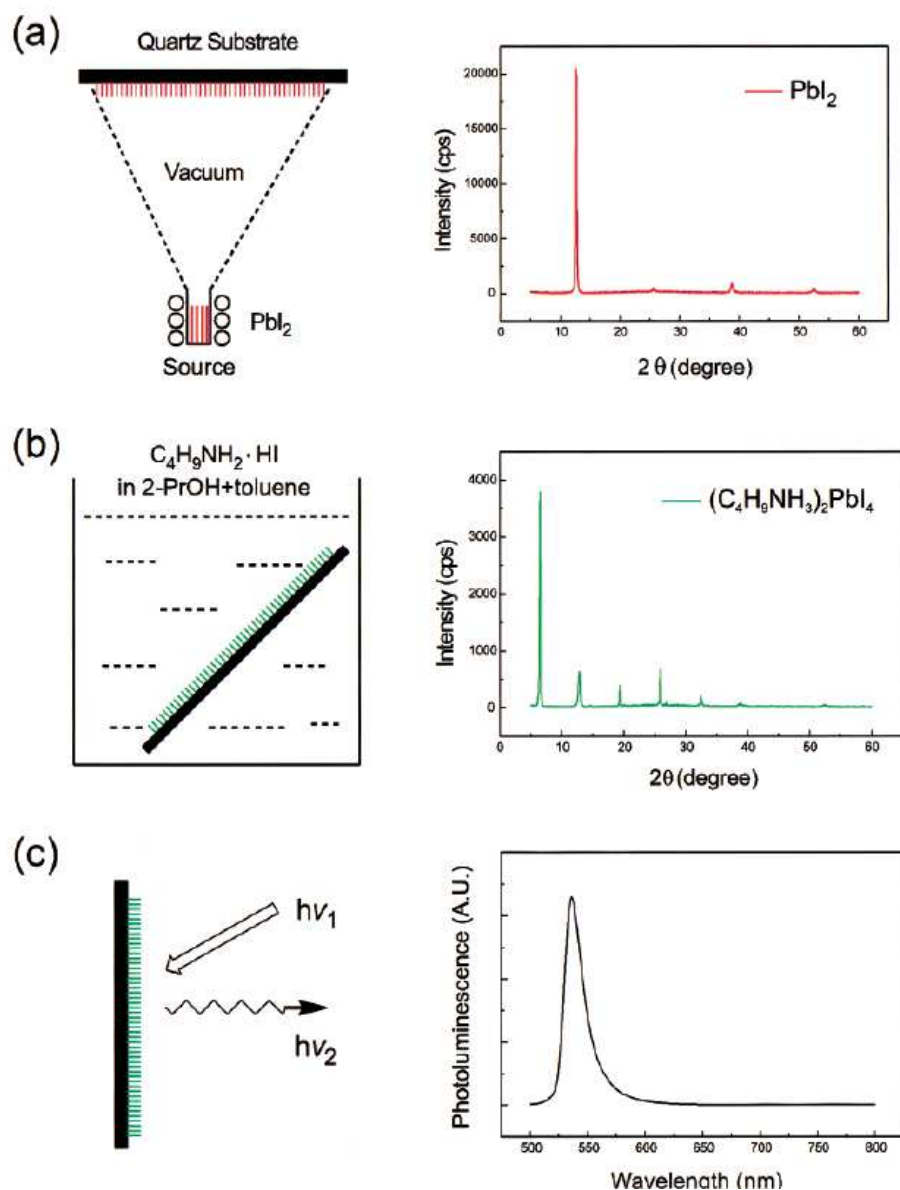
FIGURE 1.7: Schematic representation of the two-step dipping technique. In (a), a film of the metal halide (in this case PbI_2) is deposited onto a substrate using vacuum evaporation, yielding an ordered film with the characteristic X-ray pattern. The metal halide film is then (b) dipped into a solution containing the organic cation (in this case $C_4H_9NH_3{}^+$). The solvent (e.g., a mixture of 2-propanol and toluene) should be a good solvent for the organic cation but not for the metal halide or the resulting hybrid. The resulting film after dipping has the characteristic X-ray pattern of the hybrid perovskite, as well as (c) the characteristic room temperature photoluminescence spectrum of the . Mitzi (2001b)

Two-step dip-processing is a convenient method which can be used for a variety of organics and inorganics, even if they have incompatible solubility characteristics. Mitzi (2001b)

1.2.2 Thermal evaporation technique

The thermal evaporation method was firstly used by M. Era et al in 1997. They performed the dual-source vapor deposition by using lead iodide PbI_2 and organic ammonium iodide RNH_3I, in particular, the 2-phenylethylammonium iodide $C_6H_5C_2H_4NH_3I$ (PhEI). Era et al. (1997)

As it is shown in Figure 1.8(a), PbI_2 and PhEI were evaporated and deposited simultaneously on fused quartz substrates under a pressure of about 10^{-6} Torr. The deposition rate and the deposited amount were monitored with a quartz oscillator balance. Figure 1.8(b) shows the absorption spectrum of the vacuum-deposited film. The depo-
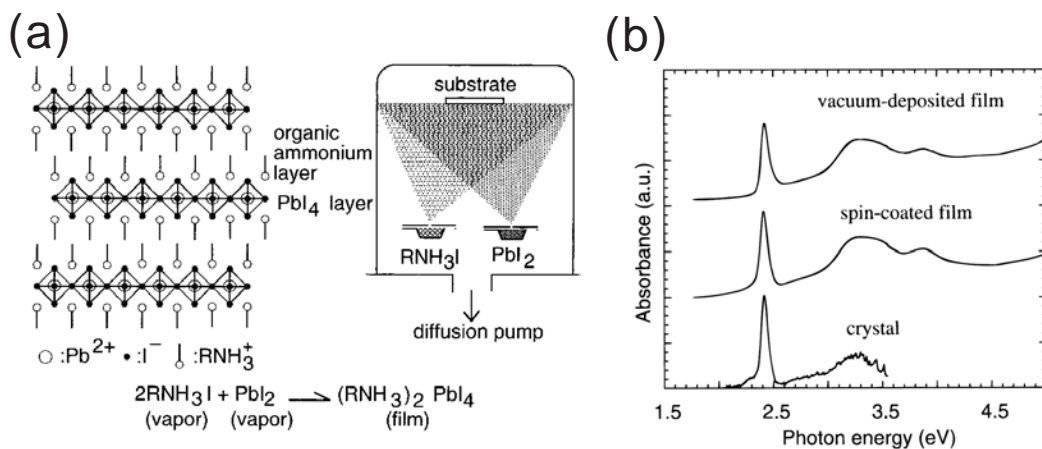
FIGURE 1.8: (a) Schematic representation of the structure of layered perovskites $(RNH_3)_2PbI_4$ and preparation process of layered perovskites using the dual-source vapor deposition. (b) The absorption spectrum of the co-deposited film of PbI_2 and phenethylammonium iodide. The absorption spectra of the spin-coated film and the crystal of the layered perovskite with phenethylammonium layer are also shown. Era et al. (1997)

sition rates of PbI_2 and PhEI were adjusted to be 7.1 and 21 ng cm^{-2} s^{-1}, respectively. The total amount deposited was 11.4 μg cm^{-2}. In the preparation, the substrates were allowed to stand at room temperature. The crucible temperatures of PbI_2 and PhEI were about 570 K and about 520 K, respectively. The spectrum of the vacuum deposited film corresponds well to those of single crystal and spin-coated films of the layered perovskite $(C_6H_5C_2H_4NH_3)_2PbI_4$. A strong exciton absorption is observed at 2.42 eV and a sharp exciton emission peak at 2.37 eV. Appearance of the strong exciton absorption and sharp exciton emission proves that the layered perovskite structure is organized in the vacuum deposited film. Era et al. (1997)

The benefits of this technique are that it is possible to precisely control the thickness and smoothness of the thin-film surfaces. However, this method has some disadvantage. It is often difficult to balance the organic and inorganic rates, an important criterion for achieving the correct compositions of the resulting perovskite films. Besides, the preparation of various perovskites using different organic components is expected to be

limited because each organic component easily contaminates the inside of the evaporation equipment. In addition, in some cases, the organic salt might not be thermally stable up to the temperatures required for evaporation, making this approach impractical for a certain number of systems.

Recently, another method was developed to deposite perovskites thin films by using a single evaporation source. Mitzi et al. (1999) The apparatus for this single source thermal ablation (SSTA) technique consists of a vacuum chamber, with an electrical feed-through to a thin tantalum sheet heater, as shown in Figure 1.9. The starting charge is deposited on the heater in the form of crystals, powder, or a concentrated solution (which is allowed to dry before ablating). Insoluble powders are ideally placed on the heater in the form of a suspension (in a quick-drying solvent), because this enables the powder to be in better physical and thermal contact with, as well as more evenly dispersed across, the sheet. After establishing a suitable vacuum, a large current is passed through the heater. While the sheet temperature reaches approximately 1000 °C in 1-2 s, the entire starting charge ablates from the heater surface well before it incandesces. The organic and inorganic components reassemble on the substrates (positioned above the tantalum sheet) after ablation to produce optically clear films of the desired product. The key aspect to this process is that the ablation is quick enough for the organic and inorganic components to leave the source at essentially the same time and before the organic component has had a chance to decompose. In many cases (especially with relatively simple organic cations), the as-deposited films are single phase and crystalline, indicating that the organic-inorganic hybrids can reassemble on the substrate at room temperature.
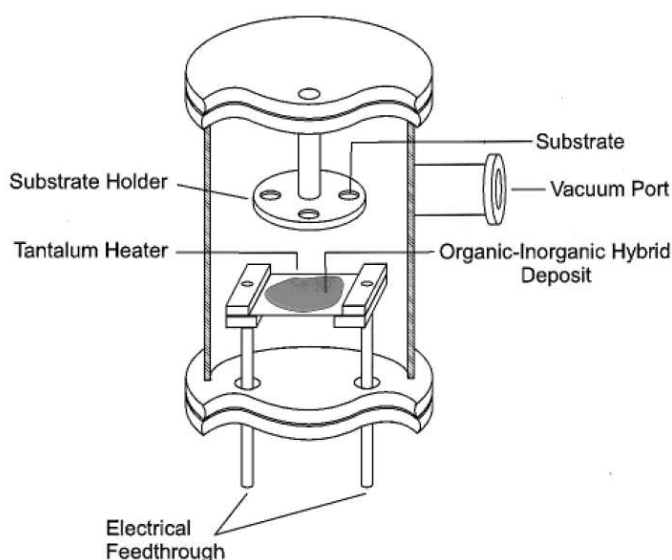
FIGURE 1.9: Schematic cross section of a single source thermal ablation chamber. Mitzi et al. (1999)

1.2.3 Spin-coating technique

Spin-coating is a very convenient technique widely applied to thin film deposition. It can be considered as a special case of solution crystal growth, which allows the formation of highly oriented layered perovskites on a substrate, while the solvent is evaporating off. Spin-coating enables deposition of hybrid perovskites on various substrates, including glass, quartz, plastic, sapphire, and silicon. The relevant parameters for this technique include the choice of the substrate, the solvent, the concentration of the hybrid in the solvent, the substrate temperature, and the spin speed. In some cases, pretreating the substrate surface with an appropriate adhesion promoter improves the wetting properties of the solution on the desired substrate. In addition, postdeposition low-temperature annealing (T < 250ºC) of the hybrid films is sometimes employed to improve crystallinity and phase purity. Mitzi et al. (2001b) Comparing with the traditional deposition technique for inorganic semiconductors, spin-coating method doesn't require cumbersome equipments while it gives high-quality films in quite short time (several minutes) in room environment. Therefore, in our study, we will adopt this method for all film sample depositions.

1.3 Applications in opto-electronic devices

The electronic structure of organic-inorganic perovskites brings a lot of interesting optical properties. These properties can be modulated to meet up the requirement of new technical and scientific studies just by modifying a single atom element or organic molecular union at the nanometer length scale. Recently, these organic-inorganic perovskites compounds have been applied to many fields such as energy transfer systems, Ema et al. (2008) electronic devices, Era et al. (1994); Chondroudis and Mitzi (1999); Kagan et al. (1999); Koutselas et al. (2011); Im et al. (2011) nonlinear phenomena study, Calabrese et al. (1991) as well as strong coupling with cavity photons or surface plasma. Bréhier et al. (2006); Lanty et al. (2008b); Symonds et al. (2007, 2008)

The interesting optical and electrical properties of organic-inorganic perovskites, along with the low cost processing make them strong potential candidates to be applied to optoelectronic devices, such as OILEDs, solar cells Kojima et al. (2009); Li et al. (2010); Koutselas et al. (2011) and solid organic lasers. Among all the applications, we choose several examples presented in the following paragraphs.

1.3.1 Electroluminescence

It has been reported by M. Era et al. that a thin film heterostructure electroluminescent (EL) device was fabricated by employing $(C_6H_5C_2H_4NH_3)_2PbI_4$ (PEPI) as

the active light emitting component. Era et al. (1994) This device was designed with the architecture of standard OLEDs, it was the first organic-inorganic electroluminescent device (OILED). Figure 1.10(a) presents the device structure. It consists of an
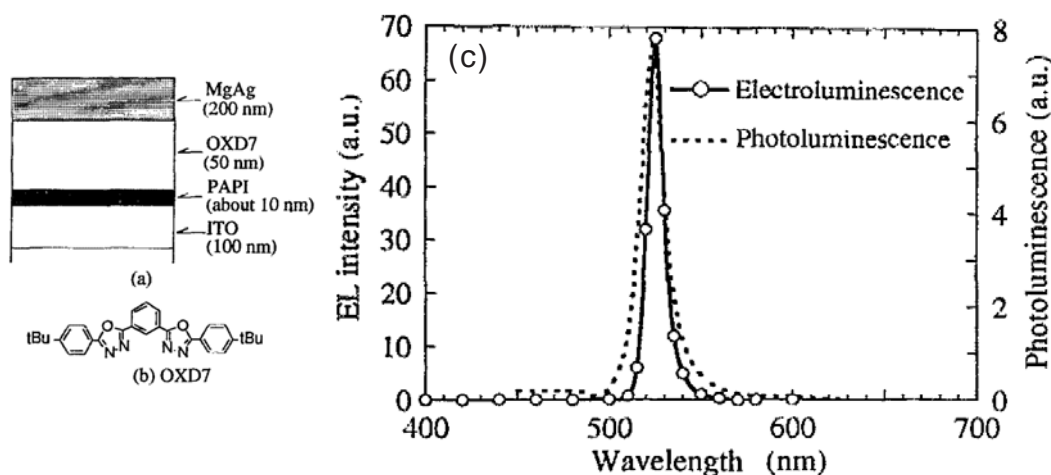
FIGURE 1.10: Device structure of an organic-inorganic heterostructure EL device using a PEPI spin-coated film (a) and molecular structure of an oxadiazole derivative OXD7 (in the scheme (a), PAPI states for PEPI) (b). Electroluminescence spectrum of an organic-inorganic heterostructure device using a PEPI spin-coated film at liquid-nitrogen temperature (c). The dotted line shows photoluminescence spectrum of a PEPI spin-coated film. Era et al. (1994)

indium-tin-oxid (ITO) anode, a PEPI emitter, an electron transport layer of an oxadiazole derivative (OXD7) and an MgAg cathode. In Figure 1.10(c), the EL spectrum of the device corresponded well to the photoluminescence spectrum of the PEPI film; the emission was peaking at 520 nm and half-width of the emission was about 10 nm at liquid-nitrogen temperature. Intense EL of more than 10 000 cd m^{-2} was obtained at 2 A cm^{-2} at liquid-nitrogen temperature in the device.

Very recently, an organic-inorganic perovskites LED working at room temperature was firstly created. Koutselas et al. (2011) This device is based on $(OL)_2PbX_4$ perovskites, where OL represents $(CH_2)_7CH=CH(CH_2)_8NH_3^+$ and X = I, Br, and Cl. Its structure is shown in Figure 1.11(a), this LED exhibits naked eye electroluminescence at room temperature. As presented in Figure 1.11(b), EL spectrum of $(OL)_2PbCl_4$ exhibits a peak at 360 nm, EL spectrum of $(OL)_2PbBr_4$ exhibits peaks at 415 and 475 nm and EL spectrum of $(OL)_2PbI_4$ exhibits peaks at 546 and 583 nm. These peaks are close to the low-energy PL peaks.

1.3.2 Solar cells

Among the optoelectronic applications, solar cell is one of the most attractive applications, because of the promising potential to transfer renewable solar energy to electrical
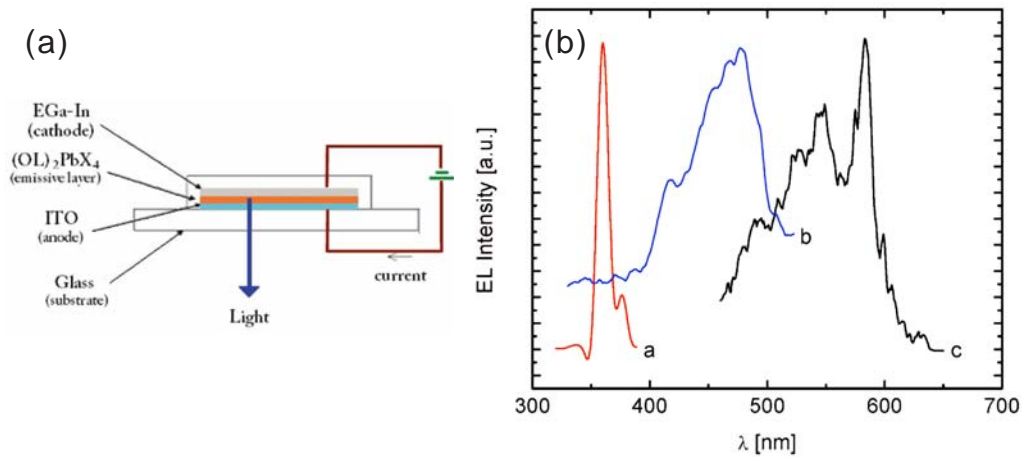
FIGURE 1.11: (a) Schematic representation of the LED device structure. (b) Electroluminescence spectra of the diodes ITO/(OL)$_2$PbX$_4$/ Ga-In where X = Cl, curve a; Br, curve b; and I, curve c. Koutselas et al. (2011)

energy. For the past years, numerous inorganic semiconductor quantum dots (QDs) materials have been tested to confirm their photovoltaic performance in QD-sensitized solar cell structures. However, photovoltaic performance was mostly poor, with conversion efficiency less than 1% at standard 1 sun illumination, until the report on CdS QD-sensitized solar cell with efficiency exceeding 1% in 2008. Lee et al. (2008) Soon after, rapid progress has been made and, as a result, 4-5% efficiencies were recently achieved by using metal chalcogenides. Chang et al. (2010); Yu et al. (2011)

Although metal chalcogenide QDs seem to be excellent inorganic sensitizers for QD-sensitized solar cells, recombination and chemical instability have been issued in ill-defined sulfur-based redox electrolyte. Hodes (2008); Im et al. (2011) To overcome such problems in metal chalcogenide QDs, lead iodide based perovskite-type sensitizers were thus introduced. Kojima et al. (2009) J. H. Im et al. have recently fabricated highly efficient quantum-dot-sensitized solar cell by using 2-3 nm sized perovskite (CH$_3$NH$_3$)PbI$_3$ nanocrystals. Figure 1.12 shows the photocurrent-voltage curve of an optimized (CH$_3$NH$_3$)PbI$_3$ QD-sensitized TiO$_2$ film. The improvement has been achieved by surface modification of TiO$_2$ with Pb(NO$_3$)$_2$ prior to deposition of perovskite QD. This QD-sensitized solar cell film exhibits a superior conversion efficiency up to 6.54%, which is so far the highest efficiency among the reported QD sensitizers.

1.3.3 Microcavities

The research on microcavities containing semiconductors is a very important topics since two decades, because such confined systems allow the control of both the electronic and photonic states, making it ideal for the study of cavity polaritons in strong coupling regime. It provides powerful tools to study the light-matter interaction, Weisbuch et al. (1992); Skolnick et al. (1998) and may lead to Bose-Einstein condensates Kasprzak et al.
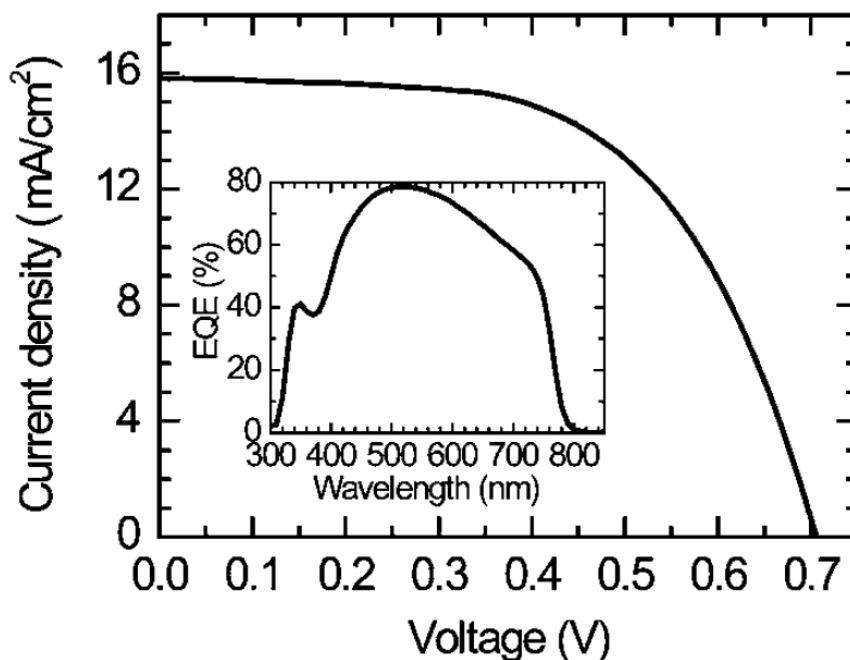
FIGURE 1.12: Photocurrent-voltage curve and EQE (External Quantum Efficiency) for the perovskite $(CH_3NH_3)PbI_3$ QD-sensitized TiO_2 film whose surface was modified with $Pb(NO_3)_2$. Thickness of TiO_2 film was 3.6 mm and the redox electrolyte used was composed of 0.9 M LiI, 0.45 M I_2, 0.5 M tert-butylpyridine and 0.05 M urea in ethyl acetate. Koutselas et al. (2011)

(2006) and the realization of low threshold polariton laser without population inversion Saba et al. (2001).

The strong coupling regime has been investigated for both inorganic and organic semiconductor materials. However, most polaritons in inorganic microcavities only exist at low temperature (for instance, the GaAs/GaAlAs quantum well cavities operating at 20 K), due to the small exciton binding energy in semiconductors (for instance 5 meV for GaAs). This disadvantage experimentally limits the application in devices. Other materials such as GaN Christopoulos et al. (2007); Antoine-Vincent et al. (2003), ZnSe Sermage and Fishman (1981), ZnO van Vugt et al. (2006), or organic molecules Lidzey et al. (1998), whose excitons survive at higher temperatures, are also candidates for room-temperature operating microcavities. But till now, the threshold density in organic cavities is still higher than the competing lasing mechanisms in the device, and the organic cavities always suffer problems of thermal-, photo- stability under illumination. In III-nitride microcavities, only modest improvement was obtained compared to weakly coupled GaN QW devices. Furthermore, the optical quality and reproducibility of the devices are often compromised by relatively large compositional inhomogeneities and structural defects. Böttcher et al. (2003); Das et al. (2011)

The 2D layered organic-inorganic perovskites, for example $(C_6H_5C_2H_4NH_3)_2PbI_4$, have large exciton binding energies up to $220(\pm30)$ meV Hong et al. (1992), which is

substantially larger than k_BT at room temperature ($\approx$25 meV). It enables the excitonic effects to be observed at room temperature and therefore it is a good choice as emission center in microcavity. Recently, strong coupling regime with large Rabi splittings of 100-200 meV has been reported at room temperature on microcavities containing perovskites such as $(C_6H_5C_2H_4NH_3)_2PbI_4$, Bréhier et al. (2006); Lanty et al. (2008a) $(C_6H_5C_2H_4NH_3)_2PbCl_4$ Lanty et al. (2008b) and $(C_6H_9C_2H_4NH_3)_2PbI_4$ Pradeesh et al. (2009b). These materials, can be used alone in a cavity, as well as be combined with another inorganic Lanty et al. (2010) or organic exciton Wenus et al. (2006). In particular, in hybrid cavities containing an inorganic semiconductor and an organic material, it is thought that it is possible to enhance the radiative rate of inorganic excitons and that it is interesting to create an electrically driven organic-inorganic laser. Agranovich et al. (1997)

1.4 Conclusion

The organic-inorganic hybrid perovskites are new materials whose use is interesting for fundamental research and applied devices, due to their unique organic-inorganic combined attributes and the enhanced quantum confinement. Till now, there has been a lot of applications fabricated with organic-inorganic perovskites and the results are quite encouraging. In the framework of this thesis, improvement of some optical properties are proposed and an optical device, a vertical microcavity working in the strong coupling regime at room temperature, is realized.

Chapter 2

Synthesis and characterization of $(R-NH_3)_2PbX_4$ perovskites

As mentioned in Chapter 1, organic-inorganic hybrid perovskites possess plenty of interesting properties. In order to get useful information for the further studies and find the most adapted application for specific perovskites, it is necessary to make clear their attributes, especially the optical and structural properties we are interested in. In this chapter we will talk about the fabrication of perovskites samples, from the synthesis of ammonium to the formation of crystals in different forms: two dimensional layered thin films, crystal bulks and nanoparticles. Experimental methods used to characterize crystal structure, surface topography, and optical resonances will be expounded.

2.1 Methods for characterization

In this section, we introduce the characterization techniques that are frequently used in our studies: structural characterization such as X-ray diffraction, atomic force microscopy as well as optical characterization methods: absorbance and photoluminescence spectra, excitation of the photoluminescence, ellipsometry. To present the characterization techniques, we use four common perovskites, which will be extensively studied in the following of this report. These four common perovskites are: phenethylamines tetraiodoplumbate $((C_6H_5C_2H_4NH_3)_2PbI_4)$, phenethylamines tetrabromoplumbate $((C_6H_5C_2H_4NH_3)_2PbBr_4)$, phenethylamines tetrachloroplumbate $((C_6H_5C_2H_4NH_3)_2PbCl_4)$ and phenylmethanamine tetraiodoplumbate $((C_6H_5CH_2NH_3)_2PbI_4)$ which are abbreviated as PEPI, PEPB, PEPC and PMPI respectively. [1]

---

[1] "PE" and "PM" stands for the phenethylamines and phenylmethanamine respectively in its organic part, their chemical structures can be found in Table 3.1; "PI" ("PB", "PC") represents the lead iodide (bromide, chloride) inorganic part of the perovskites.

2.1.1 Structural characterization

2.1.1.1 X-ray diffraction

X-ray diffraction (XRD) is a non-destructive analytical technique which reveals information about the crystallographic structure, such as crystal degree, distribution of the grain orientation, and in particular the reticular spacing. The oriented structure of a crystal behaves like a diffraction reticulum for X-ray radiation. Diffracted waves from different atoms can interfere with each other and form an intensity distribution pattern which contains information on the crystal structure. The relationship between X-rays wavelength and inter-plane distance d is given by Bragg's law: Equation 2.1

$$2dsin\theta = p\lambda. \tag{2.1}$$

Where λ is the wavelength of the X-ray, θ is the scattering angle, and p is an integer representing the order of the diffraction peak. XRD spectra are used to study crystalline structure of perovskites in their various forms: two dimensional thin films, powders, crystal bulks as well as nanoparticles. In this manuscript, XRD experiments have been performed in LPN[2] Marcoussis by L. Largeau and O. Mauguin, and in chemistry department in ECNU[3].

The following diagram 2.1 shows the XRD spectrum of a 50 nm PEPI thin film deposited on fused quartz substrate. Sharp diffraction peaks with equal distances between each other are observed which prove the high crystallinity of this PEPI thin film. The bump between 20º and 30º comes from fused quartz substrate. We can observe diffraction planes from (0 0 2) to (0 0 22), a period of 1.64 nm is accurately estimated from the patterns. This value is very coherent with those given by literature Mitzi et al. (2001b, 1999); Hattori et al. (1996) where the layer spacing d for the PEPI perovskite is found to be 1.6 nm.

2.1.1.2 AFM measurement

The Atomic Force Microscopy (AFM) is a frequently-used tool that we employ to characterize the surface topography of 2D perovskites thin films. It provides us a way to evaluate surface roughness with quantified values. The average surface roughness Δ is defined as:

$$\Delta = \sqrt{\frac{1}{N}\sum_{i=1}^{N}(x_i - x_{ave})^2}, \tag{2.2}$$

---

[2]Laboratoire de Photonique et de Nanostructures.
[3]East China Normal University.
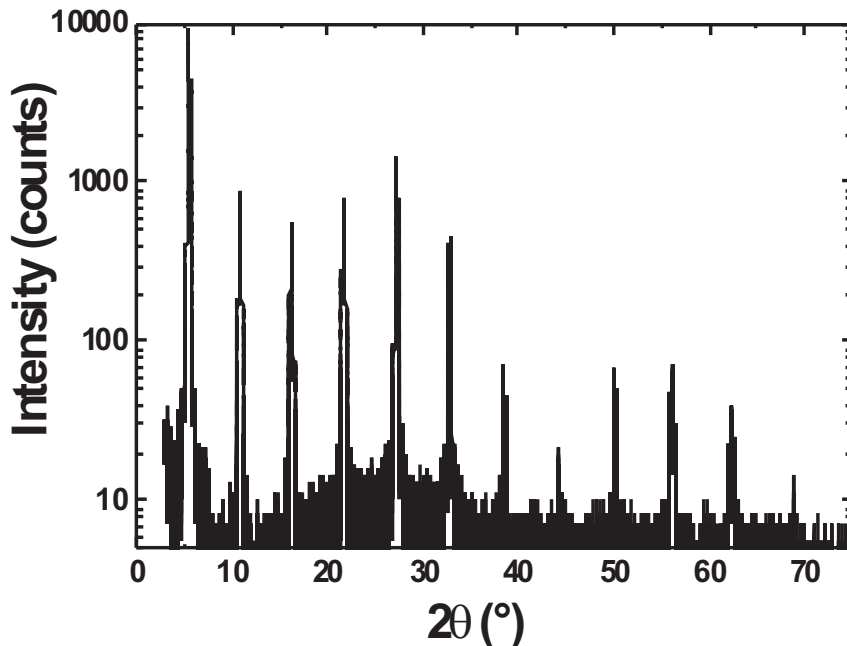
FIGURE 2.1: XRD spectrum of a 50 nm PEPI thin film, performed at LPN Marcoussis.
Gauthron et al. (2010)

where N is the total number of pixels in each AFM image, x_i the height at the *ith* pixel, and x_{ave} is the average height for each AFM image. AFM experiment is performed in PPSM[4], ENS Cachan with a Veeco instrument operating in non-contact mode.

Figure 2.2 presents a typical surface image of a perovskite film. This sample layer is prepared by depositing a 4 wt% PEPI solution by spin-coating on a glass substrate, resulting in an about 30 nm thickness. Its Δ is found to be 5.5 nm. From the image we observe irregular peak-like structures extending all over the surface, which is a common topography situation for most 2D organic-inorganic perovskites films.

2.1.2 Optical characterization

Among many features of the perovskites, optical properties are among the most interesting properties. It permits the perovskites to be used as light source and also active centers in devices. Furthermore, it provides us effective tools for studying their intrinsic electronic structure, for instance the fine quantum wells structure. In this section, we will introduce some frequently-used optical methods for the characterization

---

[4]Laboratoire de Photophysique et Photochimie Supramolécualires et Macromoléculaires.
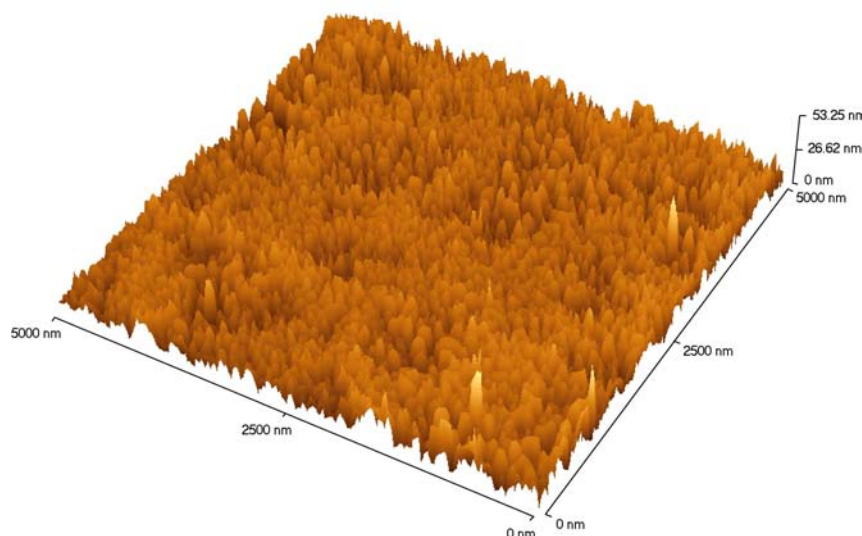
FIGURE 2.2: Topography of a PEPI thin film measured by AFM. Thickness of the film is estimated to be about 30 nm.

of perovskites. Experimental principles and set-ups for absorption, photoluminescence, excitation of the photoluminescence and ellipsometry measurement will be presented.

2.1.2.1 Absorption experiment

Like all other optical media, the absorption of a perovskite layer is quantified in term of optical density. It is also called optical absorbance and is abbreviated as "OA". Its definition is:

$$OA(\lambda) = -log_{10}(\frac{I_1}{I_0}).$$ (2.3)

I_0 is the incident intensity and I_1 is the transmitted intensity through a layer sample. OA spectra at room temperature are measured with a UV/Visible Perkin Elmer Lambda 950 spectrometer and low temperature OA spectra are measured by a home-made setup, whose experimental configuration is described in Figure 2.3.

The light source for low temperature OA measurement is a Xenon lamp Spotlight 5000. It generates a wide emission spectrum from 280 nm to over 800 nm with a highest emission peak around 468 nm, see Figure 2.4. The low temperature environment is provided by a helium exchange gas cryostat. This cryostat operates from 10 K to 325 K and it is connected with a turbomolecular vacuum pump to evacuate the inside chamber to a pressure of 1.0×10^{-4} torr or less. Light emitted from the Xenon lamp source is coupled through an optical fiber into a monochromator (SpectraPro 2150i, Princeton Instruments/Acton^{TM}). The monochromatic light is then collimated by a fused silica lens and guided to pass through the sample, which is settled on the holder inside the cryostat. One quartz slide is introduced into the optical path before the cryostat, as splitter to
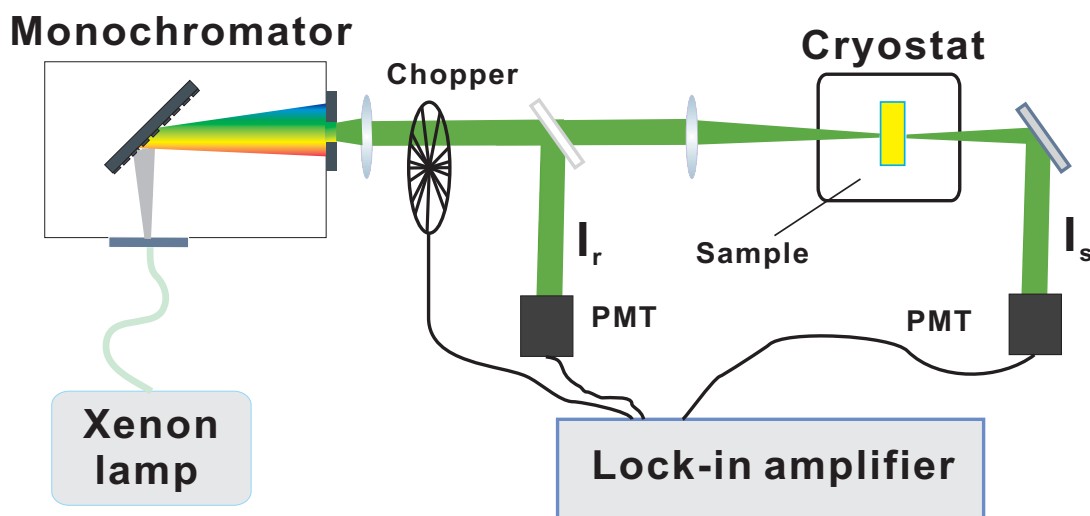
FIGURE 2.3: Experimental setup for optical absorbance measurement at low temperature.
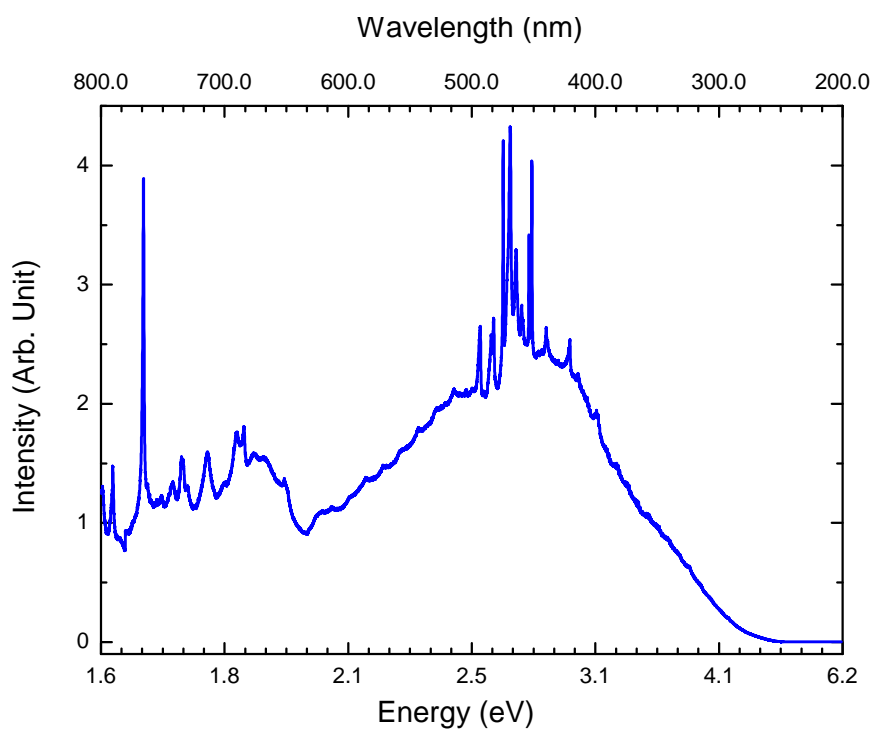
FIGURE 2.4: Emission spectra of Xenon lamp, the intensity is corrected by the response of the PMT detector.

reflect a small portion of light as a reference. The intensity of the reflected reference light I_r and the intensity of the light passed through the sample I_s are collected by two identical photomultipliers (PMT). Signals of the two PMTs are acquired by two lock-in amplifiers, connected to a computer through GPIB interfaces. Here, the measurement of the reference signal allows to correct the error that might be caused by perturbation of light source intensity. A clean quartz substrate is firstly installed on the holder of the cryostat, the PMT signals of reference light I_{r0} and transmitted light I_{s0} are then recorded as a function of light wavelength λ. Then, the perovskite film deposited on the quartz substrate is installed on the holder of the cryostat, and PMT signals of the reference light I_{r1} and transmitted light I_{s1} are recorded at low temperature. In this case,

$$OA(\lambda) = -log_{10}(\frac{I_{s1}/I_{r1}}{I_{s0}/I_{r0}}) = -log_{10}(\frac{I_{s1}}{I_{s0}} \cdot \frac{I_{r0}}{I_{r1}}). \tag{2.4}$$

With these values measured from experiment, OA can be calculated with formula 2.4. Effect of intensity fluctuations of the light source is thus removed by the presence of the ratio I_{r0}/I_{r1} in this two PMTs configuration.

Figure 2.5 shows the absorption spectra of the "PE" series perovskites: PEPI, PEPB and PEPC. The measurement is carried on at room temperature. We observe that the resonance band of each perovskite is very strong and sharp, it depends a lot on their inorganic anion: the absorbance peak of PEPI is located at 2.39 eV (518 nm), that of PEPB is at 3.07 eV (404 nm) and that of PEPC is at 3.64 eV (341 nm). And the FWHM (Full Width at Half Maximum) of them are 73 meV, 84 meV and 82 meV respectively.

2.1.2.2   Photoluminescence experiment

Photoluminescence (PL) is one of the most remarkable properties of 2D layered perovskites. Most perovskites mainly dissipate energy by efficient spontaneous emission after being promoted to an excited state by absorbing photons. The energy position and intensity of photoluminescence peaks depend a lot on the nature of the organic and inorganic components, this will be discussed in Chapter 3. The PL spectra allow to collect information on the electronic band structure and the study of PL peaks intensity as a function of illumination time allows to evaluate the photo-stability of the perovskites.

PL at room temperature

In PL experiment, the perovskite samples are excited by a light source which is the 325 nm line of a HeCd laser or the 405 nm line of a diode laser or a Xenon lamp. The PL emission signal is then collected by a SpectraPro 2500i spectrometer, coupled
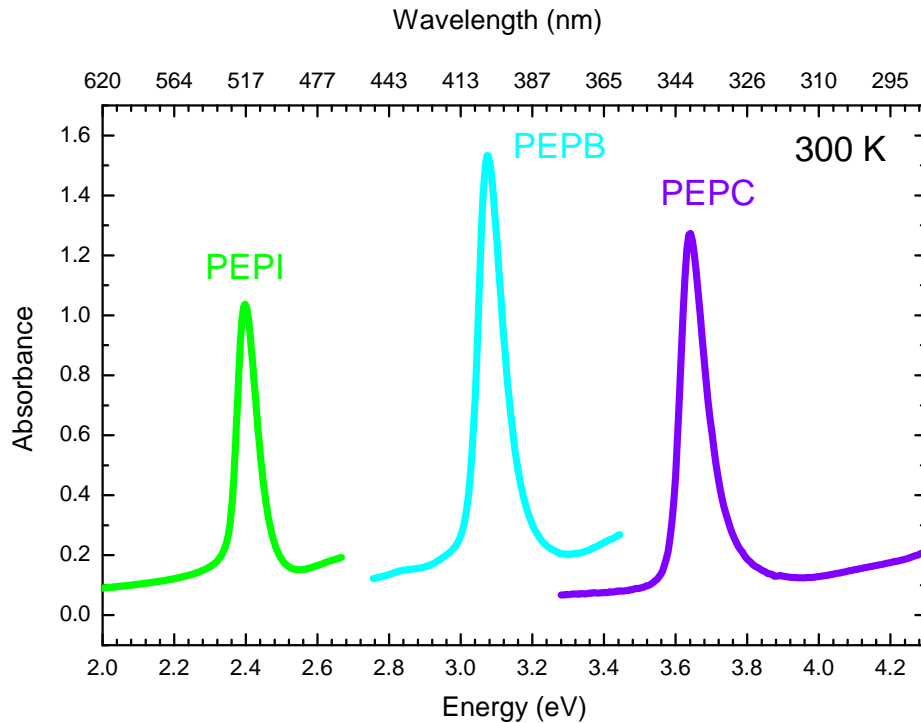
FIGURE 2.5: Absorbance (OA) spectra of PEPI, PEPB and PEPC thin films at room temperature.

to a PIXIS:100B (Ropers Scientific) CCD camera. Figure 2.6 shows the PL spectra of the three typical perovskites PEPI, PEPB and PEPC (the PL intensities are normalized to 1). Their OA spectra are also drawn for comparison. Generally, the PbI_2 based perovskites give green PL around 520 nm, while the $PbBr_2$ and $PbCl_2$ based ones emit violet light and near UV light which are around 400 nm and 340 nm respectively. These emissions are bright and can be seen by naked eyes as shown on the photos in Figure 2.7.

The PL peak position of the PEPI, PEPB and PEPC thin film are centered at 2.37 eV (523 nm), 3.04 eV (408 nm) and 3.61 eV (343 nm) respectively. The FWHM are 51 meV, 56 meV and 71 meV which are narrower than that of some luminescent organic polymers, such as DCM and pyridine, whose FWHM are as large as 300 meV. Meyer et al. (2000) The Stokes-shift, defined as the energy difference between absorption and PL maxima, is usually very small in these 2D perovskites: compared to organic dyes (670 meV for DCM for example), they are only 24 meV in PEPI thin film, 37 meV and 29.4 meV in PEPB and PEPC respectively.
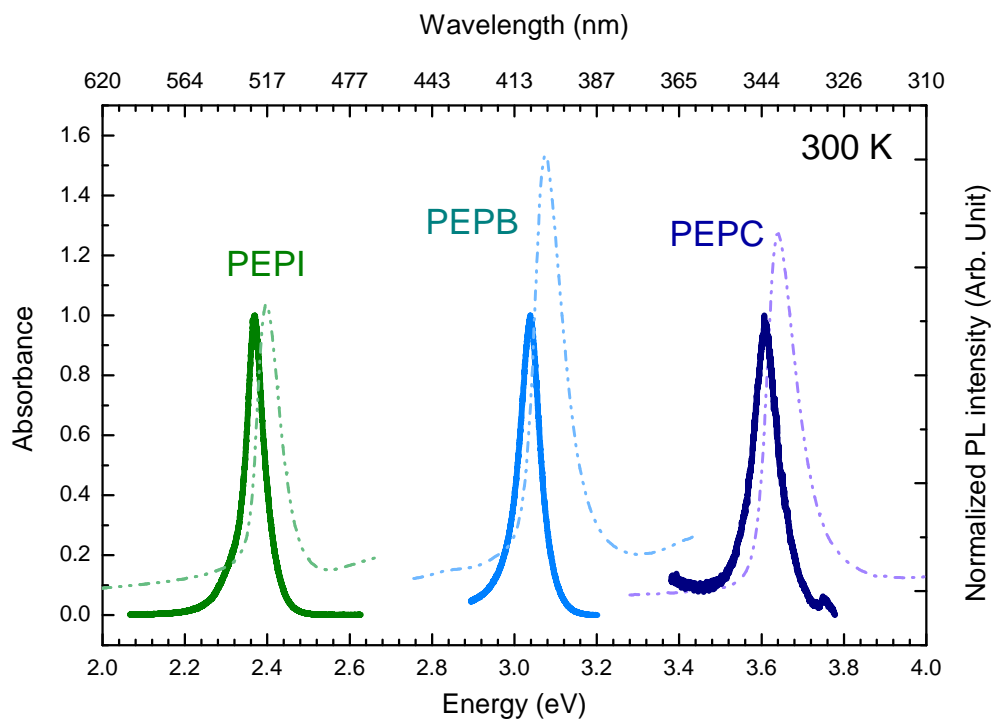
FIGURE 2.6: PL (solid lines) and OA (dashed lines) spectra of PEPI, PEPB and PEPC thin films at room temperature. The excitation is the resonant line 325 nm of a HeCd laser.
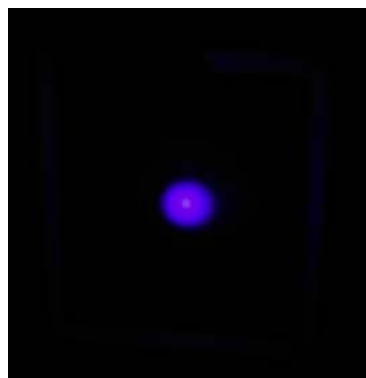
(a) PEPI thin film   (b) PEPB thin film

FIGURE 2.7: Photoluminescence of thin films of several tens nm (a) PEPI (the excitation wavelength is 405 nm, diode laser), (b) PEPB (the excitation wavelength is 325 nm , HeCd laser.

Photobleaching

Although these perovskites are brightly photoluminescent, their PL intensity declines when they are exposed under excitation light for long time, this is photobleaching. We evaluate the photostability of perovskites by measuring the evolution of their PL

intensity as a function of illumination time. From the ratio between the initial PL intensity and the PL intensity after photobleaching in the same experimental condition, we can estimate approximately the robustness of perovskites under illumination.

The following Figure 2.8 shows the photostability of PEPC, PEPB and PEPI thin films. These samples are prepared by spin-coating a 10% solution, the films have an approximate thickness of several tens of nm. This photobleaching experiment is carried
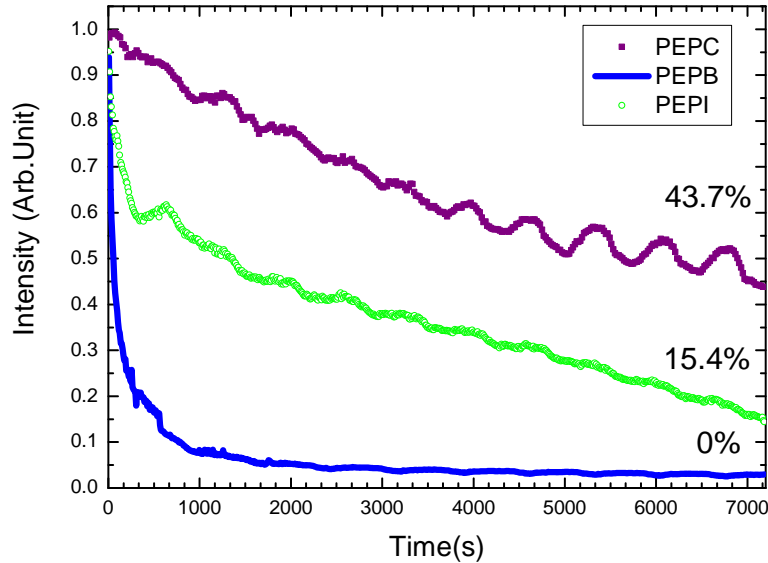
FIGURE 2.8: PL intensity as a function of illumination time for PEPI, PEPB and PEPC thin films in He environment. Laser power is 7 mW (325 nm line).

on in helium environment at 300 K. The PEPC, PEPB and PEPI samples are exposed under a 7 mW HeCd laser (325 nm line). The CCD camera connected to the spectrometer records the PL spectrum at every second during a measurement time of 7000 s. The PL intensity is calculated by integrating the whole PL main peak. We see that the PEPC sample is the most stable one in this group, 43.7% of its initial PL intensity remains after 7000 s. The PEPI sample keeps 15.4% of its initial PL intensity after 7200 s, the PEPB, whose PL intensity decreases to 0%, is the less stable one.

2.1.2.3 Excitation of the photoluminescence

Photoluminescence excitation (PLE) experiment is a specific type of photoluminescence measurement whose principle is to study the PL intensity in a fixed wavelength region while the excitation wavelength varies, as shown in Figure 2.9. To measure the PLE spectrum of perovskites, we have built up an experimental setup by ourselves as
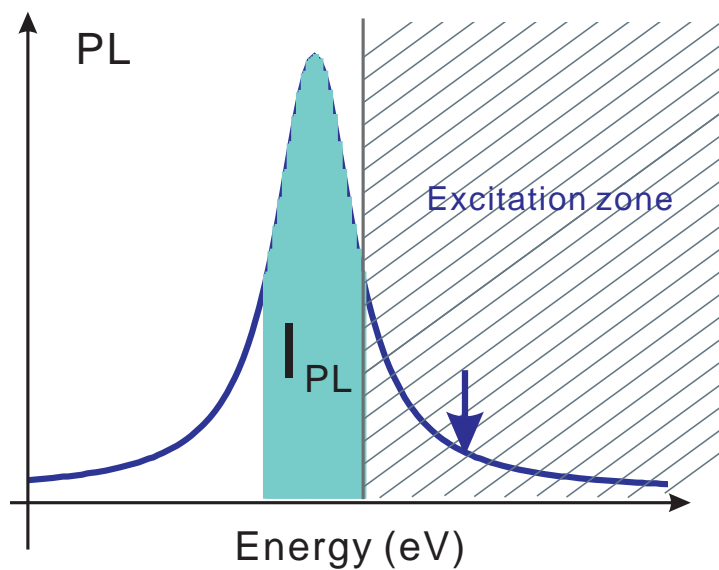
FIGURE 2.9: Principle of PLE (Excitation of the photoluminescence) measurement

shown in Figure 2.10. This configuration, equipped with a cryostat, allows us to obtain PLE spectra at different temperatures, from 10 K to 300 K.
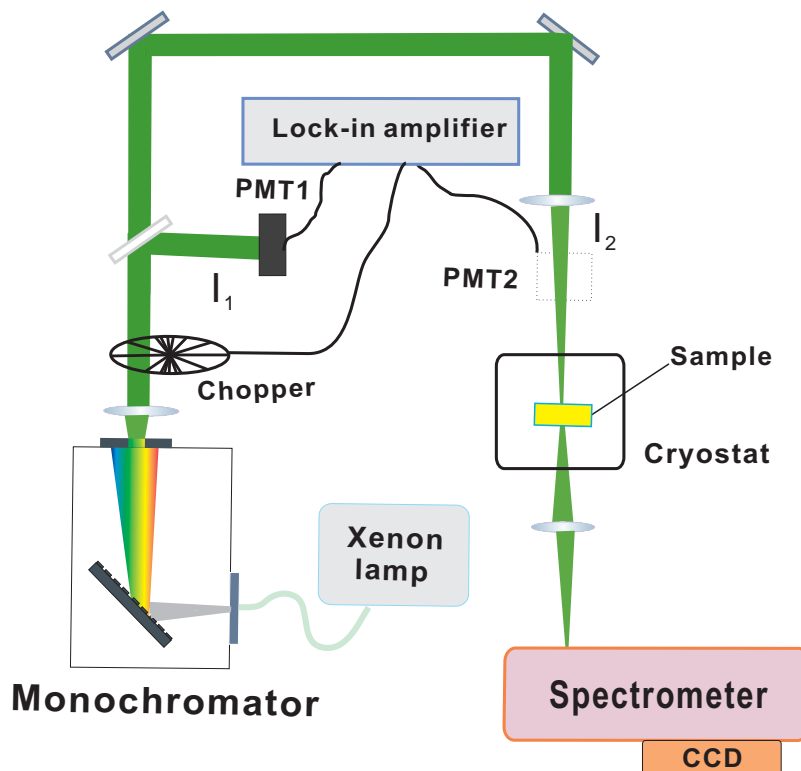
FIGURE 2.10: Experimental set-up of PLE measurement.

The PLE intensity can be described as:

$$I_{PLE}(\lambda) = I_{PL}/I_0(\lambda). \tag{2.5}$$

Where I_{PL} is PL intensity, which is calculated from the PL spectra captured by CCD camera by integrating the region that we are interested in (in blue in Figure 2.9). $I_0(\lambda)$ is the intensity of excitation light arriving on the sample for each wavelength λ.

In the experiment, the excitation source is a Xenon lamp and its output light is guided to and dispersed by a monochromator (SpectraPro 2150i). The single color light filtered from the monochromator is then splitted in two parts by a quartz slide: one part is accumulated by the photomultiplier PMT1 as reference signal I_r and the other part is then guided by several reflective mirrors and focused on the sample which is contained in cryostat chamber. PL signal is collected by a SpectraPro 2500i spectrometer coupled with CCD camera.

Since we read the light intensity from PMTs, the wavelength related response rate of PMT devices R_{PMT} should be taken into consideration:

$$I_r = \frac{V_{PMT1}}{R_{PMT1}}. \tag{2.6}$$

The blue curve in Figure 2.11 is the response curve of PMT (H9307-03) used in our experiment. It is fitted by a 4 order polynomial as followings:

$$y = 4.5928e^{-10} \cdot x^4 - 9.1272e^{-7} \cdot x^3 + 0.00056731 \cdot x^2 - 0.11744 \cdot x + 12.862. \tag{2.7}$$

The semi-transparent quartz slide and the PMT1 are placed near the excitation source because of experimental constraints: it is impossible in our experimental set-up configuration to place continuously a PMT just in front of the sample. However, $I_0(\lambda)$ is the intensity of light arriving on the sample. Between the place of PMT1 and the sample, there are some optical components which can make I_r and $I_0(\lambda)$ different. We define the factor $f(\lambda) = I_r / I_0$: for a settled experimental set-up where all optical components are fixed to their positions, the function $f(\lambda)$ versus λ is unique and is characteristic of the set-up. So, once the set-up is mounted and fixed, $f(\lambda)$ is measured at the beginning of the day, from the ratio between the signals obtained from PMT1 and PMT2, note that PMT1 and PMT2 are identical:

$$f = \frac{I_r}{I_0} = \frac{V_{PMT1}}{V_{PMT2}}. \tag{2.8}$$

The PLE intensity is thus deduced by:

$$I_{PLE}(\lambda) = \frac{I_{PL}}{I_0} = \frac{I_{PL}}{I_r/f} = \frac{I_{PL} \cdot R_{PMT} \cdot f}{V_{PMT1}}.$$
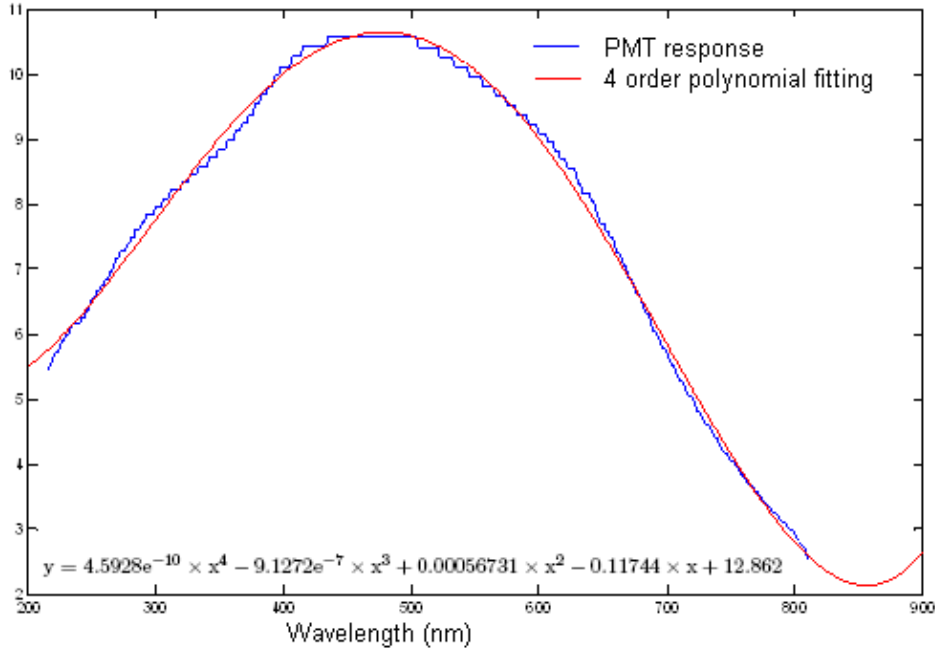
FIGURE 2.11: PMT response curve of the H9307-03 type PMT; the red curve is 4 order polynomial fitting curve

2.1.2.4 Ellipsometry

The absorption and refraction of a medium can be described by a single physical quantity: complex refractive index. It is usually given by the symbol $\tilde{n}$ and is defined by the formula 2.10:

$$\tilde{n} = n + i\kappa. \tag{2.10}$$

In this formula, the real part of the refractive index n is related to the phase speed, while the imaginary part κ indicates the amount of absorption loss when the electromagnetic wave propagates through the material.

Ellipsometry is a very sensitive measurement technique to measure the complex refractive index of thin films. It is a non-destructive method in which we use the reflection properties of a polarized light to probe the dielectric properties of a sample, see Figure 2.12 The polarization state of the light incident upon the sample may be decomposed into an s component, oscillating parallel to the sample surface, and a p component, oscillating parallel to the plane of incidence. The reflected light undergoes amplitude and phase changes for both $p-$ and $s-$ polarized light which are determined by the sample's properties, and ellipsometry measures these changes. The fundamental equation of ellipsometry is written in Equation 2.11:

$$\rho = \frac{R_p}{R_s} = tan\psi \cdot e^{i\Delta}. \tag{2.11}$$
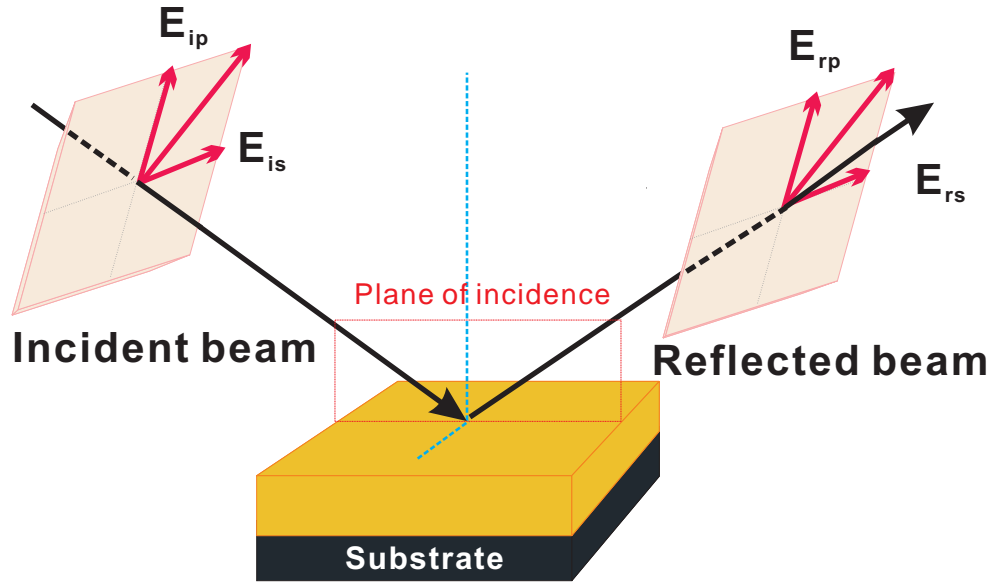
FIGURE 2.12: Principle of ellipsometry measurement

The intensity of the s and p components, after reflection, are denoted by R_s and R_p. Tanψ is the amplitude change upon reflection, and Δ the phase shift. Through an analysis of the polarization state of the light that is reflected from the sample, the technique allows an accurate characterization of a range of properties including the layer thickness and optical constants. Since an ellipsometry experiment measures the ratio of these two values (rather than the absolute value of either), it is very robust, accurate (can achieve angstrom resolution) and reproducible.

In the study of perovskites, we can obtain lots of additional information such as the dielectric constant and oscillator strength with the complex refractive index got from experiment, which are quite necessary in following studies, for example for the design of the microcavities. The type of the ellipsometer in LPQM is SOPRA GES 5 and the measurements are analyzed by software WINELLI II. To acquire the complex index of the PEPI perovskite, a film of PEPI is deposited on a silicon substrate by spin-coating. The thickness of the film is measured as 240 nm by a profilemeter. Figures 2.13 (a) and (b) present tanψ and cosΔ obtained from measurements. Having the experimental values of tanψ and cosΔ, we search for an expression of the dielectric constant $\epsilon(\lambda)$ which allows to report the behavior of the material. For that, we use a model for $\epsilon(\lambda)$ and we use this model to simulate the evolution of ρ as a function of λ. Then we adjust the parameters of this model to fit the experimental values of Tanψ and cosΔ.

To find the expression of $\epsilon(\lambda)$, we are inspired by the information given by the absorption spectrum of PEPI, as shown in Figure 2.14. Several peaks in the OA spectrum can be identified. We modelize each absorption peak as a Lorentz oscillator. The

(a)

(b)
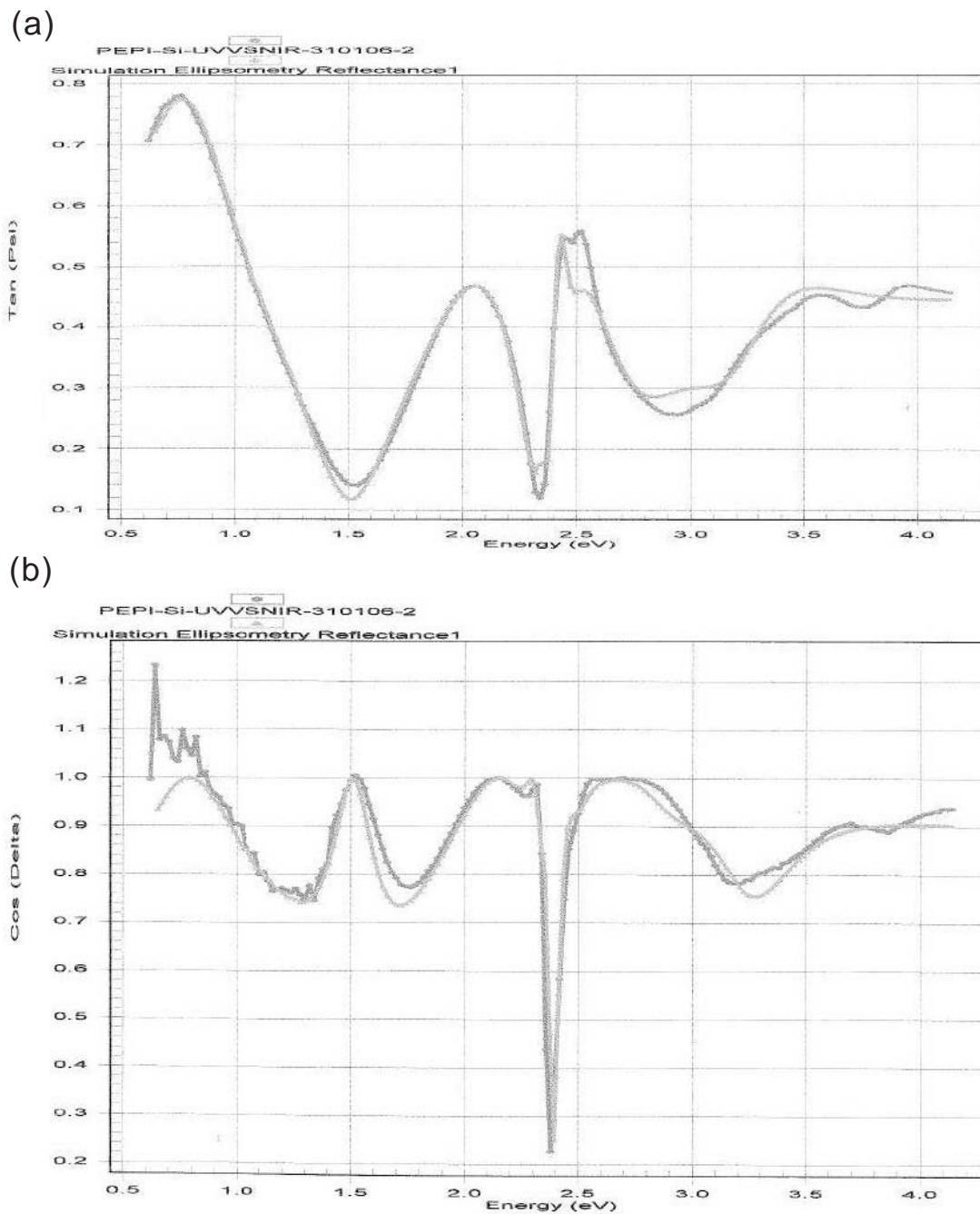
FIGURE 2.13: (a) Tanψ value and (b) CosΔ value as a function of energy for a 240 nm PEPI thin film deposited on silicon substrate. Dark line is the experimental curve and the light line is the fitting curve given by software WINELLI II
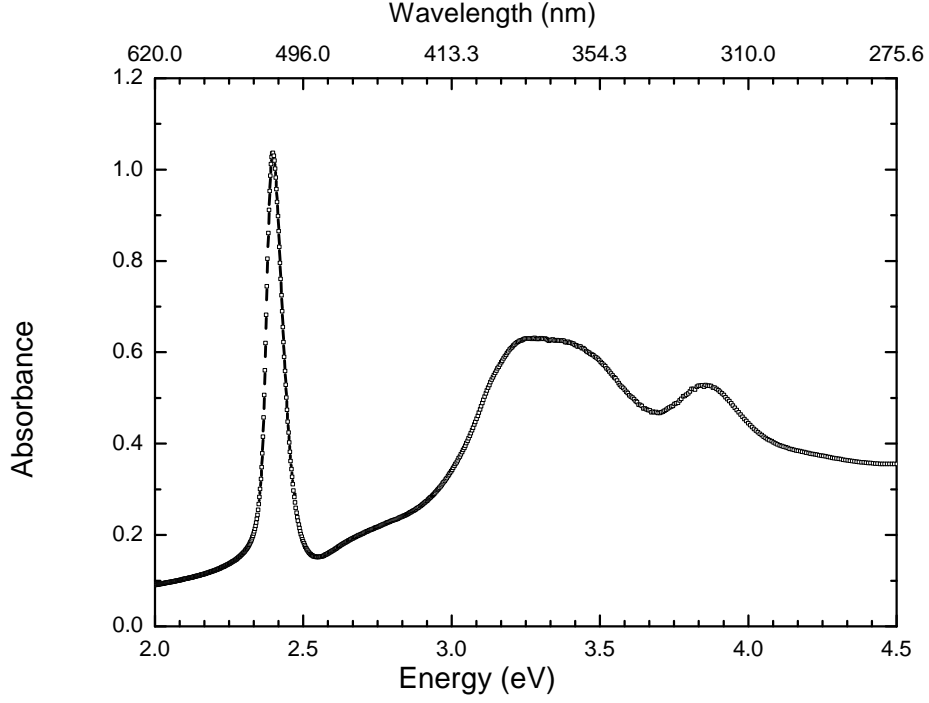
FIGURE 2.14: OA spectrum of a 50 nm thick PEPI film measured at room temperature.

contribution of each Lorentz oscillator to the dielectric constant is:

$$\epsilon(E) = \frac{A}{E_0^2 - E^2 - j\hbar\gamma E}. \tag{2.12}$$

E_0 (in eV) designing the energy position of the absorption peak, γ (in eV) the width of the absorption peak, and A (in eV^2) being related to the oscillator strength f_{osc}:

$$A = \frac{\hbar^2}{\epsilon_0 m_0} \frac{f_{osc}}{L_{tot}}. \tag{2.13}$$

Here, L_{tot} is the thickness of the film. The model of dielectric constant used for layered perovskites is composed by a continuous term and three Lorentzian functions:

$$\epsilon = \epsilon_\infty + \epsilon_1 + \epsilon_2 + \epsilon_3. \tag{2.14}$$

ϵ_∞ is a constant, ϵ_1 and ϵ_2 are related to the peaks at 2.4 eV and 3.2 eV seen in absorption spectrum respectively. ϵ_3 is a large peak which models the continuous absorption Bréhier (2007). Figure 2.15 shows the real n and imaginary (κ) parts of the refractive index ($n + i\kappa = \sqrt{\epsilon}$) of PEPI. The optimum parameters returned by fitting the experimental results are reported in Table 2.1.

The oscillator strength f_{osc} which is associated with the absorbtion of the quantum wells lying at E_{01} (coming from ϵ_1) can be obtained from Equation 2.13, knowing A_1 and
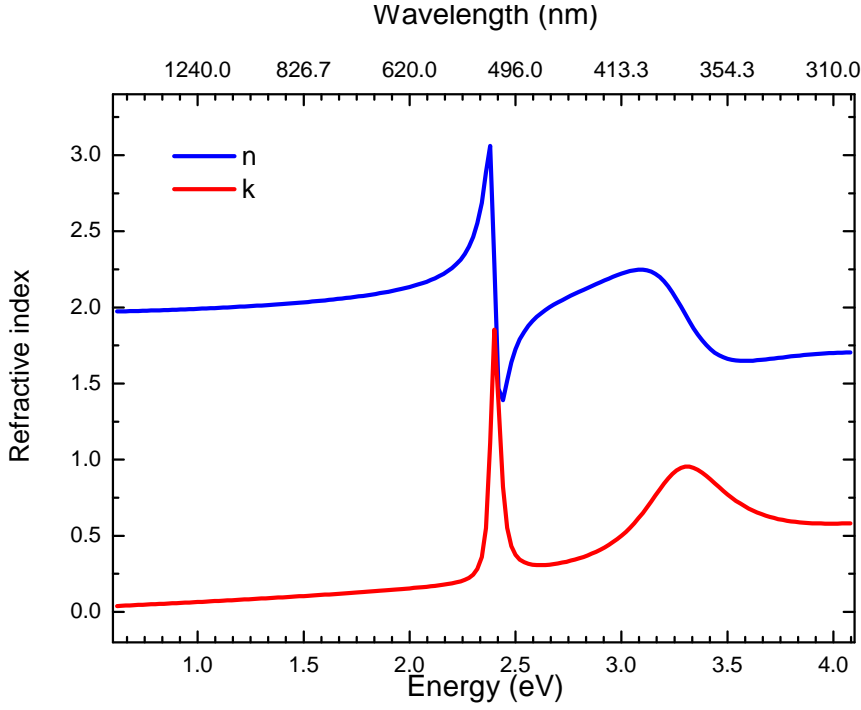
FIGURE 2.15: Refractive index $\tilde{n} = n + i\kappa$ of PEPI film obtained from the fitting of $\tan\psi$ and $\cos\Delta$ in Figure 2.13. The blue curve and red curve represent the real n and imaginary κ parts of the refractive index respectively.

L_{tot} values. We obtain $f_{osc} = 13 \times 10^{15} cm^2$ for the whole film of 240 nm thickness. Since the distance between two quantum wells is 1.6 nm and the number of quantum wells N_{QW} is approximately $N_{QW} = 150$, an oscillator strength per quantum-well $f_{QW} = f_{osc}/N_{QW}$ of about $9 \times 10^{13} cm^2$ can be deduced for PEPI. This is one order of magnitude higher than in conventional inorganic quantum wells such as InGaAs/GaAs structures. Skolnick et al. (1998)

TABLE 2.1: Parameters used to fit the refractive index of PEPI film with Equation 2.14

		A_i (eV^2)	E_{0i} (eV)	γ_i (eV)
ϵ_∞	1.86	-	-	-
ϵ_1	-	0.825	2.394	0.041
ϵ_2	-	3.73	3.25	0.45
ϵ_3	-	38.5	5.1	3.9

2.2 Perovskite based crystals

The perovskites molecules can form crystals spontaneously via interaction among molecules on proper condition, this property is called self-assembly. We are interested in

perovskite crystals because they present interesting optical properties which don't exist in solution. For instance, we see a sharp resonant peak at 517 nm in the OA spectrum of a PEPI thin film, but this peak dosen't exist for PEPI solution, as seen in Figure 2.16. In this section we will introduce the perovskites crystals realized in our laboratory in
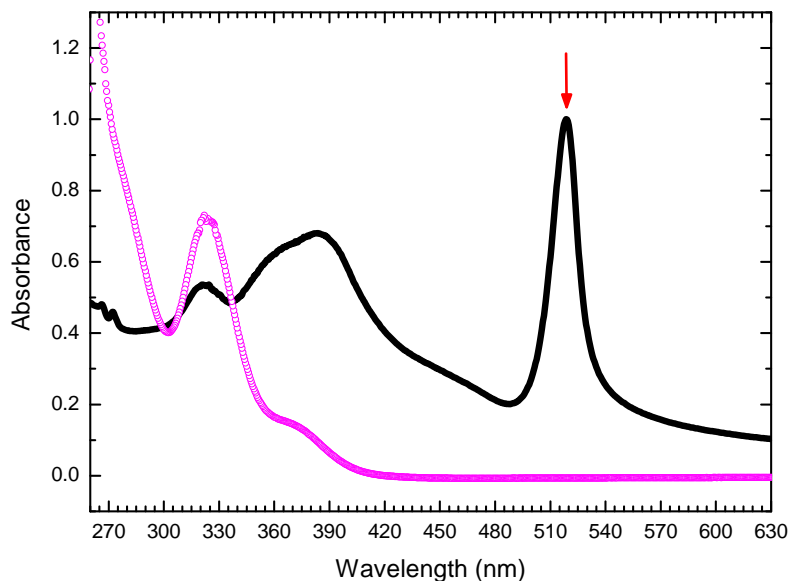
FIGURE 2.16: OA spectra of a 50 nm PEPI thin film (black line) and of a solution containing PEPI dissolved in DMF solvent (pink line).

different forms: layered films, crystal bulks and nanoparticles. Methods of preparation and some factors that may influence surface quality of layered films will be discussed.

2.2.1 Synthesis

The synthesis of perovskites is the most primary and important procedure among perovskites study. Compared with the methodology of traditional semiconductors, the fabrication of perovskites samples is relatively easy. Because they need neither series of cumbersome equipments nor strict environment condition but can be synthesized and deposited simply by soft chemical methods at room temperature, it is possible to design the perovskites as we want by working on the organic part, specially the moiety. Generally there are two steps for synthesis: synthesis of ammonium salts and preparation of perovskites solution. The precursors lead halide salts PbCl$_2$, PbBr$_2$ and PbI$_2$ are purchased from Sigma Aldrich company. For the organic part, we use sometimes commercial available amines. In order to realize some perovskites which possess special functions, such as better stability or larger photon absorption ability, we synthesize also by ourselves some new organic compounds, for instance the pentafluorophenylethyamine and

N-(2-Aminoethyl)naphthalimide whose concrete synthesis method will be introduced in appendix.

Synthesis of ammonium salts

The perovskites that we are interested in and that we synthesize are mainly in form of (R-NH$_3$)$_2$PbX$_4$. In a first step, we transform the as-prepared amines to ammonium salts by reacting the amines with halogen acid. This process is described in formula 2.15:

$$R - NH_2 + HX \Rightarrow R - NH_2 \cdot HX. \tag{2.15}$$
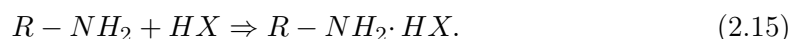
It is a neutralization reaction where the salts are easy to generate with a yield rate of relatively high level (nearly 100%). The halogen acids used to produce corresponding ammonium salts are HI 57 wt%, HBr 48 wt% or HCl 37 wt% aqueous solution. The reaction setup is shown in Figure 2.17.
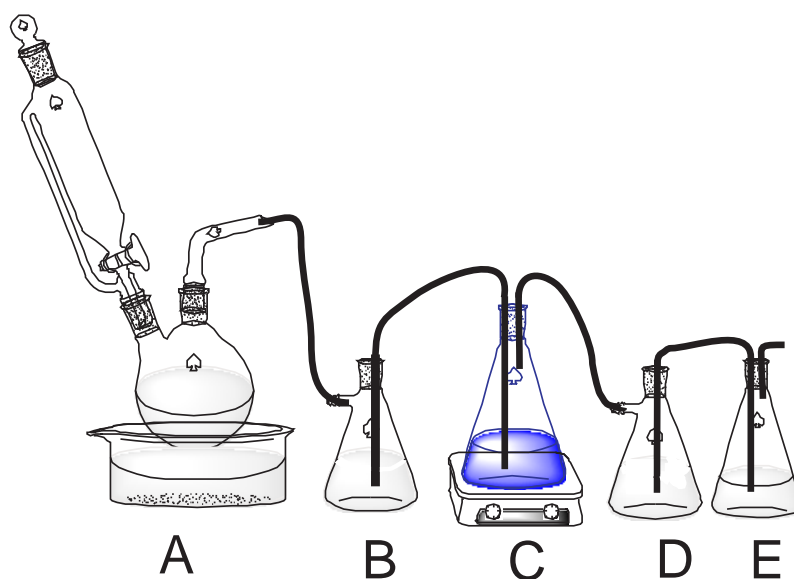
FIGURE 2.17: Reaction set-up to produce the ammonium salts.

Before the reaction, it is necessary to check air impermeability of the whole system to make sure that all pieces are well connected inside and well closed to outside. Applying some vacuum grease to joint parts is helpful for obturation. From left to right, the reaction recipients are marked as "A", "B", "C", "D" and "E" for clarity. The second (B) and the forth (D) conical flasks are used as safety flasks to avoid backwash, in case that the reaction goes on too fast, which would cause the disequilibrium of gas pressure in and out of the closed system.

In the first round bottom flask (A), excess concentrated HX acid is gingerly dropped on P$_2$O$_5$ powder. The flow speed of acid has to be well controlled to be uniform and

slow (about 4-5 drops per second), as the dehydrating process of P$_2$O$_5$ for HX solution is very violent and exothermic. We see that the mist of acid gas leaps up as soon as the acid drop contacts with P$_2$O$_5$. At the same time, it is necessary to cool down the flask with ice-water mixture bath to avoid the blast of glasswares. Gaseous HX is then guided by pipes through the first safety flask to the reaction flask (the third flask in blue) as soon as it is generated. This reaction flask (C) contains an amount of amine which is previously dissolved in diethyl ether. There are many advantages to choose diethyl ether as reaction environment: on one hand, diethyl ether is a very good solvent for amines but the salts have very low solubility in it. Therefore the generated ammonium salts tend to precipitate out of solution and the reaction equilibrium keeps on heading to the products side. On the other hand, the diethyl ether solvent enables splendid separation between reactant and final salts which insures the purity of ammonium salts. When HX gas contacts with that solution, small white grains of ammonium immediately appear in the reaction bottle under agitation. Meanwhile, an ice-water bath under reaction flask will favor the precipitation process. The unreacted gaseous HX after the reaction flask is guided to the last flask (E) which serves as gas-washing bottle containing NaOH aqueous solution to be neutralized. When the reaction is totally finished, we filter out the R-NH$_2$HX salts and rinse them with diethyl ether twice and with n-pentane once to remove the unreacted acid HX or R-NH$_2$, as well as water traces. The salts R-NH$_2$HX are then put under vacuum line for several hours to eliminate the residual solvent. After that, the salts are transferred into a desiccator to be dried.

However this gaseous acid method may cause the pipes to be eroded, and it takes relatively long time to get enough amount of acid for reaction. Besides this method, we also try to synthesize ammounium salts by adding aqueous acid to amines in diethyl ether solution directly. This method simplifies the fabrication procedure and enables us to fabricate larger quantity of ammonium products by single reaction. But it might introduce some water to reaction solution which is unfavorable for the generation of ammonium salts. As many salts have good solubility in polar solvents such as water, the rate of production declines. For example the ammonium salt of 2-cyclooctyl-ethylamine hydroiodide is very difficult to precipitate in this kind of solution environment, it remains in aqueous phase in the lower layer reaction flask. In this case we can add more diethyl ether to decrease the ratio of water/diethyl ether in order the ammonium salts are forced to precipitate.

After synthesis, the conservation of ammonium should be cautious. Because of the hygroscopicity nature of some of the salts, it is better to keep them in a dry and dark place to prevent deterioration.

Preparation of perovskites solution

After several days of drying in desiccator, the salts are dry. These dry ammonium salts are used to prepare perovskites solution. In this step, R-NH$_2$HX ammonium salt is mixed with lead halide PbX$_2$ in stoichiometric amount 2:1 in mole, and dissolved in solvent. This is a coordination reaction and it can be described by the chemical formula:

$$2(R - NH_2 \cdot HX) + MX_2 \Rightarrow (R - NH_3)_2MX_4. \tag{2.16}$$
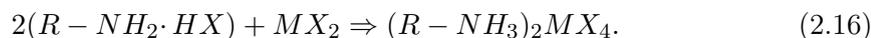
The solution is then put under agitation or in ultrasonic bath until the solutes are totally dissolved and the solution appears limpid. The choice of the solvent is important because we need to consider the solubility for both the organic ammonium and the inorganic lead halide. Dimethylformamide (DMF) or Dimethyl sulfoxide (DMSO) are good solvents in which the perovskites usually have very high solubility. For instance PEPI perovskites solubility reaches up to 25 wt% in DMF solution. Some other solvents such as acetone, or acetonitrile can also be used. But solubility of perovsites in them is relatively poor (less than 5 wt%), and it takes too long to completely dissolve the solutes. This is also the reason why we choose to use mainly DMF as the preferred solvent in our study.

2.2.2 Perovskites in solution

The molecules of perovskites are dispersed in solution. Compared with their crystals, the optical properties of perovskites in solution are very different. Figure 2.18 presents OA spectra of PEPI in DMF solution samples. For comparison, an OA spectrum of PEPI thin film is drawn (grey curve). The pink circle curve stems from diluted samples of PEPI solution (concentration lower than 1 %) contained in a quartz bottle. The black and orange curves come from the sample of PEPI solutions sandwiched between two pieces of glass slides, the concentration of the two solutions are 10 % and 2 %, respectively. The abrupt saturation in spectrum below 295 nm is due to the absorption of glass. The green curve is OA spectrum of DMF solvent that is used for these solution samples. From these OA spectra of PEPI solutions, we see that there is no typical peak at around 520 nm as in the film sample, but we observe some broader peaks in the UV region. The peak around 321 nm is thought to be due to organic components, and it exists in all the PEPI solutions spectra (for diluted solution and also solutions between slides) and also in PEPI thin film samples. Besides the peak at 321 nm, we see two other peaks at 371 nm and 421 nm for the solution samples contained between the two slides. That may be due to the pileups among molecules that accordingly form possibly dimers, trimers... They are more obvious in black and orange curves as a result of higher concentration between the two slides. This evidence helps us to understand that the

large broad band appearing in OA spectra of PEPI film samples around a region from 360 nm to 480 nm may be due to molecules stacking in solid state and informs us that in the thin film samples of perovskites, there is still a percentage of amorphous molecules which are not completely organized.
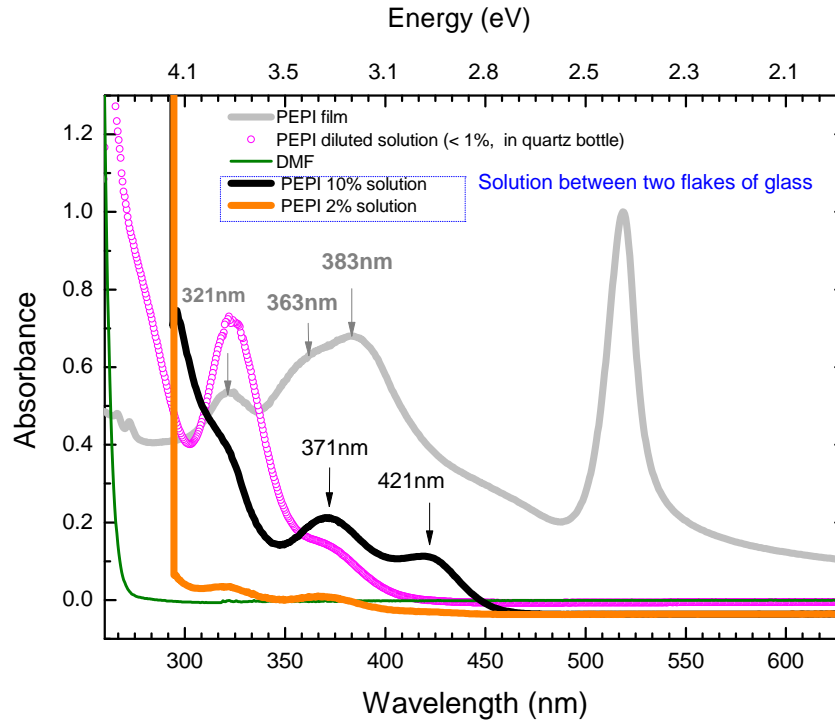
FIGURE 2.18: Absorbance of PEPI perovskites molecules dissolved in DMF solution. Measurement is carried on at room temperature. The grey line is the OA spectrum of a 50 nm PEPI thin film.

2.2.3   2D Layered Perovskites

2.2.3.1   Thin films

a) Deposition and optimization

Spin-coating

We have explained the synthesis and preparation of perovskites molecules in Paragraph 2.2.1. From the perovskites solution, 2D crystals can be obtained by evaporation of solvent. Our thin films samples are realized by spin-coating, by which the perovskites form 2D crystals by self-organization process. The spin-coating method is a technique used to apply uniform thin films to flat substrates. As it is shown in Figure 2.19, an amount of solution is dropped on the substrate which is fixed on the spin-coater, and then it is rotated at high speed in order to spread the fluid by centrifugal force.

FIGURE 2.19: Schema of the spin-coating process.

The process of spin-coating is difficult to be modeled in theory. To estimate the thickness h of a film, an empirical formula can be used: Meyerhofer (1978); Norrman et al. (2005); Krebs (2009)

$$h = \frac{C}{\sqrt{t}}\omega^{-x}.$$

(2.17)

where ω and t are the spin speed and spin duration, respectively. C is an experimentally determined constant, which depends on the evaporation rate, viscosity and density of the solution. x is also an experimentally determined parameter, which is related to the evaporation rate of the solution. $x \approx \frac{1}{2}$ for most solvents. $x \approx \frac{2}{3}$ when the evaporation rate is independent of ω, and $x \approx 1$ for slow evaporation solvent.

The solvent containing R-NH₂HX and MX₂ is first spin-coated on the substrate. 2D layered perovskites crystals are then obtained upon solvent evaporation. In the absorption spectra of 2D layered perovskites crystals, a sharp peak appears at room temperature, which is characteristic of the formation of 2D layered perovskites crystal structure (see Figure 2.6).

Actually, in order to realize a layer with the desired thickness, we modify the concentration of perovskites solution keeping the other spin-coating parameters (spin speed, acceleration and spin duration) fixed. Generally, homogeneous 2D layered perovskites films with a thickness from 10 nm to 100 nm can be obtained by carefully selecting the parameters: less concentrated solutions give thinner layers. For example we prepare some PEPI thin films from their 10%, 3% and 1% in DMF solution. The parameters of spin-coating are 2500 rpm, 2500 rpms for 30 s (the annealing conditions are 95°C for 1 min, see next paragraph). Their thicknesses measured by AFM are respectively: 36.5 nm, 25.3 nm and 6.21 nm. With the help of a profilemeter or an AFM to estimate the layer thickness, we can draw a calibration curve (thickness as a function of concentration) and adjust the concentration of solution in order to produce the desired thickness. The spin-coated 2D layered perovskites films are very reproducible, and therefore they are appropriate to be deposited on devices, for instance perovskites based microcavities. Lanty et al. (2008a)

Annealing

After the spin-coating process, the samples need to be put on a hot plate immediately for annealing in order to form 2D layered crystals. The annealing conditions are very crucial for the formation of crystals. It should provide the perovskites molecules sufficient thermal energy to realize self-organization and form well ordered crystalline structures with superior optical properties. If the annealing temperature and time are too small, the films may present relatively weak optical absorption and photoluminescence as the percentage of amorphous molecules is too large in this kind of samples; on the contrary, the perovskites will be destroyed and decomposed if the annealing temperature is too high and the annealing time too long. The annealing parameters depend a lot on the perovskite composition and also on the solvent. For instance the parameters for preparation of a 50 nm PEPI thin layer with PEPI 10% in DMF solution are: rotate speed 2000 rmp, rotate acceleration 2000 rmps for 30 s, annealing condition is 95 °C for 1 min.

Surface roughness

As we have introduced before, the tunable energy band gap and electronic structure of perovskites open a wide application potential in optoelectronic devices. However another important point which needs to be paid attention is the surface quality of the films. Especially for the multi-layered structures, a rough layer will be detrimental to the smoothness of the following layers and decrease the quality of the whole device. Considering the application of electroluminescent devices for example, the non-continuity of perovskites layers will lead to an increase of the resistance and obstruct the conduction of current in plane. Another example is the realization of microcavities containing perovskites. An active layer with large roughness badly reduces the quality factor of the cavity, prohibiting the occurrence of strong coupling.

The factors that may influence the surface quality of perovskites layers are various. It depends both on the deposition parameters and the perovskite composition. Concerning the deposition parameters, the pretreatment of substrates before deposition process is very important. The pretreatment includes the washing step and the surface treatment step. In order to remove all the residues on the substrates, we immerse the substrates in three solvents: acetone, ethanol and isopropanol successively and place the container in an ultrasonic bath for 10 min in each solvent. After that, the clean substrates are transferred to the surface treatment step. The principal idea of surface treatment is to promote adhesion between the substrate and the perovskites molecules, with hope that the perovskites layers can be smoothly spread on the substrate by this way. Generally that can be provided by a special molecule or even simply by electrostatic forces. Because of optical measurements, the substrates we use are usually quartz or glass whose main

constituent is SiO$_2$. Therefore the surfaces of the substrates will naturally possess negative charges as shown in Figure 2.20. It is known that the -O$^-$ on surface of substrate are not persistent and can easily catch the H$^+$ existing in air so that the surface becomes neutral. Considering that, we dip the substrates in a KOH solution at 0.5 mol/L during at least 10 minutes in order to take out the H$^+$ from the surface and render it negative. By this modification of surface charge, the perovskites molecules will well adhere to SiO$_2$ substrates. We have observed experimentally that the "hydrophilic property" of the surface is increased: the drops of perovskites solution spread immediately after hitting the substrates. The films homogeneity and continuity are greatly improved.
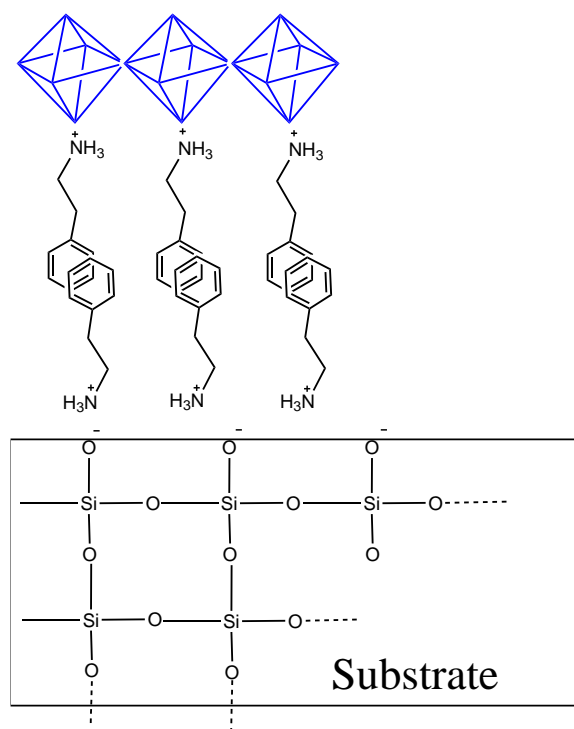
FIGURE 2.20: Schematic presentation of the effect of surface treatment.

The decrease of solution concentration helps improving the surface quality also. For a certain kind of perovskites, films deposited from solutions with lower concentration are usually smoother. Figures 2.21 (a), (b) and (c) show the topography of PEPI 10%, 4% and 1% thin films measured by AFM. The three samples are deposited by spin-coating with the parameters: 2000 rmp, 2000 rmps during 30s and annealing at 95 ºC for 1 min and their thicknesses are estimated to be about 50 nm, 27 nm and 6 nm. The average roughnesses of these samples are calculated with equation 2.2, they are 10.6 nm, 5.5 nm and 1.3 nm for PEPI 10%, 4% and 1% respectively.

These AFM figures clearly show the effect of solution concentration on surface roughness. In addition, the organic moieties greatly affect the surface roughness and this aspect will be studied in Chapter 3.

(a) PEPI 10% thin film   (b) PEPI 4% thin film   (c) PEPI 1% thin film
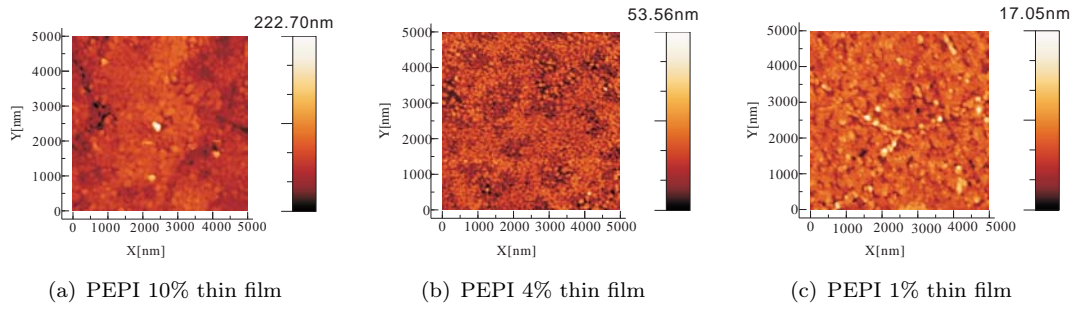
FIGURE 2.21: AFM images for PEPI thin films prepared from 10%, 4% and 1% solutions, and deposited on quartz substrate.

b) Optical characterization

Let us still take the PEPI perovskite as an example. The following Figures 2.22 and 2.23 show the OA and PL spectra of a 50 nm PEPI film sample at room temperature and at 10 K respectively . A sharp peak is observed in both curves in Figure 2.22. This resonant peak, at 2.398 eV for absorption and 2.369 eV for PL at room temperature, presenting a small Stokes-shift of 29 meV, is attributed to the excitonic transition from free excitons confined in inorganic sheets. In the 2D-layered perovskites, the excitons are highly located in the inorganic sheets because the energy gap of the organic sheets is usually much larger than that of the inorganic sheets. The absorption peak at 2.398 eV is attributed to the electronic transition from a mixture of Pb(6s)-I(5p) states (valence band) to Pb(6p) state (conduction band) for PbI₂ based 2D layered perovskites Ishihara (1994).

Figure 2.23 shows that the exciton energy in PEPI is E_{ex} = 2.346 eV at 10 K. A step-like structure (as zoomed in Figure 2.23) is also observed, which corresponds to the energy gap of PEPI (E_g = 2.548 eV). An exciton binding energy of E_b = 202 meV is then deduced for PEPI. The energy gap of PEPI can also be seen at 300 K, as a small bump in Figure 2.22(b), which is read to be about 198 meV. It is very comparable with the previously obtained value at 10 K. The binding energy of excitons in PbI₂ crystals has been determined to be 30 meV Le Chi Thanh et al. (1975). Thus, the exciton binding energy in 2D layered perovskites is much higher than that in the 3D structures. In fact, theoretical exciton binding energy is found to be four times larger in an ideal 2D structure than in a 3D structure Shinada and Sugano (1966). In addition, by virtue to the high contrast in dielectric constants between the organic layers and the inorganic PbI₄²⁻ layers, the Coulomb interaction in the well is hardly screened by the presence of the barrier, resulting in a strengthening of the interaction between the electron and the hole in the exciton. Note that the exciton binding energy in 2D thin films perovskites ($E_b \approx$ several hundreds meV) is much larger than the thermal energy at room temperature (k_BT$\approx$ 26 meV), which explains the strong excitonic absorption and PL features observed at the room temperature.
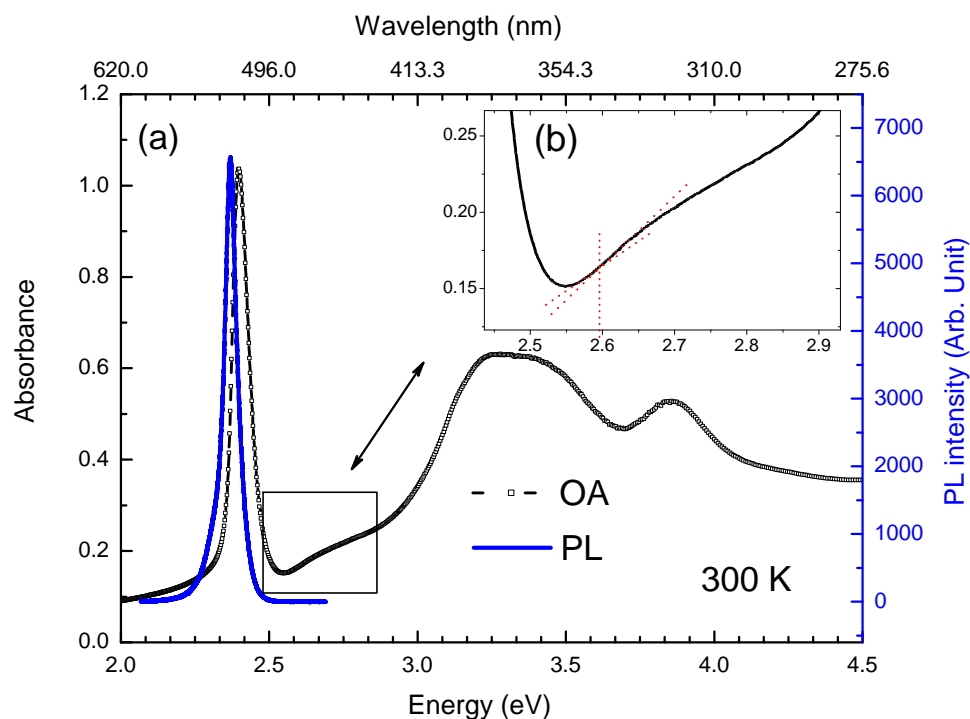
FIGURE 2.22: (a) OA spectrum and PL spectrum of a 50 nm thick PEPI film measured at room temperature. The excitation source for PL measurement is the 325 nm line of a HeCd laser, with an incident power of 0.6 mW. The insert graph (b) is a zoom of the square zone in graph (a) in order to show the step-like structure in OA spectrum.

Figure 2.24 shows the PL spectrum of a 50 nm PEPI film at low temperatures 10 K and 80 K in He environment. Two PL peaks are observed: (S1) at 2.336 eV and (S2) at 2.298 eV at 10 K, and (S1) at 2.349 eV and (S2) at 2.320 eV at 80 K. The Stokes shift between the OA peak and the (S1) peak being only 10 meV, it is thought that (S1) is related to the excitonic transition from free excitons. In order to get more information about the two PL peaks, we perform the PLE spectra of (S1) and (S2): see Figure 2.25. The blue and green scattered lines are the PLE spectra at 10 K, the orange and pink scattered lines are the PLE spectra at 80 K. The grey dashed line is, for recall, the OA spectrum of a 50 nm PEPI thin film at room temperature. We see that the PLE spectra of (S1) and (S2) have a quite similar profile for each temperature: the independence of the PLE spectra with respect to the detection energy indicates that the two emission lines are connected to the same excited states. As a consequence, we think that (S2) can not be interpreted in term of biexcitons Fujisawa and Ishihara (2004); Gauthron et al. (2010). It is possible that (S2) is related to excitons bound to defects. But to confirm this interpretation, further experiments have to be performed, such as PL measurements as a function of the incident power.
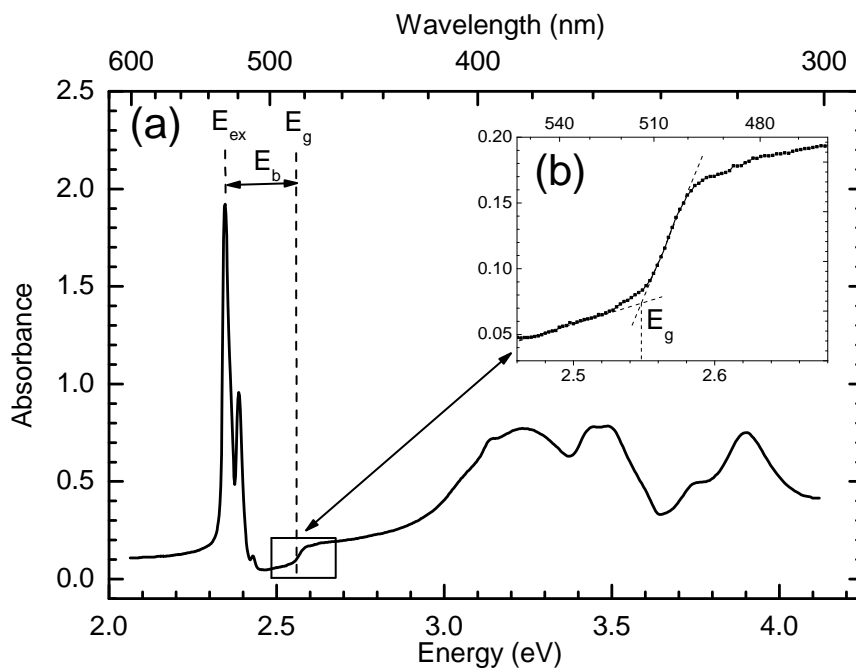
FIGURE 2.23: (a) OA spectra of 50 nm thick PEPI film measured at 10 K. The PL intensities are normalized. The inset (b) is a zoom of the square zone in order to see the energy gap. (E_{ex}, E_g, and E_b represent the exciton energy, the energy gap, and the exciton binding energy, respectively.

2.2.4 Crystal bulks (PEPI and PMPI)

The detailed electronic structure of the 2D-layered perovskites films being virtually unknown, it is necessary to consider performing calculations to improve its knowledge. Before performing calculations, crystal parameters must be well known. A precise study of the crystal bulks will be useful to determine the parameters which have to be introduced in the calculations concerning the 2D-layered perovskites. Detailed structural analysis of perovskites are still needed for studying these systems. However the growth of suitable single crystals has been a difficulty in the crystallographic study. Because of the layered nature of the perovskite structures, their crystals tend to grow as thin flakes, leading to problems with crystal distortion during the mounting process. Some methods used to generate crystals such as layered solution technique have been introduced in Chapter 1. Among them, solution evaporation has proved to be a good and simple way to grow crystal bulks. In this method, the choice of solvent is important: it should well dissolve the perovskites molecules after mixing their two precursor components. Also, the speed of evaporation under certain experimental conditions (temperature, pressure and so on) should be appropriate. Here, we present some solution methods we have tried to grow crystal bulks. Experimental details and some crucial points for generating big perovskites crystals will be discussed in the following paragraph.
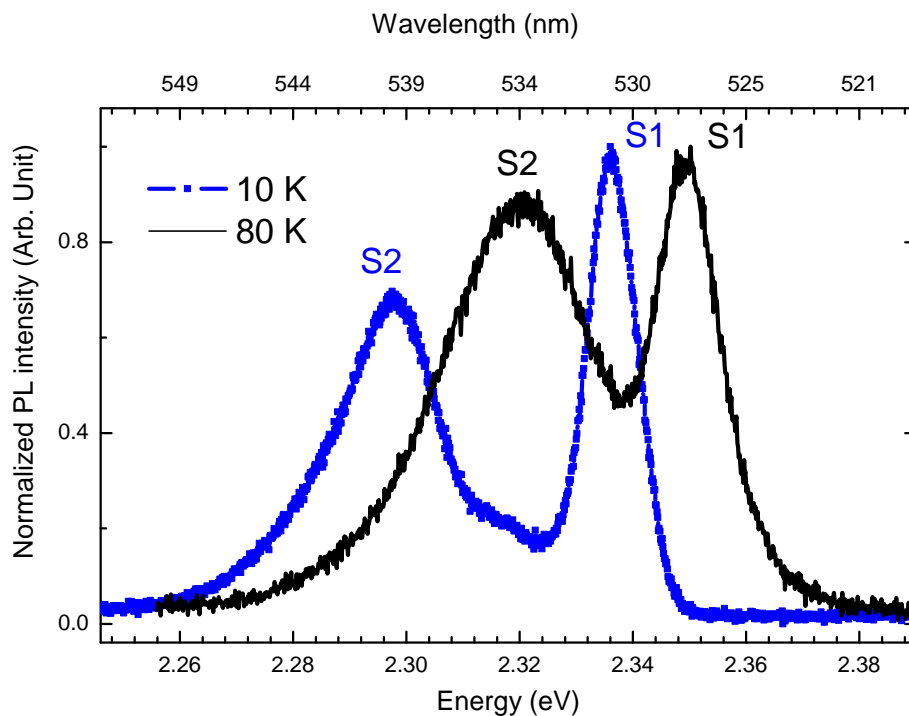
FIGURE 2.24: PL spectra of a 50 nm PEPI thin film at 10 K and 80 K. The PL intensities are normalized. The sample is placed in He bath in cryostat, the excitation source is Xenon lamp at 467 nm

Evaporation of solution

This method is tried with two lead iodide perovskites: PMPI and PEPI. 0.5 g of ammonium salt and PbI_2 in stoichiometric amounts for PMPI and PEPI are introduced in about 60 g acetone solvent. As the solubility of perovskites in acetone is low at room temperature (compared with DMF), some white precipitates are soon observed under agitation. These precipitates, which have different appearance compared to their precursors (ammonium salt and PbI_2) have been checked to be perovskites compounds in amorphous form. See Figure 2.26: the sharp absorption peaks of the films deposited from the "white precipitates" in DMF solution are located at 2.4 eV they superpose very well with that of the PEPI prepared in conventional ways, that is to say deposited directly from PE ammonium+PbI_2 in DMF solution, as introduced in Paragraph 2.2.1. However, the absorbance band in the UV range is obviously stronger than the main resonant peak at 2.4 eV contrary to the conventional PEPI film spectrum and the spectra differ a little bit around 3.03 eV for different positions on samples. According to the interpretation we have given for the UV band from OA spectra of perovskites in solution (Paragraph 2.2.2), we can say that the absorption UV bands observed here are largely due to molecules stacking in solid state. As long as the perovskites precipitate in some kind of solid form (even amorphous form), it will take more energy to detach the molecules and it
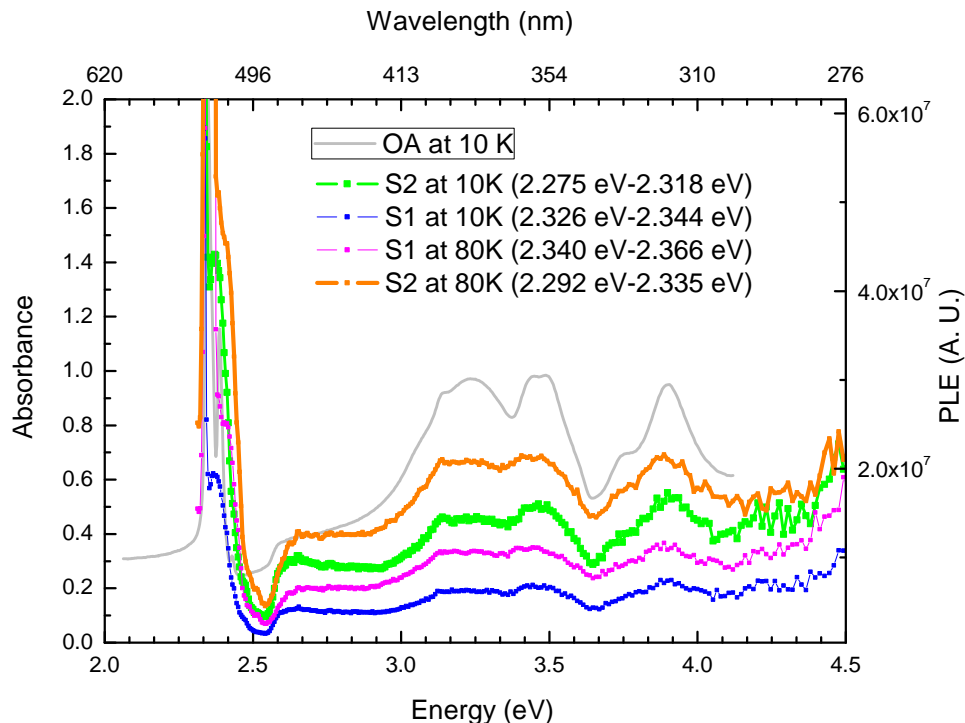
FIGURE 2.25: PLE spectra of S1 and S2 PL peaks (observed in Figure 2.24) of a 50 nm PEPI thin film at 10 K and 80 K. The grey curve is absorption spectrum measured at 10 K. The energy interval between brackets is the energy interval on which the PL intensity of S1 and S2 peaks are calculated.

will be more difficult to redissolve them again. Therefore it causes the differences in curve profiles which may result of the inhomogeneous stacking of perovskites molecules in solution.

The white precipitates are filtered out and we leave the saturated solution in conical flask evaporate at room temperature. Unluckily, we don't get crystal bulk with this method neither for PEPI nor PMPI. After several days, when the liquid acetone has all evaporated out, we don't see crystals but some "coffee stains" like solids at the bottom of the flask. We think that the growth of crystal is generally a relatively slow course: while the bp (boiling point) of acetone is quite low: only 56 °C, leading to a too quick process to form crystal bulks. To avoid that point, we then try, for PEPI, another solvent as acetonitrile which has higher bp: 82 °C, so it evaporates slowly at ambient environment. After a long evaporation time of 5 months for 500 ml PEPI in acetonitrile saturated solution, we finally obtain some thick flakes of PEPI orange crystals and these crystals emit bright green photoluminescent under UV lamp.

The proper solution condition for good crystallization can be realized by mixing two solvents with different boiling points. We have tried to use the mixture of nitromethane, whose bp is 101 °C and acetone. 55 ml of the PEPI in acetone saturated solution is mixed with 45 ml nitromethane and is kept in a sealed flask at air environment with a
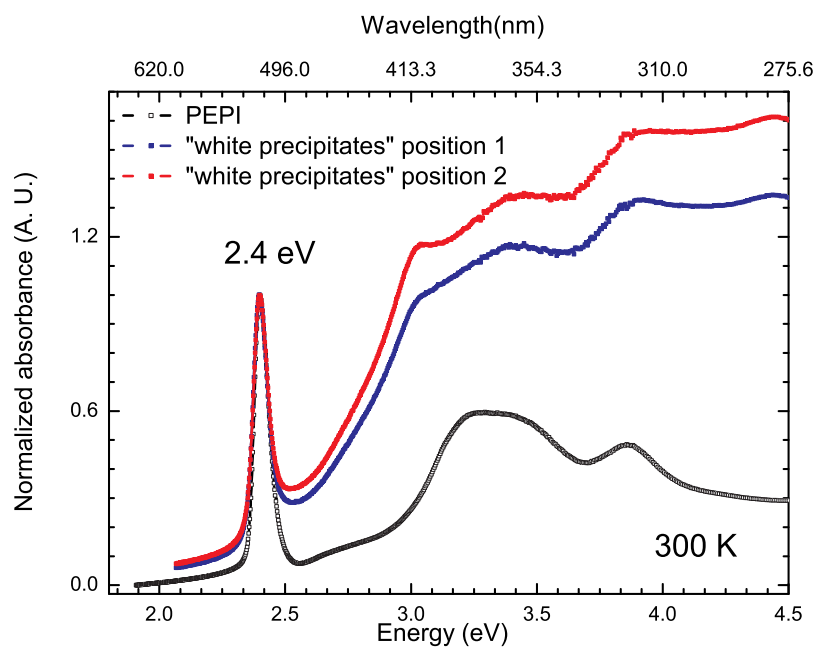
FIGURE 2.26: OA spectra of PEPI thin films deposited from the "white precipitates" in DMF solution as explained in the text. The black curve is the absorption spectrum of a 50 nm PEPI thin film prepared in conventional ways.

small hole on top to evaporate the solvents. After 9 months, we successfully obtain two pieces of brown crystals of PEPI, see Figure 2.27. The dimensions of the larger one are about 8 mm × 4 mm × 15 mm. They are very luminous under UV lamp and their PL spectrum is measured at room temperature, as seen in Figure 2.28(a) and (b). The PL intensity of PEPI crystal bulk is normalized, and for comparison a normalized PL curve of a 50 nm PEPI thin film is reported. We see that the peak center and FWHM of the PL of PEPI perovskite in form of film and crystal bulk are the same.

FIGURE 2.27: Photo of the PEPI crystal bulks grown from nitromethane/acetone mixed solution.
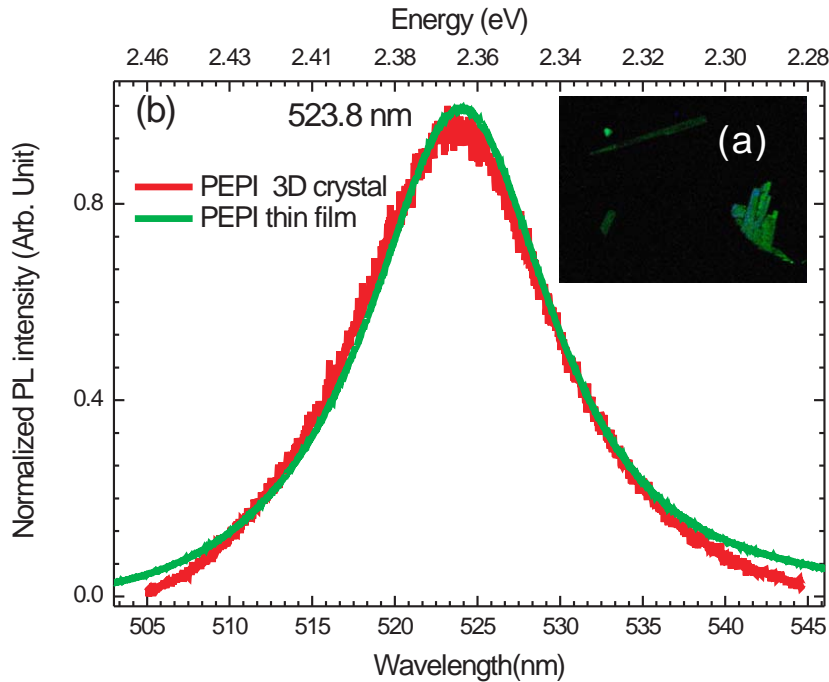
FIGURE 2.28: PL of PEPI crystal bulk grown from nitromethane/acetone mixted solution: (a) photo of the 3D crystals under a 312 nm UV lamp; (b) PL spectra measured at room temperature of the PEPI crystal bulk and of a 50 nm PEPI thin film. The PL intensity is normalized, the excitation laser is HeCd at 325 nm, with incident power of 0.6 mW. The normalized PL of a PEPI thin film is drawn for comparison.

Slow solution exchange

For PMPI, we develop a Slow solution exchange method, which allows to control the growth of crystals in slow means. It is realized by using two volatile solvents (we call them solutions A and B to simplify) : solvent A is the one in which perovskites are soluble while in solvent B the perovskites can not be dissolved. Solution A (containing perovskite) and solvent B are contained in two different containers that communicate as shown in Figure 2.29(a), the whole setup is well sealed against outside atmosphere. This special setup enables the two solvents to evaporate in a closed space and slowly permeate into each other. Little by little, the perovskites in solution A will precipitate as a result of the change of solution environment. In our experiment, we use the perovskites PMPI and its acetone saturated solution as solution A. As the solubility of perovskites is quite low in diethyl ether, it is thus a good choice for solution B. In Figure 2.29(a), the inner beaker contains saturated perovskites in acetone solution and this beaker is placed in another bigger backer containing diethyl ether. In the following days, the immersion of diethyl ether molecules in acetone solution force the perovskites to precipitate out gradually. After one month of crystallization, we successfully obtain a thick brown PMPI crystal bulk of about 7 mm × 5 mm × 3 mm, as seen in Figure 2.29(b). Green photoluminescence under UV lamp observed by naked eyes proves that ordered quantum wells structure in this crystal is well formed.
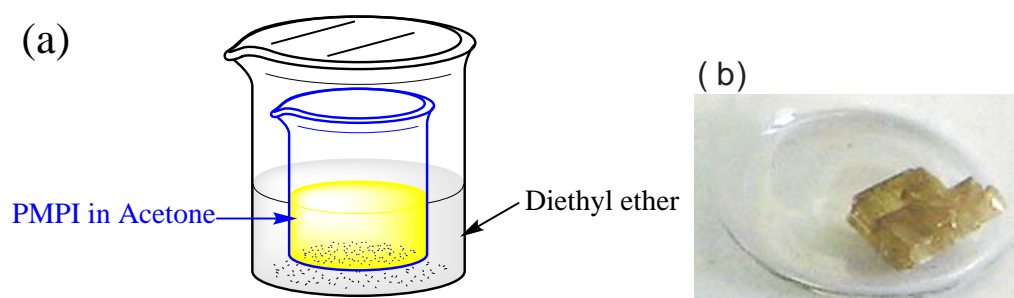
FIGURE 2.29: (a) Setup of slow solution exchange method and (b) a PMPI crystal grown by this method.

2.2.5   Nanoparticles

Perovskites in form of luminescent nanoparticles are another interesting kind of crystals which has attracted great interest recently. Being a bridge between bulk materials and atomic or molecular structures, the nanoparticles display very specific properties with potential applications in various fields such as sensing or LEDs. Nanoparticles often possess particular optical properties as they are small enough to confine their electrons and produce quantum effects. Consequently, the fabrication process which decides the size of nanoparticles is very important.

2.2.5.1   Spray-drying method

Before this thesis, P. Audebert and C. Boissière (LCMC, UPMC) have realized luminescent nanoparticles by a spray-drying (or nebulization/lyophilization) method Audebert et al. (2009). Similarly to the spin-coating method, the ammonium salts whose organic parts are PE, AM and CM as shown in Table 2.2 and PbBr$_2$ or PbI$_2$ semiconductors are firstly dissolved in DMF solvent in stoichiometry of 2:1. 5% DMF solutions were used for the nanoparticles spray drying. The preparation method is sketched in Figure 2.30. The experimental spray drier, shown in Figure 2.30, is composed of an aerosol generator and an evaporation chamber which is settled in an oven maintaining at 250 °C. Droplets with initial mean diameter of 0.35 μm are carried by dry air ($3 \, L \cdot min^{-1}$) from the aerosol generator to the evaporation chamber. Dried particles are collected onto a 0.2 μm cutoff Teflon filter and are stored at ambient temperature.

The particles exhibit an intense luminescence at ambient temperature, as shown on the Figure 2.31.

TEM measurements show that these particles are spherical and their sizes are of the order of 50 to 500 nm, see Figure 2.32. The X-ray diffraction spectra of the nanoparticles in Figure 2.33 show that the particles are fully crystalline. In the case of AMPI and CMPB based nanoparticles, a single crystalline phase is observed, showing therefore the high degree of organization of these particles. In the case of PEPI based nanoparticles,

TABLE 2.2: Chemical structure, complete name and abbreviation of the amines part of perovskites used to prepare nanoparticles
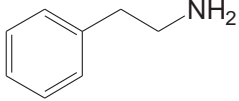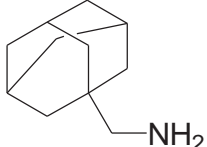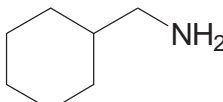
Chemical structure	Name	Abbreviation
(structure) NH₂	2-phenylethanamine	PE
(structure) NH₂	1-Adamantanemethylamine	AM
(structure) NH₂	cyclohexylmethanamine	CM
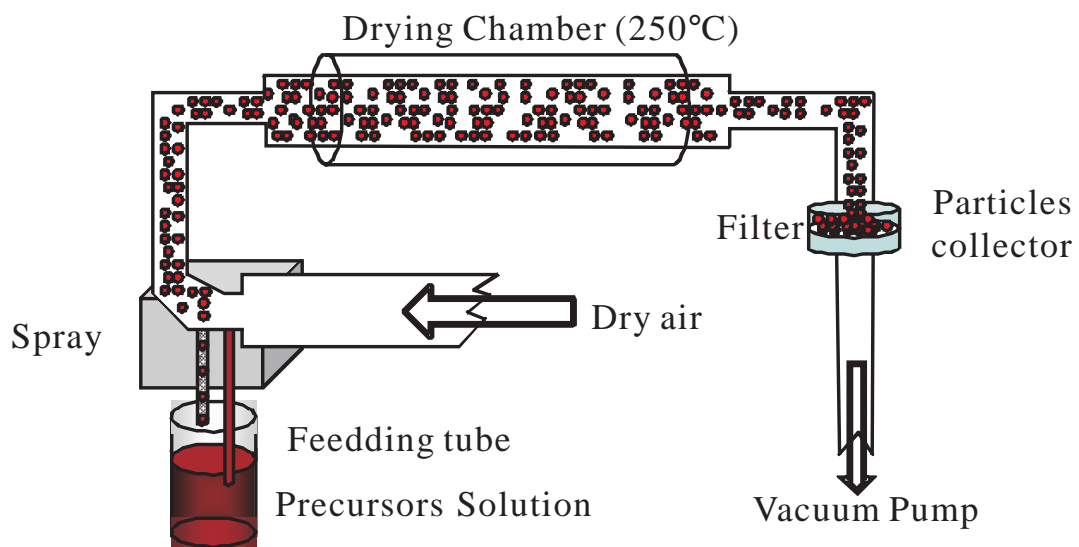
FIGURE 2.30: Sketch for the preparation of organic-inorganic perovskite nanoparticles by spray-drying method.

mainly one phase is observed, even though a very small additional peak exists aside, which could be attributed to the presence of another phase. Figure 2.33 shows also the X-ray spectra of the bulk samples dried in the air: a very small additional peak can be seen in each spectrum, suggesting that the bulk samples display mainly one crystalline phase but can be weakly polluted by another phase. The X-ray spectra of the PEPI bulk sample and PEPI based nanoparticles are quite comparable to the ones of PEPI spin-coated layers we have performed or we can find in the literature Mitzi et al. (2001b, 1999); Hattori et al. (1996) and also to X-ray spectra performed in a single crystal of PEPI, Calabrese et al. (1991); Ishihara (1994) where the layer spacing of the PEPI perovskite

FIGURE 2.31: Luminescence, under UV lamp, of the nanoparticles dispersed in hexane: left, PEPI; right, CMPB.
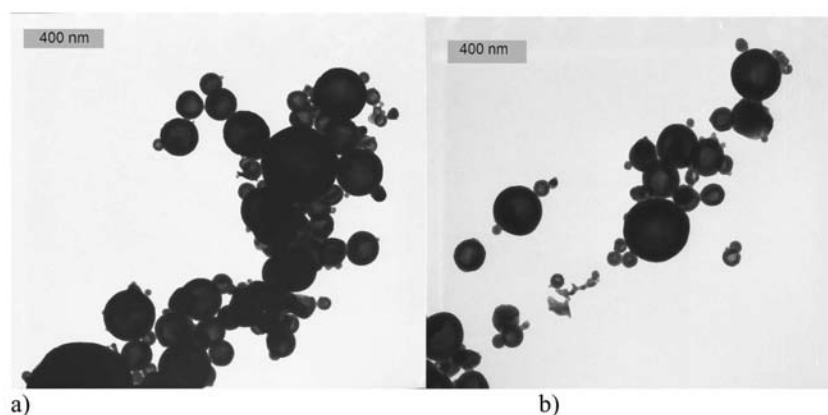
FIGURE 2.32: TEM pictures of the nanoparticles (a) AMPI and (b) CMPB. The hollow character of large particles is quite apparent in (b). Audebert et al. (2009)

is found to be 1.6 nm.

Figure 2.34 reports the photoluminescence spectra of the three nanoparticles samples. For CMPB based nanoparticles, the maximum of the luminescence is observed at 411 nm, while the maximum of the absorption occurs at 408 nm, providing a small Stokes-shift value of 3 nm. This value of the Stokes-shift is quite coherent with the Stokes-shift value of 4 nm we have measured in a CMPB spin-coated layer. Additionally, we have reported in Figure 2.34 the PL spectra of self-assembled thin layers obtained by
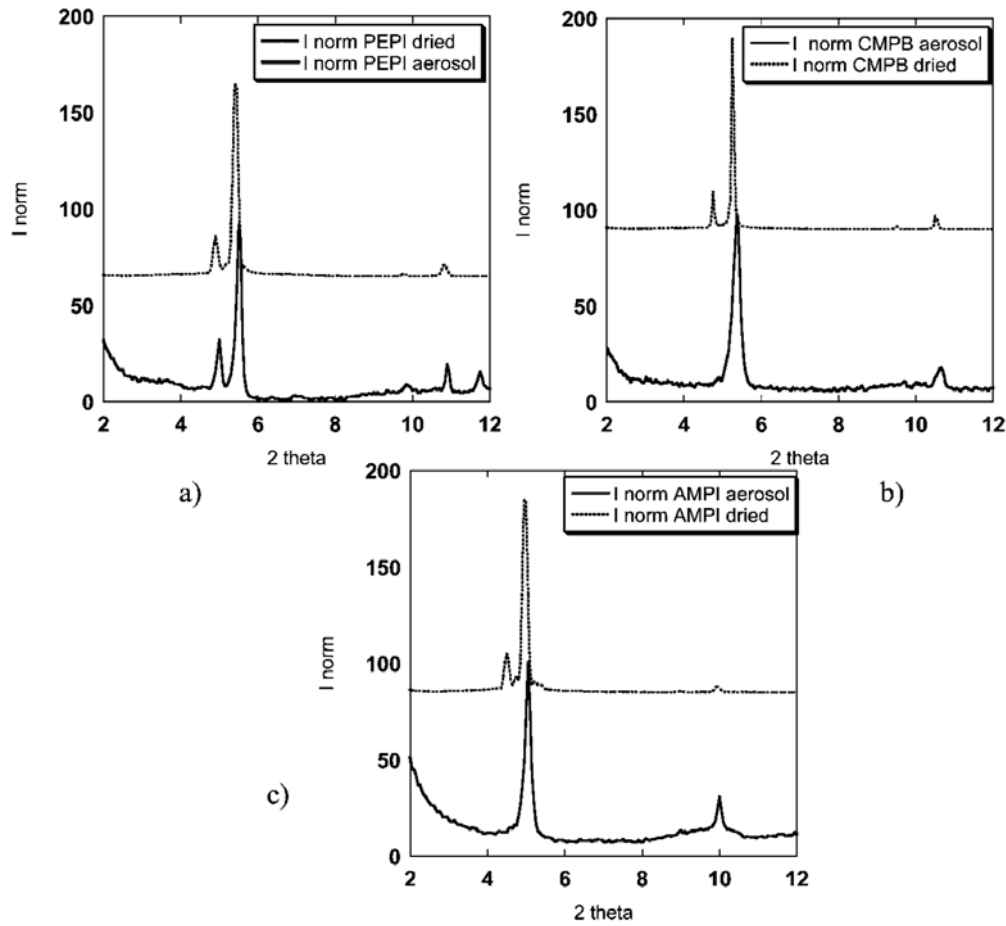
FIGURE 2.33: X-Ray diffraction spectra of the (a) PEPI, (b) CMPB, and (c) AMPI perovskites. The full lines correspond to the spectra of the nanoparticles and the dotted lines to the spectra of a bulk sample dried in the air.

spin-coating the three perovskites on a glass substrate. It can be seen that the nanoparticles and the thin layers emit in the same range: only a very slight wavelength shift of several nanometers is observed between the PL maximum energy positions of the nanoparticles and the spin-coated layers. It is also worth noting that the FWHM of the PL peaks of the nanoparticles and of the spin-coated layers are of the same order of magnitude. All these observations lead to the conclusion that the optical characteristics of the nanoparticles do not depend on their size. Following Ishihara et al. and as explained in Chapter 1, Ishihara et al. (1990, 1989); Ishihara (1995) the bidimensionnal perovskite spin-coated layers form a crystal which presents a multiple quantum well electronic structure, having a period of 1.6 nm: the quantum wells consist of lead tetrahalogenide octahedrons monolayers (thickness around 0.6 nm), and the barriers consist of the organic alkylammonium layers (thickness around 1 nm). The excitons are strongly localized in the quantum well layers, that is, in the PbX_4^{2-} octahedrons, and their Bohr radius is about 1.7 nm. Hong et al. (1992) The size of the nanoparticles, from 50 to 500 nm, is large compared to the Bohr radius of the excitons so that the optical properties

of each nanoparticle are dominated by the optical properties of the 2D crystal. The X-ray spectra confirm this fact as we have seen previously that the X-ray spectra of the nanoparticles are quite similar to the ones of the spin-coated layers or of the bulk samples. As a consequence, we can deduce from our PL and X-ray measurements that each nanoparticle is a small crystal having a bidimensional perovskite structure, emitting at a wavelength which does not depend on the size of the nanoparticle. Nevertheless, we have observed that a slight wavelength shift of several nanometers is observed between the PL maximum energy positions of the nanoparticles and those of the spin-coated layers. These differences can be assigned to different strain states inside the samples. Indeed, the nanoparticles and the spin-coated layers have not been grown in the same conditions. Additionally, the boundary conditions are very different between the two kinds of samples. In inorganic semiconductor crystals, it is well-known that different growth conditions and different boundary conditions induce distortions and different strain states, inducing some changes in the electronic structure, Gil et al. (1995) so that PL energy positions are slightly modified.
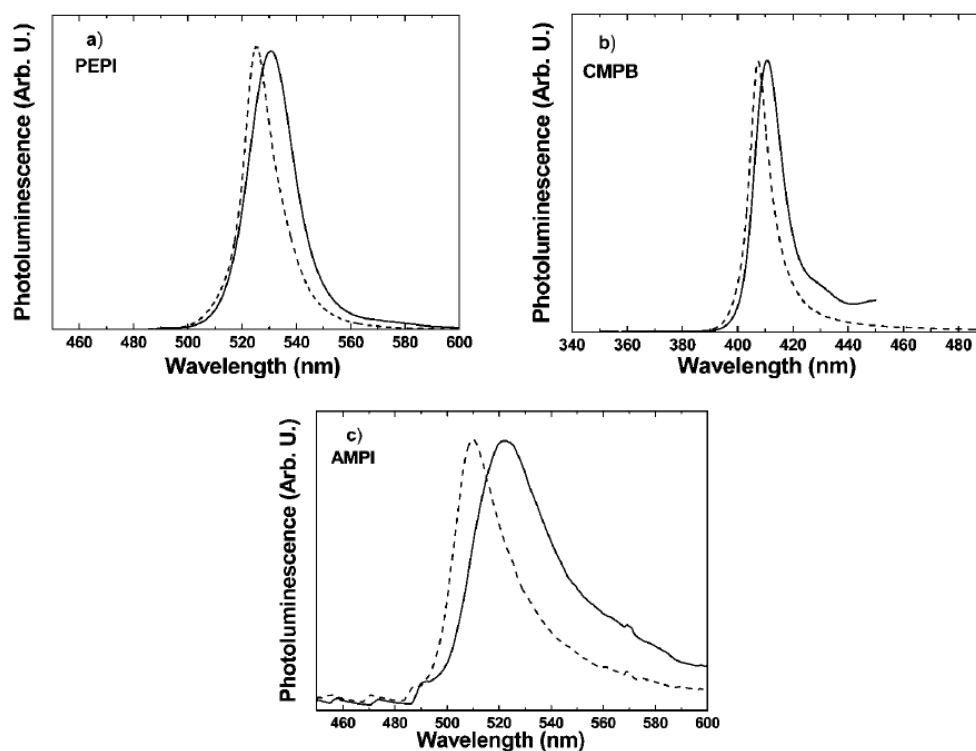
FIGURE 2.34: PL spectra of the three nanoparticles samples (solid lines) and of the spin-coated layers (dashed lines) obtained with the three perovskites (a) PEPI, (b) CMPB, and (c) AMPI. The excitation wavelength is 325 nm for AMPI and CMPB based samples and 405 nm for PEPI based samples. The PL curves have been normalized with their respective maximum intensities.

2.2.5.2 Solution method

Wet chemistry strategy is a convenient way to synthesize particles. Because it has no requirement in equipments, all the processes of preparation can be carried on at room temperature.

This method is carried on by two steps: we firstly fabricate PbI_2 nanoparticles and then react them with their corresponding ammonium salts. Considering the fabrication of PEPI particles for example, the generation of PbI_2 is executed by reacting lead acetate trihydrate with HI. In this step the preparation of HI is quite crucial because the concentration and production rate of I^- in reaction environment strongly decides the nucleation and then the growth of PbI_2 particles. In order to control precisely the generation speed of I^-, we develop a solution approach, producing gradually I^- from CH_3I alcoholysis, as described in the formula 2.18:

$$CH_3I + Alcohol \rightarrow HI. \tag{2.18}$$

The iodomethane CH_3I assay 99% is purchased from Sigma-Aldrich company. The alcohol is used as a mixed solution, for instance methanol mixed with isopropanol (or other inert solvent such as acetonitrile). The methanol is an active alcohol and it is nucleophilic but isopropanol is less reactive. Meanwhile we use acetonitrile as a solvent for the reaction. By adjusting the ratio among the solvent components in the alcohol mixture, it makes possible the control of the speed of the reaction described in formula 2.18. The reaction is carried on with a reflux setup heated by an oil bath at 75 °C. In the reaction flask, we dissolved 1.2 g lead acetate trihydrate in 300 ml acetonitrile and then add 60 ml methanol to the solution. The reaction process is described in Equation 2.19 and 2.20. The HI generated in solution reacts immediately with the lead acetate trihydrate in solution. Yellow precipitates of PbI_2 are evidently observed after 3 h of reaction. We leave the reaction last for one night and then collect the particles of PbI_2 dispersed in solution. It is measured by a particle size analyzer that the size of these particles are around 200 nm.

$$CH_3I + CH_3OH \rightarrow HI + CH_3 - O - CH_3. \tag{2.19}$$

$$HI + Pb(CH_3COO)_2 \rightarrow PbI_2 + CH_3COOH. \tag{2.20}$$
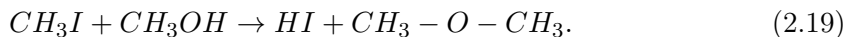
After the fabrication of PbI_2 particles, the second step is to mix organic salts with them (reaction 2.21).

$$2(C_6H_5C_2H_4NH_2 \cdot HI) + PbX_2 \Rightarrow (C_6H_5C_2H_4NH_3)_2PbI_4. \tag{2.21}$$

The as-prepared PEI ammonium salt is synthesized as described in Paragraph 2.1. 2g (over dose) salt of PEI ($C_6H_5C_2H_4NH_2 \cdot$ HI) are dissolved in 30 ml isopropanol and 180 ml
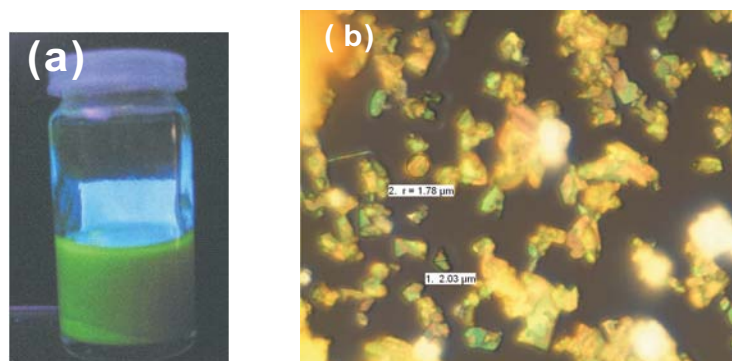
FIGURE 2.35: (a) PEPI particles dispersed in toluene solvent. Green luminescence is observed under UV lamp. (b) Photo under microscope for one drop of PEPI particles deposited on quartz substrate. The diameter of these crystals is around 2μm.

toluene mixed solvent. The toluene solvent contributes to separate particles. The PbI$_2$ synthesized in the last step is then mixed to PEPI solution. At the moment of mixing, we see the particles dispersed in solution change from yellow to orange immediately which indicates the generation of PEPI particles. We wash these particles with toluene two times and then stock them in a small bottle. A bright green luminescence is observed when they are excited under a UV lamp as it is shown in photo 2.35(a).

To characterize them, one drop of this solution is casted on quartz substrate and dried by annealing. We observe under microscope that these small pieces of crystals, crystallized from PEPI particles, are around 2-4 μm in diameter. PL spectrum is measured at room temperature, see Figure 2.36 and compared to the PL spectrum of PEPI thin films. The change in PL peak position is very obvious: the PL of PEPI thin film deposited by spin-coating is centered at 523 nm and that of PEPI particles is at 533.5 nm. The FWHM of the two perovskites are quite similar: around 16 nm. This bathochromic shift is also observed with nanoparticles fabricated by spray method, as we have discussed in the previous paragraph.

However, these PEPI particles still have a problem of large and inhomogeneous size. To solve this problem, we can try to put the suspending solution containing particles in a strong ultrasonic bath in order to break large clusters to smaller pieces. Besides, to optimize the perovskites particles monodispersity, we need to work systematically on the first step of synthesis by testing other alcohols mixture as well as the optimal ratio among them. In fact, the replacement of methanol by water in alcohol mixture may help to form HI more quickly. It should enable the generation of PbI$_2$ starting points in solution to be more temporally synchronous and therefore should lead to the growth of PbI$_2$ particles more uniform in size.
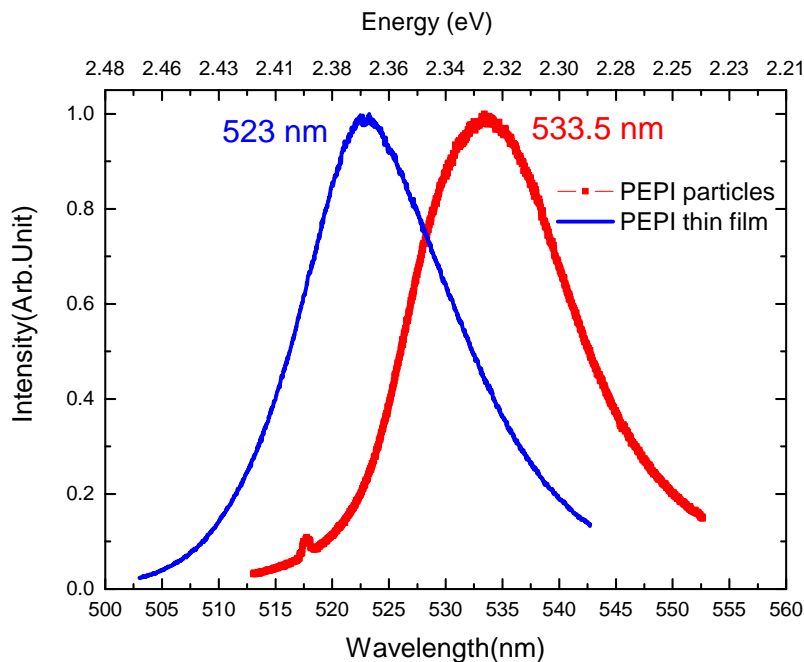
FIGURE 2.36: PL spectra of a 50 nm PEPI thin film (blue curve) and PEPI particles dispersed on quartz substrates (red curve). The excitation source is the 325 nm line of a HeCd laser.

2.3 Conclusion

This chapter has presented the structural and optical characterization means, as well as the roughness of the perovskites. We adopt soft chemistry method to synthesize organic ammonium and perovskites, and spin-coating method is used for depositing 2D layered perovskites samples. Besides, we explored several other methods to fabricate nanoparticles and large crystals of perovskites. The solution method we developed is a convenient way which permits to obtain small size particles at room temperature. And the spray is actually the most efficient method to generate nanoparticles with good optical quality and identical sizes. The particles synthesized by the two methods are well photoluminescent under UV excitation, and X-diffraction experiment on the nanoparticles obtained by spray reveals that these particles are of oriented crystal structure. For growing crystal bulks, we mainly tried the room temperature evaporation method and worked on several different solvents. It has been proved that the control of the growth speed is very important. Too fast growth process will lead to small sized and no luminescent crystals, which indicates that it should take relatively longer time to form perovskite crystal bulks with good quality at room temperature and in air atmosphere. Therefore, the choice of solvent is critical. With the method developed, we finally obtained a 7 mm × 5 mm × 3 mm PMPI crystal grown by slow solution exchange method with acetone and ether solvent, and a 8 mm × 4 mm ×15 mm PEPI crystal grown from

mixed solution nitromethane/acetone, which shows bright green photoluminescence at room temperature.

Chapter 3

Flexibility of 2D-layered perovskites

Among all the unique features of 2D-layered perovskites, one of the most important is their strong flexibility. Combining attributes of organic and inorganic materials in each compound molecule, the electronic band structure of perovskites can be modified by either changing organic ammonium group or the elements in inorganic lead halide part. In this section, we will focus our attention on the study of flexibility of perovskites regarding their optical characteristics. From some experimental results, several important factors that affect excitonic bands, photoluminescence efficiency and surface quality will be discussed, in order to find some tendencies allowing to select and design perovskites molecules presenting optimized properties.

3.1   Flexibility of organic moiety

The flexibility of perovskites mainly thanks to the variety of their organic parts. The infinite diversification of the large organic molecules family, combining with the support of organic synthesis methods, provides us a great freedom to choose the molecules that we desire and enables us to realize plenty of new chemical structures with interesting properties.

From a great deal of experimental research works, we have observed that each kind of perovskites film exhibits different photoluminescence intensity and absorbs different quantity of photons under some given excitation conditions, depending on the nature of the organic moiety. This phenomenon may be due to the self-organization ability of perovskite molecules, which is related to their intrinsic properties. As mentioned earlier, the optical properties of perovskites depend on the conformation of MX_6^{4-} octahedra in inorganic sheets as well as the chemical structure of organic molecules. For 2D-layered perovskites, the size of their organic cations exceeds the tolerance factor. They are therefore too big to fill in the rigid 12-fold holes between the octahedra so they extend to the space between layers. We have introduced in Paragraph 1.1.1.1 that PbX_2

based 2D-layered perovskites can be generally sorted into two groups: $(R\text{-}NH_3)_2PbX_4$ for monoammoniums and $(NH_3\text{-}R\text{-}NH_3)PbX_4$ for diammoniums, where the organic R cation is generally a long alkylammonium or a single benzene ring combined alkylammonium. The interaction between organic cations hold together the whole framework of perovskites. Consequently, the lengths of alkyl chains and the R type will dramatically influence the molecular rigidity as well as the distance between inorganic sheets and furthermore the self-assembly ability, it can also influence the contrast of dielectric constants between organic and inorganic layers.

3.1.1 $(R\text{-}NH_3)_2PbX_4$ perovskites

To investigate the influence of the organic cations on the optical properties of the $(R\text{-}NH_3)_2PbX_4$ 2D-layered perovskites , three groups of perovskites films based on different lead salts: lead bromide, lead iodide and lead chloride, have been prepared. The amines used in organic parts are listed in table 3.1.

Table 3.1: Chemical structure, complete name and abbreviation of the amines part of perovskites used in experiment
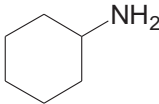
Chemical structure	Name	Abbreviation
	Cyclohexanamine	C
	Cyclohexylmethanamine	CM
	2-Cyclohexylethanamine	CE
	2-Cyclohexenylethanamine	CHE
	C-(Tetrahydro-pyran-3-yl)-methylamine	TPMA
	(Tetrahydrofuran-2-yl)methanamine	TFM
	5-Methyl-2-furanmethanamine	MFM
	Cyclooctanamine	CO
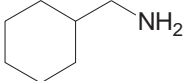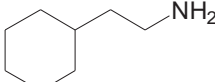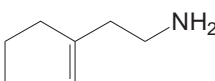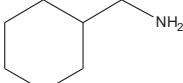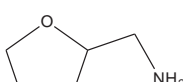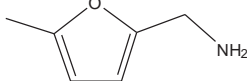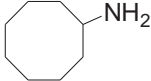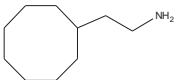
	2-Cyclooctyl-ethylamine	COE
	Phenylmethanamine	PM
	2-Phenylethanamine	PE
	3-Phenylpropan-1-amine	PP
	2-Aminoindan	A5
	1,2,3,4-Tetrahydro-naphthalen-2-ylamine	TNY
	Chroman-3-ylamine	CY
	N-(2-Aminoethyl)phthalimide	PH
	N-(2-Aminoethyl)naphthalimide hydroiodide	APHI
	1-Adamantanamine	A
	1-Adamantanemethylamine	AM
	Myrtanylamine	M
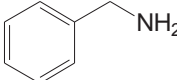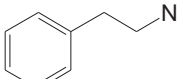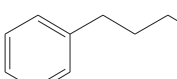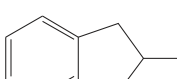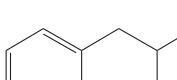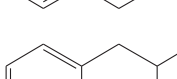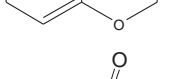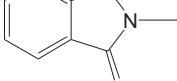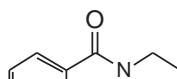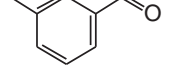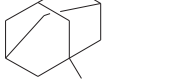
Thin layers of these perovskites are prepared on quartz substrates by spin-coating and annealed on hot plate. We measure the OA and PL spectra for each of these perovskites films, modifications of the energy gap and of the optical properties are observed. Figures 3.1, 3.2 and 3.3 show the OA and PL spectra for these amine based lead bromide, lead iodide and lead chloride perovskites respectively.
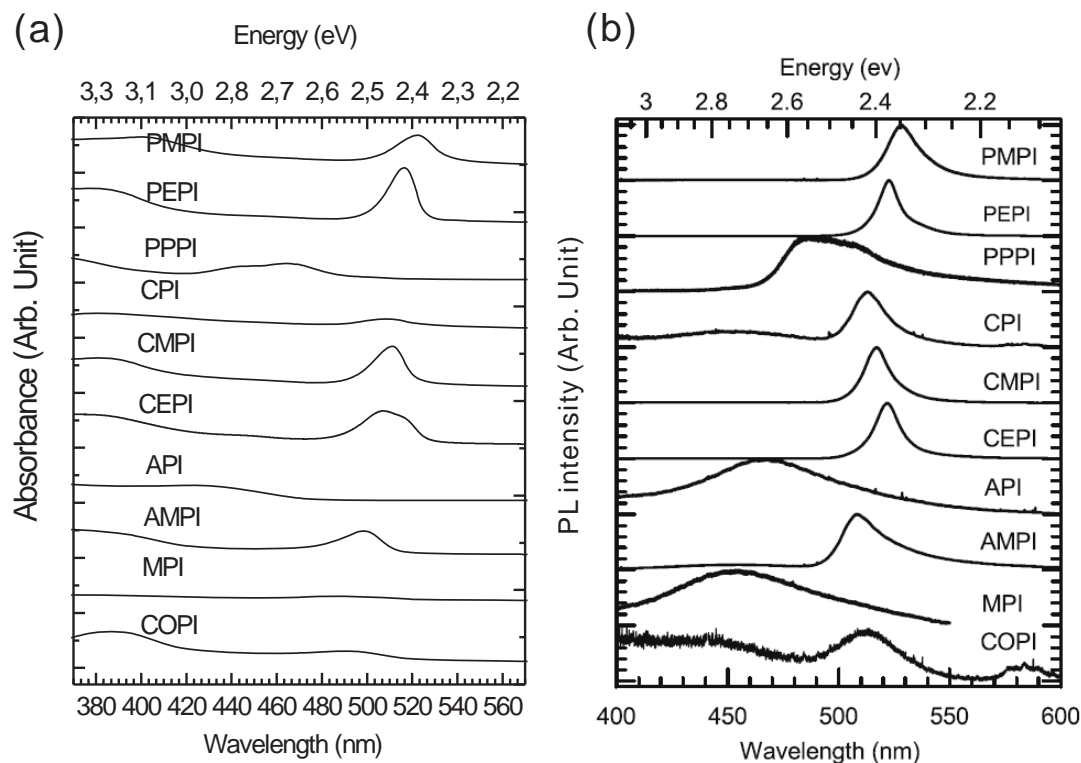
FIGURE 3.1: (a) Optical absorbance (OA) and (b) PL spectra of lead iodide 2D layered perovskites containing 10 different organic groups. PL curves are normalized. The curves are displaced vertically for clarity. The experiments are carried on at room temperature and the excitation source for PL is the 325 nm line of a HeCd laser, the power is 1 mW.

We notice that the wavelength positions of the OA and PL maxima vary a little bit among each given PbX_4^{2-} group. The Stokes-shifts of perovskites are small, of the order of several nm. In "PB" group it is generally a little bit larger than in "PC" group and a little bit smaller than in "PI" group: see Table 3.2 to compare PI and PB groups, Stokes-shifts of PMPC, PEPC and CMPC are 2 nm, 0.7 nm and 1.4 nm respectively. In fact, the optical properties of 2D-layered perovskites are closely correlated with their quantum well structure which refers to two aspects. One of this aspect is the dielectric constant contrast between organic sheets and inorganic sheets: different organic molecules with different dielectric properties will certainly cause variations of the band gap. The other aspect is related to the precise structure of the inorganic sheets, such as the bond angles and the bond lengths in metal halide unions Mitzi et al. (2001). On one hand, it depends on the specific element type of "M" and "X". On the other hand, organic cations
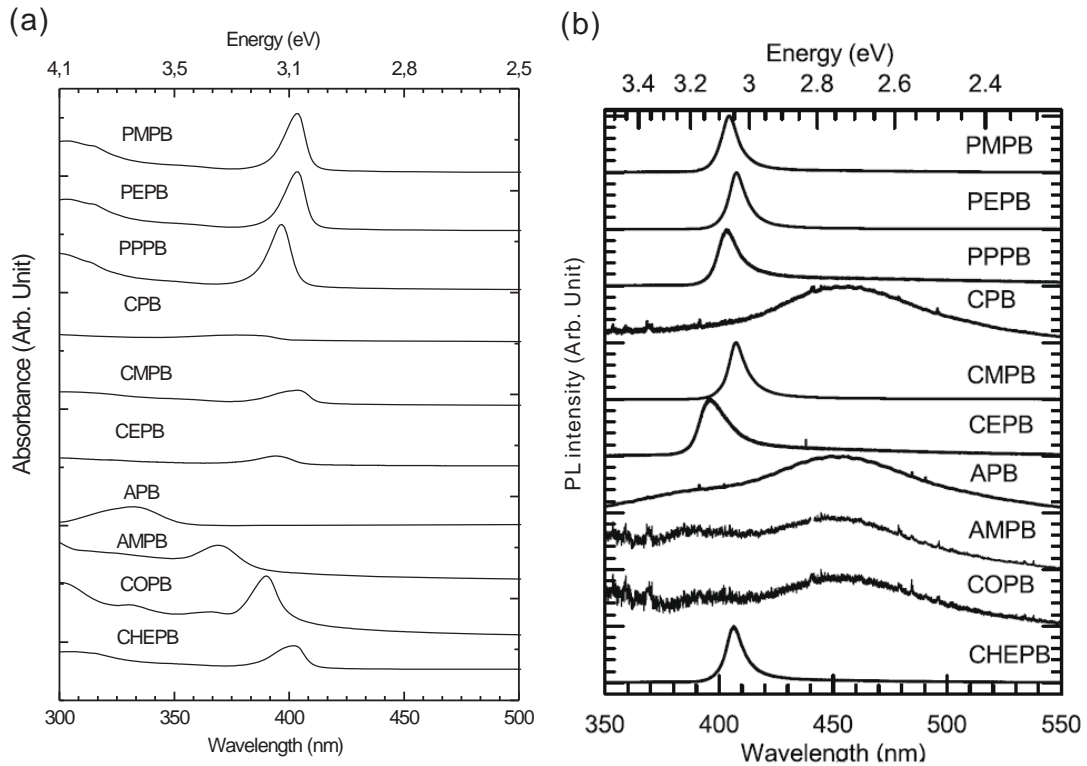
FIGURE 3.2: (a) Optical absorbance (OA) and (b) PL spectra of lead bromide 2D layered perovskites containing 9 different organic groups. PL curves are normalized with their respective maximum intensities. The curves are displaced vertically for clarity. The experiments are carried on at room temperature and the excitation source for PL is the 325 nm line of a HeCd laser, the power is 1 mW.

in some extent will influence the inorganic sheets by deforming the MX_6^{4-} octahedra differently. For example, changing the alkyl chain length not only changes the distance between main organic groups and inorganic sheets, but also changes the orientation of the main organic group. When the bi-organic layers interact with each other to form a self-organized 2D-layered perovskites, differently orientated main organic groups distort the MX_6^{4-} octahedra in different ways, therefore resulting in slightly different optical properties.

We will now study the influence on the PL efficiency of several characteristics of the organic moiety: length of the alkyl chain, steric encumbrance and structure flexibility of R. In order to compare the photoluminescence efficiency of the different perovskites thin layers, we define the ratio $\rho = I/(P_{laser} \cdot a)$, where I is the integrated intensity of the photoluminescence peak, P_{laser} is the excitation power and a is the absorption factor of this material at the excitation wavelength. Since the PEPI film is one of the perovskites which presents the best photoluminescence efficiency and has been the most frequently studied in literature, we take the PL efficiency ratio of PEPI ρ=1 as a reference. The PEPB photoluminescence efficiency is thus found to be 3.59. Note that the "PB" group perovskites usually have superior PL efficiency than the "PI" group.
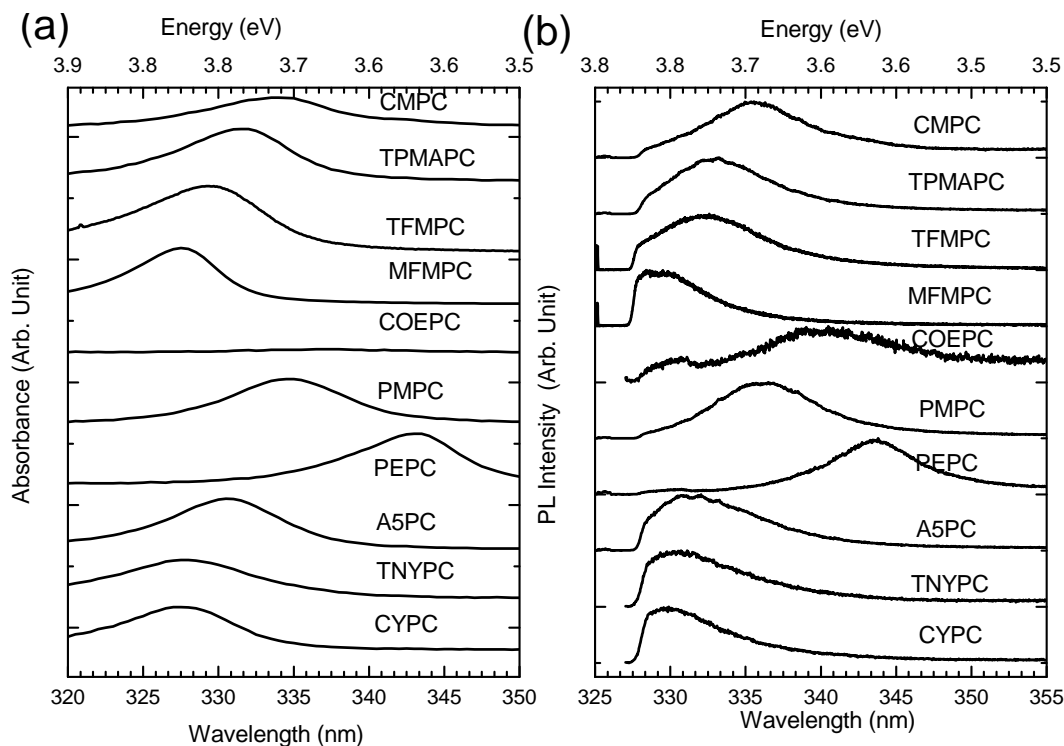
FIGURE 3.3: (a) Optical absorbance (OA) and (b) PL spectra of lead chloride 2D layered perovskites containing 10 different organic groups. PL curves are normalized. The curves are displaced vertically for clarity. The experiments are carried on at room temperature and the excitation source for PL is the 325 nm line of a HeCd laser, the power is 1 mW.

3.1.1.1 Influence of the length of the $(CH_2)_n$ alkyl chain in $(T\text{-}(CH_2)_nNH_3)_2PbX_4$

We firstly consider the case n = 0: CPB, APB, MPB and COPB for the bromide perovskites, CPI, API, MPI and COPI for the iodide perovskites. The PL efficiencies of CPB, APB, MPB and COPB of the bromide perovskites are calculated to be 0.23, 0.12, 0 and 0.07 respectively; for CPI, API, MPI and COPI, the PL efficiencies are found to be 0.09, 0.02, 0.18 and 0.04 respectively. See Table 3.2. These values are quite low, that may be due to the fact that the ammonium unit penetrates the inorganic sheet when it binds to the metal halide octahedron through hydrogen bonding. The three hydrogen bondings on each ammonium head are generally formed either by two bridging halogens and one terminal halogen (as shown in Figure 1.3) or by one bridging halogen and two terminal halogens due to the geometry constraint of the ammonium unit Mitzi (1999b, 2001a). If the main organic group is small enough to fit into the hole within the inorganic sheet, the perovskite will become a 3D (R-NH$_3$)MX$_3$ structure instead of the 2D (R-NH$_3$)$_2$MX$_4$ one. In the 3D case, the exciton binding energy is four times smaller than that in a pure 2D case, that makes its PL more difficult to form at room temperature. Additionally, for these n=0 perovskites, the alkyl chain is too short to remove the main organic group away from the ammonium unit and the 2D self-organization can not occur.

TABLE 3.2: Stokes-shift and PL efficiency of some 2D layered perovskites, from Figures 3.1 and 3.2. PL efficiencies ρ are calculated as explained in the text, relatively to the PL efficiency of PEPI, fixed at the value 1.

Name	stokes-shift(nm)	ρ
(a)		
CPI	4.1	0.09
CMPI	4.9	0.58
CEPI	14.6	0.54
PMPI	5.9	0.16
PEPI	5.8	1
PPPI	19.4	0.07
API	46.7	0.02
AMPI	9.2	0.09
MPI	33	0.18
COPI	20.8	0.04
COEPI	2.9	0.27
(b)		
CPB	68.6	0.23
CMPB	4.0	7.64
CEPB	2	1.16
PMPB	4.2	0.69
PEPB	4.2	3.59
PPPB	6.4	0.15
APB	119.9	0.12
AMPB	81	0.18
MPB	-	0
COPB	64.2	0.07

Now let's examine the influence of n for a fixed characteristic of T. The alkyl chain plays as a spacer, it enables to remove the T unit away from the -NH$_3^+$ head which is tied to inorganic sheets. In the series PMPX, PEPX, PPPX containing phenyl-based molecules, the alkyl chain length has been systematically varied from 1 to 3 carbon atoms, and in the series CPX, CMPX, CEPX containing cyclohexane-based molecules, the length of the alkyl chain has been varied from 0 to 2 carbon atoms. Experimental results show that the PL efficiencies ρ are improved by the introduction of the alkyl chain spacer: the PL efficiencies of CMPB (CMPI) and CEPB (CEPI) are much higher than that of CPB (CPI), the PL efficiency of PEPB (PEPI) is higher than that of PMPB (PMPI), see Table 3.2. It can also be seen that the PL efficiencies are highly sensitive to the value of n: for the series PMPB, PEPB, PPPB, when n increases from 1 to 2, the PL efficiency becomes five times higher. However, when n increases further from 2 to 3, the PL efficiency of PPPB is only 4% that of PEPB. Therefore, changing the length of the alkyl chain, even by only one carbon atom, can drastically change the optical properties of 2D-layered perovskites. Note that the optimal value of n is different depending on the T-group of the perovskites: a clear maximum of the PL efficiency is obtained for n = 1

in the case of the cyclohexane-based perovskites, while it is for n = 2 in the case of the phenyl-based perovskites.

3.1.1.2   Influence of the steric encumbrance of R

In order to investigate the influence of the steric encumbrance of R on the optical properties of 2D-layered perovskites, we fix the length of the alkyl chain spacer n = 1 and compare the bromine-based perovskites PMPB, CMPB, AMPB, MPB, and the iodine-based perovskites PMPI, CMPI, AMPI, MPI. Figures 3.2 (a) and (b) show that the excitonic absorption and PL peaks of PMPB and CMPB are much more pronounced than those of AMPB and MPB, the PL efficiencies of PMPB and CMPB are higher than that of AMPB (Table 3.2(b)). The same trend can also be found from the OA and PL spectra of PMPI, CMPI, AMPI and MPI in Figure 3.1, Table 3.2(a). In addition, we have noted that the deposition by spin-coating of the AMPX and MPX perovskites on a glass substrate is not good, indicating that the self-assembling is difficult. The difference between PMPX, CMPX and AMPX, MPX, comes from their main organic group: the adamantane and myrtanyl are more voluminous than the phenyl and cyclohexane groups. In fact, the steric encumbrance of the organic molecule is quite important. If the projection of the cross-sectional area of the organic molecule on the inorganic sheet can approximately fit into the space provided by the square outlined by the terminal halogens from four adjacent corner sharing octahedra, the structure will be able to accommodate the discrepancy by allowing the organic molecules to tilt or interdigitate, and in this case, 2D self-organization is possible and PL efficiency is correct Mitzi (1999b). However, if the area required by the organic molecule is too large, the perovskite structure is not able to adapt and a different structural type will be formed. In this latter case, the PL efficiency will be low.

Therefore the cross-sectional area of T should be neither too large nor too small compared to one period of the inorganic sheet lattice. Since the exact orientation of the organic groups T in the 2D layered perovskite is not known, it is impossible to calculate precisely the projection area on the inorganic sheet, but it is possible to estimate it. The maximum atomic distances in T for phenyl, cyclohexane, adamandane and myrtanyl are estimated to be 4.97 Å, 5.00 Å, 5.03 Å and 5.84 Å , respectively, from simulation with the software GAUSSIAN. In the bi-organic layer configuration $(R-NH_3)_2PbX_4$, two organic groups R should fit into the space of one period of the inorganic sheet lattice, that is to say, if we take the lattice constants of lead halide inorganic sheets: 5.657Å for $PbCl_2$, 5.90Å for $PbBr_2$ and 6.33Å for PbI_2. The phenyl and cyclohexane are plate-shaped, so that two R groups can be aligned face to face and fit into the area of the inorganic lattice. However, the adamantane and myrtanyl are stereo-shaped and it is very difficult to fit two R groups into one lattice space. This is why bulky R molecules such as adamantane or myrtanyl are not favorable for producing bi-organic 2D-layered perovskites.

It should be noted that for a R group which is favorable for one kind of perovskites containing halogen X, it isn't always also favorable for another halogen X'(X, X' = Cl, Br or I). For example we have prepared PH amine based perovskites with PbX_4^{2-}(X = Cl, Br and I). We saw good PL for PHPI perovskites, weak PL for PHPB perovskites, but very poor optical properties for PHPC. The reason is that the size of PbX_6^{4-} octahedra decreases from I, Br to Cl. Accordingly, the space provided by the square outlined by the terminal halogens from four adjacent corner sharing octahedra decreases at the same time. The PH amine structure matches well with PbI_6^{4-} but is too big for $PbBr_6^{4-}$ and $PbCl_6^{4-}$. Following PHPI, another perovskite APHPI which has a similar structure was also synthesized. Comparing the structure of their organic parts, they have both approximately flat shapes and the length from the ammonium head to the benzene ring end is almost the same. Whereas, APHI ammonium has an additional benzene ring compared to PHI ammonium, which increases the horizontal width by 3.3 Å. Consequently, the PbI_6^{4-} matrix cannot afford its big volume in ordered crystal arrangement. Therefore the self-organization is not possible and no PL signal from APHPI is detected.

3.1.1.3   Influence of the structure flexibility of R

a) Inffluence on optical properties

Let us now compare the PMPB and CMPB perovskites where the alkyl chains have the same lengths. We find that the PL efficiency of CMPB is 11 times higher than that of PMPB. And it is even two times higher than that of PEPB. This improvement in the PL efficiency is believed to be due to the higher flexibility of the cyclohexane structure compared with the phenyl structure. There are generally two kinds of configurations of cyclohexane as it is presented in Figure 3.4. They can form either like a "chair" or a "boat". On the contrary, for benzene, the strong intramolecular interactions in the phenyl moiety make its structure rather rigid and result in a configuration completely flat. The structure of the cyclohexane moiety being relatively more flexible than the phenyl moiety, it results in a better match with the inorganic sheet. This trend is confirmed again with the CHEPB perovskite, which presents PL efficiency smaller than that of CEPB: the organic part CHE has less flexibility than the organic part CE.

The rigidity of organic moieties can be further adjusted by fine modification in chemical structure. The TPMA and TFM amines with an oxygen atom on cyclohexane becomes less flexible because the two C-O bonds beside the oxygen atom are much more rigid than C-C bond. Analogically, with a -O- in 5 carbons cycloalkane structure, and further two more double bonds as "C=C", MFM is even more rigid than TPMA and TFM. For the perovskites based on A5, TNY and CY, we introduced a cycloalkane structure between the benzene cycle and their $-NH_3^+$ head. Comparing with PE based perovskites, the motion of confined alkyl chain part is undoubtedly limited and thus
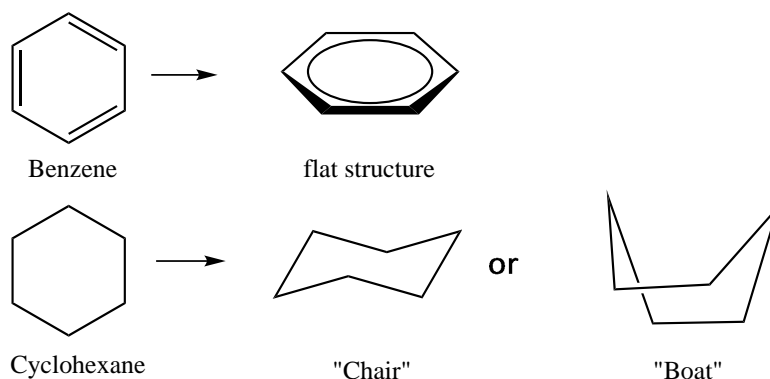
FIGURE 3.4: Structural configurations of benzene and cyclohexane.

more rigid than single alkyl chain in PE amine. Consequent changes are observed in their properties: from Figure 3.3, we see that the resonance bands of A5PC, TNYPC, CYPC shift to higher energy than PEPC. Also, those of TPMAPC, TFMPC and MFMPC shift to higher energy than CMPC. We think that this phenomenon is closely related to the structure rigidity of the organic part.

b) Influence on surface quality

Since the self-assembly property of perovskites results from noncovalent interactions among molecules, it depends a lot on the properties of organic components which have a direct influence on arrangement of the molecules during crystal growth. The crystallization patterns (sizes and shapes) of a perovskite thin film deposited by spin-coating from a certain solution concentration are relatively reproducible. Figure 3.5 presents the images of PEPI and PMPI thin films observed under microscope. It is clearly seen that the size of the crystallites of PMPI is larger than those of PEPI which is one explanation of the reasons why the PMPI surface roughness is larger than the PEPI surface roughness.

(a) PEPI thin film   (b) PMPI thin film
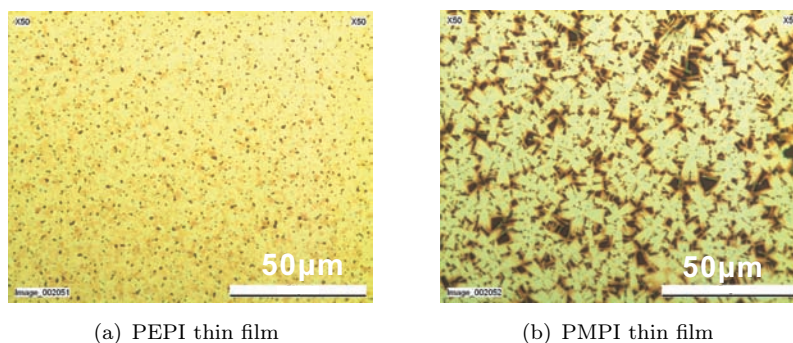
FIGURE 3.5: Images under microscope for (a) a PEPI thin film and (b) a PMPI thin film

We find that the thin films obtained from phenyl-based perovskites have smoother surfaces than those obtained from other kinds of perovskites such as cyclohexane-,

myrtanyl- etc.. The reason is that the phenyl-based ammoniums interact with each other by $\pi - \pi$ stacking while the other kinds of ammoniums interact by Van der Waals or hydrogen interactions. The former force is much stronger than the latter two cases , it therefore associates more tightly the perovskites structure between sheets. As seen in Figure 3.6, some chloride based perovskites: PEPC, A5PC, CMPC and TPMPAPC, which are deposited from a 1.5 wt% solution by spin-coating, are observed under a microscope. Comparing (a) and (c), we see obvious differences in surface continuity: CMPC

(a) PEPC thin film

(b) A5PC thin film

(c) CMPC thin film
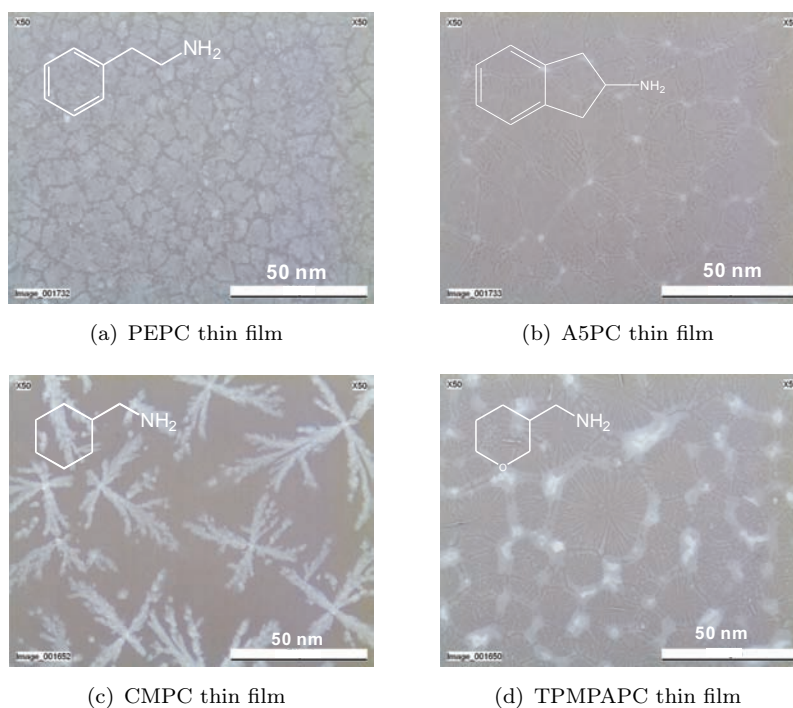
(d) TPMPAPC thin film

FIGURE 3.6: Images under microscope of PEPC, A5PC, CMPC and TPMPAPC thin films. The small chemical structures included in each image represent the corresponding organic amines in perovskites

film presents much more areas without deposition than PEPC film. To study the surface roughness, the topography of these samples is measured by an AFM in an area of 20 μm×20 μm, as shown in Figure 3.7. From (a) and (c), we find that the average roughness of PEPC is 7.3 nm, which is much smaller than that of CMPC, 17.2 nm.

Besides the reason of the type of interaction between organic groups, another trend we find is that slight modification of the organic moiety structure can further optimize the surface smoothness of thin films. As seen in Figure 3.6(b), the A5PC belonging to a group of phenyl-based perovskites with more restrained structure in the alkyl chain (like CYPC and TNYPC), is relatively more rigid than PEPC and leads to more flat conformation in ammonium molecular configuration. The molecules in organic sheets can thus better stack with each other resulting in a smoother film surface. Similarly, the TPMPAPC, with an oxygen atom introduced in cycloalkane, becomes less flexible at each side of -O- and is more flat in plane than CMPC. It therefore exhibits better surface

(a) PEPC thin film

(b) A5PC thin film

(c) CMPC thin film
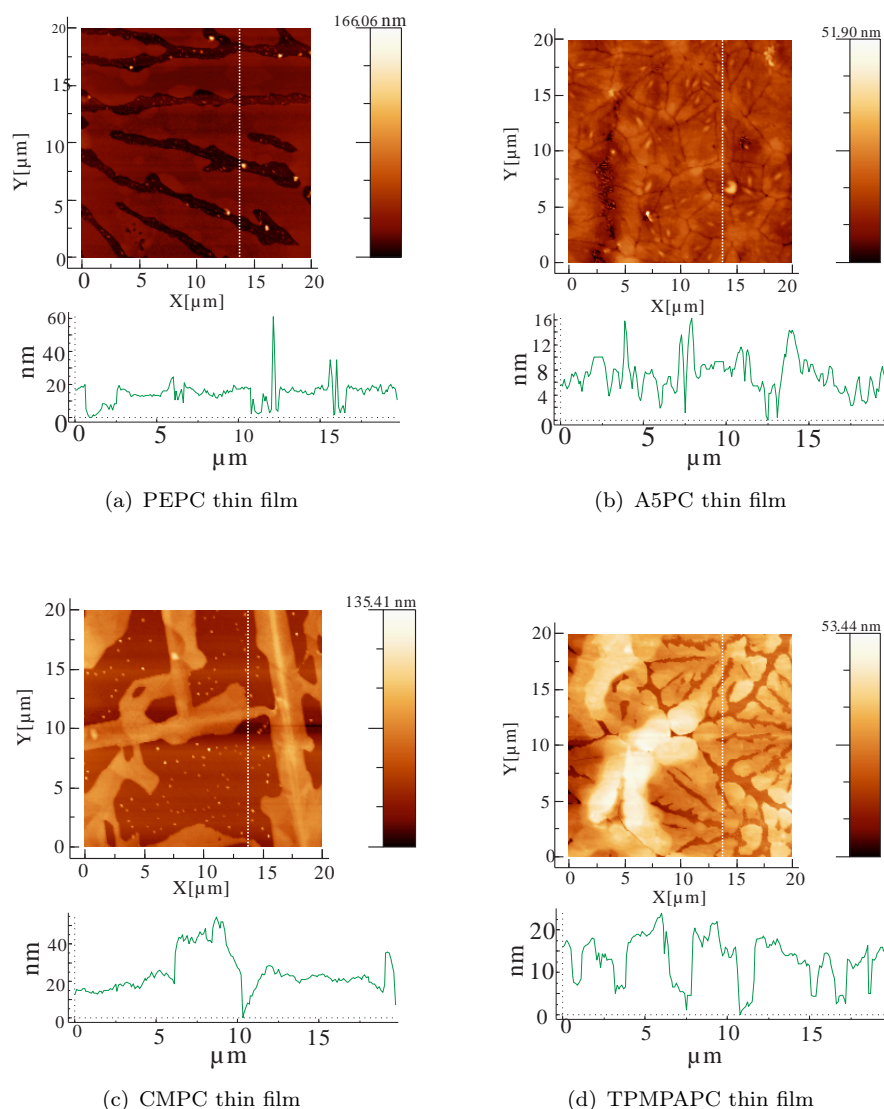
(d) TPMPAPC thin film

FIGURE 3.7: AFM images of PEPC, A5PC, CMPC and TPMPAPC thin films. The vertical cross-sections marked with white dotted lines in (a), (b), (c) and (d) are presented in graphs below, for each perovskite thin film.

quality. Figure 3.7(b) and (d) present the topographies of A5PC and TPMPAPC thin films, their roughnesses are found to be 2.7 nm and 6.0 nm respectively. Comparing with their corresponding perovskites with less rigid structures: CMPC and PEPC, a great improvement in surface quality is obtained.

3.1.2 $(NH_3$-R-$NH_3)PbX_4$ perovskites

Besides the monoammoniums, some perovskites based on diammoniums have been synthesized. While $(R-NH_3)_2PbX_4$ perovskites experience weak interactions between organic parts, the $(NH_3$-R-$NH_3)PbX_4$ perovskites with two -NH_3^+ heads have more tight connections: covalent bonds between inorganic sheets.

The 2D-layered perovskites samples are deposited by spin-coating with a thickness of about 50 nm. Table 3.3 shows some diammoniums we use to prepare perovskites.

Table 3.3: Chemical structure, complete name and abbreviation of the amines part of some diammoniums perovskites used in experiment
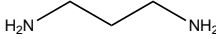
Chemical structure	Name	Abbreviation
	1,3-Diaminopropane	13D
	1,4-Diaminobutane	14D
	1,6-Hexanediamine	16D
	C-(Tetrahydro-pyran-3-yl)-methylamine	18D
	1,12-Dodecanediamine	112D
	Trimethylhexamethylenediamine (2,2,4- and 2,4,4- mixture)	TMD
	1,3-Cyclohexanebis(methylamine)	C3D
	1,4-Cyclohexanebis(methylamine)	C4D
	3(4),8(9)-Bis(aminomethyl) tricyclo [5.2.1.0] decane	TCD
	1,4-Phenylenedimethanamine	P4D
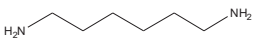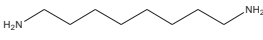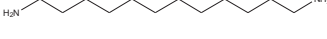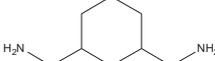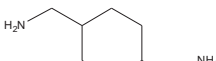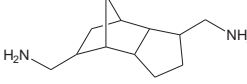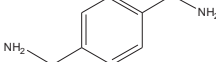
Optical properties of lead bromide perovskites based on these ammoniums have been studied from OA and PL measurements. Spectra are shown in Figure 3.8.

The 13DPB, 14DPB, 16DPB, 18DPB and 112DPB are a series of $(NH_3\text{-}(CH_2)_n\text{-}NH_3)PbBr_4$ perovskites, with n=3, 4, 6, 8, 12. We vary the n value in the aim to adjust the distance between inorganic sheets and flexibility of perovskites alkyl chain. When n grows, the flexibility of alkyl chains increases. From the OA and PL spectra, we see that these lead bromide perovskites absorb in near UV range, PL peak position varies from several nm with n. In the Table 3.4, OA, PL peak positions and relative PL efficiency of these perovskites (supposing ρ=1 for 112DPB in this group) are reported.
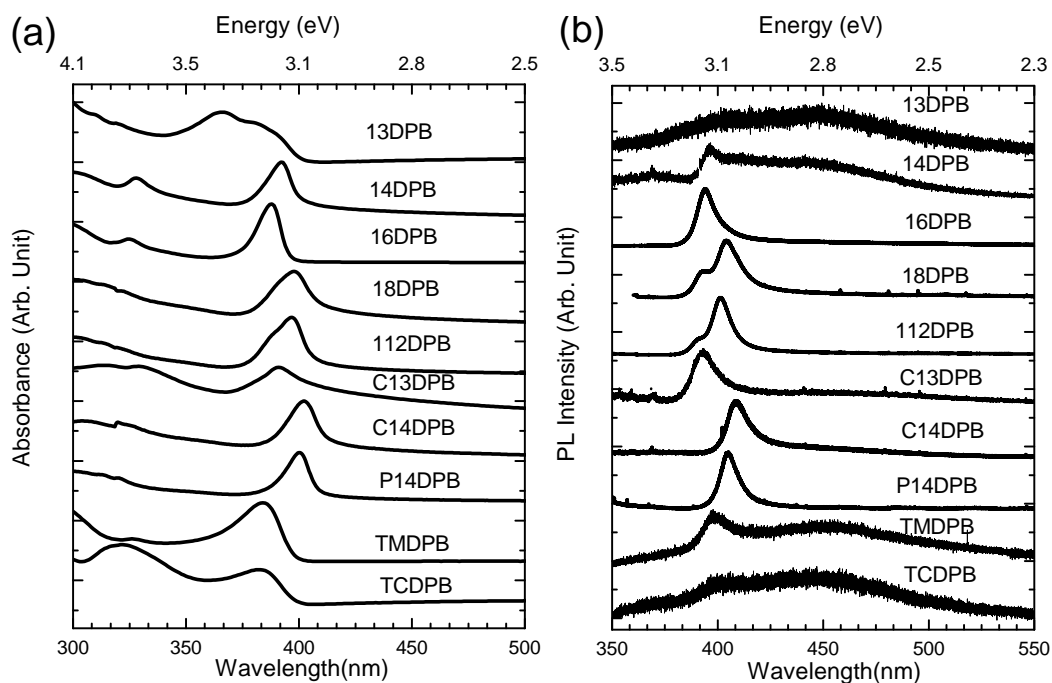
FIGURE 3.8: (a) OA and (b) PL of some lead bromide diammoniums based 2D layered perovskites. PL curves are normalized. The curves are displaced vertically for clarity. The experiments are carried on at room temperature and the excitation source for PL is the 325 nm line of a HeCd laser, the power is 1 mW.

It is found that the PL efficiencies of TMDPB, TCDPB, 13DPB, 14DPB and 16DPB are relatively inferior to PL efficiency of 112DPB. And it seems that the organic amines conformations of TMDPB and TCDPB are not favorable for the self-organization. For 13DPB and 14DPB which have the most rigid structure in this series, nearly no PL emission is detected. The ρ value is slightly improved in perovskites C3DPB, C4DPB and P4DPB in which the diammoniums have a distance of 5, 6 and 6 carbons respectively between the two $-NH_3^+$ heads, but with a cyclo- or -phenyl structure in the middle of their alkyl chain. This particular structure is similar to the n=5 and n=6 $(NH_3\text{-}(CH_2)_n\text{-}NH_3)PbBr_4$ perovskites but more rigid than them because being restrained by cyclo- or -phenyl structures. PL efficiency is higher in 16DPB perovskites which are more flexible than C4DPB and P4DPB perovskites. And when n increases from 3 to 12, PL efficiency increases: ρ=1 for n=12 (112DPB) but ρ=0.002 for n=3 (13DPB), so about 500 times larger efficiency is obtained for n=12.

With the optimized values n=8 and n=12 for diammoniums, we then prepare the lead iodide perovskites 18DPI and 112DPI. The OA and PL spectra at room temperature are measured and shown in Figure 3.9, the spectral informations are summarized in Table 3.5, we suppose the ρ value of PEPI is 1 among this group. The PL peak of 18DPB lies at 376 nm, which is very different from the energy position of the PL peaks of 112DPB and PEPI. Additionally, comparing the ρ values, 3.5 times smaller PL efficiency is obtained when n value varies from 12 to 8. The 112DPI film absorbs and emits at

TABLE 3.4: OA and PL spectral informations of some lead-bromide diammoniums based perovskites (from Figure 3.8). λ_{OA} and λ_{PL} are the wavelength of the OA and PL maxima respectively, a_{325} is the absorption coefficient at 325 nm. PL efficiencies ρ are calculated as explained in the text, relatively to the PL efficiency of 112DPB, fixed at the value 1.

Name	$\lambda_{OA}(nm)$	a_{325}	$\lambda_{PL}(nm)$	ρ
13DPB	365.5	0.148	447.0	0.002
14DPB	392.1	0.524	396.2	0.002
16DPB	387.8	0.472	394.9	0.142
18DPB	398.0	0.108	404.1	0.390
112DPB	396.5	0.098	401.5	1
C3DPB	391.0	0.761	393.5	0.022
C4DPB	406.0	0.472	408.9	0.045
P4DPB	400.0	0.138	404.8	0.099
TMDPB	384.0	0.234	398.4	0.006
TCDPB	383.0	0.257	401.1	0
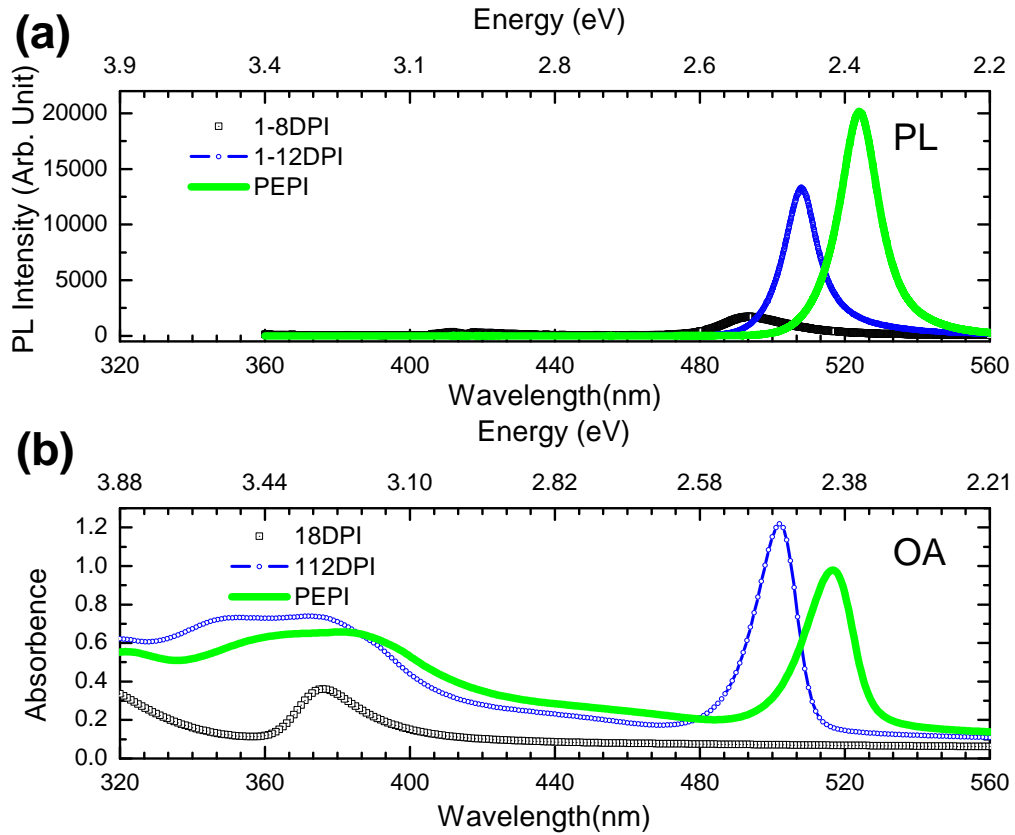
FIGURE 3.9: (a) OA and (b) PL of 18DPI, 112DPI lead iodide diammoniums based 2D layered perovskites. PEPI OA and PL spectra are reported as reference. The samples are excited with the 325 nm line of a HeCd laser at 1 mw in air.

508 nm and has good optical properties: relatively thin and intense PL peak is seen, comparing with the standard layer PEPI, its PL efficiency is about 0.59 times the one of

TABLE 3.5: OA and PL spectral informations of 18DPI, 112DPI lead iodide diammoniums based 2D perovskites, from figure 3.9. PEPI values are reported as a reference. PL efficiencies ρ are calculated as explained in the text, relatively to the PL efficiency of PEPI, fixed at the value 1.

Name	$\lambda_{OA}(nm)$	a_{325}	$\lambda_{PL}(nm)$	ρ
18DPI	376.0	0.282	493.3	0.17
112DPI	502.0	0.61	507.9	0.59
PEPI	516.5	0.55	524.1	1

PEPI. Furthermore, topography properties of 18DPI and 112DPI films are characterized by AFM measurements on a 5 μm $\times$ 5 μm dimension zone of each sample, see Figure 3.10. The thicknesses of 18DPI and 112DPI are 55 nm and 51 nm respectively. On the surface of 18DPI, crack structures appear, the average roughness is $\Delta = 7.6$ nm. 112DPI is smoother with $\Delta = 3.6$ nm. So we confirm here the correlation between the optical properties and surface properties.

(a) 18DPI thin film, $\Delta = 7.6$ nm   (b) 112DPI thin film, $\Delta = 3.6$ nm
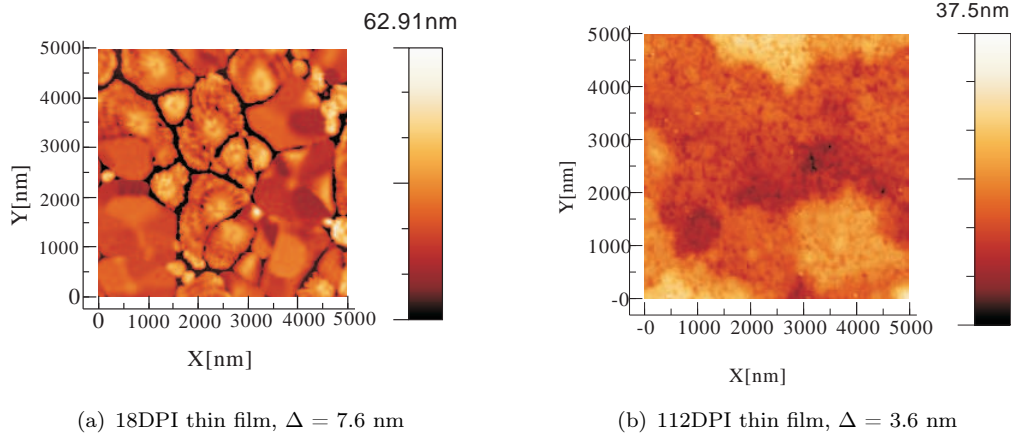
FIGURE 3.10: Topography of a 55 nm 18DPI thin film and a 51 nm 112DPI thin film.

3.2   Mixed perovskites

In this section, we will present another way of tuning the optical properties of perovskites. In previous Paragraph 3.1, each perovskite compound consists of one single kind of organic ammonium cation and one single kind of inorganic anion. In this paragraph, we will study two groups of mixed perovskites: the group with mixing of halogenide ions in the organic part: $(R-NH_3)_2PbY_xZ_{4-x}$ and the group with mixing of the ammonium cations in the organic part: $(RR'-NH_3)PbX_4$. This study enlarges the possibilities to fabricate new types of perovskites by combining the properties of some known perovskites, and no doubt opens a wide way for their applications.

3.2.1 Mixing in the inorganic part: mixed perovskites $(R\text{-}NH_3)_2PbY_xZ_{4-x}$

3.2.1.1 Mixed perovskites $(R\text{-}NH_3)_2PbY_xZ_{4-x}$

A typical way to fabricate the mixed perovskites $(R\text{-}NH_3)_2PbY_xZ_{4-x}$ is to mix the inorganic salts of two different kinds of halogens while keeping the organic moiety unique, x is the molar ratio between Y and Z halogens. The synthesis of $(C_6H_5C_2H_4NH_3)_2PbCl_xBr_{4-x}$ and $(C_6H_5C_2H_4NH_3)_2PbBr_xI_{4-x}$ is reported in reference Kitazawa (1997a) but the optical properties are not studied in details in this paper. Here we synthetize some mixed perovskites $(C_6H_5C_2H_4NH_3)_2PbCl_xBr_{4-x}$ which we abbreviate as $PEPC_xB_{4-x}$. The synthesis method simply consists in mixing the PEPC and PEPB solutions in a certain ratio : for example to prepare the solution in a concentration of 0.05 mol/L of $PEPC_2B_2$ mixed perovskite, where the Cl and Br are 1 :1 in molar quantity, we need to take the same volume of PEPC 0.05mol/L DMF solution and PEPB 0.05 mol/L DMF solution and mix them together. The 2D-layered film is then prepared by spin-coating this 0.05 mol/L solution on quartz slides at 2000 rpm for 30 seconds, followed by an annealing at 95 °C for 1 min. The thickness is about 25 nm.

Similarly, we prepare another series of mixed perovskites $CMPC_xB_{4-x}$. We choose in particular the CM group because the chemical structure of CM (see its structure in table 3.1) is more stable than PE, as we will see in Chapter 4. Samples are prepared from their 0.026mol/L in DMF solution and deposited by spin-coating.

In order to confirm the crystal structure of the mixed perovskites we have fabricated, XRD measurements are carried on for these series of perovskites. The XRD experiments have been performed in ECNU, China, on a Rigaku Ultima IV type equipment, at CuKα. The resolution is 0.01° and scan speed is 10°/min. The XRD spectra are presented in Figures 3.11 for $PEPC_xB_{4-x}$ and Figure 3.12 for $CMPC_xB_{4-x}$. Sharp diffraction peaks are seen, which reveal that these crystals are well self-organized structures, presenting a single phase. A quantitative study could not be made, but it can be seen that the position of the first diffraction peak slightly and continuously varies when the concentration x varies, indicating that the lattice parameters of the mixed perovskites vary between the lattice parameters of the pure perovskites.

OA and PL spectra of these films are measured at room temperature and reported in Figure 3.13 for $PEPC_xB_{4-x}$ and in Figure 3.14 for $CMPC_xB_{4-x}$. A very important thing has to be noticed first, which is surprising: we don't observe two peaks corresponding to the pure bromide and chloride perovskites, but only one OA (PL) peak, lying between the OA (PL) peaks corresponding to the pure bromide and chloride perovskites. When some Br atoms in bromide perovskites are replaced with a percentage of Cl atoms, the OA and PL peaks gradually shift to shorter wavelength. As a consequence of this experimental observation, we can affirm that we have not some distinct clusters of bromide and chloride perovskites inside the layer, but really we have a crystal where the Br and Cl atoms are
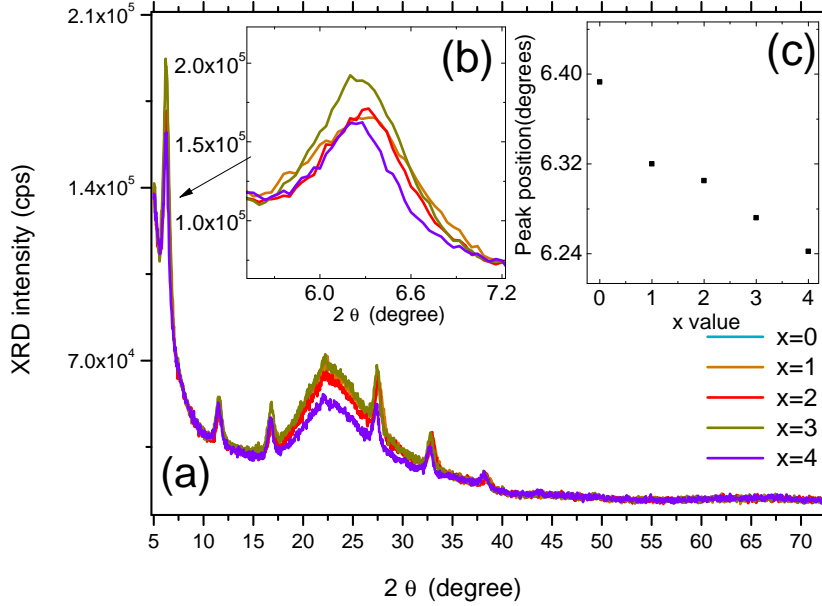
FIGURE 3.11: (a) X-ray Diffraction pattern for $PEPC_xB_{4-x}$ mixed perovskites fabricated on quartz substrate. The solutions used for deposition are 0.05 mol/L. The insert graph (b) is the a zoom of the first peak around 6.35 °. The insert graph(c) shows the evolution of the peak position of the first mode versus x value.

distributed in a randomized way inside the inorganic layers, that is to say that each Pb atom is surrounded by both Br and Cl atoms, as seen in Figure 3.15.

Thus we can have the idea that the band gap modulation with concentration can be analyzed as in the ternary inorganic alloys such as as $Ga_{1-x}Al_xAs$, $ZnSe_xTe_{1-x}$ .... Naumov et al. (1993); Yang et al. (2003) The concentration dependent energy gap variation can be described phenomenologically by the following second degree equation 3.1:

$$E_{ex}(x) = E_{ex}(4)\frac{x}{4} + E_{ex}(0)(1 - \frac{x}{4}) - b\frac{x(4 - x)}{16}. \tag{3.1}$$

b is named the bowing parameter, $E_{ex}(4)$ and $E_{ex}(0)$ are the exciton energies of the pure perovskites. For $CMPC_xB_{4-x}$, the fitting of the experimental results, exhibited in Figure 3.16, provides $b_{abs} = 0.208$ eV for the fitting of the OA peak positions ($E_{ex}^{abs}(0)$ = 3.08 eV and $E_{ex}^{abs}(4) = 3.73$ eV are fixed from the OA spectra of CMPB and CMPC respectively) and $b_{PL} = 0.4099$ eV for the fitting of the PL peak positions ($E_{ex}^{PL}(0) =$ 3.04 eV and $E_{ex}^{PL}(4) = 3.69$ eV are fixed from the PL spectra of CMPB and CMPC respectively).

Furthermore it can be seen in Figures 3.13 and 3.14 that the OA and PL peaks of the mixed perovskites are broader than the OA and PL peaks of the pure perovskites.
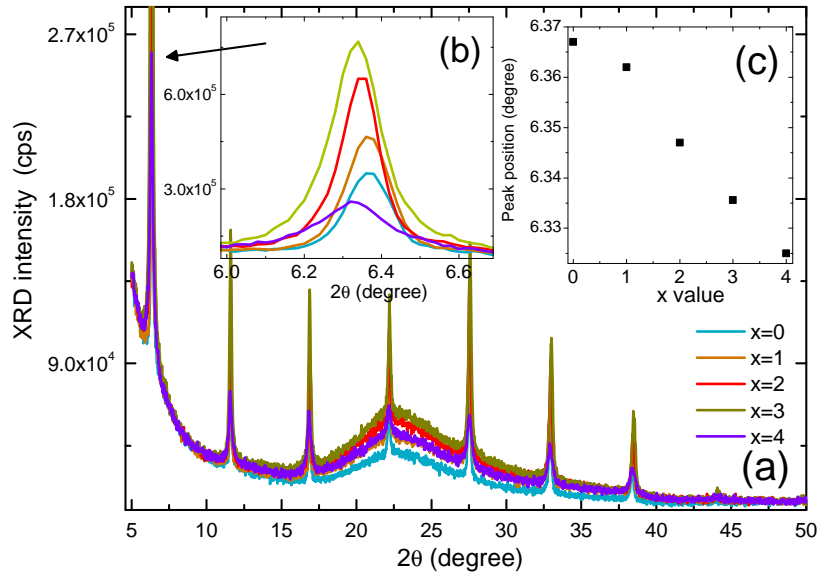
FIGURE 3.12: (a) X-ray Diffraction pattern for CMPC$_x$B$_{4-x}$ mixed perovskites fabricated on quartz substrate. The solutions used for deposition are 0.026 mol/L. The insert graph (b) is the a zoom of the first peak around 6.35 °. The insert graph (c) shows the evolution of the peak position of the first mode versus x value.

The FWHM of OA and PL peaks of CMPC$_x$B$_{4-x}$ are reported in Figure 3.16(b): the FWHM of pure perovskites CMPB and CMPC are typically 108 meV for OA of CMPB, 69 meV for PL of CMPB, 136 meV for OA of CMPC and 85 meV for PL of CMPC. For mixed crystals, FWHM is larger and the largest FWHM is seen for x= 2 (216 meV for OA of CMPC$_2$B$_2$). x = 2 corresponds to the maximum of disorder of the distribution of Br$^-$ and Cl$^-$ halogens around each Pb atom.

These two features: the continuous shift of the OA and PL peaks of the mixed perovskites between the peaks of pure perovskites, and the existence of a maximum for FWHM at x = 2, corresponding to the greatest disorder, can be found also in ternary inorganic semiconductors alloys such as Ga$_{1-x}$Al$_x$As. In these ternary alloys, the Al atoms are randomly distributed on the Ga sites. The excitons are Wannier excitons having a large Bohr radius (about 100 Å), then the excitonic wavefunction covers a large number of elementary cells and the excitonic properties are averaged properties. In our mixed perovskites, the fact that we find similar alloy effects indicates that the exciton wavefunction covers enough elementary cells to produce an averaging effect of the optical properties. It provides thus an important information about the excitonic properties: with exciton binding energies as high as several 100 meV, it can be thought that the excitons are very localized ones, Frenkel excitons. But the experimental findings concerning the alloy effect seem to indicate that the excitonic wavefunction is delocalized
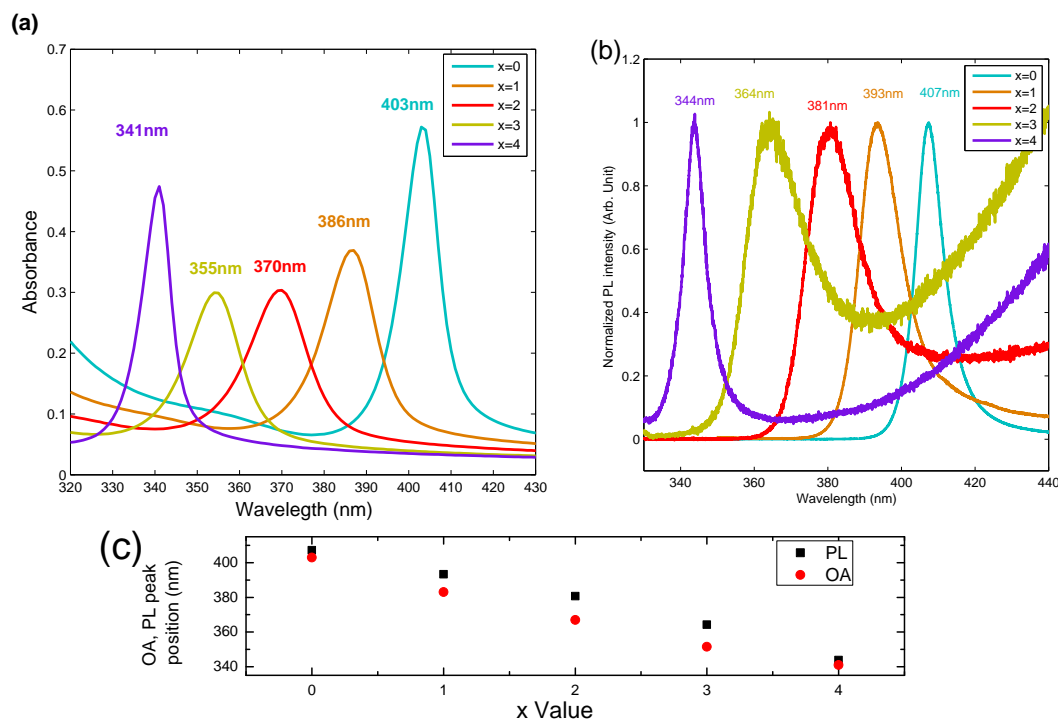
FIGURE 3.13: (a) Optical absorbance (OA) spectra and (b) Photoluminescence (PL) spectra of PEPC$_x$B$_{4-x}$ thin films. PL spectra are normalized. The excitation source is the 325 nm line of a HeCd laser and the spectra are measured at room temperature. (c) Evolution of the resonance peaks positions as a function of x value.

enough in the layers plane (over several elemenary cells) to produce an average of the excitonic properties.

In Figure 3.16(c), the Stokes-shift between OA and PL spectra is reported as a function of the concentration x for CMPC$_x$B$_{4-x}$. It can be seen that the Stokes-shift is of the order of several meV, so relatively small, indicating that the excitons are probably free excitons or slightly bound excitons. But it can be also seen that the Stokes-shift of the mixed perovskites is larger than the Stokes-shift of the pure perovskites: the largest Stokes-shift happens for x=2. These changes of Stokes-shift can be attributed to deformation of inorganic layer caused by lattice distortion in mixing crystals.

In order to have more information about these mixed perovskites, we have performed low-temperature (10 K) OA spectra. Figures 3.17 and 3.18 show OA spectra for several PEPC$_x$B$_{4-x}$ and CMPC$_x$B$_{4-x}$ perovskites respectively. The absorbance peaks lie at 3.055 eV, 3.175 eV and 3.635 eV for PEPB, PEPC$_1$B$_3$ and PEPC respectively, and the absorbance peaks lie at 3.01 eV and 3.176 eV for CMPB and CMPC$_1$B$_3$ respectively.

From the energy difference between the main resonant peak and the step-like structure, we can deduce an order of magnitude of the exciton binding energy: 332 meV for PEPB, 448 meV for PEPC, and the exciton binding energies of the mixed perovskites are of the same order of magnitude : 348 meV for PEPC$_1$B$_3$, 449 meV for CMPC$_1$B$_3$.
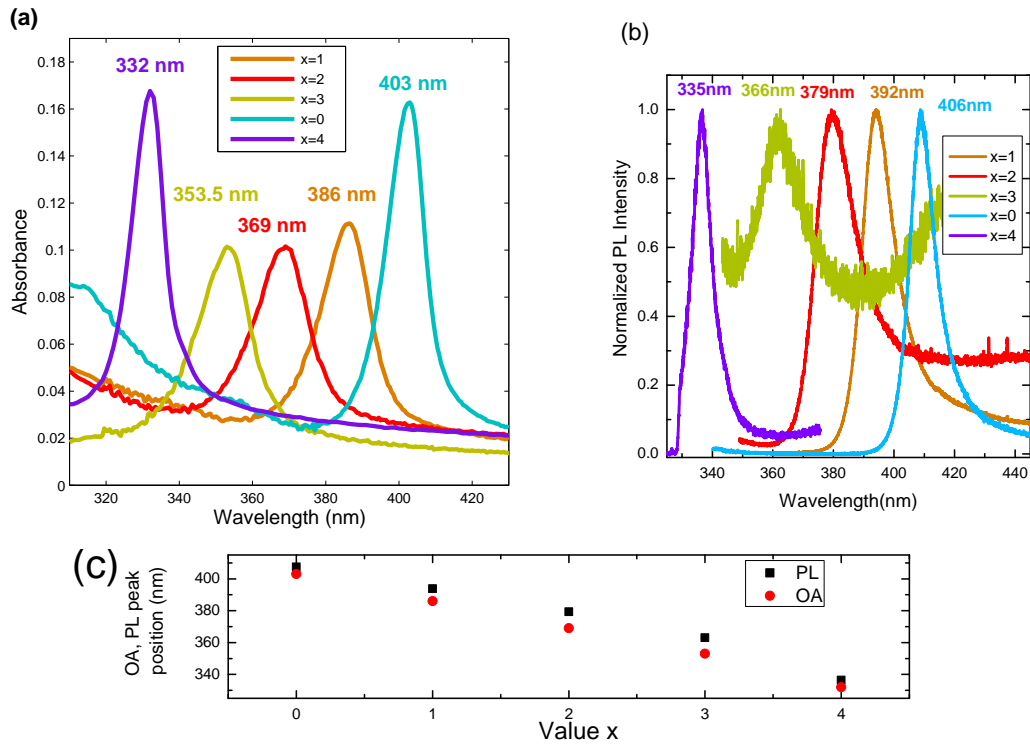
FIGURE 3.14: (a) Optical absorbance (OA) and (b) Photoluminescence (PL) spectra of $CMPC_xB_{4-x}$. PL spectra are normalized. The excitation source is the 325 nm line of a HeCd laser and the spectra are measured at room temperature. (c) Evolution of the resonance peaks positions as a function of x value.
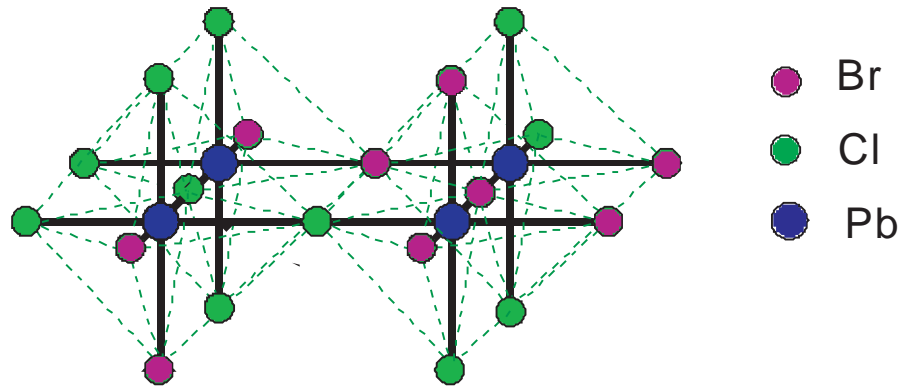
FIGURE 3.15: Schema of $PbCl_xBr_{4-x}^{2-}$ mixed wells. The Br and Cl atoms are distributed in a randomized way inside the inorganic layers.

Photobleaching measurements are carried on at room temperature in order to examine the photostability of the series of mixed perovskites. The films are exposed under the 325 nm line of a HeCd laser, with a power of 7 mW during 1 hour. See Figure 3.19(a) for $CMPC_xB_{4-x}$ and (b) for $PEPC_xB_{4-x}$. The ratio between the PL intensity at the last second (at 3600 s) I_{3600} and the initial intensity (at 0 s) I_0 is reported in Figure 3.19(c). PEPC shows a better photostability than PEPB: it can be seen that $PEPC_xB_{4-x}$ exhibits a photostability which is intermediate between PEPB and PEPC, so in this case also, the optical properties of the mixed perovskites seem to be averaged between the
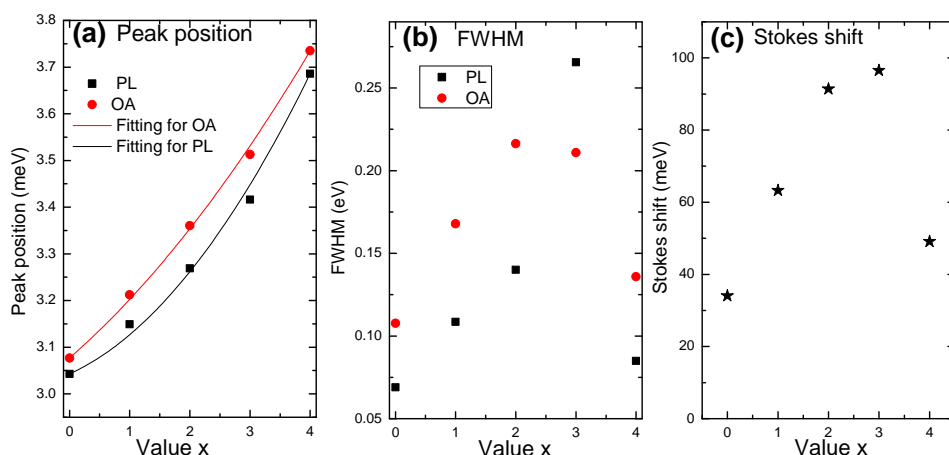
FIGURE 3.16: (a) OA and PL peak positions, (b) FWHM, and (c) Stokes-shift for $CMPC_xB_{4-x}$ mixed perovskites. Data informations are extracted from OA and PL spectra in Figure 3.14. Parameters used for the fits are indicated in the text.
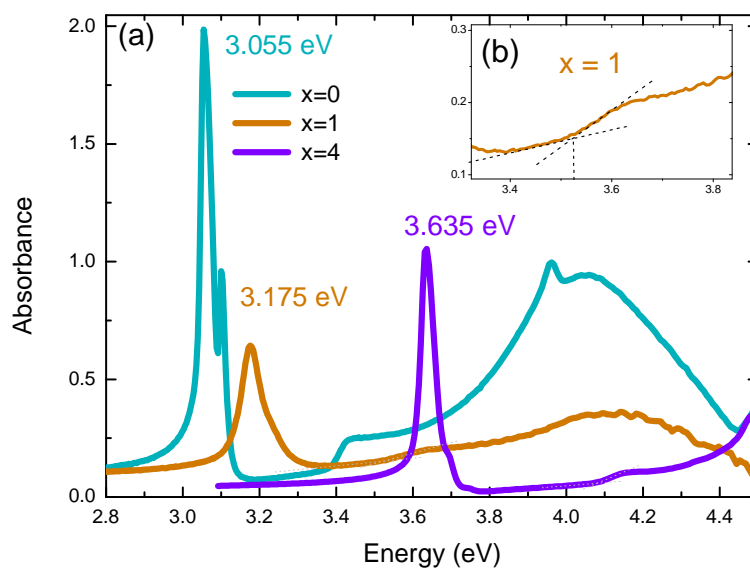
FIGURE 3.17: (a) OA spectra measured at 10 K in He environment for $PEPC_xB_{4-x}$ mixed perovskites with x=0, 1 and 4. The insert graph (b) is a zoom of x = 1 case, in order to see clearly the step-like structure.

optical properties of the pure perovskites. We have however to note that $CMPC_xB_{4-x}$ shows another behavior: CMPC is more photostable than CMPB but $CMPC_3B_1$ and $CMPC_2B_2$ exhibits a better photostability than CMPC, this fact is not understood for the moment.

In conclusion, we have synthesized $CMPC_xB_{4-x}$ and $PEPC_xB_{4-x}$ mixed crystals.
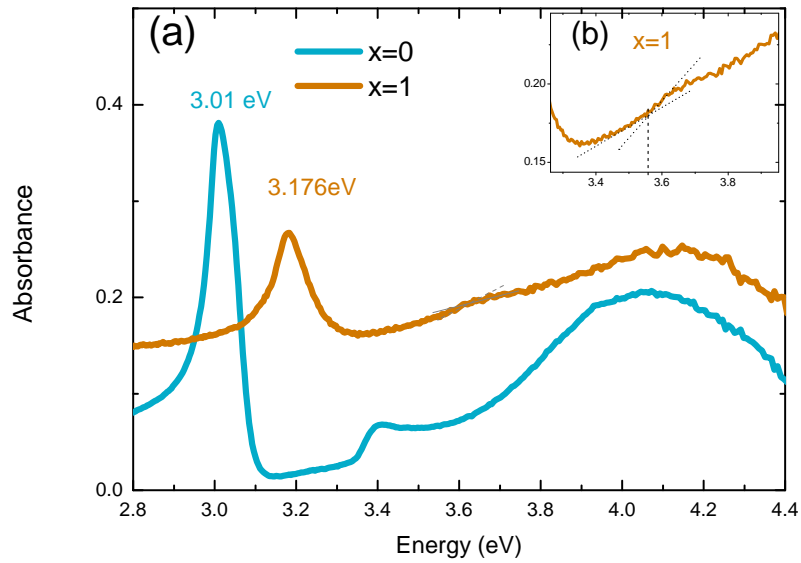
FIGURE 3.18: (a) OA spectra measured at 10 K in He environment for CMPB and CMPC$_1$B$_3$ perovskites. The insert graph (b) is a zoom of x = 1 case, in order to see clearly the step-like structure.
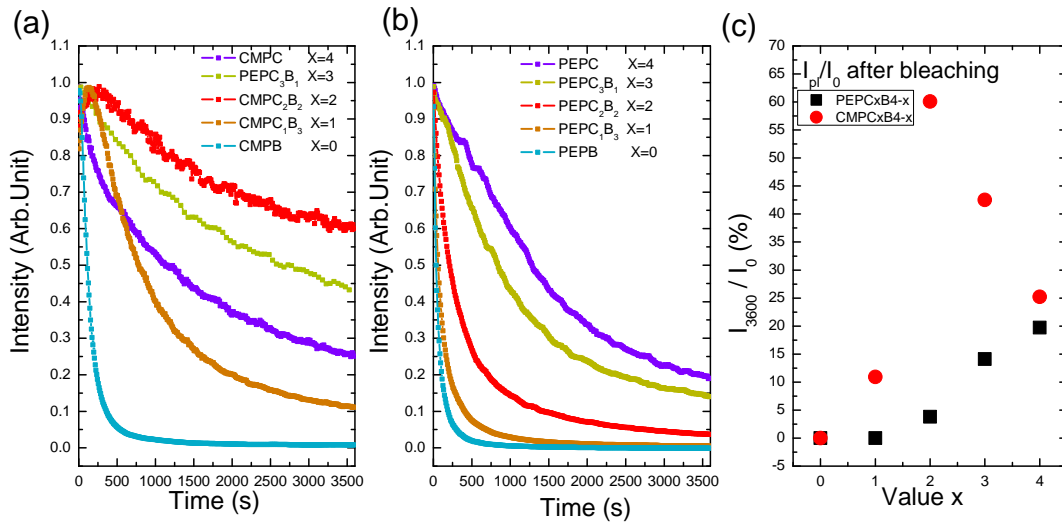
FIGURE 3.19: Photobleaching measurements at room temperature for (a) CMPC$_x$B$_{4-x}$ and (b) for PEPC$_x$B$_{4-x}$. The laser power is kept at 7 mW, the excitation wavelength is 325 nm. (c) I$_{3600}$/I$_0$ (as defined in the text), as a function of x.

XRD spectra proved that these mixed perovskites are well self-organized. These mixed 2D-layered crystals show strong excitonic properties, as in the pure perovskites. By varying x, we have means to tune continuously the wavelength of the excitonic transition. Furthermore, the photostability in the CM mixed series is remarkable for CMPC$_2$B$_2$

crystal which keeps still 60.1% of its PL intensity after 3600 s under intense illumination. These encouraging results will surely be useful for following studies and practical applications.

3.2.1.2   Mixed crystals R-NH$_3$X + PbY$_2$

Another possible method of mixing perovskites consists in mixing ammonium salts and inorganic salts having different halogen species in a single molecule during the second step of synthesis (see Formula 2.16). In this study, we mix the organic salt 4-Fluorophenethylamine hydrobromide abbreviated as 4FPEB (we will see some details concerning molecule in Chapter 4) and PbI$_2$ (lead iodide). We call this mixed perovskites as 4FPEB-PbI$_2$ hereafter. The introduction of halogen Br from organic salts to PbI$_2$ matrix will change the coordination condition around Pb^{2+} ions in inorganic sheets and consequently causes distortion in lattice structure.

Thin films of 4FPEB-PbI$_2$ have been prepared by spin-coating their DMF solution on quartz substrate and annealed at 95 °C for 1 minute. The 4FPEB-PbI$_2$ film has a thickness of 85 nm. Figure 3.20 shows the OA and PL spectra of this mixed crystal.
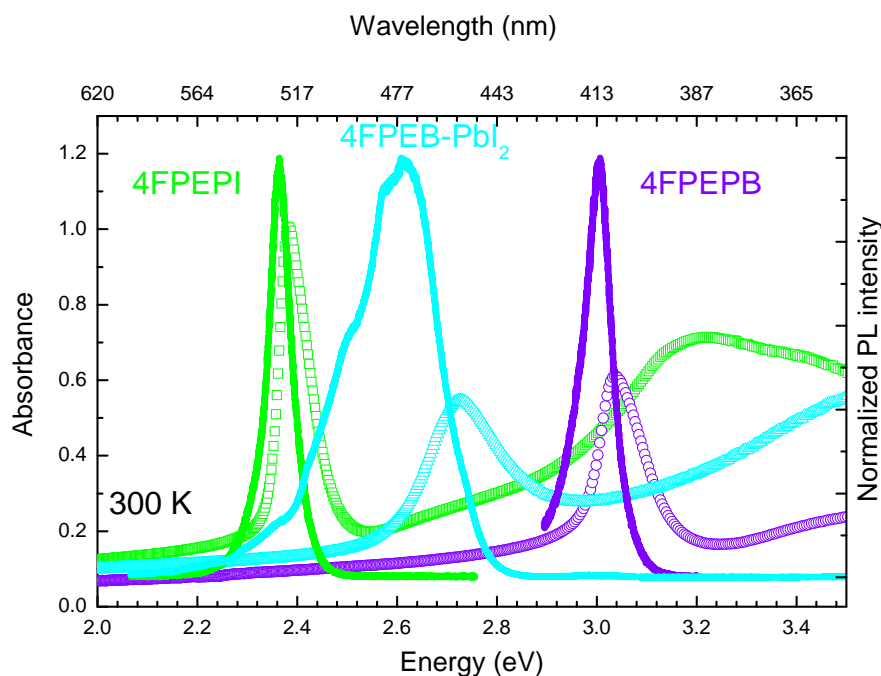
FIGURE 3.20: OA (scattered lines), PL (solid lines) spectra of 4FPEB-PbI$_2$, 4FPEPI and 4FPEPB thin films. Experiments are carried on at room temperature. The PL intensities are normalized to 1, and the 325 nm line of HeCd laser is used as an excitation source for PL spectra.

For comparison, we put the spectra of 4FPEPB and 4FPEPI pure perovskites. A strong

resonant band of 4FPEB-PbI$_2$ around 2.6 eV, which situates between the resonant bands of 4FPEPB (3 eV) and 4FPEPI (2.37 eV), is observed.

The 4FPEB-PbI$_2$ layer has a good PL efficiency, equal to 0.64 times the PL efficiency of PEPI. The FWHM in OA and PL spectra is obviously larger for 4FPEB-PbI$_2$ than that of pure perovskites: while the FWHM of the PL peaks are 9.2 nm (49 meV) and 10.9 nm (67 meV) for 4FPEPI and 4FPEPB respectively, the FWHM of the PL peak at room temperature is about 27.3 nm And the Stokes-shift of the mixed perovskite is large: 14.5 nm (84 meV), while the Stokes-shift for 4FPEPI and 4FPEPB are 4.6 nm (33.5 meV) and 4.9 nm (21.4 meV) respectively. This might be due to inhomogeneity in mixing conditions: the distribution of Br$^-$ and I$^-$ ions around each Pb^{2+} ion is inhomogeneous, causing complication of local hybridization and thus diversity in electronic energy band structures. However, this mixture is confirmed to be a well ordered crystal. The diffraction spectrum, performed in LPN, reveals that the 4FPEB-PbI$_2$ films are multi-layered structures and highly ordered with single phase, see Figure 3.21. Lattice parameter is found to be 1.64 nm which is quite similar to that of 4FPEPI thin layer, which is 1.65 nm.
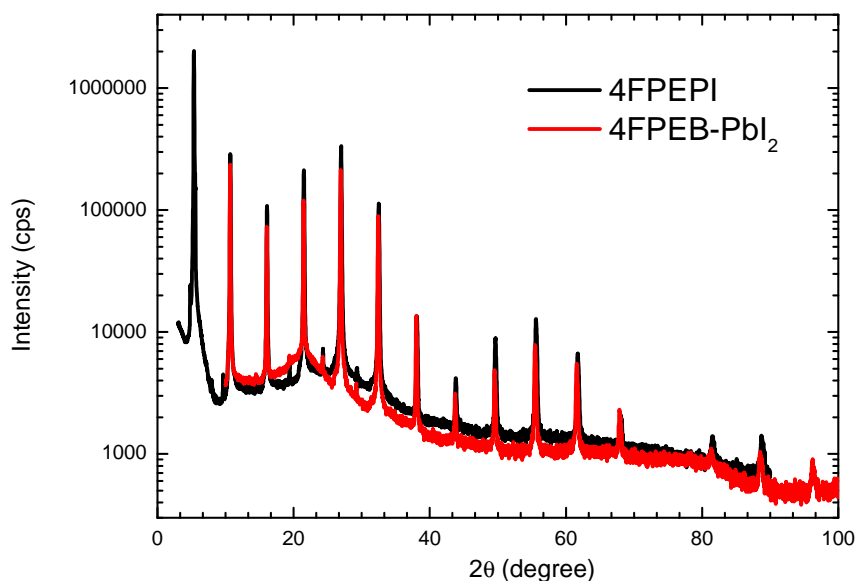
FIGURE 3.21: X-ray diffraction of a 4FPEB-PbI$_2$ (red line) and a 4FPEPI thin film (black line). The two samples, having a thickness of 85 nm and 50 nm respectively, are prepared by spin-coating.

The surface properties are observed with a microscope, it is continuous but rough, as seen in Figure 3.22.
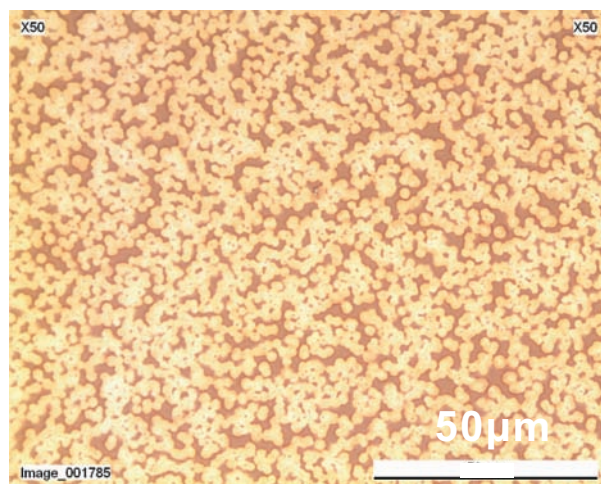
FIGURE 3.22: Microscope image of a 85 nm 4FPEB-PbI$_2$ thin film deposited by spin-coating on a quartz substrate.

Stability of the 4FPEB-PbI$_2$ thin film has been checked under the illumination of an 325 nm line HeCd laser at 7 mW, see Figure 3.23. A satisfactory result has been obtained:
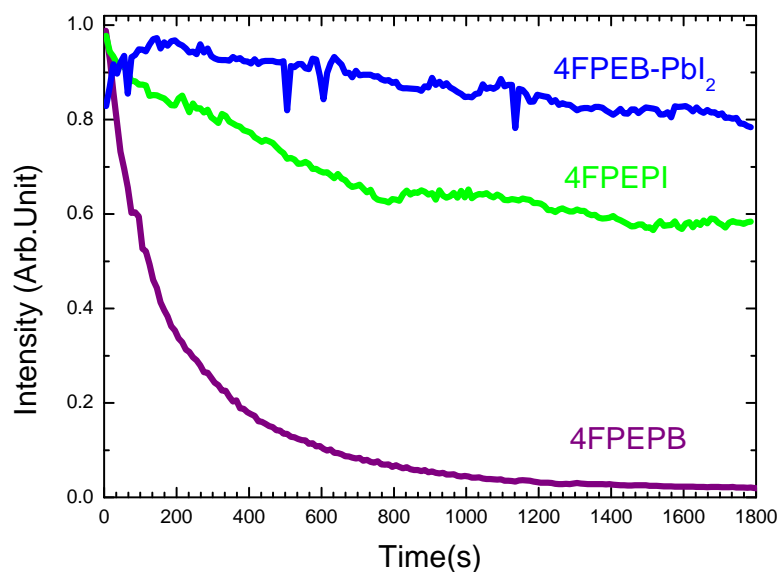
FIGURE 3.23: Comparison of photostability of 4FPEB-PbI$_2$, 4FPEPB and 4FPEPI thin films. These three samples are prepared by spin-coating from their 10 wt% in DMF solution. The exitation source is the 325 nm line of a HeCd laser, the power is 7 mW.

this 4FPEB-PbI$_2$ mixed perovskite with broad bright PL presents outstanding stability at room temperature. During an illumination of 1800 s, its PL intensity decreases of only 21% compared with its initial PL intensity while the 4FPEPI and the 4FPEPB

layers loss 41% and 100% respectively. This enhancement in stability is supposed to be impurity related, but hasn't been completely understood and is still under study.

3.2.2 Mixing in the organic part: mixed AB-$(NH_3)_2PbX_4$ perovskites

In order to optimize the structural and optical properties, we synthesize a new kind of perovskites AB-$(NH_3)_2PbX_4$ where the inorganic component is fixed and two kinds of ammoniums A and B are present in the organic layer. We hope to combine the advantages, regarding photoluminescence efficiency and surface homogeneity, of each perovskite (A-$NH_3)_2PbX_4$ and (B-$NH_3)_2PbX_4$.

TABLE 3.6: Chemical structure, complete name and abbreviation of the amines parts of PEPB, CMPB and BDMPB perovskites
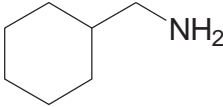
Chemical structure	Name	Abbreviation
	Cyclohexylmethanamine	CM
	2-Phenylethanamine	PE
	1,4-Benzodioxane-2-methylamine	BDM
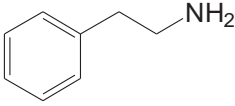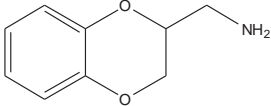
Let us focus our attention on some lead bromide perovskites: PEPB, CMPB and BDMPB (information on their chemical structure, complete name and abbreviation of amines part is shown in Table 3.6) since this inorganic group has the best PL efficiency among lead halide species. As seen previously, the PEPB thin film presents relatively good surface homogeneity and PL efficiency. CMPB is found to have strong local self-organized ability with better PL efficiency than PEPB (see Table 3.2), however, its film surface is not continuous. As shown in Figure 3.24(c), the CMPB crystals are very dispersed on the substrate and there are some parts of the substrate where there is no deposition obviously. The BDMPB thin film presents better surface homogeneity than CMPB but its PL intensity is relatively low, see Figures 3.24(b) and 3.26. The idea is to create mixed crystals by mixing CMPB and PEPB on one hand, BDMPB and PEPB on the other hand (the mixing perovskites will be abbreviated as CMPEPB and BDMPEPB hereafter), in the aim of obtaining new materials with optimized properties.

The method for synthesizing these perovskites is the same as described in Paragraph 2.2.1. The solutions of CMPB, PEPB, BDMPB used in experiment are all 10 wt%

(a) PEPB thin film　　　　　(b) BDMPB thin film　　　　　(c) CMPB thin film

(d) BDMPEPB thin film　　　　　　　(e) CMPEPB thin film
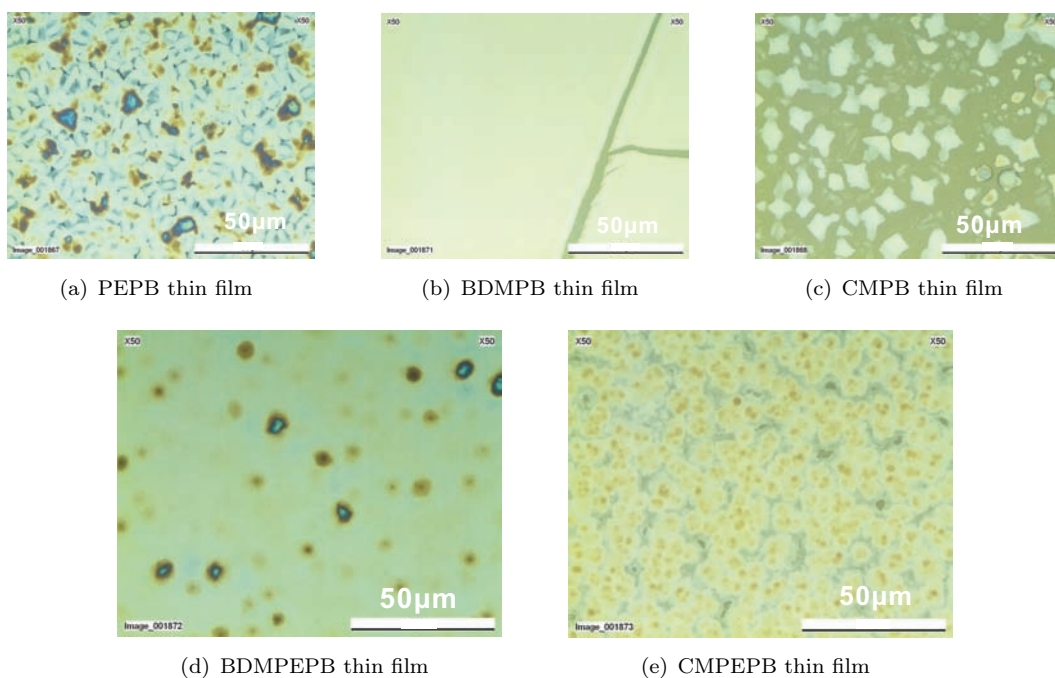
FIGURE 3.24: Images under microscope for PEPB, BDMPB and CMPB pure perovskites films and films obtained with their mixtures. Samples in (a), (b) and (c) are prepared from 1:10 solution of pure perovskite PEPB, BDMPB and CMPB respectively. (d) and (e) are mixed crystals of CMPEPB and BDMPEPB which are prepared by mixing two kinds of 1:10 solution of pure perovskites by 1:1 in volume

(a) PEPB thin film　　　　　(b) BDMPB thin film　　　　　(c) BDMPEPB thin film
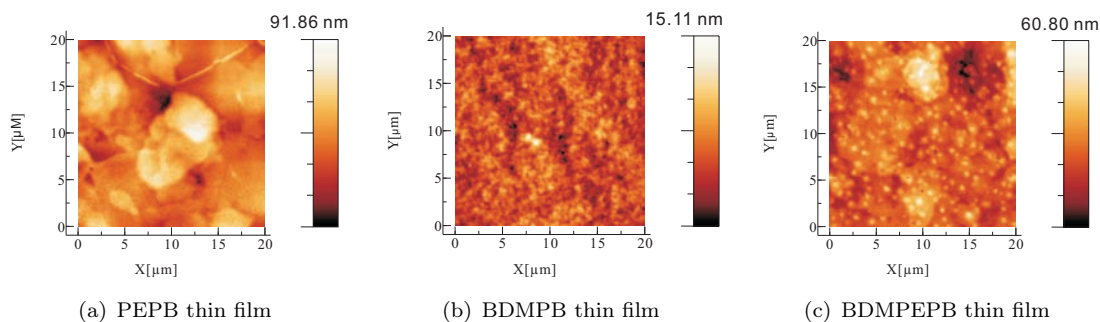
FIGURE 3.25: AFM images measured by taping mode for (a) PEPB, (b)BDMPB and (c) BDMPEPB thin films.

solution. CMPEPB solution is prepared by mixing CMPB and PEPB solutions by 1:1 in volume. BDMPEPB solution is prepared in the same way. Then, thin films are deposited by spin-coating. The thickness of these films is around 70 nm.

From Figure 3.24 (d) and (e), we see that the mixed perovskites CMPEPB and BDMPEPB have medium surface quality compared to their two pure perovskites precursors. For example the surface roughness of PEPB and BDMPB measured by AFM are $\Delta = 9.9$ nm and $\Delta = 1.3$ nm respectively while the surface roughness of their mixture BDMPEPB is $\Delta = 6.0$ nm, see Figure 3.25.
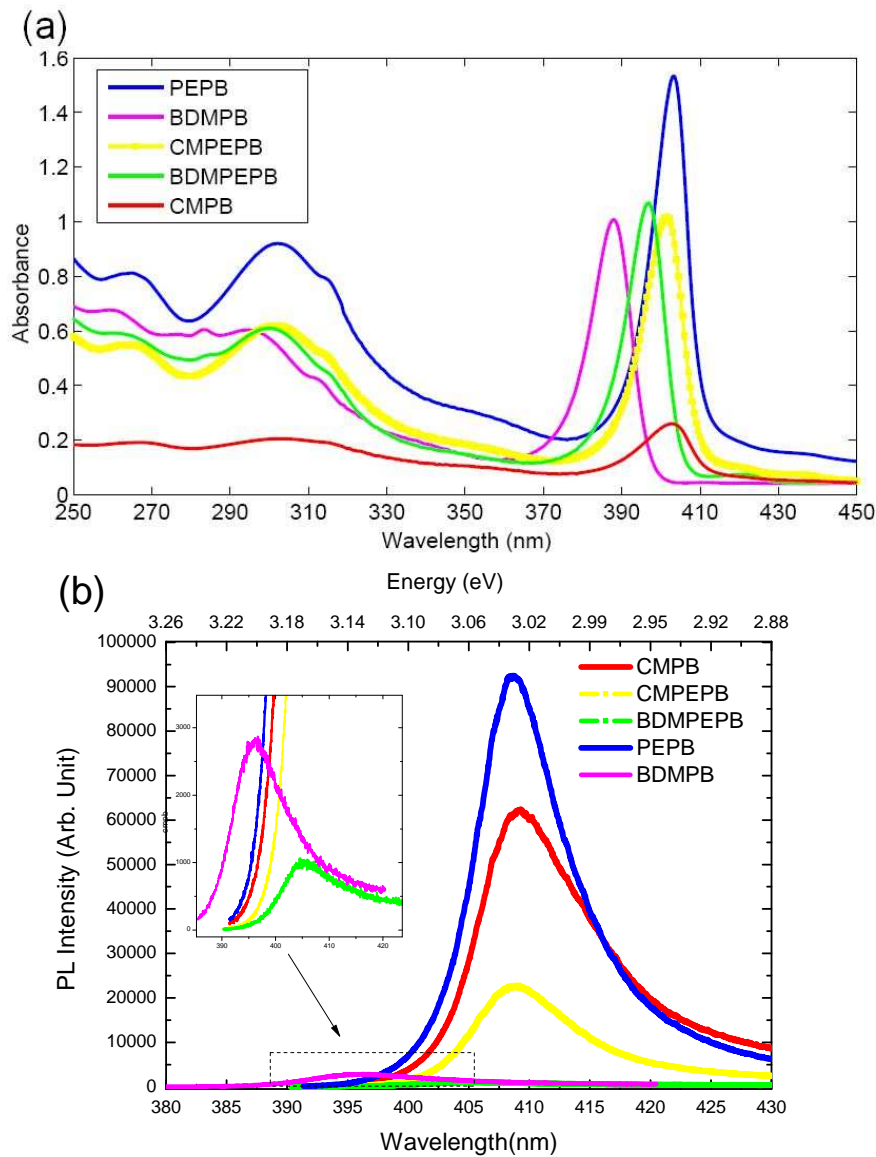
FIGURE 3.26: Optical spectra measured at room temperature: (a) OA spectra (b) PL spectra for PEPB, BDMPB, CMPB, BDMPEPB and CMPEPB thin films. The laser used as excitation is the 325 nm line of HeCd laser, the power is fixed at 5 mW.

XRD experiments are carried on for the mixed crystals: CMPEPB and BDMPEPB, see Figure 3.27. These spectra are measured by L. Largeau and O. Mauguin in LPN. The regular and numerous sharp diffraction peaks prove that these films are well oriented multilayered structures. Contrary to the XRD spectra of pure perovskites films, there are double peaks in each diffraction mode. It therefore reveals that two periods, very close from each other, exist in these mixed crystals: the periods of CMPEPB are found to be 16.7 Å and 16.9 Å, and those of BDMPEPB are 17.6 Å and 17.8 Å respectively.

Figure 3.26 presents the OA and PL spectra of pure perovskites and their mixed perovskites thin films at room temperature. This series of perovskites shows strong resonance lines in the near UV range. Both the main OA and PL peak positions of each
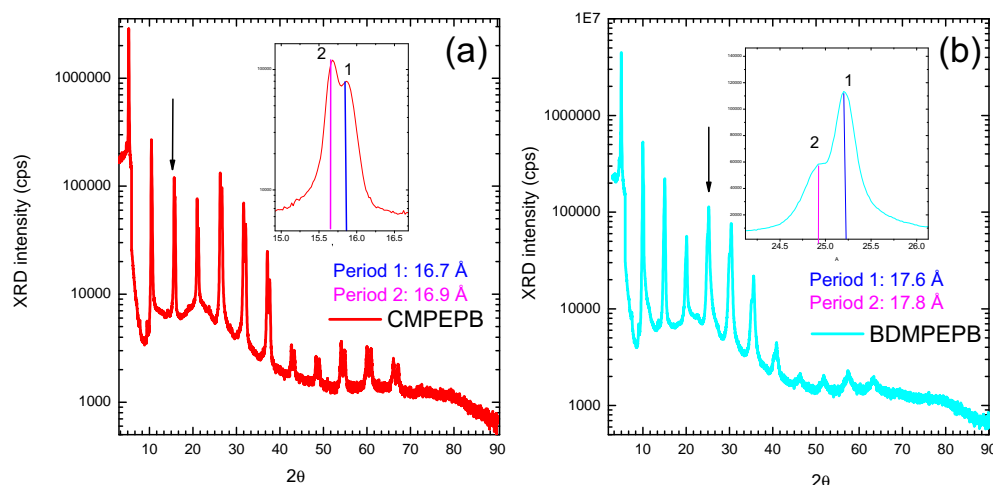
FIGURE 3.27: X-ray diffraction spectra of (a) CMPEPB and (b) BDMPEPB mixed perovskites thin films. The insert graphs are zooms of a particular single diffraction peak indicated by an arrow.

mixed crystal locate between the peak positions of the two pure perovskites precursors. Spectral informations are reported in Table 3.7. It should be noticed that the FWHM of the OA peaks of these mixed crystals are relatively small: 100.8 meV for CMPEPB and 96.7 meV for BDMPEPB at room temperature, that are similar to the FWHM of PEPB, CMPB and BDMPB. This phenomenon is quite different from the case of the mixed perovskites $(R-NH_3)_2PbY_xZ_{4-x}$. Take the $PEPC_xB_{4-x}$ for example, the FWHM of $PEPC_2B_2$ in which PEPC and PEPB are mixed by 1:1 in mol is as large as 203.8 meV, while that of PEPB and PEPC are 80.7 meV and 91.3 meV respectively. We think that the excitons are principally located in the inorganic sheets: as a consequence, it is coherent to find that the peak positions and the FWHMs are more affected in $(R-NH_3)_2PbY_xZ_{4-x}$ perovskites than in $AB-(NH_3)_2PbX_4$ perovskites.

Photostability properties are also studied and estimated by recording the integrated PL peak intensity as a function of illumination time, the excitation is a 325nm HeCd laser at 5 mW in air, during 1300 s. We see from Figure 3.28 that the stability of the mixed CMPEPB is superior to its precursor PEPB and inferior to CMPB. Similarly, BDMPEPB shows better stability than PEPB and worse than BDMPB. Therefore, we conclude that the properties of mixed perovskites are an average of the properties of the two precursors.

From the optical results, we think that the method of mixing organic parts may form a new mixed organic layer with a mean value of dielectric constant. A possible structure of CMPEPB is sketched in Figure 3.29: the organic layer is composed with two organic ammoniums (CM and PE salts) stacking one with another via interaction among molecules: (a) $\pi - \pi$, (b) Van der Waals or (c) hydrogen bond. We know that the organic layers act as barriers and they alternate with inorganic layers in 2D layered

TABLE 3.7: Information extracted from absorption and photoluminescence spectra of CMPB, PEPB, BDMPB and their mixed crystals CMPEPB and BDMPEPB at 300K (Figure 3.26) and 10 K (Figure 3.30)

Name	E_{OA} (eV)	FWHM$_{OA}$ (meV)	E_{PL} (eV)	FWHM$_{PL}$ (meV)	Stokes-shift (meV)
300 K					
CMPB	3.054	147.3	3.032	82.6	49.0
PEPB	3.069	80.5	3.039	67.1	37.7
BDMPB	3.196	107.7	3.131	103.8	64.6
CMPEPB	3.073	100.8	3.042	67.7	31.3
BDMPEPB	3.116	96.7	3.067	101.2	48.6
10 K					
CMPB	3.04	55.1			
PEPB	3.054	33.9			
BDMPB	3.186	63.7			
CMPEPB	3.039	56.5	3.028	24.0	10.7
BDMPEPB	3.100	48.7	3.076	30.9	24.4
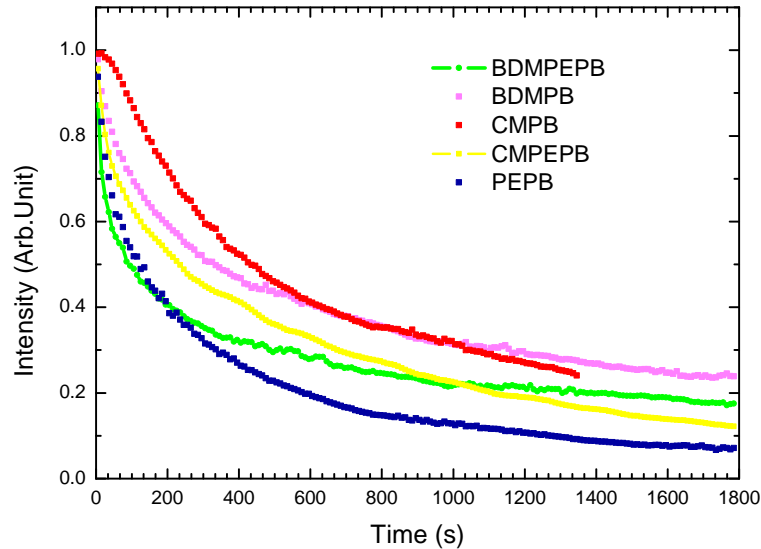
FIGURE 3.28: Evolution of PL intensity as a function of illumination time for PEPB, MFMPB, CMPB and their mixed perovskites CMPEPB and BDMPEPB thin films. The PL spectra are excited with a 325 nm line HeCd Laser at 5 mw in air.

structure. The differences in spatial configurations and physical flexibilities of the two ammoniums, as well as the subtle change between interaction forces between organic molecules, deform the shape of inorganic framework of $PbBr_6^{4-}$. Consequently, electronic structure of the mixed materials is changed because affected by the dielectric confinement effect. Macroscopically, the two kinds of organic molecules mixed together provide the
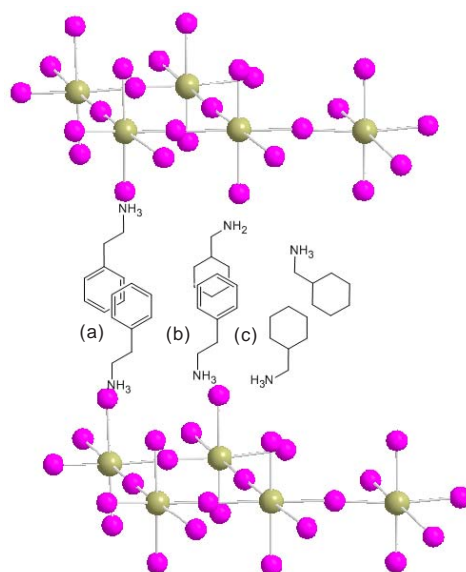
FIGURE 3.29: Sketch of a possible structure of CMPEPB. The mixed organic layer is composed with two organic ammoniums (CM and PE salts) stacking one with another via interaction among molecules: (a) $\pi - \pi$, (b) Van der Waals or (c) hydrogen bond.

opportunities to average the surface quality of their films as a result of their different size.

Low temperature optical experiments

Low temperature OA and PL measurements are carried on in He environment at 10 K (Figure 3.30, the data are collected in Table 3.7. At 10 K the Stokes-shifts of the mixed crystals are rather small: 10.7 meV for CMPEPB and 24.4 meV for BDMPEPB at 10 K, of the same order of magnitude as the ones of the pure perovskites precursors. That proves that the optical transitions are from free excitons or slightly bound excitons. The exciton binding energy can be evaluated from the OA spectra obtained at low temperature by reading the difference between the main absorption line and the continuum (presenting a step-like structure). The mixed crystals have an exciton binding energy of the order of magnitude of 300 meV, as their precursors.

Optical experiments as a function of temperature

OA and PL measurements are carried on for BDMPEPB and CMPEPB as a function of temperature, spectra are shown in Figure 3.31 and Figure 3.32 respectively. The PL and OA intensities have been normalized.

In PEPI thin films, we have found that the main PL peak is red shifted Gauthron et al. (2010). We observe a blue shift in the case of CMPEPB thin film up to 200 K, above
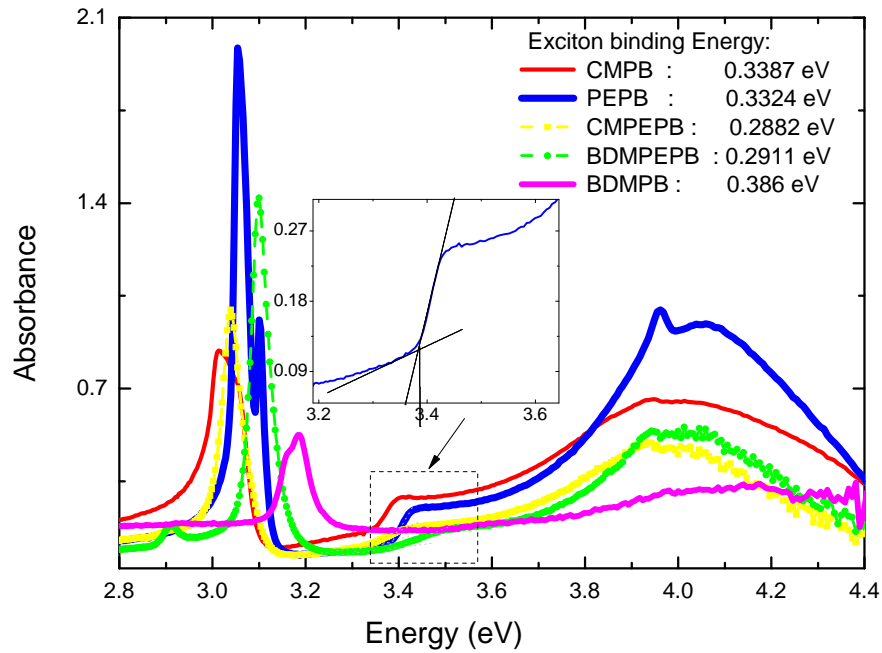
FIGURE 3.30: Absorption spectra for PEPB, CMPB, BDMPB, as well as CMPEPB and BDMPEPB at 10K in He environement. The insert graph shows the step-like structure around 3.4 eV for PEPB.

200 K it seems that the blue shift decreases. In BDMPEPB thin films, we find that the PL peak position presents a blue shift below 150 K and a red shift above 150 K. These different behaviors, depending on the nature of the organic part, prove the importance of the barrier nature for the understanding of the perovskite electronic structure. The electronic structure depends on the exact composition of the barrier, because indeed the dielectric constant difference ε_{QW} - ε_B between the barrier and the quantum well may increase or decrease with temperature depending on the nature of the components of the barrier. And, through the dielectric confinement, the exciton energy in perovskite QWs is mainly related to ε_{QW} - ε_B . Additionally, the strains in the QWs might be different depending on the nature of the barrier and might also influence the exciton energy dependance on temperature. As a result, changing the barrier composition may lead to very different, sometimes opposed temperature behaviors of the exciton transition energy. Ishihara et al. (1990).

The FWHM of the PL peaks continuously increase from 10 K to 300 K for CM-PEPB and BDMPEPB (see Figures 3.31(c) and 3.32(c)). We have found the same trend in PEPI thin films Gauthron et al. (2010). We have attributed this broadening to exciton interaction with phonons, and the interpretation of the experimental results with a phenomenological model often used in inorganic QWs allowed us to conclude
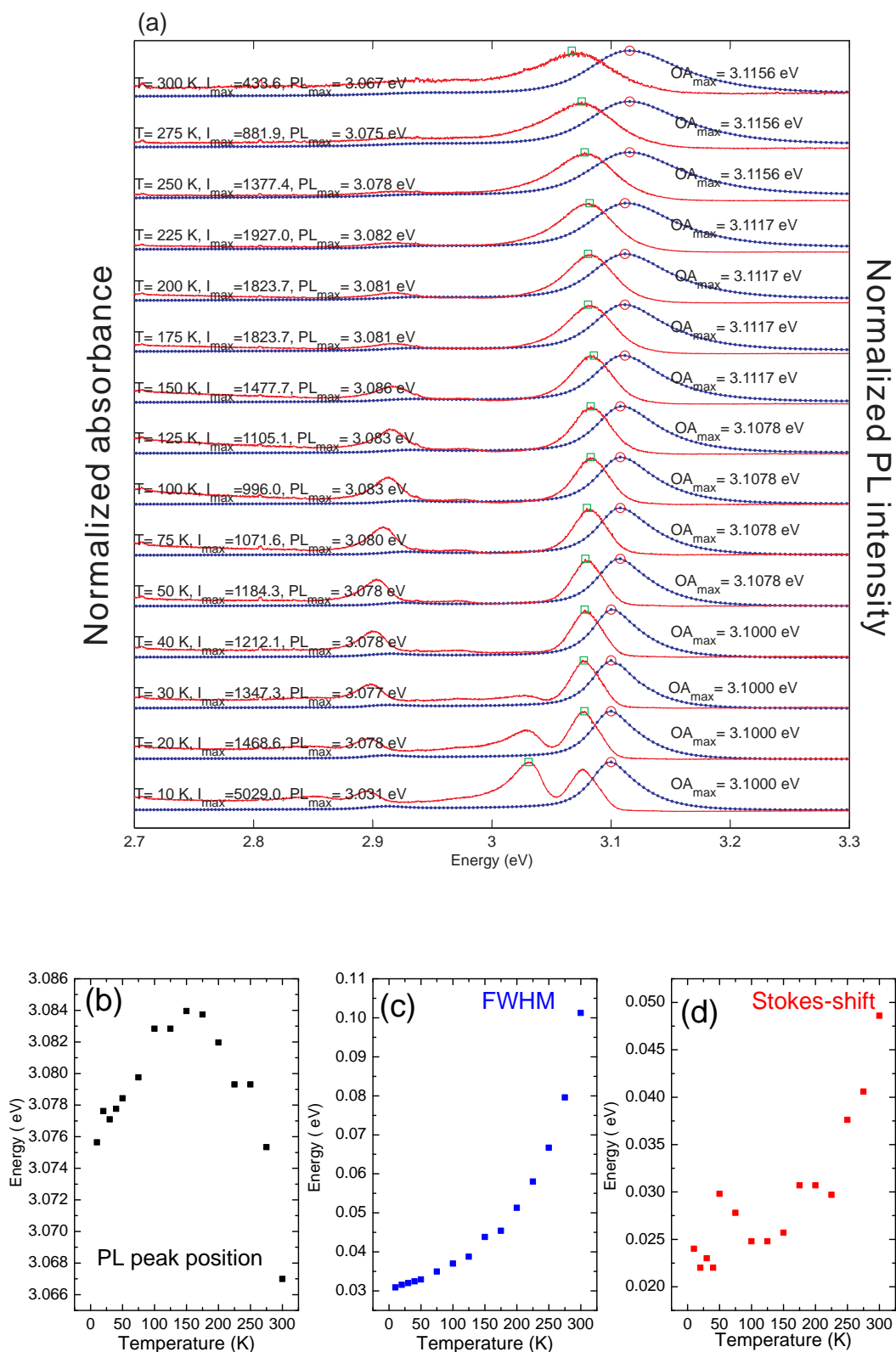
FIGURE 3.31: (a) OA (blue line) and PL (red line) spectra of BDMPEPB from 10 K to 300 K. (b) PL peak position (c) FWHM (d) Stokes-shift as a function of temperature. The excitation source for PL is the 325 nm line of HeCd laser, the power is 0.2 mW.
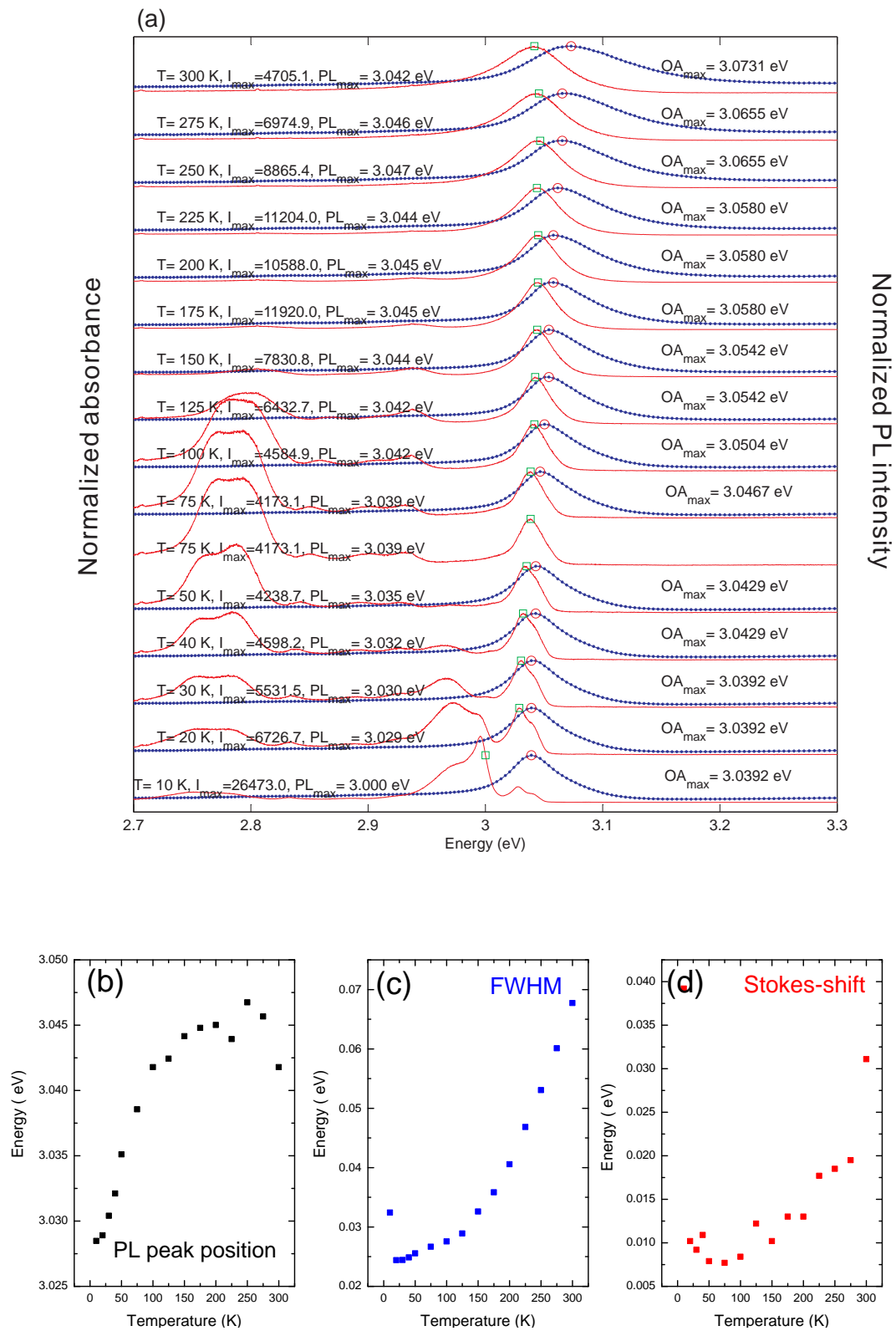
FIGURE 3.32: (a) OA (blue line) and PL (red line) spectra of CMPEPB from 10 K to 300 K. (b) PL peak position (c) FWHM (d) Stokes-shift as a function of temperature. The excitation source for PL is the 325 nm line of HeCd laser, the power is 0.2 mW.

that exciton-interaction with acoustical and optical phonons is more than one order of magnitude higher in perovskite QWs than in GaAs QWs.

The Stokes-shifts are almost constant up to 200 K and above 200 K, they increase, both in CMPEPB and BDMPEPB (see Figures 3.31(d) and 3.32(d)). In PEPI thin films, we have found that the Stokes-shift don't depend on temperature up to 300 K Gauthron et al. (2010). This temperature dependent behavior, is quite different from that observed in inorganic quantum wells where the Stokes-shift is usually due to exciton localization in potential minima induced by disorder, and decreases with temperature and eventually vanishes when the thermal energy $k_B T$ overcomes the trapping potential. Since we know that exciton-phonon interaction is stronger in perovskites than in inorganic QWs, we think that the main PL peak of perovskites has to be described in a polaron model, leading to the existence of self-trapped excitons.

In the PL spectra of BDMPEPB and CMPEPB thin films, low energy peaks exist below the main PL peak (around 3.03 eV for BDMPEPB and around 2.97 eV) and disappear above 40 K. As well, peaks located around 2.9 eV in BDMPEPB and around 2.78 eV in CMPEPB disappear at higher temperature (around 150 K). We think that these peaks are due to the He environment because such peaks are not seen when the experiment is carried on with a cold finger cryostat (in which the samples are in vacuum): He being a little atom, it is possible that the He atoms are incorporated in the perovskites structure, introducing additional structural phases.

3.3 Conclusion

In this chapter, we have presented the flexibility of perovskites regarding the optical properties and filmability. Their electronic band structure, surface quality, photostability can be easily varied by either changing inorganic part or organic part. These various possibilities enable us to tailor and design new perovskites with virtues we are interested in for advanced functional active layers. Meanwhile some trends in selection of the components of perovskites have been found.

Comparing phenyl and cyclohexane groups, we have seen that phenyl and cyclohexane groups have advantages and disadvantages regarding the formation of self-assembled 2D layered perovskites: the phenyl group is rigid but the intermolecular interactions between the R groups are strong; the cyclohexane group is more flexible but the intermolecular interactions are weak. An organic group R combining both cyclohexane and phenyl, such as (4-phenylcyclohexyl) methanaminium or 2-(4-phenylcyclohexyl) ethanaminium, may possess both the advantages of strong intermolecular interactions and good structural flexibility. Therefore, this kind of organic group can be expected to further improve the optical performance of 2D perovskites.

The mixing methods for fabricating new perovskites provide us a convenient means to optimize materials artificially by molecular engineering. It enables us to combine the advantages of each perovskite or introduce some special cations simply by mixing. A lot of new functionnalities could thus be imagined. For example, active layers which are not continuous are a problem in optoelectrical applications. If it is possible to mix the BDM, A5 and TNY etc. based perovskites which present a smooth surface with some other perovskites presenting high mobility such as $PESnX_4$, it could be a great improvement and lead to a wider prospect for applications.

Chapter 4

Photostability of perovskites

The realization of efficient OILEDs and new optoelectronic devices based on 2D-layered organic-inorganic perovskites needs to optimize several properties of the hybrid molecules such as the luminescence efficiency, the surface roughness (these two properties have been studied in Chapter 3), and also the photostability. Improving the photostability is very important in the framework of long life-time optoelectronic devices but also in the framework of fundamental studies, where a great reproducibility of the optical results is necessary and where the study of the non-linear effects requires high incident laser power. Gauthron et al. (2010); Patterson (2000)

The degradation of perovskites under laser illumination is commonly observed and this degradation is complicated to explain because it can be caused by many reasons and influenced by multiple mechanisms at the same time. We know that in the 2D layered perovskites, the corner shared lead halide octahedra which compose inorganic sheets extend in two dimensional planes. Between the lead halide sheets, ammoniums stack together to form organic layers with hydrogens bonding to the halide atoms lying in the neighbor inorganic layers. The benzene based organic ammoniums interact each other by π-π interaction, while other ammoniums interact via Van der Waals force. Therefore, either the structure of organic salts or the nature of the atom species in organic part will delicately influence photostability of perovskite molecules.

In order to clarify the origin of degradation and improve the photostability of perovskites, we summarize some former studies and carry on new experiments with some newly synthesized $(R-NH_3)_2PbX_4$ perovskites. By analyzing the photobleaching evidences obtained in experiment, some reasons that may influence their photostability will be discussed in this chapter.

4.1   Photostability related factors

In this section, several factors, which influence the photobleaching, are studied and mechanisms explaining the photobleaching are sought.

4.1.1   Influence of the presence of oxygen

The oxidation is first supposed to be an important reason to the degradation of perovskites, and in Kitazawa's work, they indeed reported that the oxidation induced halogen elimination is one possible reason for degradation. Kitawawa et al. (1999). In order to prevent the attack by oxygen in air, we put a transparent polymer PMMA layer on the top of perovskites layer or put the perovskites samples in He environement. By doing this, the stability is slightly improved, but in fact the degradation of perovskites is still very obvious, which indicates that there are surely more predominant reasons influencing the stability.

4.1.2   Thermal induced decomposition

As barriers in 2D layered perovskites quantum wells, the organic sheets are regarded as optically inert. However, any decomposition of the organic part certainly would lead to the collapse of the whole perovskite framework and influence the optical properties of the perovskite. When the perovskites are exposed under illumination of UV light, the high energy photons can be absorbed by the organic part. As a result, the materials will be heated and can be seriously deteriorated.

The organic ammonium salts are relatively stable in ambient environment, however they undergo decomposition if they are overheated. To check it, we test the weight change of several typical $T-(CH_2)_n-NH_2 \cdot HCl$ salts (the chemical structures of their organic amine part are reported in Figure 4.1) by using a PerkinElmer Thermogravimetric analyzer (Pyris 6 TGA) in PPSM ENS Cachan. Approximately 3 mg of each organic ammonium salt is put into an aluminium oxide container for each examination. The aluminium oxide container is rinsed with distilled water and acetone, and is burned in a flame from 35% propane and 65% butane gas (Rothenberger) for 15 seconds prior to each loading of organic salt. The thermal ramp is set first stabilizing 5 min at 30 °C, then increasing from 30 °C to 400 °C at a speed of 10 °C /min, and finally holding at 400 °C for 2 min. 20 ml/min nitrogen gas flow is applied to protect the samples from oxygen. Thermogravimetric analysis, reported in Figure 4.2(a), shows that, as the heating temperature rises, TPM and MFM salts, which have similar two double bonds and a O or S substitution on the 5 atoms cycle, are the less stable and decompose at 150 °C. They are followed by the CHE salt. All the other salts containing benzene cycles begin to decompose at around 200 °C. These trends agree well with the photo-stabilities of
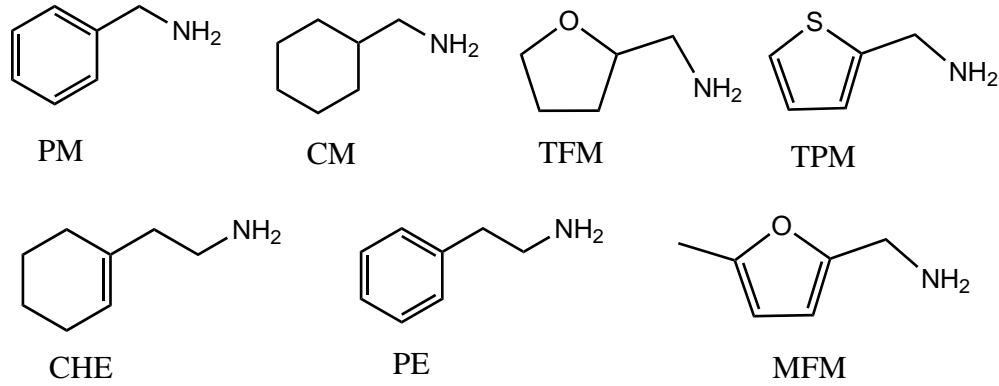
FIGURE 4.1: Chemical structures of some amines used as organic part for $PbCl_4^{2-}$ based perovskites in thermogravimetric analyzer.

their perovskites in Figure 4.2(b): CMPC > PEPC > CHEPC > TPMPC > MFMPC. Zhang et al. (2011)
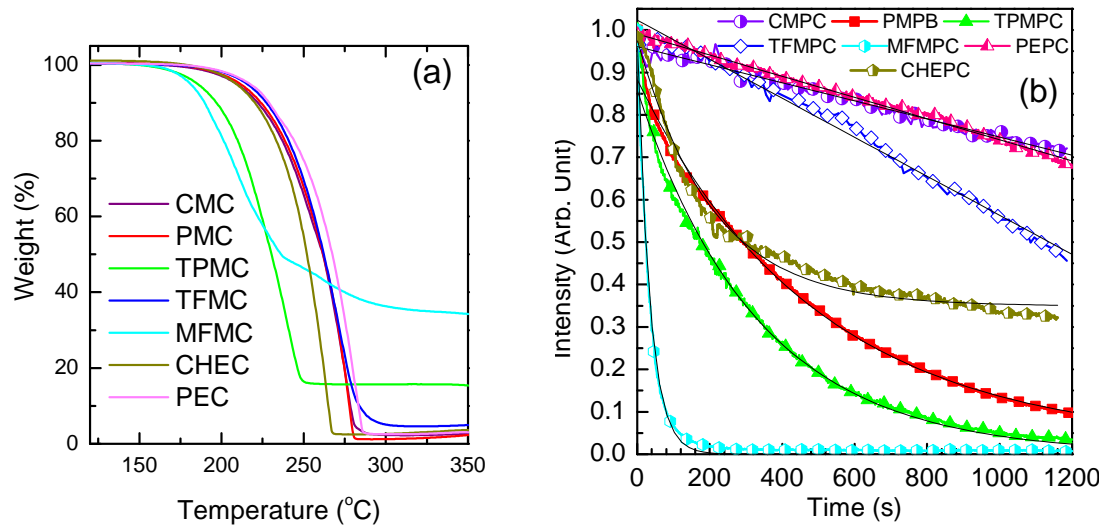
FIGURE 4.2: (a) Thermogravimetric measurements of organic salts, and (b) evolution of PL intensity versus time for the UV $(T-(CH_2)_nNH_3)_2PbCl_4$ perovskites. The measurements are performed in air at room temperature. PL is excited at 325 nm with a HeCd laser with incident power of 18 mW.

Another evidence related to thermal induced decomposition is found experimentally: the lead bromide perovskites are generally less stable than lead iodide perovskites: see for instance the most popular phenethylamimne ("PE") based perovskites in Figure 4.3. It is known that in an excited system, energy mainly relaxes along two ways: one is radiative, it is photoluminescence; the other one is nonradiative relaxation such as emission of phonons. The "PB" group generally exhibits stronger PL efficiency than the "PI" group. Since the refractive index of perovskites (e.g $n_{PEPI} \approx 1.8$) is larger than that of air ($n_{air} = 1$), there is a large amount of photons which can not be emitted out of perovskites media as a result of total reflection. Therefore the more photons are emitted by photoluminescence, the larger amount of photons undergo internal reflections inside

perovskites layer. The internal reflection of photons is thought to cause thermal effects which may accelerate the degradation of the perovskites.
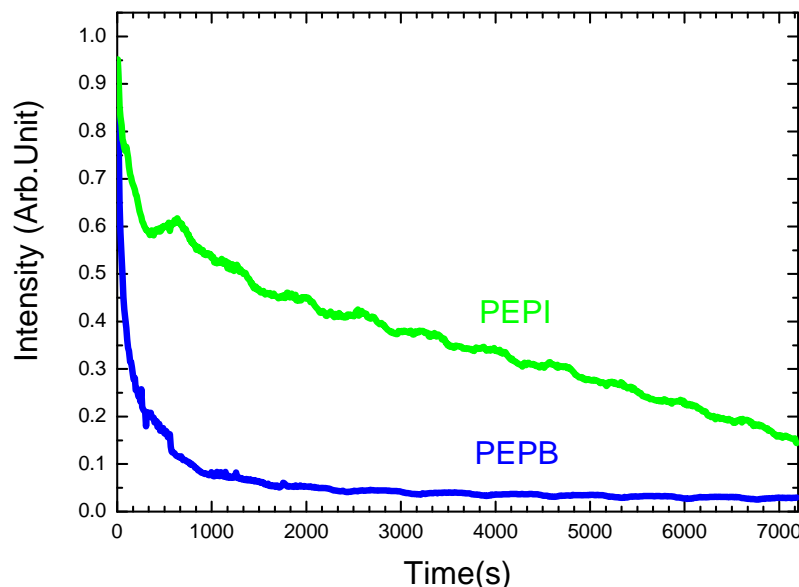
FIGURE 4.3: PEPI, PEPB thin films, thickness of several 10 nm, exposed under the 325 nm line of a HeCd laser at 10 mW. The measurement is carried on at 300 K in He environment.

4.1.3   Degradation through HX photoelimination

The ammoniums ions are located close to the lead halide plans. Although no literature evidence did already consider this, is quite possible that photoexcitation enhances the basicity of the octaedra top halide ions, which can in consequence induce deprotonation of the ammonium, leaving amines now very vulnerable to photooxidation. The photo-assisted elimination from the perovskites of the hydrogen bonds H-X (specially H-I) which connect organic sheets and inorganic sheets being suspected to be one of the reasons for perovskites degradation, we prepare "heavy PEPI" where all hydrogen atoms on the terminal -NH_3^+ part of the ammonium group are changed for deuterium -ND_3^+. For the preparation, we simply dissolve the PEI ammonium salt in heavy water D_2O. This D_2O reagent (Deuterium oxide) is bought from Sigma-Aldrich company, with an isotopic purity 99.98 atom % $\pm$ 0.01 atom %. The PEI in D_2O solution is then kept in dry box in the presence of an abundant quantity of phosphorus anhydride. A week after, all the water has been sucked out and the dry crystals of heavy PEI have formed at the bottom of the recipient. The infrared spectrum of heavy salt PEI shows two evident double peaks around 2200 cm^{-1} and 2300 cm^{-1} which proves that the -NH_3^+ of normal PEI has been successfully changed to -ND_3^+, see Figure. 4.4 Then the heavy PEPI perovskite is prepared as usual. We mix the heavy salt with PbI_2 in stoichiometric
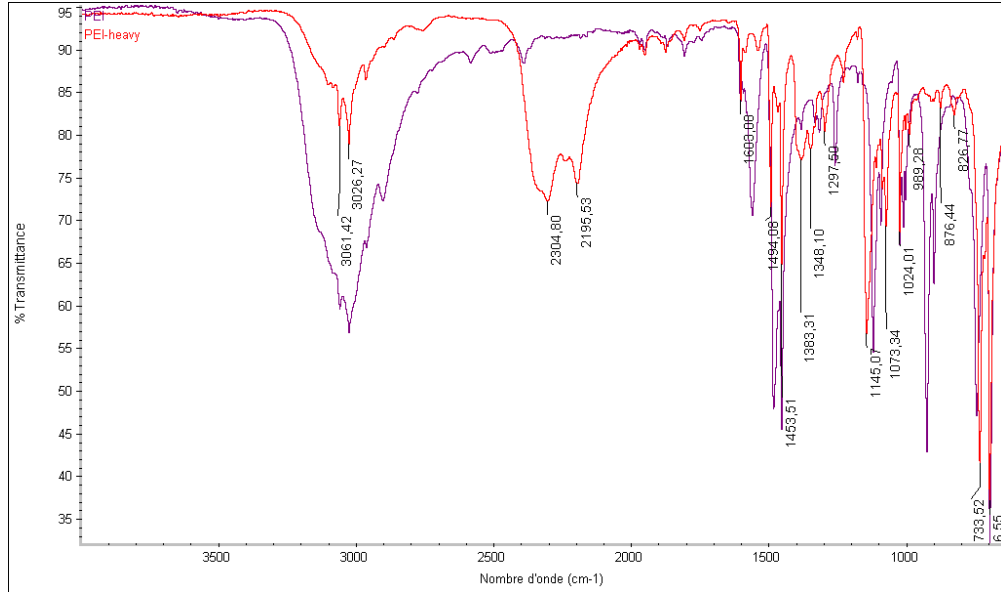
FIGURE 4.4: Infrared spectrum of PEI (magenta line) and heavy PEI (red line) ammonium salts.

amounts and then the solid mixture is dissolved in anhydrous DMF by weight ratio 1:10. The heavy PEPI solution is thus ready for deposition. Two thin films: one deposited from heavy PEPI solution and the other deposited from normal PEPI solution are prepared and photobleaching measurements are performed. The HeCd laser power used as the excitation source is 7 mW and the experiment is carried on in air environment. Although it is believed that the bond angles and bond strength of $-NH_3^+$ and $-ND_3^+$ are greatly different, the photostabilities of the two samples are similar, as seen in Figure 4.5. Therefore, from this result, we conclude that the breakage of hydrogen bond H-I, thus the elimination of HI, is not a reason for perovskite degradation.

4.1.4 Oxidation and elimination of halogen species in inorganic parts

We concentrate our interest on the lead halide based perovskites because the lead atom and its compounds are relatively stable in air. The PbX_6^{4-} octahedra form well structured inorganic layers which lead to bright visible luminescence at room temperature. Actually, it has been long known that the optical absorption energies depend mainly on the electronegativity of halogenide involved. The absorption wavelength respectively belongs to the UV range for the chlorides, the blue range for the bromides and the green range for the iodides, the organic part playing only a minor role on the wavelength tuning. Identifying coarsely the absorption energies to the energies of an ionic bond Pb^{2+}-X^- in an octahedral configuration Mitzi (1999b); Zhang et al. (2010), it seems very likely that the excited state corresponds to an electron transfer between the lead and one halogenide and therefore takes the transient $Pb^{\bullet+}$-$X^\bullet$ configuration.
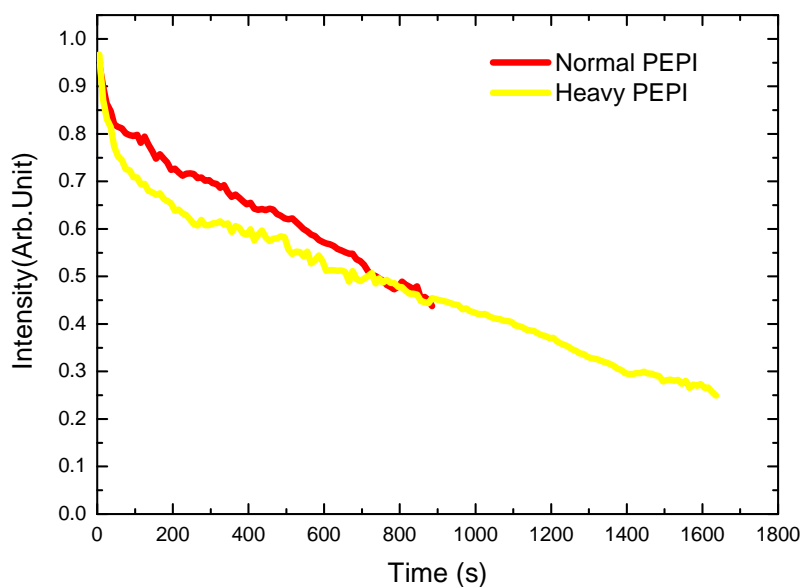
FIGURE 4.5: Evolution of PL intensity as a function of illumination time for normal
PEPI (red line) and heavy PEPI (yellow line). The laser power is 7 mW at 325 nm.

Consequently the photostability of the perovskites would be linked to the becoming of
the photogenerated $X^\bullet$ radical in its local environment.

In Kitazawa's work, the authors reported that the oxidation induced halogen elim-
ination is one possible reason for degradation. Actually we have checked in a control
experiment that long term illumination of iodide based perovskites indeed induces the
elimination of iodine. As shown in the photo of Figure 4.6(B), we prepare two bottles
of solution in which an amount of iodine indicator is dissolved in solvent cyclohexane,
and thin films of CMPI are immersed in each bottle of solution. Before illumination
both solutions are limpid and colorless. Then the bottle containing CMPI on the right is
exposed to the illumination of the 325 nm line of a HeCd laser during 2 h, the incident
power being about 27 mW. The other one is kept aside as a reference. We clearly see in
Figure 4.6(B) that the solution in the right bottle becomes purple after illumination: it
indicates that some $I^\bullet$ is eliminated from CMPI and become I_2, which is revealed by the
indicator.

However, the iodine content is quite dependent on the organic part. We carry on
the same experiment with a PEPI thin film as seen in Figure 4.6(A): we see in the right
hand bottle under illumination that not so much I_2 appears in solution. It seems that in
this case the aromatic groups are much more likely to undergo a radicalar substitution
on the aromatic ring, while unreactive spacers (e.g. aliphatic) on the other hand would
in fine generate molecular iodine from a radical coupling in the solid. We therefore are

inclined to think that the photodegradation of perovskites possessing an aromatic ring is due to the attack of the ring by an electrophilic radical.
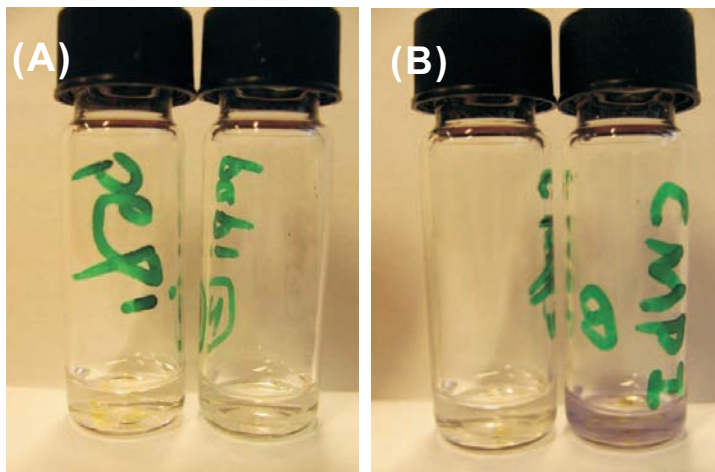
FIGURE 4.6: Results of the photodegradation of two perovskites (A) PEPI (containing a phenyl ring) and (B) CMPI (alkyl based), both immersed in cyclohexane. On the left stand the vials before irradiation, and on the right after irradiation. The colour comes from a starch-based iodine revelating substance, and shows the relative release of traces of molecular iodine. The alkylammonium based perovskite CMPI photodegradation releases a quite discernible and rather larger amount of iodine than the phenylammonium based perovskite PEPI.

4.1.5 Photostability dependence upon the structure of the organic part of chloride-based perovskites

Considering the previous results on the iodine detection, it seems likely that radicals are photogenerated in the degradation process. Therefore we examine the behavior of a large range of chloride based perovskites. We should observe first a faster degradation than in bromide and iodide based perovskites since the chloride radical has the highest reactivity, and second, a high dependence on the ammonium structure, .

The following Figure 4.7 shows the chemical structure of some $PbCl_4^{2-}$ based perovskites that we have used for photobleaching measurements. (For detailed information see Table 3.1) Methods of synthesis have been described in Chapter 2 and their optical properties have been reported in Chapter 3.

Perovskites thin films containing these amines are prepared by spin-coating from 1.5 wt% solution. The samples are exposed under the illumination of a 325 nm HeCd laser at 7 mW for 1800 s. From Figure 4.8 ,we can first clearly see that the photostability of chloride based PEPC is much lower than the one of the corresponding PEPI and PEPB.

The photostability range is also quite informative, see Figure 4.9 . Ranging from a strong to weak resistance in this series, we find: CMPC> PEPC> TPMAPC> PMPC>
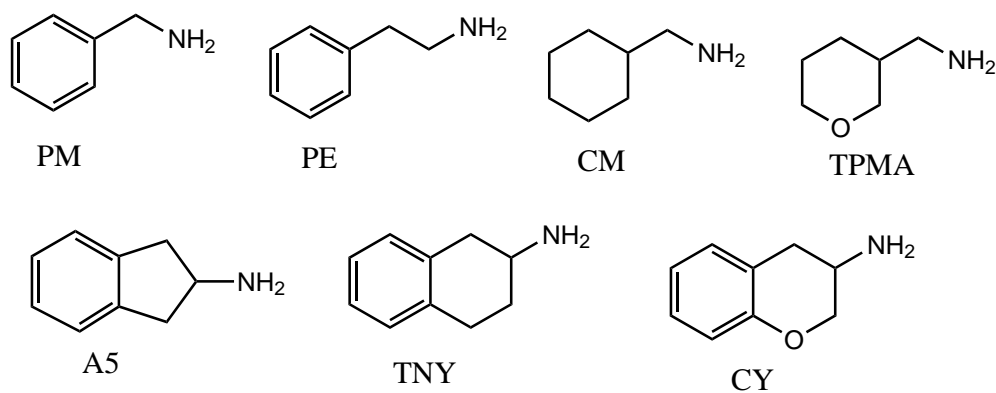
FIGURE 4.7: Chemical structures of some amines used as organic part for $PbCl_4^{2-}$ based perovskites in photostability study.
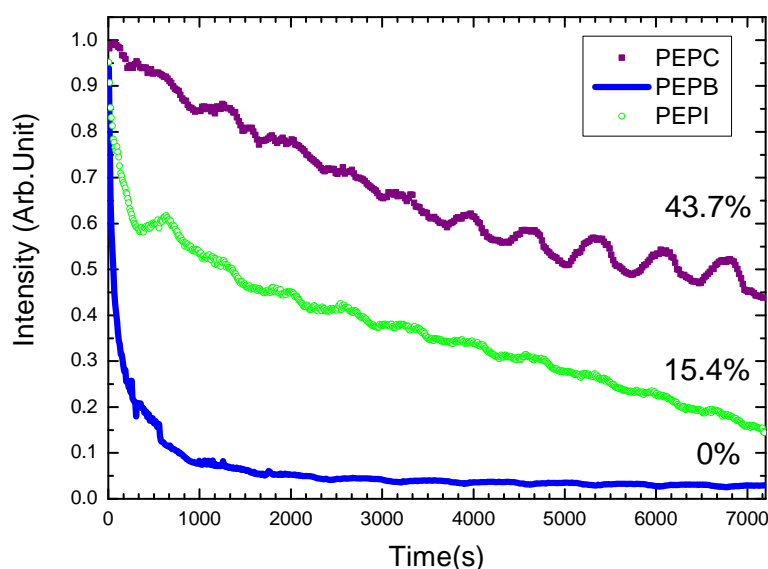
FIGURE 4.8: PL intensity as a function of illumination time for PEPI, PEPB and PEPC thin films in He environment. Laser power is 7 mW (325 nm line).

A5PC /TNYPC > CYPC. It is clear that the most resistant perovskites come from the ammoniums with a saturated backbone, while the aromatic ones degrade faster, as it could be expected from the reaction with an electrophilic radical. In addition, among the aromatic perovskites, we see that the most resistant are the ones where the benzene ring is the less activated (PEPC and PMPC) while the ammoniums with an electron-rich dialkylbenzene, or even richer chroman-type ring, degrade very fast. This is in perfect accordance with a degradation through an electrophilic attack on the aromatic part if the ammonium, likely due to an electrophilic photogenerated $Cl^{\bullet}$ species.

Considering all these trends, we think that if we could decrease the electron density on the organic part, the more stable the perovskites will be. One possible method to do
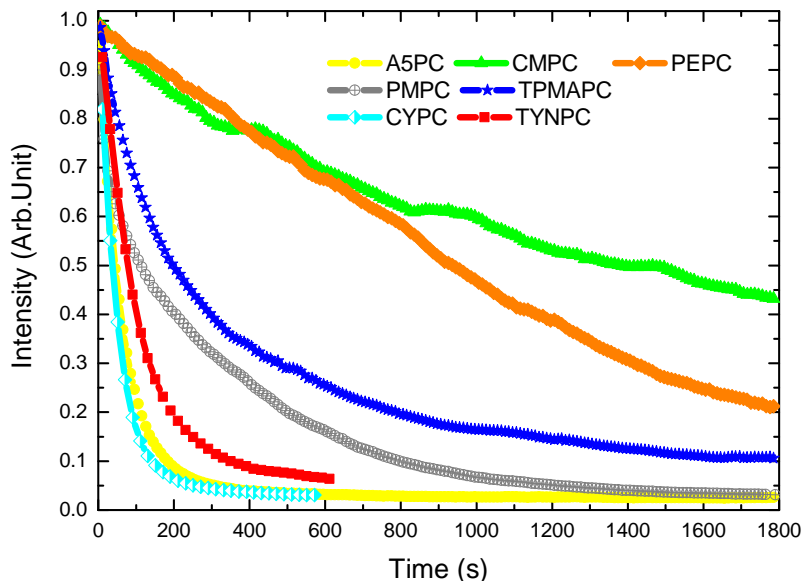
FIGURE 4.9: Photobleaching curves for PEPC, PMPC, CMPC, A5PC, TPMAPC, TNYPC and CYPC in air. The laser power is 7 mW at 325 nm.

this is to substitute the H atoms by a F atom or a NO_3^- group whose electronegativity is high, thus decreasing the electron density on benzene ring. As F atom is small in size, the steric hindrance will not be changed and the photoluminescent properties should remain. We will present fluoro-substituted perovskites in Paragraph 4.2.

4.1.6 Influence of temperature

Another experimental constatation is that the photostability of a given perovskite, especially in the case of bromide based ones, is temperature dependent. Figure 4.10 (a) shows the evolution of PL intensity as a function of illumination time for a PEPB thin film at 10 K, 80 K and 300 K under 10 mW illumination of a HeCd laser in He environment. We see that PEPB film is the most stable at 10 K, the least stable at 300 K. Although common sense makes believe that chemical reactivity should decrease at lower temperatures, it is not always the case. For example, as can be seen on Figure 4.10 (b) and (c), CMPB has surprisingly the best stability at 300 K, MFMPB is the most stable at 80 K. The origin of these discrepancies is not clear, but we can see that, again in the case of an attack by an electrophilic radical, in the framework of a purely aliphatic ammonium, where the reactivity is low and has also slow kinetics, the bromation of the aliphatic ammonium can be in competition with dimerization trapping of the radicals. On the other hand, in the case of PEPB which is based on an aromatic ammonium salt, the main degradation path is radicalar attack on the alkylbenzene ring. In this case,

radical coupling is always much slower and is not observed, and degradation normally goes faster with the increasing temperature.
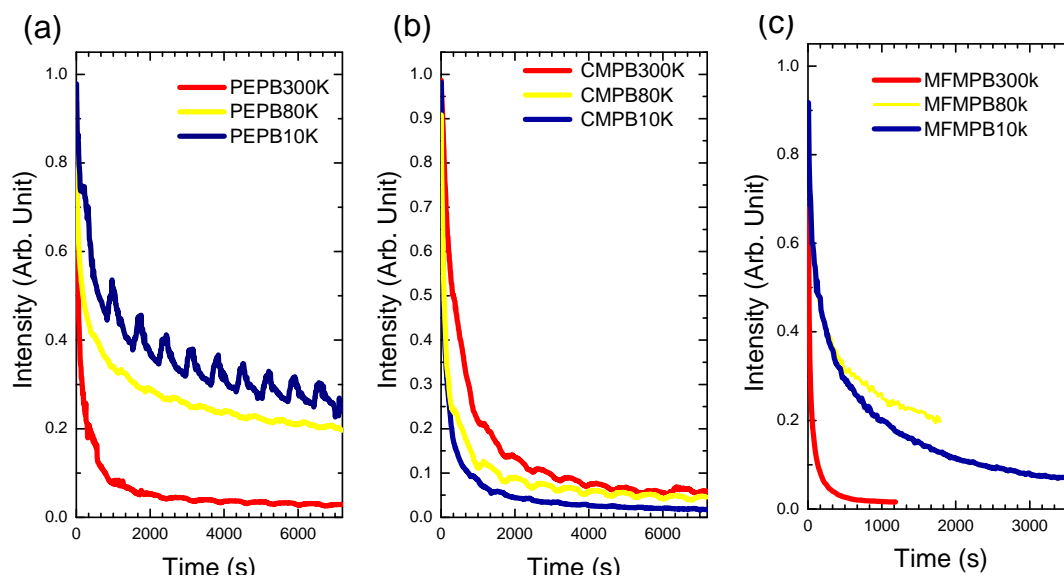
FIGURE 4.10: Evaluation of PL intensity as a function of time for thin films (a) PEPB (b) CMPB (c) MFMPB. The laser power is 10 mW at 325 nm, all samples are kept in He environment.

4.1.7   Influence of the spatial arrangement

2D layered perovskites are layered structures containing an organic sheet of about 1 nm and an inorganic sheet of about 0.6 nm. They spread out infinitely in 2D plane, named the a-b plane. The layers stack together layer by layer along the c axis direction. However, this stacked thin layers structure of the perovskites films bring some technical difficulties for XRD measurement and thus structure study of the film samples: we know well the information between layers along c axis such as space constant d_c, but it is difficult to acquire information of d_a and d_b along the a-b plane. There have been several XRD published experimental results Gauthron et al. (2010); Kikuchi et al. (2004); Liang et al. (1998); Kitazawa (1997a); Ishihara et al. (1990); Pradeesh et al. (2009a) which assess that the d_c value is quite similar (around 1.6 nm) for 2D perovskites with different organic moieties. However, the d_a and d_b values, which might vary according to the deposition parameters, especially the concentration of the casting solution, can probably be related to an effect on the stability of perovskites crystalline stacking. We observed that some perovskites films prepared from solutions of different concentrations exhibit different photostabilities. For example the PEPC films deposited from 1% solution and 10% solution have very different degradation kinetics under UV illumination, as we can see on Figure 4.11(a) . The XRD spectra of the two PEPC thin films show that both films are well oriented crystals with a single phase present. However, comparing the position of the diffraction peaks, we see clear displacement between the two curves in 4.11(b) (insert), as already noticed by Kitazawa. Kitazawa (1997b)
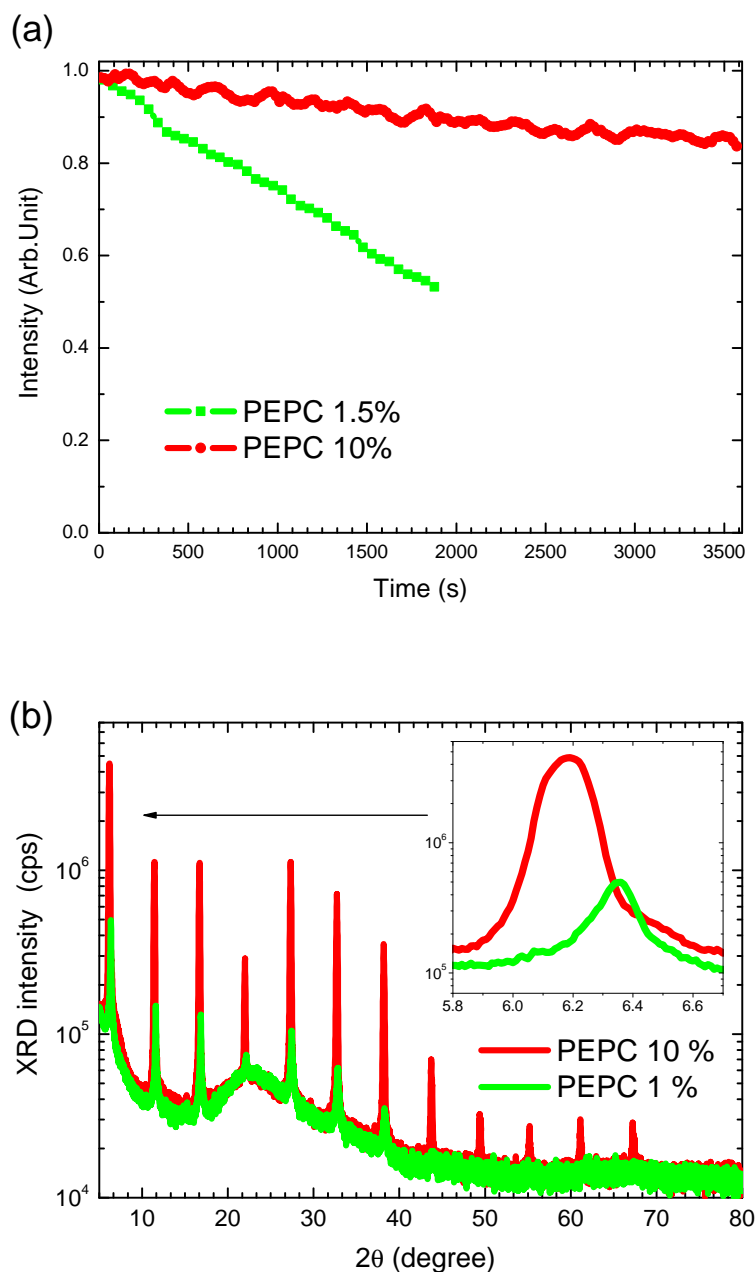
FIGURE 4.11: (a) Evaluation of PL intensity as a function of illumination time for two PEPC thin films prepared from 1% and 10% in DMF solution. The laser power is 7 mw at 325 nm. (b) XRD spectra of PEPC thin films prepared from 1% (green line) and 10% (red line) in DMF solution.

The shape and the size of organic molecules also influence the super-lattice arrangement. We synthesize some fluoro-PEPI perovskites whose organic amine has a fluorine atom substituted on different positions of benzene ring called ortho-, meta-, para- fluorophenethylamine tetraiodoplumbate: these molecules will be presented in details the following Paragraph 4.2. They exhibit bright green photoluminescence around 520 nm at room temperature. Although their chemical structures are similar, the stabilities of these

fluorinated amines based perovskites differ under intense irradiation of laser, as shown in Figure 4.12. First, we notice that 2FPEPI and 3FPEPI are the less stable materials
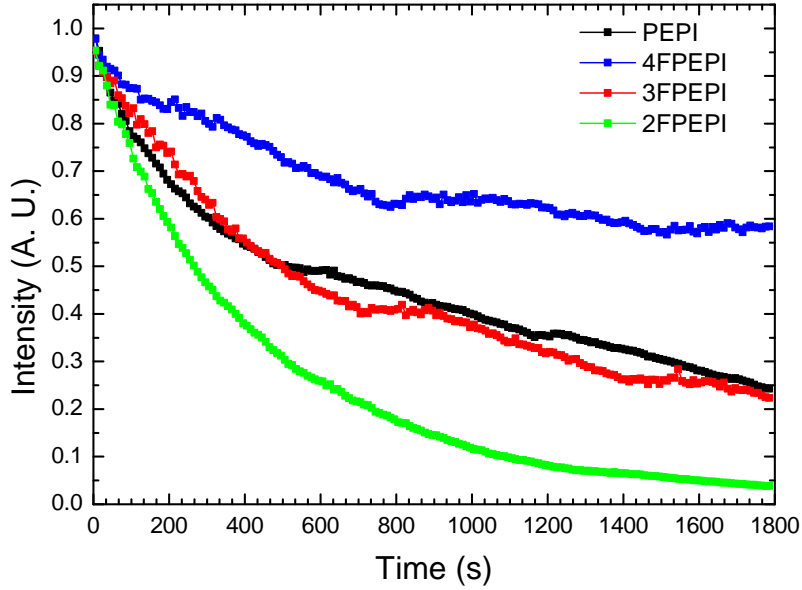
FIGURE 4.12:   Photobleaching of iodide based perovskites layers deposited from 10wt% solutions. The measurement is carried on in air at room temperature, the laser power is 7 mW at 325 nm.

in this group. Secondly, we find the largest Stokes-shift for 2FPEPI and 3FPEPI (see table 4.1). And thirdly, we notice that the PL peak position shifts from lower to higher energy before and after photobleaching, see Figure 4.13 and Table 4.1, and the largest shifts are found for 2FPEPI and 3FPEPI.

TABLE 4.1: PL peak shift before and after long time illumination of UV laser and Stokes-shift comparison

Name	Shifts of PL peak center	(Difference)	Stockes-shift
PEPI	523.83 nm → 523.21 nm	(0.62 nm)	4.96 nm
2FPEPI	515.34 nm → 513.32 nm	(2.02 nm)	6.30 nm
3FPEPI	517.94 nm → 516.90 nm	(1.04 nm)	5.10 nm
4FPEPI	524.96 nm → 524.13 nm	(0.83 nm)	4.05 nm

Our interpretation is that this phenomenon is due to defaults in superlattices. In fact, we have observed in Chapter 3, at low temperature, that the perovskite films show generally two PL peaks (see Figures 3.31 and 3.32), the lower energy PL peak has been supposed to come from defects in crystal lattice. Experimentally, we found that the two PL peaks present different photobleaching properties: the PL peak at lower energy is always the less stable one. By linking these two experimental findings, we attribute the lowest stability of the 2FPEPI and 3FPEPI PL to presence of defaults in the perovskite
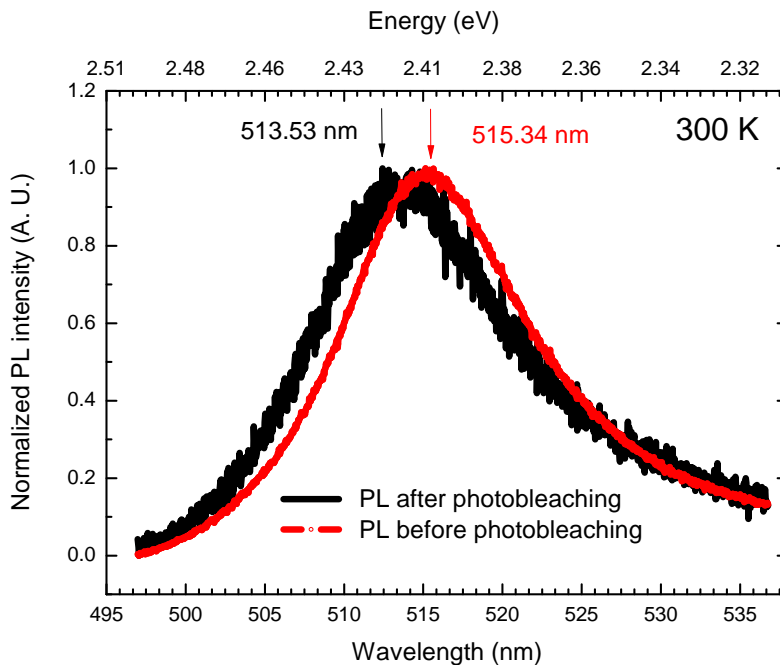
FIGURE 4.13: PL spectra of 2FPEPI before (in red) and after (in black) photobleaching. The measurement is carried on in air at room temperature, the laser power is 7 mW at 325 nm. PL intensities are normalized to 1.

structure.Concerning the fluoro-PEPIs, the defects could be caused by the dissymmetry of the amine configuration. See Figure 4.14, 4FPEPI and PEPI have a more symmetrical structure thus we think they cause less defaults in crystals arrangement. We think that more defaults exist in dissymmetric structures because it has been reported in article Mitzi et al. (2001) that $(4\text{-FPEA})_2\text{SnI}_4$ is a fully ordered structure while $(2\text{-FPEA})_2\text{SnI}_4$ and $(3\text{-FPEA})_2\text{SnI}_4$[1] are poorly ordered due to the mismatch between sheets, as schematized in Figure 4.15.
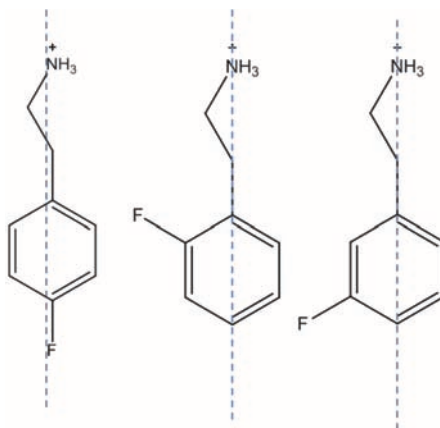
FIGURE 4.14: Comparison of structure symmetry for 2FPEI 3FPEI and 4FPEI ammonium.

---

[1]The organic part "2-FPEA", "3-FPEA" and "4-FPEA" are the same as 2FPE, 3FPE and 4FPE in our case.
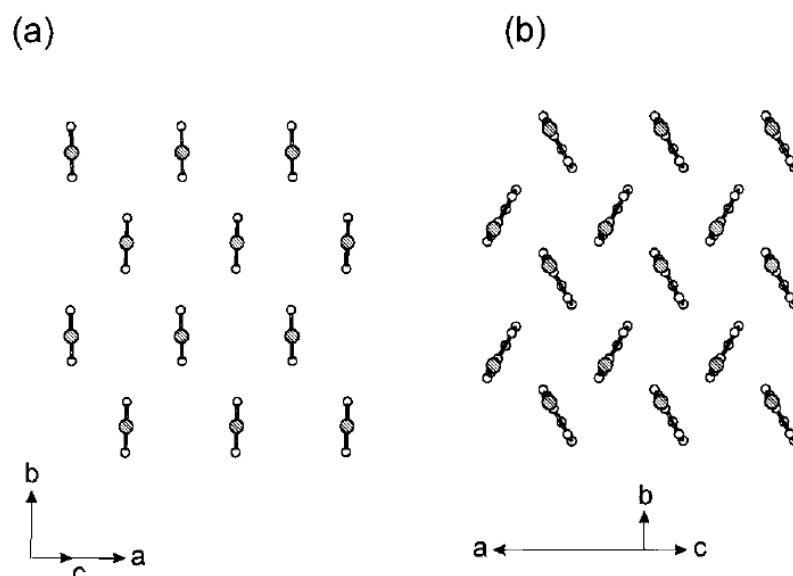
FIGURE 4.15: View parallel to the phenyl ring plane in a single layer of fluorophenethylammonium cations in (a) $(4\text{-FPEA})_2SnI_4$ and (b) $(3\text{-FPEA})_2SnI_4$. For clarity, the ethylammonium tethering group for each cation and the tin(II) iodide component of the structure has been removed. Mitzi et al. (2001)

4.2   Fluorinated organic-inorganic hybrid $(\text{R-NH}_3)_2\text{PbX}_4$ semiconductors

In recent years, phenylalkylammonium based perovskites have been extensively studied by us Zhang et al. (2010); Gauthron et al. (2010); Zhang et al. (2011); Parashkov et al. and others Ishihara; Ishihara et al. (1990); Mitzi (1999a); Kitazawa (1997a); Dammak et al. (2009) in the literature. In this section, we prepare new compounds from this family of phenylethylammonium based perovskites, and try to modify the phenyl group in order to improve the photostability, by introducing fluorine atoms on the ring. This is expected to considerably reduce the vulnerability to the attack by electrophilic species like $X^\bullet$ as discussed in section 4.1, while keeping a quasi- identical steric hindrance: the outer radius of a fluorine atom, equal to 1.47 Å, is only slightly larger than an hydrogen one, equal to 1.20 Å Bégué and Bonnet-Delpon (2005). For each new material, we analyze the important properties: luminescence efficiency and filmability, checking out the influence of the introduction of fluorine atoms into the perovskite structure and processing.

4.2.1   Preparation and structure characterization

Actually, the most extensively studied perovskite systems are based on the phenylethyl ammonium salts Ishihara; Ishihara et al. (1990); Bréhier et al. (2006); Lanty et al. (2010, 2008b); Wei et al. (2012). Our previous works in Chapter 3 have demonstrated that most

of the time, and especially in the case of a phenyl-based organic barrier, a two-carbon chain is the optimal length to get the strongest luminescence. We therefore decide to circumvent our work to the subclass of the phenyethyl amine based perovskites, owning a fluorine-substituted phenyl ring. This is a particular subclass of perovskites which have a general formula $(T-(CH_2)_2NH_3)_2PbX_4$ and where T consists of a fluorinated phenyl ring. We have studied different cases: the fluorine sitting in the ortho, meta or para position Kikuchi et al. (2004), and the perfluorinated ring. We show that the position of the fluorine atom strongly affects both the photostability, but somewhat strangely also considerably the emission efficiency of the thin films.

The structure of the perovskite produced from para-fluorophenylamine for example, is represented in Scheme 4.16, based on the analogy with the generic $(C_6H_5(CH_2)_2NH_3)_2PbX_4$ structure and considering that the steric hindrance of a fluorine atom is almost the same than the one of an hydrogen.
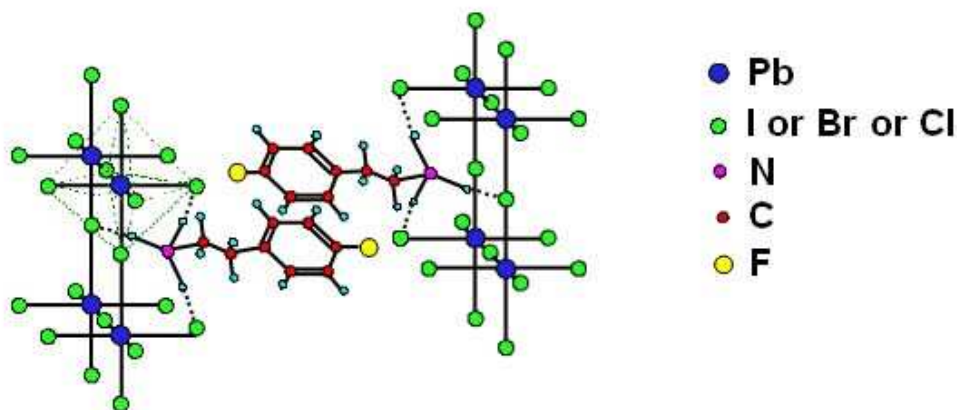
FIGURE 4.16: Sketch of the 3D structure of the $(4\text{-}FC_6H_4(CH_2)_2NH_3)_2PbX_4$ (X = I or Br or Cl) perovskites.

Table 4.2 shows the chemical structures, the names and the abbreviations of the amines $T-(CH_2)_2NH_2$ used in this study. For example, the bis(phenethylammonium) tetraiodoplumbate is noted as PEPI. When fluorine is present, the amine is simply designated by xFPE, the number x labeling the position of the fluorine atom on the phenyl ring: x= 2 for ortho, x= 3 for meta, and x= 4 for para. The perfluorophenyl ring amine will be designated by 5FPE. For clarity this has been summarized in the Table 4.2. The ammonium salts have been prepared by simple protonation of the considered amines, and the properties of the corresponding perovskites will be analyzed in comparison with the generic PEPX compounds containing no fluorine.

TABLE 4.2: Chemical structure, complete name and abbreviation of the amines part
of the fluorinated perovskites

Chemical structure of amines	Name	Abbreviation
	2-Phenylethanamine	PE
	2- Fluorophenethylamine	2FPE
	3- Fluorophenethylamine	3FPE
	4- Fluorophenethylamine	4FPE
	Perfluorophenethylamine	5FPE
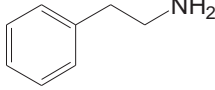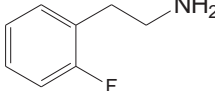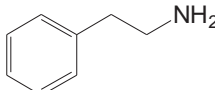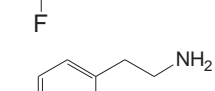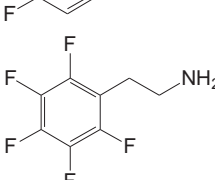
Preparation

The amine bases of 2FPE, 3FPE and 4FPE are purchased from Sigma-Aldrich company. The amine 5FPE is not commercially available and it is synthesized from pentafluorophenylacetonitrile as it is explained in appendix A. These amines are then transformed to ammonium salts and consequently dissolved in stoichiometric amounts with their corresponding inorganic PbX_2 in DMF to prepare $(T\text{-}(CH_2)_2NH_3)_2PbX_4$ solution. This method is exactly the same as the one introduced in Paragraph 2.1. Thin films are deposited by spin-coating and annealed. The deposition parameters are: 1500 rmp, 1500 rmps, 30 s; annealing condition is 95 °C for 1 min.

Microscopy characterizations

Figure 4.17 displays the optical microscopy images of layers made from various perovskites, along with PEPI for reference. Except 3FPEPI which presents more roughness, it seems that all compounds show similar surface roughness. Figure 4.18 shows the AFM pictured obtained on a 2FPEPI layer and a PEPI layer, that shows the smoothness of the layers that is generally obtained. AFM measurements provide: $\Delta = 9.4$ nm for 2FPEPI, $\Delta = 10.55$ nm for PEPI Wei et al. (2012). Thus, the presence of only one fluorine atom doesn't affect significantly the quality of the spin-coating process.
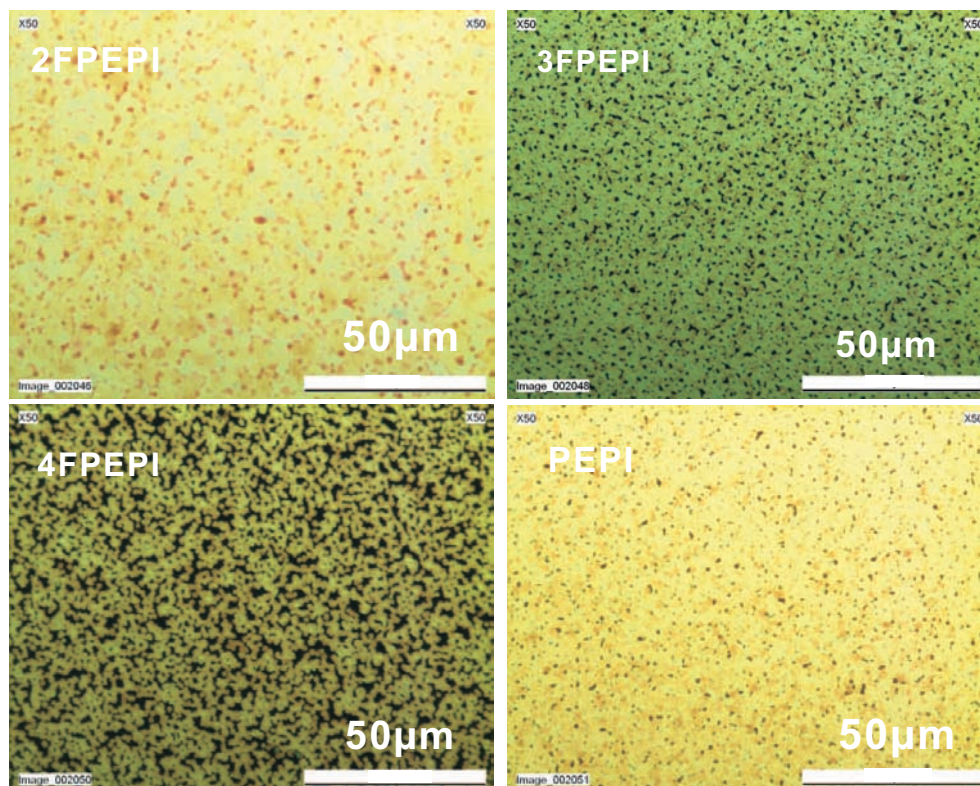
FIGURE 4.17: Optical microscope pictures of different perovskite layers prepared from 10% solutions.
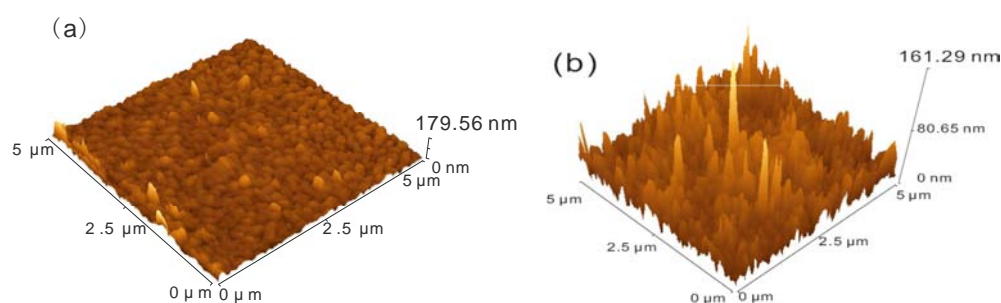
FIGURE 4.18: AFM pictures of (a) the 2FPEPI layer, (b) the PEPI layer, obtained by tapping mode. Be careful that the vertical scales are different in these two images.

On the other hand, the 5FPEPI and 5FPEPB unfortunately give relatively poor quality spin-coated films, certainly due to the high surface energy coming from the five fluorine atoms, which diminishes the cohesion of the layers, as well as adherence on glass substrates. The images of a 5FPEPI and 5FPEPB thin layers under a microscope are given in Figure 4.19.

X-ray diffraction of the spin-coated layers

Room temperature XRD measurements for FPEPB thin films are shown in Figure 4.20. These measurements have been done at ECNU. These FPEPB films are deposited on fused quartz by spin-coating.
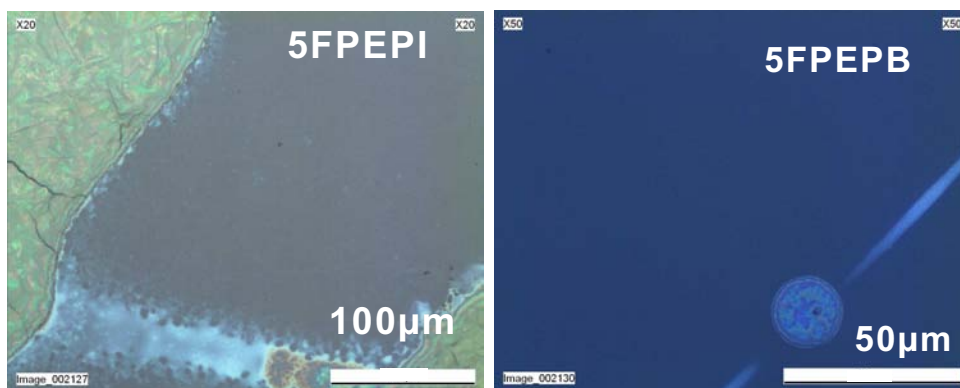
FIGURE 4.19: Spin-coated layers of 5FPEPI and 5FPEPB. The dewetting of the solution is shown, and the deposit lets appear inhomogeneous areas.

The instrument is a Rigaku Ultima IV type with CuKα radiation, wavelength 0.154056 nm. The voltage applied is 40 kV, intensity is 30 mA. The step length of measurement is set to be 0.01 nm; and the scan speed is 10°/min. As shown in Figure
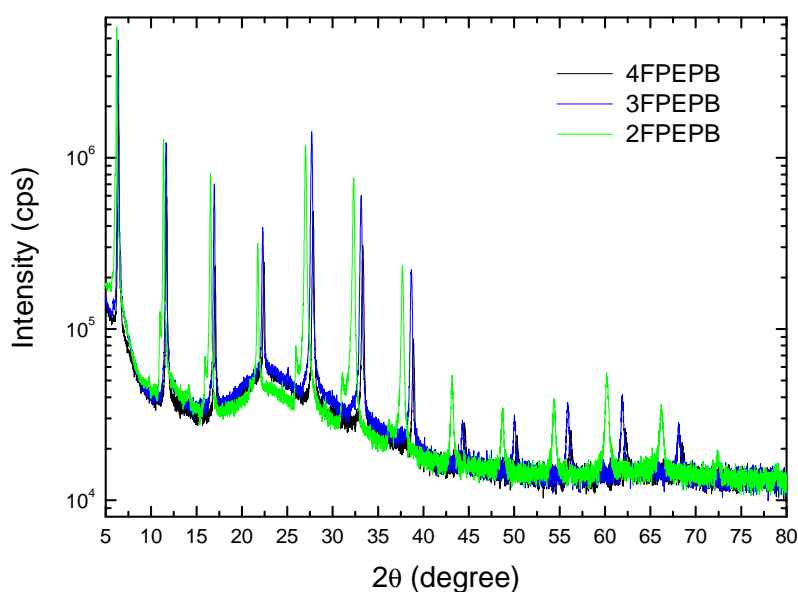
FIGURE 4.20: X-ray diffraction spectra of 4FPEPB, 3FPEPB and 2FPEPB spin-coated layers

4.20, sharp single diffraction peaks are observed for each xFPEPB (x=2, 3, 4) film sample which reveals that the xFPEPB crystals are well ordered multi-layered structures with single phase.

4.2.2 Optical characterization

4.2.2.1 Bromide containing perovskites

The absorption and the photoluminescence of the layers prepared from bromide based perovskites are registered and analyzed, comparatively with the generic PEPB molecule. The absorption is exhibited on Figure 4.21(a) while the photoluminescence is shown on Figure 4.21(b). While the absorption spectrum lets appear two bands, a broad
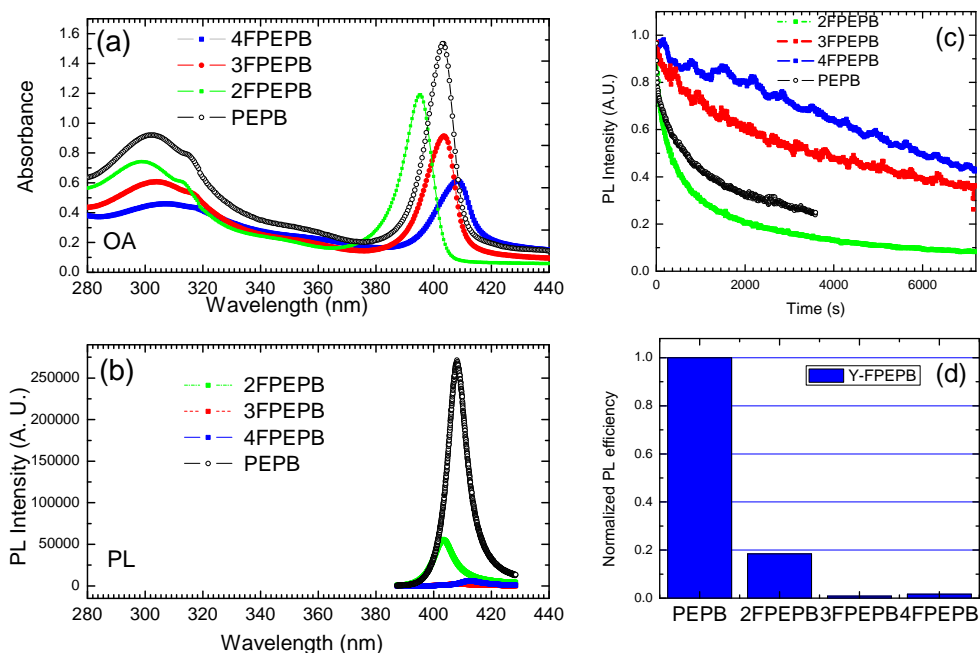
FIGURE 4.21: Comparative (a) absorbance, (b) photoluminescence and (c) photo-bleaching rate of bromide based perovskite layers made from 10wt% solutions. The excitation laser is the 325 nm line HeCd laser. For the PL and bleaching rate, the power is 1 mW. (d) Normalized PL efficiency of these perovskites layers.

one around 300-320 nm, and a large one around 400 nm, the luminescence arises only from the latter. In addition, it is quite surprising to notice that substitution of a single fluorine atom has such a huge effect, not only on the absorption and emission wavelengths, but drastically on the luminescence intensity. Unfortunately, in this case, the introduction of the fluorine seems to weaken the emission, but it is rather surprising to consider that this phenomenon seems to be quite sensitive to the place of the substituent. Figure 4.21(d) shows the relative emission intensity for each xFPEPB perovskite layer. In order to compare the PL efficiencies of the molecules, we define the ratio $\rho = I/(P_{laser} \cdot a_{325})$ where I is the integrated intensity of the photoluminescence peak, P_{laser} is the excitation laser power and a_{325} is the absorption factor at the excitation wavelength 325 nm. In Figure 4.21(d), the ratios $\rho_{xFPEPB}/\rho_{PEPB}$ (that we will design as the normalized PL efficiency) are reported for each x. We see that the ortho substitution affects greatly the

emission yield (compared with the PEPB reference), on the other hand meta and para substitutions lead to a relative extinction of the emission.

We also investigated the stability of the layers under illumination, in order to estimate the quenching rate of the emission. Figure 4.21(c) shows the relative decrease of the emission of perovskite layers as a function of the exposition time. It is clear that some fluorinated perovskites are more resistant than the standard PEPB, unfortunately the more resistant compounds are the ones that display the smallest luminescence intensity initially. However it seems that globally the introduction of one fluorine atom leads to an improvement of the materials resistance to bleaching.

4.2.2.2 Iodide containing perovskites

Similarly to the preceding part, iodide based perovskites have been prepared and studied, both on the point of view of the absorbance and photoluminescence, but also the photoresistance of the films is estimated. The absorbance of four films, issued from different iodide based perovskites, is represented on the Figure 4.22(a). This time again,
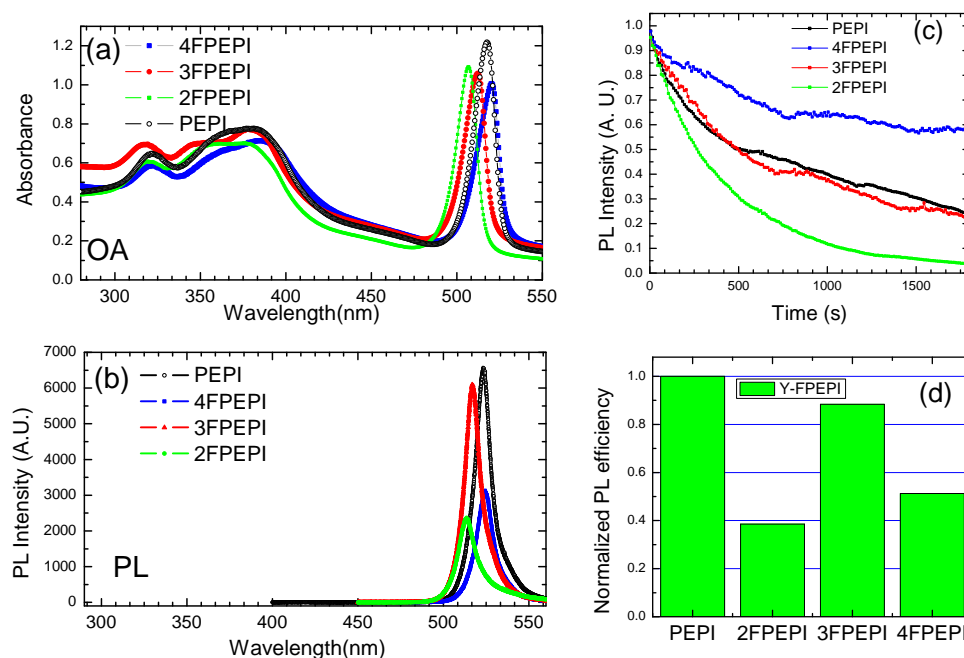
FIGURE 4.22:   Comparative (a) absorbance, (b) photoluminescence and (c) photo-bleaching rate of iodide based perovskite layers made from 10wt% solutions. The excitation laser is the 325 nm line HeCd laser. For the PL, the excitation laser power is 0.6 mW, for the bleaching rate, it is 7 mW. (d) Normalized PL efficiency of these perovskites layers

a clear effect of the substitution is noticeable on the spectra, but the effect is hypsochromic (except 4FPEPI), the sharp peak characteristic of the perovskite arising this

time at shorter wavelengths, with E_{4FPEPI} - E_{PEPI} = 1 nm, E_{3FPEPI} - E_{PEPI} = -5 nm and E_{2FPEPI} - E_{PEPI} = -10 nm. The luminescence of the iodide-based perovskites is represented on the Figure 4.22(b). Apart from the correlated hypsochromic shift of the emission, it appears that only one fluorinated perovskite, which has a meta fluorine atom, shines almost as strongly as PEPI, while for the two others the emission yield is lower, as seen in Figure 4.22(d).

The photobleaching of the perovskite emission is shown on Figure 4.22(c), and again important differences can be observed according to the place of the fluorine substituent, which is quite unexpected. The para substitution seems to provide the most resistant character. On the other hand, substitution by a meta fluorine atom changes extremely little the behaviour of the perovskite, either regarding the fluorescence yield or the stability, while the other positions affect both.

4.2.2.3   Chloride containing perovskites

In order to obtain more information on the special case of 4FPE amine as the organic salt, we also prepare the chloride based perovskites PEPC and 4FPEPC, respectively stemming from the classical phenylethylamine and its 4-fluorophenyl analogue. The absorption and fluorescence of these two particular perovskites are represented on the Figure 4.23. It is interesting to remark that, in this case, not only the normal perovskite structure is obtained, but the relative luminescence yield of the fluorinated perovskite is higher than in the generic PEPC, see Figure 4.23(d). Another interesting feature in this case is the complete absence of influence by the fluorine substitution on the absorption or emission wavelength, contrarywise to the bromide and the iodide based perovskites.

To summarize the relative emission intensity of the perovskites layers for each halogenide, it is clear that fluorine substitution impedes the bromide based perovskites emission, while it improves the chloride based perovskites emission and it leaves the iodide based perovskites emission less affected. This is quite complicated to explain, but it is possible that this effect is related to an unexpected enhancement of non-radiative decays in the case of bromide based compounds, maybe because of resonance with the vibrational energy of the C-F bond. However, we have seen above that in many occasions the resistance of the layers to photobleaching is improved, which constitutes an improvement, especially if device life-time has to be considered in the future.

4.2.3   Perfluorophenyl perovskite

We present this perovskite separately in a dedicated part, since its properties notably differ from the ones of the monofluorinated perovskites. The absorption and normalized emission spectra of this perovskite are exhibited on Figure 4.24 in the case of both iodide and bromide compounds.
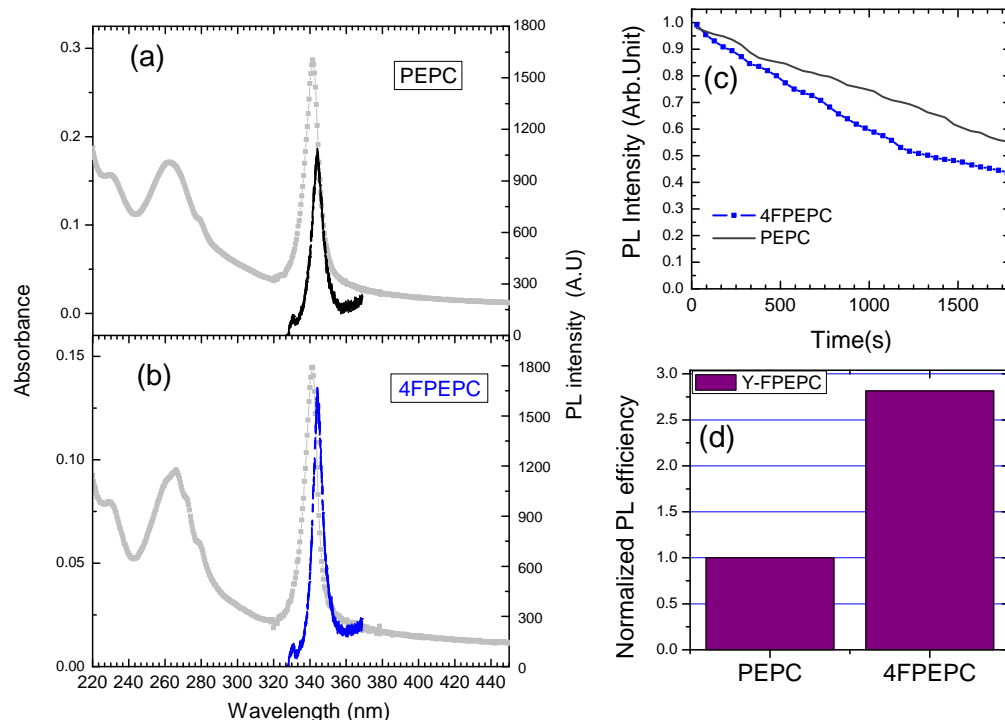
FIGURE 4.23:   Comparative (a) absorption, (b) photoluminescence and (c) photobleaching rate of PEPC and 4FPEPC layers, made from 1.5wt% solutions. The excitation laser is the 325 nm line HeCd laser. For the PL, the excitation laser power is 2 mW, it is 7 mW for the bleaching rate. (d) Normalized PL efficiency of these perovskites layers.

The substitution of a single fluorine atom has been found to have little or no influence on the emission wavelength of the perovskite. On the other hand, replacement of all hydrogens by fluorine leads to a notable hypsochromic shift on the emission: E_{5FPEPI} - E_{PEPI} = -16.14 nm, E_{5FPEPB} - E_{PEPB} = -13.4 nm, where E_{xFPEPX} is the energy position of the PL peak maximum. However, the most striking result on 5FPEPI is the stability to bleaching, which is superior, for the long times, to all compounds xFPEPI and PEPI (Fig. 4.24(c)). It seems therefore clear that the substitution of all hydrogen atoms by fluorine ones considerably reduces the rate of the degradation reactions. Our interpretation is that the 5 fluorine atoms suppress the one-electron oxidation of the phenyl which has been considered as one reason for the photodegradation.

4.3   Perovskites doped PMMA layer

We have talked in Paragraph 4.1.1 that the perovskites layers protected with PMMA present a slightly improved photostability and in paragraph 4.2, we have synthesized some fluoro-perovskites presenting a highly improved photostability. To improve further this problem of unsatisfactory stability, we introduce nanometer-sized crystals in a PMMA
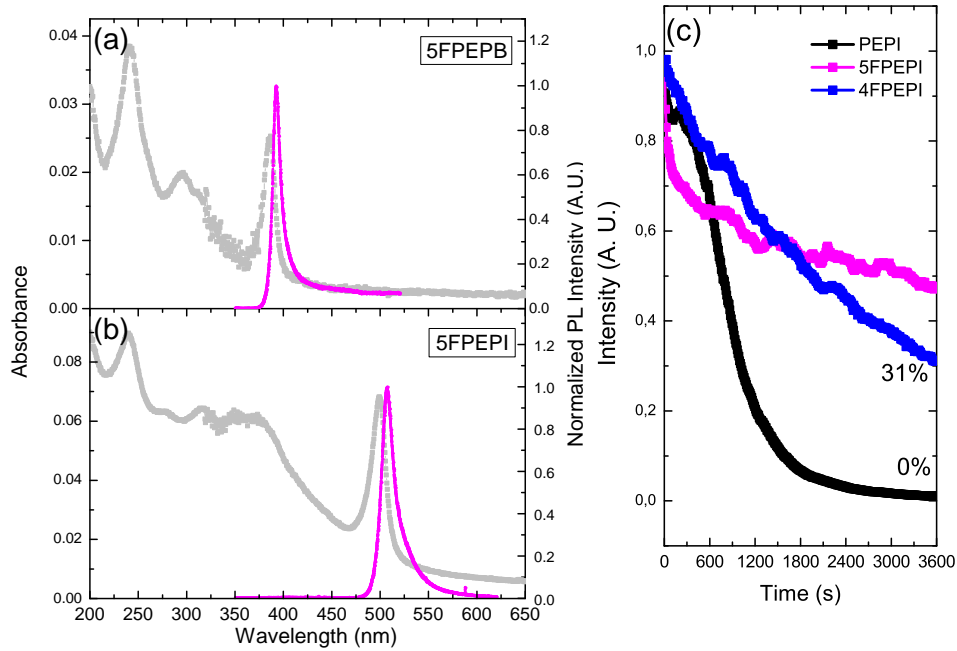
FIGURE 4.24: Comparative (a) absorbance, (b) normalized photoluminescence and (c) photobleaching rate of perfluorophenyl perovskite layers made from 10wt% solutions. The excitation laser is the 325 nm line HeCd laser. For the PL, the excitation laser power is 3 mW for 5FPEPB and 1 mW for PEPI. For the bleaching rate, the excitation laser power is 7 mW.

matrix. This approach has been used in Kitazawa's work for PEPI Kitazawa (1998); Kitazawa et al. (2002); Kitazawa and Watanabe (2002), and remarkable improvements of thermal- and photo-stability were achieved for instance with $(C_6H_5C_2H_4NH_3)_2PbI_4$ doped PMMA films Kitazawa and Watanabe (2002). Furthermore, it is expected that the use of PMMA polymer greatly improves the surface smoothness of the thin films compared to pure perovskites layers. The nanocrystals of perovskites included in PMMA layer still keep a good crystal structure and an adequate electronic structure, therefore good optical properties. These advantages make the perovskites doped PMMA layers very promising for the fabrications of optical devices. Here we prepare some phenylalkylammonium based perovskites doped PMMA layers, optical properties and methods to optimize the fabrication are introduced in the following paragraphs.

4.3.1 Preparation

The perovskites doped PMMA layers are deposited on SiO_2 glass substrates by a conventional spin-coating method as reported previously in Paragraph 2.2.2.2. To prepare the solution, a transparent polymer PMMA (Poly Methyl MethAcrylate) and a stoichiometric amount of the ammonium salt and PbX_2 (X = I, Br and Cl) are dissolved

into DMF. The concentration of PMMA in DMF is 20 wt% and the weight ratio of perovskite/PMMA is fixed at 1:5 in our study. With this solution, spin coating is performed at 2000 rpm for 30 s. The solution in concentration 20 wt% gives a layer of thickness about 1 μm. Thinner layers can be realized by lowering the concentration of solution. For example the 4FPEPI doped PMMA layer used in a Fabry-Perot microcavity in Chapter 5 with a thickness of 350 nm is realized with a solution where the concentration of PMMA in DMF is 10 wt%.

4.3.2   Annealing condition

After spin-coating, these films need to be subsequently dried in a hot place. This step is especially important for perovskites doped PMMA layers because the PMMA component makes the solution quite viscous and thick, which suppresses the movement of perovskites molecules in solution environment. Therefore the annealing time and annealing temperature should be appropriately raised to promote the self-organization process. The concrete conditions of annealing are not identical for different species of perovskite compounds. For a given perovskite doped PMMA layer, proper annealing condition will trigger the formation of a good crystal structure with less defaults and optimized optical properties. But the perovskite compounds can be destroyed by over heating. Some experimental examples will be given to specify this point in relation with optical characterization. For each kind of perovskites, the annealing conditions will be investigated in the following paragraphs.

4.3.3   Characterization

4.3.3.1   Structure

In order to investigate the structure of the perovskites doped PMMA layers we focus our attention on two typical layers: a PEPI doped PMMA layer and a 4FPEPI doped PMMA layer. Their images under microscope are shown in Figure 4.25 (a) and (b) respectively. In Figure 4.25 (a), we see PEPI crystals dispersed in PMMA and in Figure 4.25 (b), 4FPEPI crystals dispersed in PMMA. PEPI doped PMMA layers are more continuous than 4FPEPI doped PMMA layers.

Figure 4.26(b) presents the AFM image from a 4FPEPI doped PMMA layer, a PEPI doped PMMA layer and a PEPI standard layer, the average roughnesses of these layers are about 0.86 nm, 0.94 nm and 10.55 nm respectively.

These two layers are then used in XRD experiment. The XRD measurements were carried on in LPN by L. Largeau. As seen in Figure 4.27(a) and (b), sharp (0 0 2l) diffraction peaks associated with PEPI and 4FPEPI crystals were clearly observed. Their
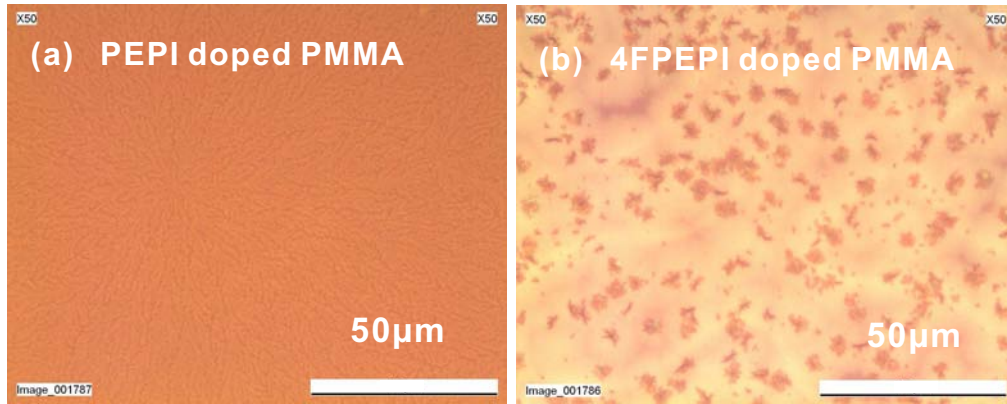
FIGURE 4.25: Optical microscope images of (a) a 641 nm PEPI doped PMMA layer and (b) a 1.1 μm 4FPEPI doped PMMA layer.
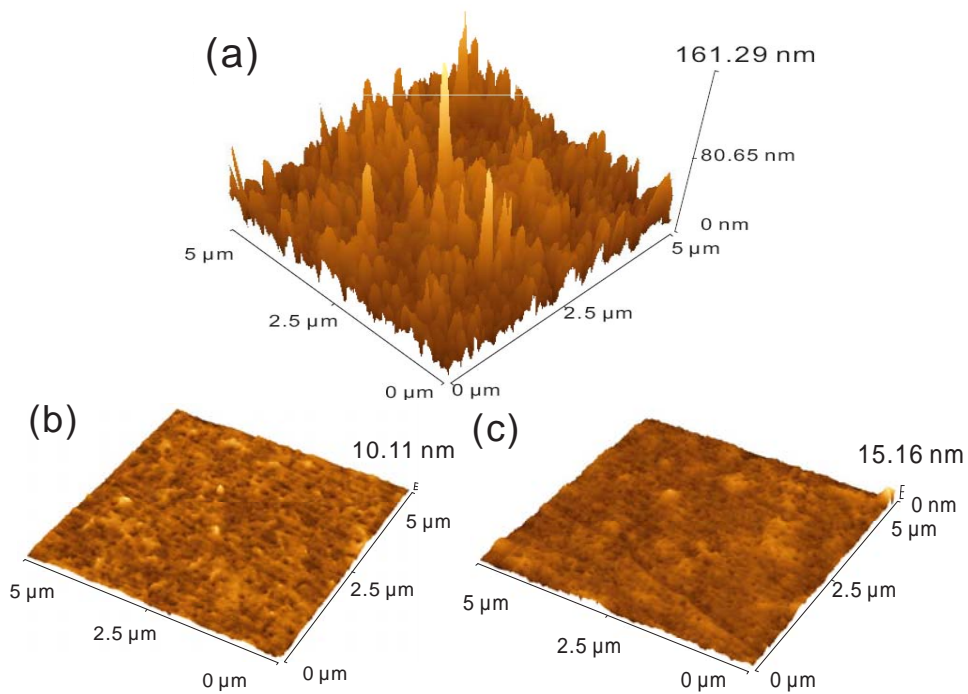
FIGURE 4.26: AFM images of (a) a 50 nm PEPI layer, (b) a 1 μm 4FPEPI doped PMMA layer and (c) a 1 μm PEPI doped PMMA layer. Be careful that the vertical scales are different in these two images

lattice constants perpendicularly to the layer plane (c-axis) are found to be 1.61 ± 0.01 nm and 1.64 ± 0.01 nm respectively. These XRD results reveal that PEPI and 4FPEPI crystals which precipitate in the PMMA matrix are highly oriented, with the c-axis perpendicular to the substrate surface. Comparing XRD spectra of perovskites doped PMMA layer with their pure perovskites spin-coated layer (as seen in 4.27(c)), we see the same diffraction angles for the sharp peaks. But there are also some broad low peaks as marked in Figure 4.27(b). We think these broad peaks are associated with the precipitation of oriented hexagonal PbI_2 small particles generated during the annealing process.

(a)

(b)

(c)
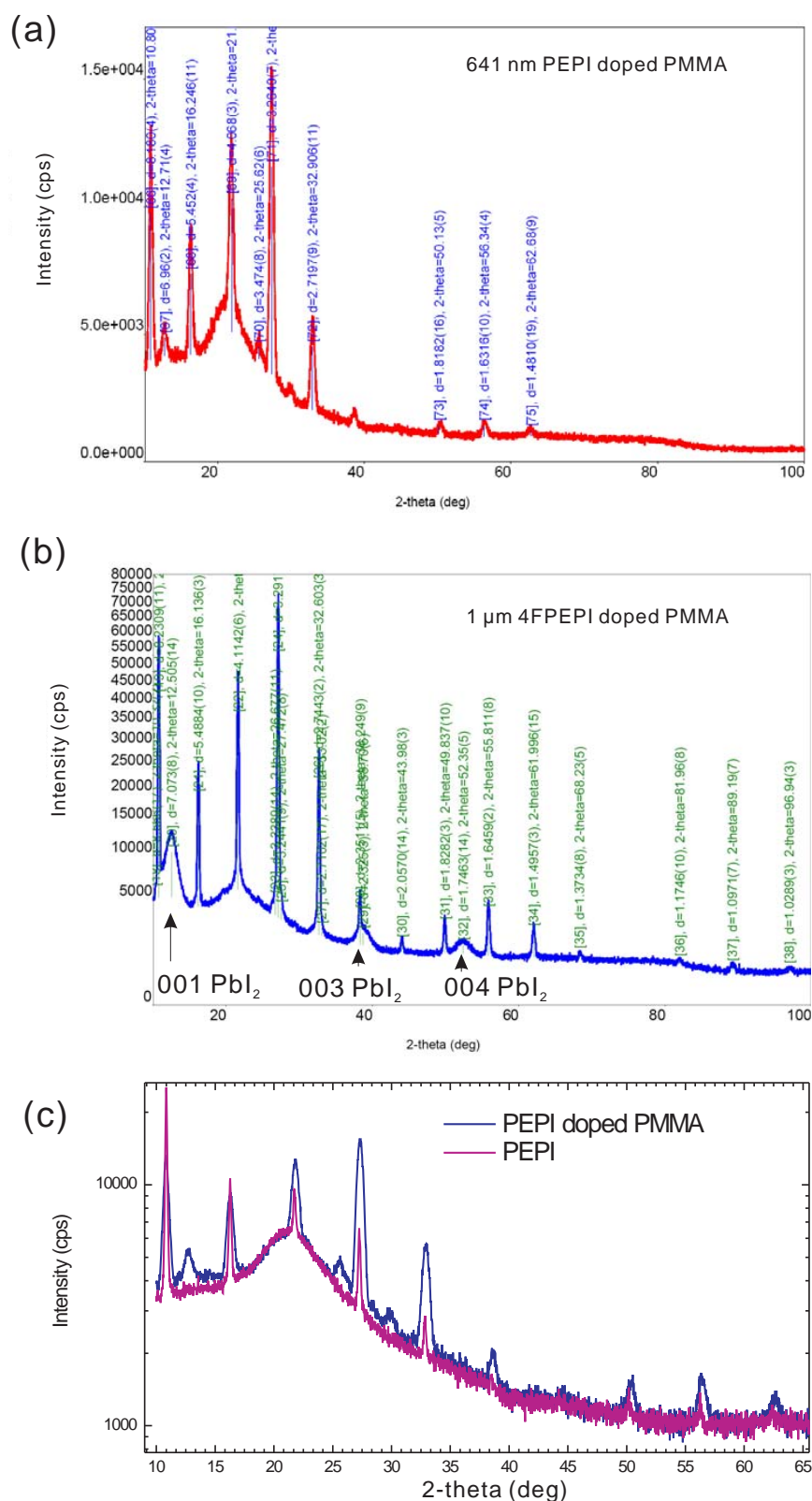
FIGURE 4.27: XRD spectrum of (a) a 641 nm PEPI doped PMMA layer and (b) a 1.1 μm 4FPEPI doped PMMA layer. (c) Comparison between XRD spectra of a 641 nm PEPI doped PMMA layer and a 50 nm PEPI spin-coated layer.

4.3.3.2 Absorption and Photoluminescence spectra

a) 4FPEPI doped PMMA layer

In this study, 4FPEPI doped PMMA layers are prepared from their 20% solution. With this 1.1 μm layer, the annealing parameters manifest a more important role than in other samples. Figure 4.28 presents the OA spectra of the 4FPEPI doped PMMA layers annealed at different temperatures and durations.
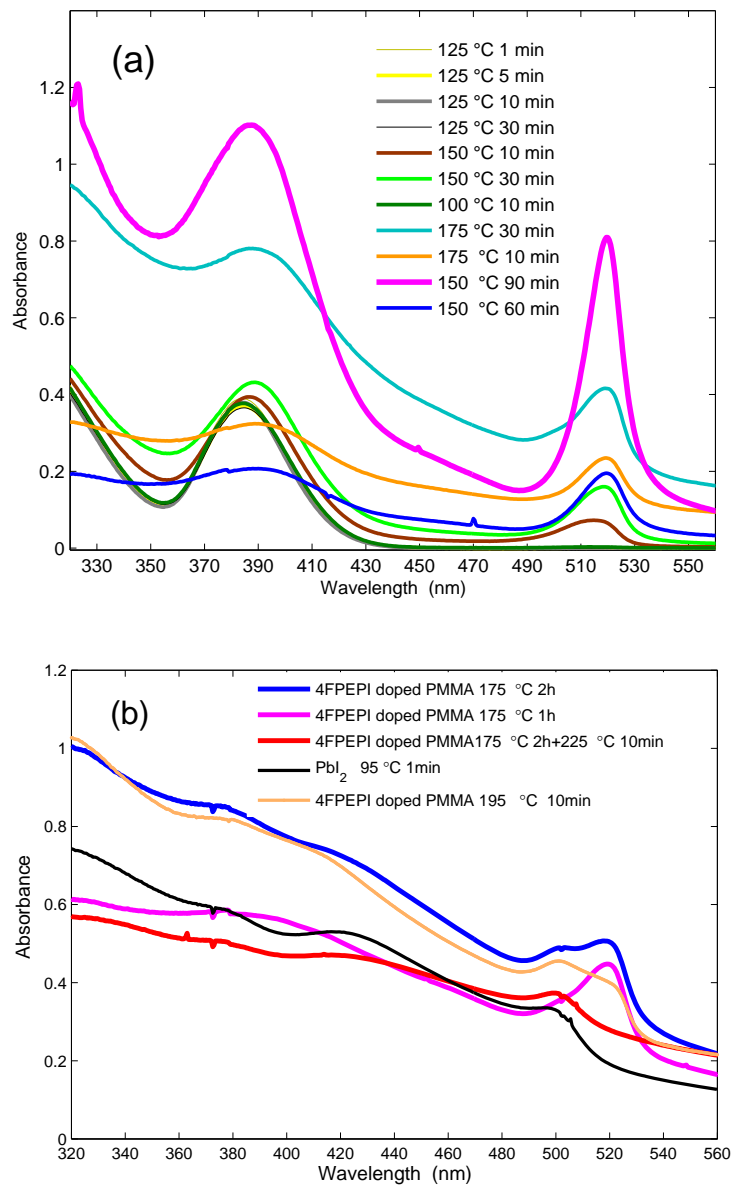
FIGURE 4.28: Comparative absorbance of 4FPEPI doped PMMA layers made from 20 wt% solutions. These samples are annealed at different temperature, and exhibit different absorption intensities, as seen in (a). (b) The 4FPEPI doped PMMA layers annealed at over high temperature condition. Measurement is carried on at room temperature.

The strong absorbance located at 519 nm is due to the 4FPEPI perovskites. The wide peak around 385 nm might result from a portion of amorphous molecules which are not completely self-organized in layer. When the annealing temperature is set at 125 °C, the main resonant peak dosen't appear but only the amorphous peak around 385 nm is there. When the temperature is raised to 150 °C, an absorbance peak at 519 nm arises. This absorption peak reaches a maximum value among all the samples for annealing at 150 °C during 90 min. The intensity declines again as the annealing temperature goes up to 175 °C. A longer annealing duration at 175 °C or a higher annealing temperature will destroy the perovskites molecules. In Figure 4.28(b) we see that the absorption resonance of the two 4FPEPI doped PMMA samples annealed at 175 °C for 1 h and 2h tends to collapse meanwhile another peak at 500 nm grows. This collapse is more obvious when the samples are heated at higher temperature: see for instance the layer annealed at 175 °C for 2 h followed by an annealing at 225 °C for 10 min, and the sample annealed at 195 °C for 10 min. The OA spectrum of a PbI_2 film deposited from its DMF solution is also drawn for comparison. It is clearly seen that the 500 nm OA peak of the over annealed 4FPEPI doped PMMA layers is quite similar to the OA peak of PbI_2, which reveals the decomposition of 4FPEPI perovskites compounds during annealing with probable degradation of the ammonium salts.

PL experiments are carried on at room temperature under the excitation at 325 nm of a HeCd laser with a power of 10 mW. From Figure 4.29(a) we see that the layers annealed below 150 °C don't present a sharp PL peak at 520 nm but a wide low peak around 454 nm. This wide peak is attributed to the large amount of amorphous state molecules inside the layer and it decreases with increasing annealing temperature. At 125 °C, we see a very small peak at 525 nm. At annealing temperature 150 °C, this peak becomes predominant meanwhile the peak at 454 nm weakens. This phenomena proves that a large percentage of 4FPEPI molecules transforms from amorphous state to well oriented state by proper annealing process. In Figure 4.29(c) the 4FPEPI doped PMMA layers are further optimized with annealing condition. For comparison, the PL of a 50 nm PEPI thin layer annealed at 95 °C for 1 min is drawn in graph. The PL intensity of 4FPEPI doped PMMA layer reaches the highest value when the sample is annealed at 150 °C for 90 min, and then declines as annealing temperature goes up to 175 °C.

We equally prepared 3FPEPI doped PMMA layers, PEPB doped PMMA layers, 3FPEPB doped PMMA layers and 4FPEPB doped PMMA layers from their corresponding 20 wt% solution. Sharp optical resonances arise from their respective perovskite crystals included in PMMA. Equally, we observed that the PL peak intensity varies with annealing conditions, as shown in Figure 4.30 spectra for PEPB doped PMMA layer and 4FPEPB doped PMMA layers. The OA and PL spectra show that the resonant peak positions are quite the same as the ones of their corresponding thin film deposited from perovskites in DMF solution. 125 °C is an appropriate annealing temperature for PEPB doped PMMA layers to achieve fine optical properties, and that for 3FPEPI
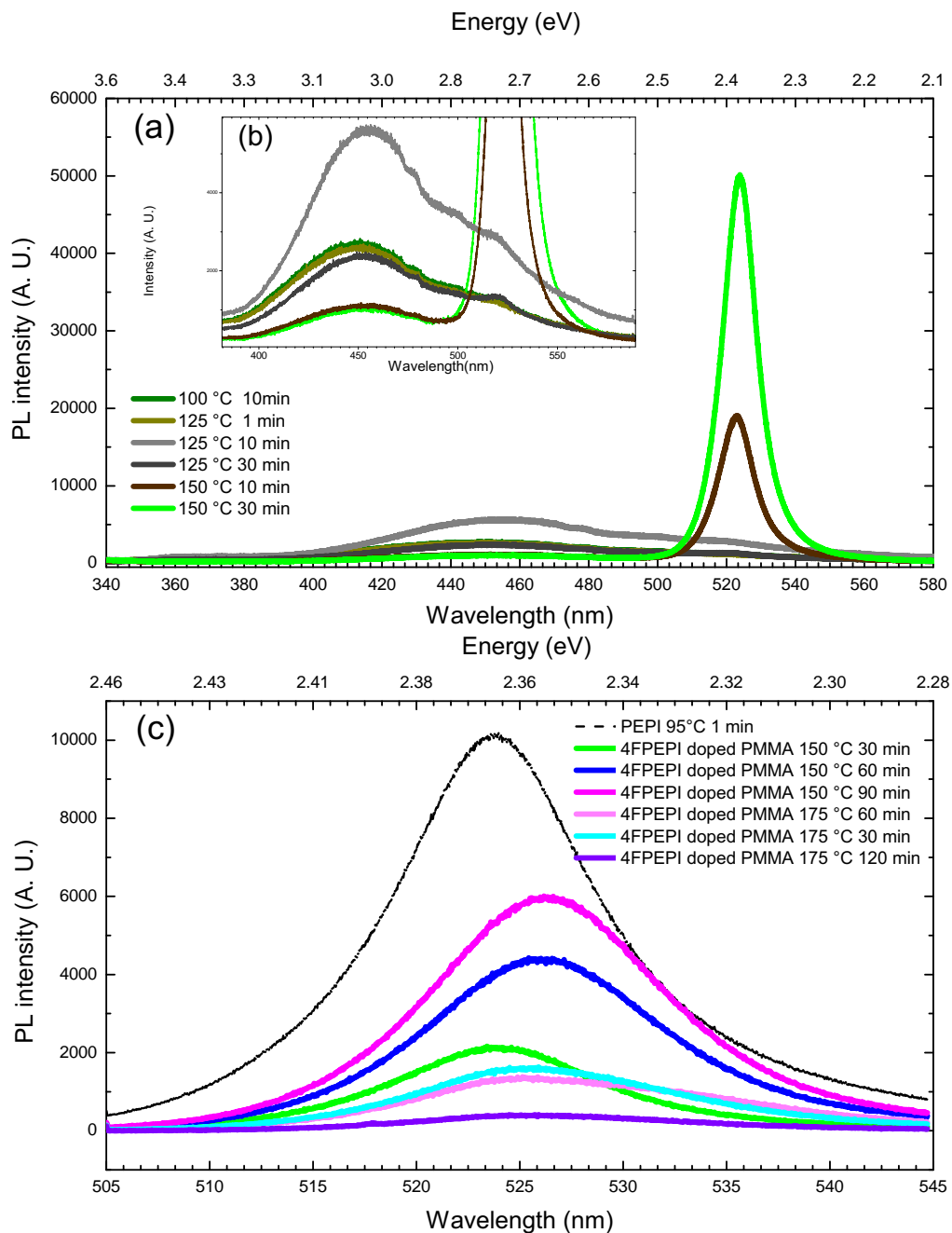
FIGURE 4.29: Comparative photoluminescence of (a) 4FPEPI doped PMMA annealed at 100 °C 10 min to 150 °C 30 min, the included graph (b) is a zoom of (a). (c) Comparative photoluminescence of 4FPEPI doped PMMA annealed at 150 °C 30 min to 175 °C 120 min. The PL spectrum of a PEPI thin film layer is drawn in the same graph for comparison. The excitation source is a 325 nm HeCd laser, the power is 10 mW. Measurement is carried at room temperature.

doped PMMA layers, 3FPEPB doped PMMA layers and 4FPEPB doped PMMA layers is found to be 150 °C.
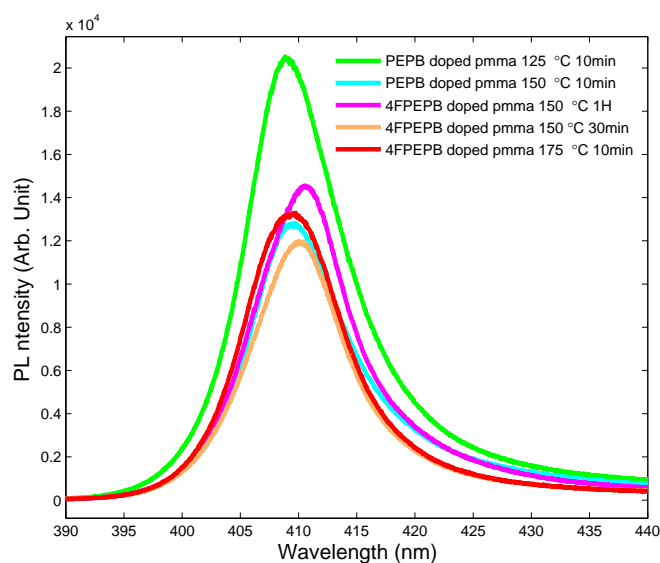
FIGURE 4.30: Comparative photoluminescence of PEPB doped PMMA layer and 4FPEPB doped PMMA annealed at different conditions. The excitation source is a 325 nm HeCd laser, the power is 10 mW. Measurement is carried at room temperature.

b) PEPI doped PMMA layer

Similarly, all the PEPI doped layers are deposited from a 20% solution as described previously, while the annealing conditions are varied. OA and PL measurements of these layers are carried on at room temperature.

Figure 4.31 shows the OA and PL spectra for different annealing conditions. When the annealing temperature is fixed at 125 °C, the OA peaks positions are located at 514 nm and PL peaks are located at 520 nm for the two layers annealed for 10 min and 15 min. As the annealing temperature is raised to 150 °C, the main resonant peaks change a little: 518.5 nm for OA and 522 nm for PL. The resonant band of PEPI doped PMMA layers seems to be at a little bit higher energy than PEPI thin film whose absorbance and PL peak position situate at 516 nm and 523.5 nm (see Figure 2.6.) From the spectra, we see that the OA and PL intensities of layers vary with annealing temperature and duration. The most optimized annealing condition for the optical properties are obtained for annealing at 125 °C for 15 min.

4.3.3.3   Photostability

Being protected by the PMMA polymer, the perovskites exhibit much more stable over time optical properties than their thin films. For example the PEPI thin films degrade quickly in one month: the main resonant PL peak at 525 nm disappears as a result of the attack of moisture and oxygen existing in air. By contrast, the PEPI doped
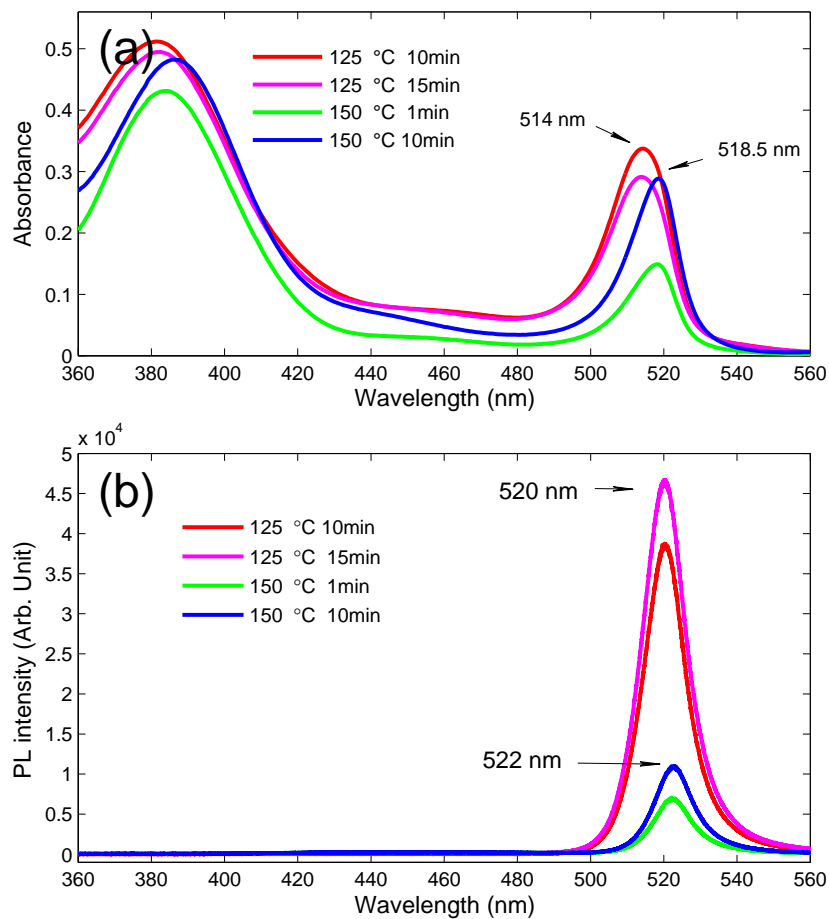
FIGURE 4.31: Comparative (a) absorbance, (b) photoluminescence of PEPI doped PMMA layers made from 20wt% solutions. For the PL, the excitation source is the 325 nm HeCd laser, the power is 10 mW. Measurement is carried at room temperature.

PMMA layers still keep bright PL 6 months after there are fabricated and can present good optical properties during an even longer time.

To investigate photostability of these layers, photobleaching measurement is carried on under UV illumination. From Figure 4.32 we see that the perovskites doped PMMA layer: PEPI doped PMMA and 4FPEPI doped PMMA are more stable than their corresponding thin film samples: PEPI and 4FPEPI. The 4FPEPI doped PMMA layer degrades less under illumination than PEPI doped PMMA layer since the 4FPEPI molecules possesses a better stability than the PEPI molecules as we introduced in paragraph 4.2.2.2. Being the most robust layer with optimized optical properties, the 4FPEPI doped PMMA therefore becomes a good candidate to be introduced into a microcavity as it will be discussed in Chapter 5.

The photostability of 4FPEPI doped PMMA layer is also studied at low temperature: the sample is placed in the cryostat chamber in a helium environment. See Figure 4.33.
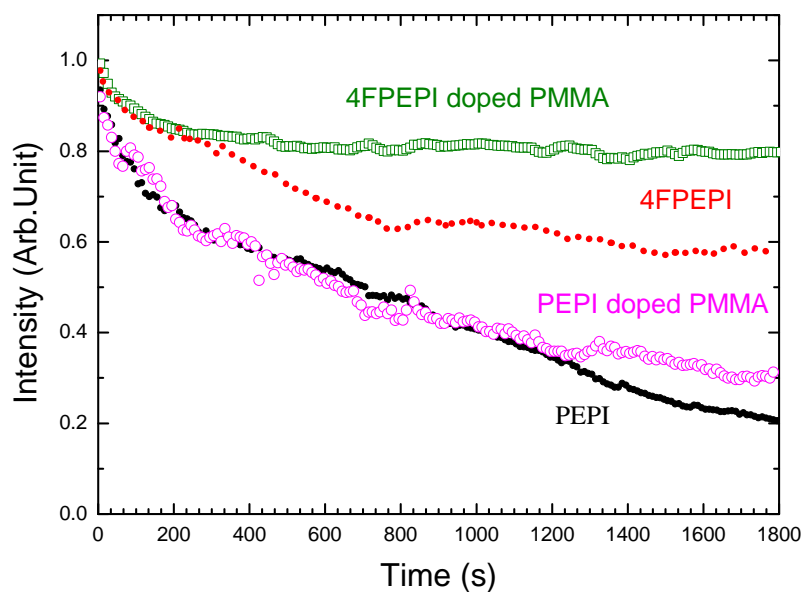
FIGURE 4.32: Photobleaching of 4FPEPI doped PMMA, 4FPEPI, PEPI doped PMMA, PEPI thin layers under the 325 nm line of a HeCd laser during 1800 s, the excitation power is 7 mW. The measurement is carried on at room temperature. The thickness of PEPI and 4FPEPI films are about 50 nm, PEPI doped PMMA and 4FPEPI doped PMMA layers are around 1 μm.

This layer is deposited from a 10 wt% solution and annealed at 150 °C for 30 min.[2] The excitation laser is kept at 10 mW 325 nm and the measurement is performed at 10 K, 80 K and 300 K respectively. We observe that the stability varies according to the temperature: at 80 K, the PL intensity after 7200 s of illumination is still 87 % of its initial value which is exceptionally stable, more stable than those at 10 K and 300 K. The stability of 4FPEPI doped PMMA layer at 80 K is quite remarkable and it is also the most stable sample among all the perovskites layers we have worked on.

4.4   Conclusion

In this chapter we have studied the photodegradation of 2D layered organic inorganic hybrid perovskites. From experimental results we find that the photostability process is a complex process into which many factors work together. Being attacked by oxygen in air, the halogen species in inorganic parts tend to be eliminated. Besides, a photo-induced thermal effect and a photochemical reaction can equally cause decomposition of the organic components in perovskites. To improve the photostability of perovskites, we have worked on two aspects: the first one is to improve the stability of the organic

---

[2]The sample in Figure 4.33 has experienced different annealing conditions compared to the sample of Figure 4.32, it explains probably the variation of the photobleaching observed at 300 K in the two figures.
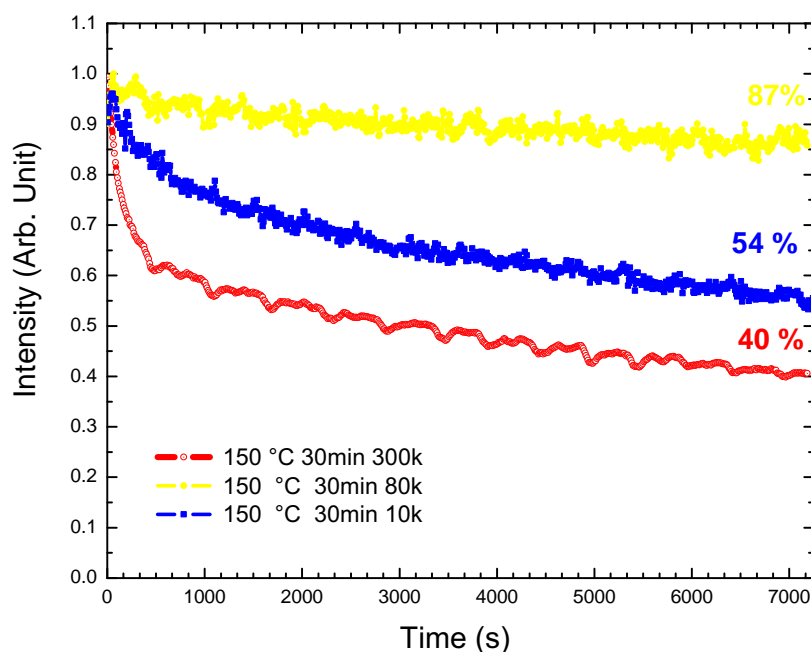
FIGURE 4.33: Photobleaching of 4FPEPI doped PMMA thin layer under the 325 nm line of a HeCd laser during 7200 s, the excitation power is kept at 7 mW. The measurement is carried on at room temperature. The thickness of 4FPEPI doped PMMA layer is around 1 μm.

molecules used in perovskites; and the second one is to protect perovskites crystals by including them in a transparent PMMA matrix. For the first one we have prepared and studied several new perovskites based on fluorophenylethylamines. The results show that the introduction of a fluorine atom in the organic part of the perovskite has a stronger influence than could have been forecast. Our former hypothesis that the introduction of fluorine on the phenyl ring would lead to a photostability improvement is now comfirmed. The position of the fluorine atoms plays an important role: the introduction of fluorine sometimes quenches the fluorescence, but in other cases seems to have little effect, or even in one case leads to a fluorescence improvement, the underlying reasons are probably not obvious. However, we have shown that globally, the introduction of fluorine atom(s) on the phenyl ring leads to an improvement of the perovskites resistance to bleaching and, among the main families investigated here (iodide, bromide, of chloride), the new material 4FPEPB, 4FPEPI and 5FPEPI exhibit superior photostability than the generic PEPX materials.

For the perovskites doped PMMA layers where the perovskite molecules are included in PMMA polymer matrix and thus protected from moisture and oxygen in air, the increase of their photostability is significant. We have realized a very stable layer: the 4FPEPI doped PMMA layer. This type of layer exhibits high PL at room temperature and high resistance to bleaching under illumination with a UV laser. Remarkably, it remains 87% of it initial PL intensity after illumination under a 10 mW HeCd laser for 2 hours at 80 K. It is very interesting for perovskites applications in optical devices and

fundamental studies. Next chapter will present an example of device realized with this optimized material operating at 300K.

Chapter 5

Planar microcavity and strong coupling

Light-matter interaction in vertical microcavities, and more particularly the strong-coupling regime, has been intensively studied since two decades Houdré (2005); Gibbs et al. (2011). The first observation of the strong coupling regime was discovered by C. Weisbuch et al. in Fabry-Perot cavities containing III-V inorganic semiconductor in 1992. Weisbuch et al. (1992) Soon after strong coupling was also found in II-VI semiconductor, Kelkar et al. (1995) and nitrides. Semond et al. (2005) In molecular materials, the strong coupling has been demonstrated recently at room temperature with zinc porphyrin Lidzey et al. (1998), J-aggregates Lidzey et al. (1999), sigma-conjugated polysilane Takada et al. (2003), anthracene Kéna-Cohen et al. (2008) and perovskite molecules Fujita et al. (1998); Bréhier et al. (2006); Lanty et al. (2008b). These meaningful works, especially the cavities operating at room temperature, such as the cavities containing GaN, ZnO and perovskites, provide a good mean to study the coherent and stimulated optical effects which are expected in such confined systems at room temperature and which can lead to realization of new optoelectronic devices such as low threshold polariton laser Saba et al. (2001); Kéna-Cohen and Forrest (2010). Furthermore it reveals deep physical phenomena which are studied for the moment at low temperature in GaAs or CdTe based microcavities: such as BEC (Bose Einstein Condensation) and superfluidity.

In this chapter, we will talk about some basic principles on microcavities and focus our attention on two perovskites based microcavities: PEPI based cavity and 4FPEPI based cavity. Experimental methods used for samples preparation and optical characterization will be introduced. From experimental results, we will discuss in details the strong coupling regime observed in our microcavities.

5.1   Generalities

5.1.1   Fabry-Perot cavity

The simplest 1D microcavity structure is a planar Fabry-Perot cavity, closed with two parallel reflecting mirrors M1 and M2. The geometry of a simple planar cavity is shown in Figure 5.1.
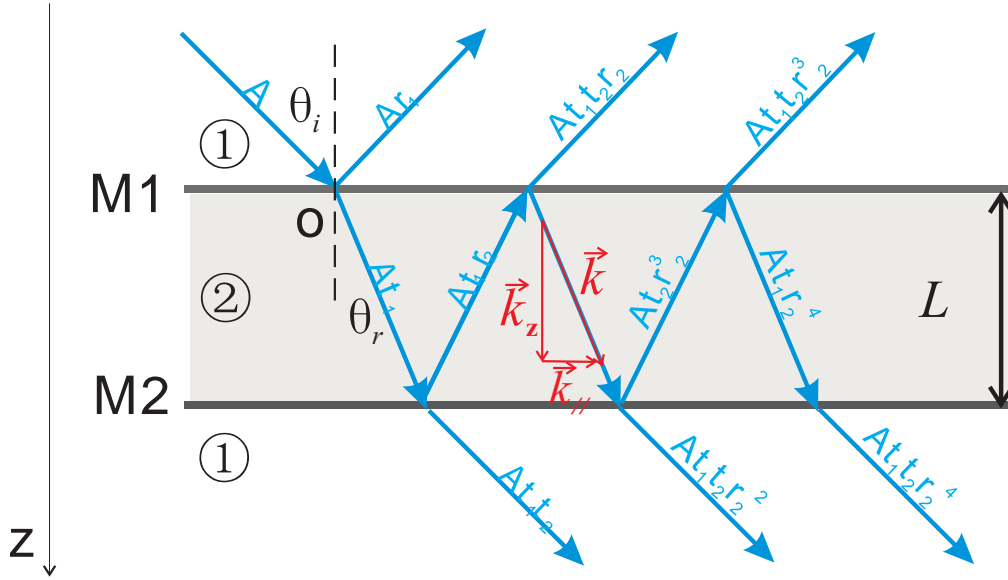
FIGURE 5.1: Geometry of a simple planar cavity

Let us suppose that a monochromatic polarized electromagnetic plane wave $\overrightarrow{E_0}=A\overrightarrow{\varepsilon}e^{i(\overrightarrow{k}\cdot\overrightarrow{r}-\omega t)}$ propagates in y = 0 plane in medium 1 and enters into medium 2 through cavity mirror interface M1 at point O, the polarization $\overrightarrow{\varepsilon}$ can be perpendicular to the incident plan (Transverse Electric "TE") or parallel to the incident plane (Transverse Magnetic "TM"). We note its amplitude A and its wavelength λ, the incident angle is θ_i and θ_r is the refraction angle. The phase difference between each succeeding reflections is given by:

$$\Delta\phi = (\frac{2\pi}{\lambda})\delta = \frac{4\pi nL cos\theta_r}{\lambda}. \tag{5.1}$$

δ is the optical path difference between each succeeding reflections. Here we consider an ideal optical cavity composed of a homogeneous layer having a length of L between two parallel mirrors. r_1 (r_2) is the reflection coefficient of an incident electromagnetic wave propagating in medium 1 (2) on medium 2 (1), and t_1 (t_2) is the transmission coefficient from medium 1 (2) to medium 2 (1). n is the average refractive index of medium 2 (inside the cavity) and the refractive index of medium 1 outside cavity (air) equals to 1. The reflection and transmission coefficients for a TE wave can be expressed

as:

$$\begin{cases} r_1 = \dfrac{cos\theta_i - ncos\theta_r}{cos\theta_i + ncos\theta_r} \\ t_1 = \dfrac{2cos\theta_i}{cos\theta_i + ncos\theta_r} \end{cases} \tag{5.2}$$

$$\begin{cases} r_2 = \dfrac{ncos\theta_i - cos\theta_r}{ncos\theta_i + cos\theta_r} \\ t_2 = \dfrac{2ncos\theta_i}{ncos\theta_i + cos\theta_r} \end{cases} \tag{5.3}$$

The total transmission and reflection of the incident electromagnetic wave at each side of cavity are caused by interference of multiple beams reflected and transmitted by the two mirrors. The total complex amplitude of transmitted (reflected) electromagnetic wave E_t (E_r) can be described as a sum of all transmitted (reflected) amplitudes:

$$E_r = Ar_1 + At_1t_2r_2e^{i\Delta\phi} + At_1t_2r_2^3e^{i2\Delta\phi} + \cdots \tag{5.4}$$

$$E_t = At_1t_2 + At_1t_2r_2^2e^{i\Delta\phi} + At_1t_2r_2^4e^{i2\Delta\phi} + \cdots \tag{5.5}$$

So, the total intensity of transmitted light is:

$$I_t = \vec{E}_t\vec{E}_t^* = \frac{A^2(t_1t_2)^2}{(1 - r_1r_2e^{i\Delta\phi})(1 - r_1r_2e^{-i\Delta\phi})} = \frac{A^2(1 - r_1r_2)^2}{1 - 2r_1r_2cos\Delta\phi + r_1^2r_2^2}. \tag{5.6}$$

We find

$$I_t = TI_0 = \frac{I_0}{1 + \dfrac{4r_1r_2}{(1 - r_1r_2)^2}sin^2\dfrac{\Delta\phi}{2}}. \tag{5.7}$$

Where I_0 is the intensity of the incident light and T is defined as the total transmission coefficient. Similarly, we get the total intensity of reflected light and the total reflection coefficient R, supposing that there is no absorption in cavity (R+T = 1):

$$I_r = RI_0 = \frac{I_0}{1 + \dfrac{(1 - r_1r_2)^2}{4r_1r_2sin^2\dfrac{\Delta\phi}{2}}}. \tag{5.8}$$

The following Figure 5.2 draws the R and T coefficients as a function of $\Delta\phi$, taking two sets of parameters: $r_1 = 0.78$, $r_2 = 0.85$ (in red); $r_1' = 0.28$, $r_2' = 0.25$ (in blue). For a given cavity with fixed length, the phase difference $\Delta\phi$ only depends on incident angle θ_i (or θ_r). We see from the two examples in Figure 5.2 that the minima of reflectivity (maxima of transmissivity) always happen for $\Delta\phi = 2m\pi (m = 1, 2, 3, \cdots)$, whatever the r_1 and r_2 values are. The higher reflectivity the mirrors have, the deeper and thinner

the resonance peaks are:a small deviation from $2m\pi$ position results in great increase (decrease) in reflectivity (transmissivity).
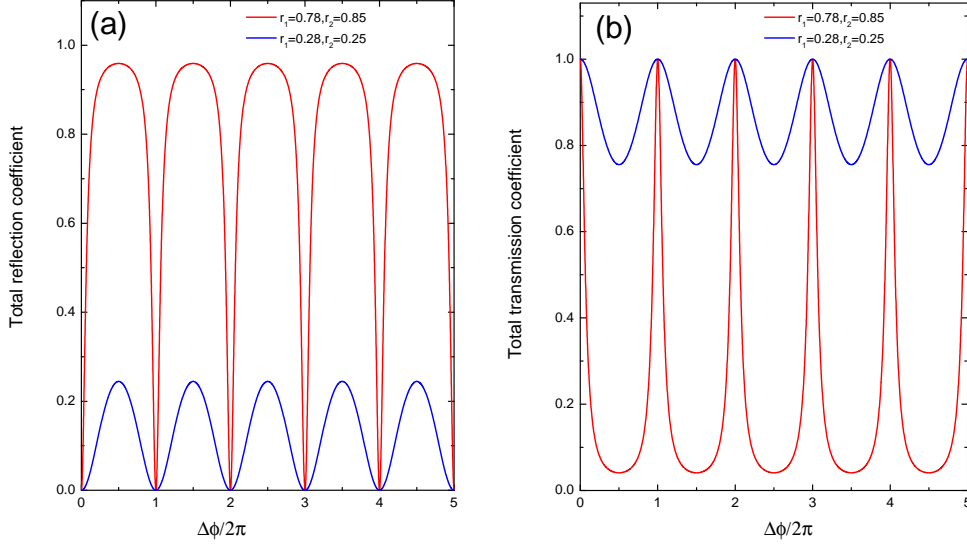
FIGURE 5.2: Total reflection (a) and transmission (b) coefficients for two sets of parameters: r_1=0.78, r_2=0.85 (in red); r'_1=0.28, r'_2=0.25 (in blue).

To characterize a cavity system, the concept of quality factor Q has to be used. It is defined as the ratio of resonance frequency to the width of resonance curve:

$$Q_m = \frac{\nu_m}{\Delta\nu_{1/2}}, \qquad (5.9)$$

where ν_m is the resonance frequency for the mode m and $\Delta\nu_{1/2}$ is the full width at half maximum of the resonance peak. Optical cavities designed for resonance at a certain mode are often wanted to have high quality factor. Especially for the cavities working in the strong coupling regime, a long lifetime of photons τ_{ph}, which is directly related to the quality factor, is quite crucial to obtain a relatively steady interaction between photon and exciton. The relationship between τ_{ph} and Q_m is:

$$\tau_{ph} = \frac{Q_m}{2\pi\nu_m} \qquad (5.10)$$

Where c is the speed of light. Therefore cavity mirrors with low lost and high reflectivity are required to achieve longer photon lifetime. For this reason, the mirrors for high Q microcavities are strongly suggested to be Distributed Bragg Reflectors.

Now let us consider the photon mode. The thickness L of the cavity layer should satisfy the relationship in formula 5.11 to obtain resonance at a specified wavelength λ and a specified m value:

$$\Delta L = 2nLcos\theta_r = m\lambda. \qquad (5.11)$$

Let us take the case of the fundamental cavity mode $m = 1$. Because of quantification of wave vector along z axis (k vector is represented in 5.1)

$$k_z = kcos\theta_r = 2n\pi cos\theta_r/\lambda. \tag{5.12}$$

we then get:

$$k_z = \pi/L \tag{5.13}$$

The energy of a photon having a wave vector k, and propagating in a medium of refractive index n can be expressed as:

$$E_p = \frac{\hbar ck}{n}. \tag{5.14}$$

Therefore the parallel component of wave vector (along x and y axis) is:

$$k_{//} = \frac{nE_p}{\hbar c}sin\theta_r. \tag{5.15}$$

The electromagnetic wave comes out from the cavity system to air ($n = n_0 = 1$) with an angle θ , the $k_{//}$ thus checks:

$$k_{//} = \frac{E_p}{\hbar c}sin\theta. \tag{5.16}$$

Thanks to this relationship, the momentum in a microcavity system can be probed by detecting photons emitted out of the cavity with an angle θ. Starting from formula 5.16, angle resolved reflectivity and photoluminescence experiments have been designed and will be introduced later in Paragraph 5.2.2.

E_p can be expressed as a function of the incident angle. From Snell-Descartes' law $sin\theta_i = nsin\theta_r$, and from formula 5.11 and 5.14, we easily get for every m:

$$E_p^m = \frac{hc}{\lambda} = \frac{mhc}{2nLcos\theta_r} = \frac{mhc}{2nL\sqrt{n^2 - sin^2\theta_i}}. \tag{5.17}$$

5.1.2   Distributed Bragg reflector

DBRs (Distributed Bragg Reflectors), which are also called dielectric mirrors, are a kind of highly reflective mirrors usually applied as reflectors in planar cavities. A DBR is made of several identical pairs of two dielectric layers : one has high optical index n_H, thickness l_H and the other one has low optical index n_L, thickness l_L. They are designed to obtain an interference enhancement for a certain wavelength λ desired in cavity, the relationship should satisfy:

$$n_Hl_H + n_Ll_L = m\lambda/2. \tag{5.18}$$

Taking m = 1, the thickness of layers in a DBR are thus given by:

$$n_Hl_H = \lambda/4, n_Ll_L = \lambda/4. \tag{5.19}$$

For a large number N of pairs, a DBR presents a frequency range ("stop band") in which the reflectivity is close to unity, whose center is determined by the $\lambda/4$ condition, and whose width $\delta\lambda$ is governed by the difference between the refractive indexes of the two constituents. Savona et al. (1995)

$$\delta\lambda = \frac{4\lambda}{\pi} arcsin(\frac{|n_L - n_H|}{n_L + n_H}). \tag{5.20}$$

So, the larger the difference $|n_L - n_H|$ is, the larger $\delta\lambda$ we obtain. We have used some DBRs whose stop band is centered at 515 nm under normal incidence. These mirrors are realized by Layertec company. They are suitable for cavities containing iodide based perovskites which resonate in green wavelength region. The structure of mirror consists in 6.5 pairs of two different layers with $n_H = 2.36$ and $n_L = 1.46$, see figure 5.3(a). These layers are deposited on a fused silica substrate and a 10 nm thick silica layer is deposited on the top in order to ensure the deposition quality of perovskites in following steps.

The following Figure 5.3(b) shows reflectivity curve simulated by transfer matrix method (the principles of this method will be reminded hereafter in paragraph 5.1.3.2) at normal incidence. The two dips at 1.88 eV and 2.95 eV are Bragg modes of this DBR mirror. A wide flat stop band from 1.9 eV to 2.9 eV (FWHM) with high reflectivity of about 0.98 is seen.
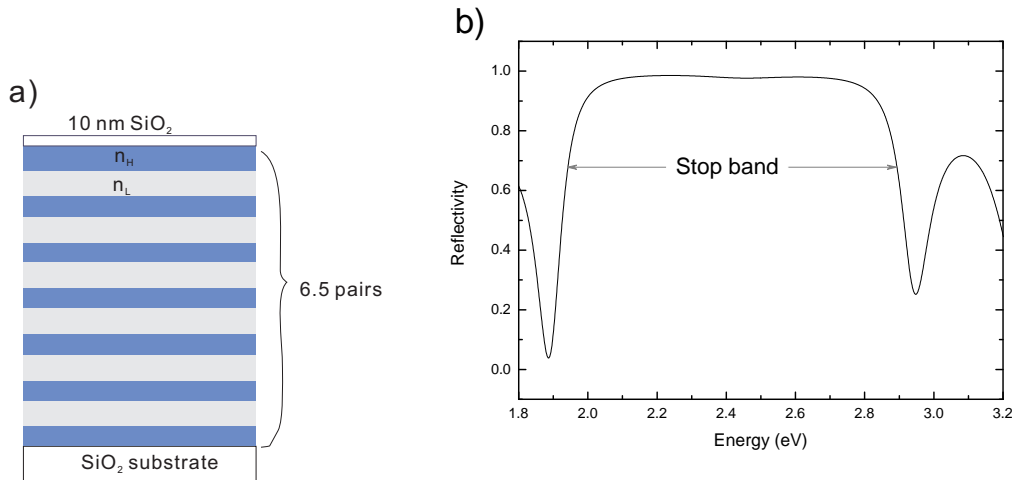
FIGURE 5.3: a) Structure of a DBR fabricated by Layertec. The blue bands represent the layers with $n_H = 2.36$ and the light grey bands represent the layers with $n_L = 1.46$; b) simulated reflectivity of a DBR fabricated by Layertec. The stop band is centered at 515 nm at normal incidence.

5.1.3 Physics in cavities

5.1.3.1 Strong/weak coupling regime

Embedding an optical emitter inside a microcavity system can lead to additional effects due to the change in the optical density of photon states. Generally, emission from microcavities is modified in two kinds of regimes: weak coupling and strong coupling.

Kleppner emphasized that in the atomic case, the atom releases its energy because of its interaction with the optical field of the vacuum, so that if the interaction could be "switched off", the atom would remain forever in its excited state. And Purcell made a lot of efforts to realize the opposite effect, that is to say to increase the interaction in order to get a faster release of the excitation. Purcell et al. (1946); Kavokin et al. He found that for an emitter embedded inside a microcavity, the photon density of states can be locally modified when being confined in an optical cavity. If the linewidth of emitter is smaller than that of the cavity mode, the emitter can be considered to couple to an optical continuum and the emission kinetics is given by Fermi's golden rule. See Figure 5.4(a). The spontaneous emission rate will be enhanced when the energies of the emitter mode and of the photon mode are in resonance. This discovery is called Purcell Effect and the enhancement is given by the Purcell factor:

$$F_p = \frac{3}{4\pi^2} \frac{\lambda_c^3}{n^3} \frac{Q}{V_{eff}}. \tag{5.21}$$

where λ_c is wavelength in vacuum, n is the refractive index of the cavity, Q and V_{eff} are the quality factor and volume of the cavity. In the description of the emission above, the reabsorption is neglected, since this coupling effect is thought to be weak.

If a resonant exciton has strong and narrow absorption band and if the lifetimes of exciton and photon are long compared to their interaction time, the coupling rate of cavity photons and excitons is larger than the total rate at which they escape out of the cavity. In this case, the reabsorption is stronger and the system is in a dynamic process of absorbing and emitting energy, which is named Rabi oscillations, the strong coupling thus takes place. In the strong coupling regime, the photon and exciton are no longer eigen modes, new eigen modes: polaritons, emerge: see Figure 5.4(b). The polaritons are linear combination of photon and exciton modes, they are described as quasiparticles. It is thought that the polaritons behave as bosons. An anticrossing appears in the microcavity polaritons dispersion, the energy width of this anticrossing is called the Rabi splitting $\hbar\Omega$, see Figure 5.5, which defines the coupling strength. Kavokin et al.; Pradeesh et al. (2009b)

a)

M1   M2   Optical continuum

E_{ex} k_z

b)

M1   M2

UP

E_p E_{ex} k_z

$\hbar\Omega$

LP
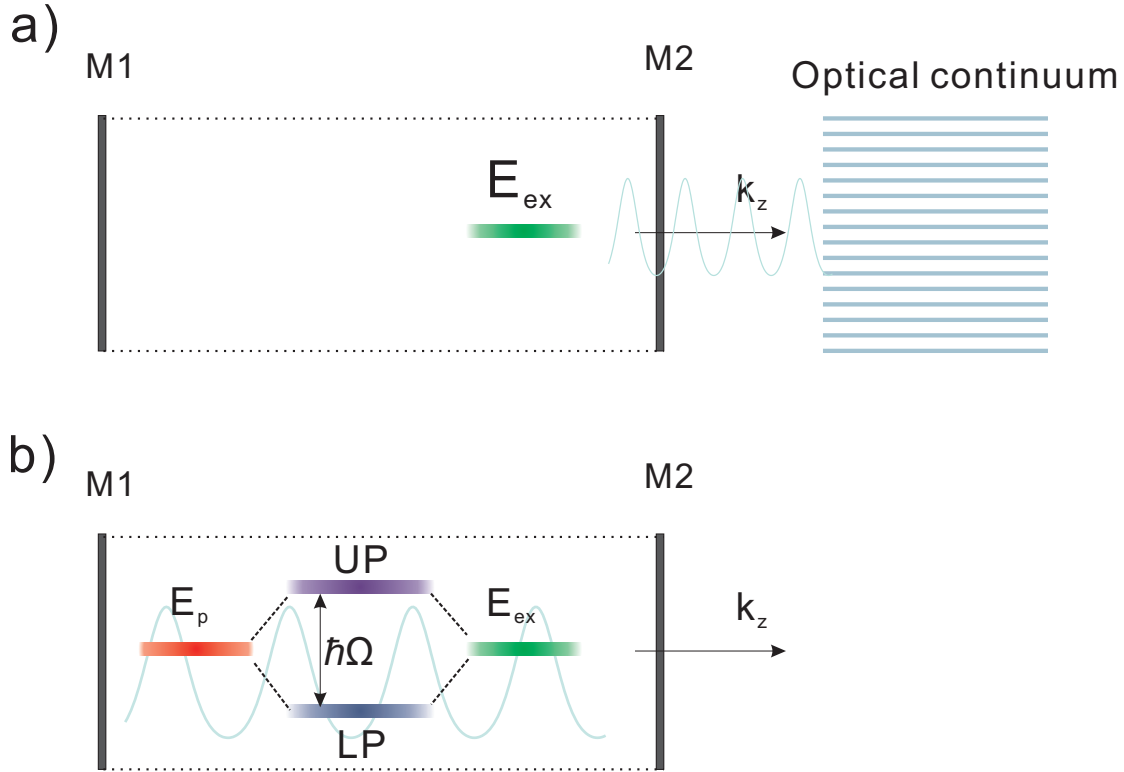
FIGURE 5.4: a) An exciton state coupled to the photon continuum states out of the cavity, resulting in emission in weak coupling regime. b) An exciton state coupled with discrete photon mode, upper polariton (UP) and lower polariton (LP) emerge in the case of the strong coupling regime.

The situation of strong light-matter interaction has been of intense interest for the study of the coherent and stimulated optical effects. Therefore, in the following paragraphs, we will emphatically talk about the study of strong coupling phenomena in our microcavities.

5.1.3.2   Description of photon-exciton coupling

Transfer matrix method

Light is modeled as a classical monochromatic electromagnetic plane wave $\vec{E}(M,t){=}\vec{E_0}e^{i(\vec{k}\cdot\vec{r}-\omega t)}$ and the excitonic resonances in the material are treated as Lorentz oscillators, corresponding to the system of electron and hole bound by a spring. The transfer matrix model allows to calculate the reflectivity spectra of some multi-layered systems, such as microcavities and DBR mirrors. It calculates also the profile of the electric field amplitude in microcavities. We will use a matricial writing of this method.

The plane wave $\vec{E}(M,t){=}\vec{E_0}e^{i(\vec{k}\cdot\vec{r}-\omega t)}$ is incident on a planar multi-layered structure: see Figure 5.6, the layers are stacked along the z axis. θ_i is the angle between the $\vec{k_1}$
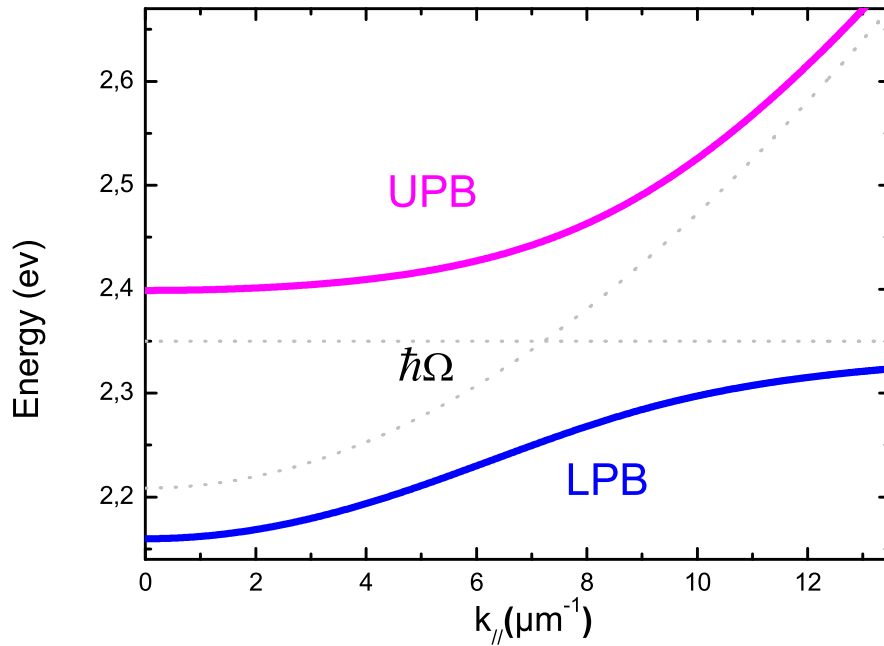
FIGURE 5.5: Dispersion curves of two polaritons in strong coupling regime: upper polariton branch (UPB) in magenta and lower polariton branch (LPB) in blue. Rabi splitting is noted as $\hbar\Omega$ at the anti-crossing.

wave-vector and the normal axis (perpendicular to the layers plane). We assume that the incident wave has a linear polarization perpendicular to the incidence plane (TE polarization).

When the incident wave meets the interface between the media 1 and 2, located at z=0, a part of the wave is transmitted and another part is reflected : we will note $E_1^+(z)$ the incident wave in the medium 1, which spreads forwards (towards z positive in the scheme 5.6), $E_1^-(z)$ is the reflected wave in the medium 1, and $E_2^+(z)$ is the transmitted wave in the medium 2. Due to the presence of the following layers, a wave propagating backwards (towards z negative) in the medium 2 exists also (due to the reflection at the interface between the layers 2 and 3) : we note this wave $E_2^-(z)$.

With the TE polarization, the continuity of the tangential component of the electric field at z=0 is :

$$E_1^+(0) + E_1^-(0) = E_2^+(0) + E_2^-(0). \tag{5.22}$$

The continuity of the tangential component of the magnetic field $H_t = H\cos\theta$ at z=0

FIGURE 5.6: (a) Schema of a multi-layered structure. (b) A plan wave propagates from medium 1 to medium 2.

allows to establish a second relationship between the media 1 and 2, from the Maxwell-Faraday law :

$$n_1 cos\theta_1(E_1^+(0) - E_1^-(0)) = n_2 cos\theta_2(E_2^+(0) - E_2^-(0)) \tag{5.23}$$

This system of equations can be written as

$$E_1^-(0) = \frac{1}{t_{12}}E_2^-(0) + \frac{r_{12}}{t_{12}}E_2^+(0) \tag{5.24}$$

$$E_1^+(0) = \frac{r_{12}}{t_{12}}E_2^-(0) + \frac{1}{t_{12}}E_2^+(0) \tag{5.25}$$

Where r_{12} and t_{12} are the amplitude reflexion and transmission coefficients:

$$r_{12} = \frac{n_1 cos\theta_1 - n_2 cos\theta_2}{n_1 cos\theta_1 + n_2 cos\theta_2} \tag{5.26}$$

$$t_{12} = \frac{2n_1 cos\theta_1}{n_1 cos\theta_1 + n_2 cos\theta_2} \tag{5.27}$$

This system of equations can be expressed with a matricial form :

$$\begin{pmatrix} E_1^-(0) \\ E_1^+(0) \end{pmatrix} = \frac{1}{t_{12}} \begin{pmatrix} 1 & r_{12} \\ r_{12} & 1 \end{pmatrix} \begin{pmatrix} E_2^-(0) \\ E_2^+(0) \end{pmatrix} \tag{5.28}$$

We will use in the following the simplifed notation :

$$(E_1(0)) = (P_{12})(E_2(0)) \tag{5.29}$$

(P_{12}) is the transition matrix at the interface between the media 1 and 2:

$$(P_{12}) = \frac{1}{t_{12}} \begin{pmatrix} 1 & r_{12} \\ r_{12} & 1 \end{pmatrix} \tag{5.30}$$

The propagation of the wave in medium 2, over a distance of d_2, leads to a phase shift for the field E_2:

$$E_2^-(d_2) = E_2^-(0)e^{-ik_{2z}d_2} \tag{5.31}$$

$$E_2^+(d_2) = E_2^+(0)e^{ik_{2z}d_2} \tag{5.32}$$

where $k_{2z} = k_2 cos\theta_2$, θ_2 is deduced from θ_1 with the refraction Snell-Descartes' law, and $k_2 = 2\pi/\lambda n_2$ This equation can be written with a matricial notation :

$$\begin{pmatrix} E_2^-(0) \\ E_2^+(0) \end{pmatrix} = \begin{pmatrix} e^{ik_{2z}d_2} & 0 \\ 0 & e^{-ik_{2z}d_2} \end{pmatrix} \begin{pmatrix} E_2^-(d_2) \\ E_2^+(d_2) \end{pmatrix} \tag{5.33}$$

We will use in the following the simplified notation : $(E_2(0)) = (D_2)(E_2(d_2))$ with

$$(D_2) = \begin{pmatrix} e^{ik_{2z}d_2} & 0 \\ 0 & e^{-ik_{2z}d_2} \end{pmatrix} \tag{5.34}$$

As well, at the interface between the media 2 and 3 : $(E_2(d_2)) = (P_{23})(E_3(d_2))$ and we can express $(E_1(0))$ as a function of $(E_3(d_2))$: $(E_1(0)) = (P_{12})(D_2)(P_{23})(E_3(d_2))$.

At the end, step by step, we can write the relationship between the electric field in medium 1 and the electric field in medium j : $(E_1(0)) = (S_j)(E_j(L))$ with $(S_j) = (P_{12})(D_2)(P_{23}) \cdots (D_{j-1})(P_{j-1,j})$ and $L = d_2 + d_3 \cdots + d_{j-1}$. The matricial

relationship between the electric fields in the medium 1 and in the medium j is then :

$$
\begin{pmatrix} E_1^-(0) \\ E_1^+(0) \end{pmatrix} = \begin{pmatrix} S_{11} & S_{12} \\ S_{21} & S_{22} \end{pmatrix} \begin{pmatrix} E_j^-(L) \\ E_j^+(L) \end{pmatrix}
\tag{5.35}
$$

Taking $E_j^-(L) = 0$, because no wave propagates to the left in the medium j (this medium is infinite for z > L), we obtain the amplitude reflection and transmission coefficients of the multilayered structure :

$$
t = \frac{E_j^+(L)}{E_1^+(0)} = \frac{1}{S_{22}},
\tag{5.36}
$$

$$
r = \frac{E_1^-(0)}{E_1^+(0)} = \frac{S_{12}}{S22}.
\tag{5.37}
$$

The intensity reflection and transmission coefficients are $R = |r|^2$ and $T = (n_j/n_1)|t|^2$.

Quasi-particle model

The material can be described by quantum theory with a two level model. We consider a microcavity where the two oscillators: photon mode and exciton mode are in resonance. In a single quantum well structure, the in-plane translational invariance imposes that an exciton within the light cone couples to the photons of the same in plane wavevector $k_{//}$. In this quantum mechanical approach, the hamiltonian of the system exciton-photon in interaction is written, in the basis of the photon state $|E_p >$ and exciton state $|E_{ex} >$:

$$
H = H_0 + W = \begin{pmatrix} E_p(k_{//}) & 0 \\ 0 & E_{ex}(k_{//}) \end{pmatrix} + \begin{pmatrix} 0 & V \\ V & 0 \end{pmatrix}.
\tag{5.38}
$$

The hamiltonian H_0 describes the system without light-matter interaction and W is the coupling hamiltonian which describes the interaction between photon and exciton states. $E_p(k_{//})$ and $E_{ex}(k_{//})$ are the dispersion relations of the photon mode and of the exciton mode in $k_{//}$ plane. The energy of coupling V is supposed to be real and independent on $k_{//}$, and has a relation with the Rabi splitting as:

$$
2V = \hbar\Omega.
\tag{5.39}
$$

As a result of the coupling existing in the system, the $E_p(k_{//})$ and $E_{ex}(k_{//})$ are no longer eigenvalues. The total hamiltonian can be diagonalized and the eigenstates $|E_U >$, called the Upper energy polariton, and $|E_L >$, called the Lower energy polariton, are linear superpositions of photon state $|E_p >$ and exciton state $|E_{ex} >$. The new eigenvalues of H are then found to be:

$$E_U(k_{//}) = \frac{1}{2}(E_p(k_{//}) + E_{ex}(k_{//})) + \frac{1}{2}\sqrt{(E_p(k_{//}) - E_{ex}(k_{//}))^2 + \hbar^2\Omega^2}, \qquad (5.40)$$

$$E_L(k_{//}) = \frac{1}{2}(E_p(k_{//}) + E_{ex}(k_{//})) - \frac{1}{2}\sqrt{(E_p(k_{//}) - E_{ex}(k_{//}))^2 + \hbar^2\Omega^2}. \qquad (5.41)$$

$E_U(k_{//})$ and $E_L(k_{//})$ are the energies of the upper and lower polariton branches (UPB and LPB) respectively. The new photon-exciton mixed states are related to non coupled states as followed:

$$|E_U> = X_k|E_p> + P_k|E_{ex}>, \qquad (5.42)$$

$$|E_L> = -P_k|E_p> + X_k|E_{ex}>. \qquad (5.43)$$

The square modulus values of P_k and X_k: $|P_k|^2$ and $|X_k|^2$, which are called Hopfield coefficients, satisfy $|P_k|^2 + |X_k|^2 = 1$ and respectively correspond to the photonic and excitonic fraction of polaritons. They describe the probability for the mixed exciton-photon particle to be found in either one of these states. They are given by the formula:

$$|P_k|^2 = \frac{1}{2}[1 - \frac{E_p - E_{ex}}{\sqrt{(\hbar\Omega)^2 + (E_p - E_{ex})^2}}], \qquad (5.44)$$

$$|X_k|^2 = \frac{1}{2}[1 + \frac{E_p - E_{ex}}{\sqrt{(\hbar\Omega)^2 + (E_p - E_{ex})^2}}]. \qquad (5.45)$$

The energy difference between photon and exciton $E_p - E_{ex}$ at $k_{//} = 0$ is called detuning and is usually denoted by δ_{p-ex}. When $\delta_{p-ex} > 0$ (blue-detuned regime), lower polariton branch(LPB) is exciton-like; when $\delta_{p-ex} < 0$ (red-detuned regime), LPB is photon-like. In the following Figure 5.7, we show examples corresponding to three detuning values: δ_{p-ex} = -50 meV, δ_{p-ex} = 0 meV and δ_{p-ex}= 50 meV. The dispersion curves present photon, exciton, LPB and UPB modes as a function of in-plane $k_{//}$. Rabi splitting is set as $\hbar\Omega$ = 60 meV and energy of exciton is taken as E_{ex} = 2.3 eV. The photon mode is modified by varying the length of cavity.

5.1.3.3 Bottleneck and polariton photoluminescence

The bottleneck was firstly observed in time-resolved measurements of the polariton emission in II-VI based microcavities. Müller et al. (1999) M. Müller et al. found an abrupt decrease of the polariton PL decay time when the character of the polariton state changed from photon like to exciton like. This observation indicates that the relaxation process into polariton states having a high photon fraction slows down. Tartakovskii
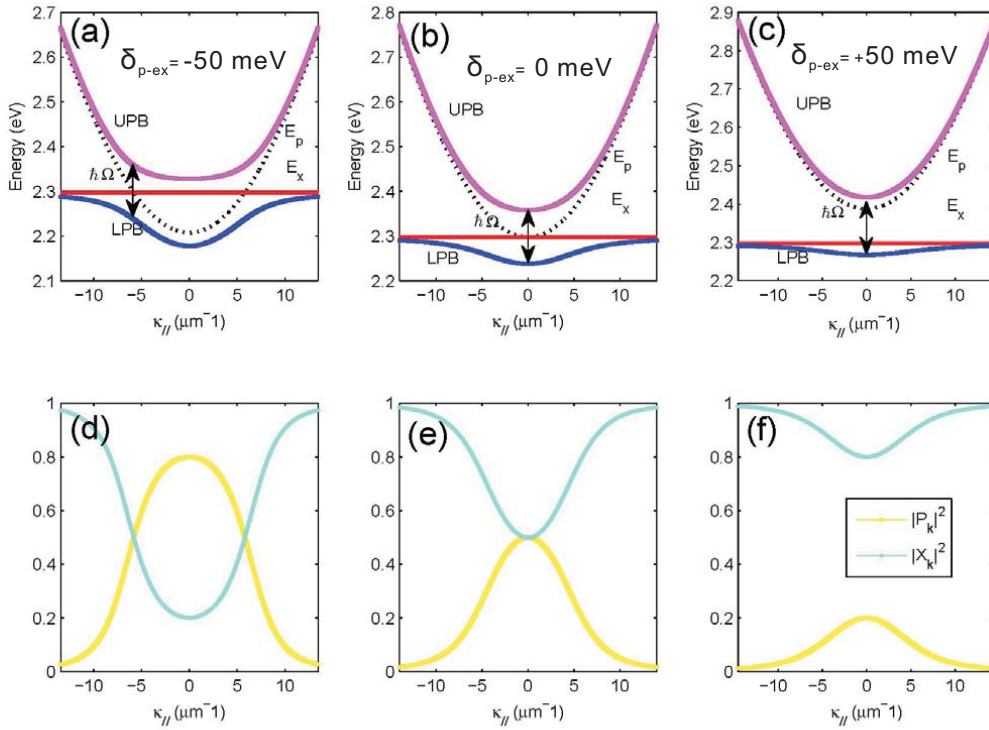
FIGURE 5.7: Dispersion curves of UPB and LPB and Hopfield coefficients for three different detunings: (a), (d) δ_{p-ex} = -50 meV; (b), (e) δ_{p-ex} = 0 meV and (c), (f) δ_{p-ex} = 50 meV.

et al. (2000) Such effects have been much discussed theoretically for the cavity polariton system. Tassone et al. (1997); Tassone and Yamamoto (1999)

The happening of bottleneck effect is largely due to the special dispersion curve shape of polaritons. In strong coupling regime, the semiconductor is optically excited at high energy, producing an amount of free electron-hole pairs. These electron-hole pairs form very quickly excitons and populate the polariton states. For a negative detuning cavity, the lower polariton is photon-like, characterized by an effective mass which is four orders of magnitude lighter than the exciton mass and by a short lifetime (1-2 ps). Kasprzak (2006) The polaritons confront decay or relaxations as soon as they are generated, there are generally three cases as described in Figure 5.8. Case (a) presents a polariton situated at an arbitrary $k_{//}$ state which decays by leaking photonic component (the leaked photon has the same energy as polariton). Case (b) shows a polariton which relaxes efficiently along the exciton-like part of the LPB by emitting optical and acoustic phonons by interacting with free carriers present in the system. And case (c) presents polariton-polariton many-body Coulomb interactions induced scattering where two polaritons with the same wave vector become one polariton with larger $k_{//}$ and the other one with smaller $k_{//}$, according to the conservation of momentum and energy.
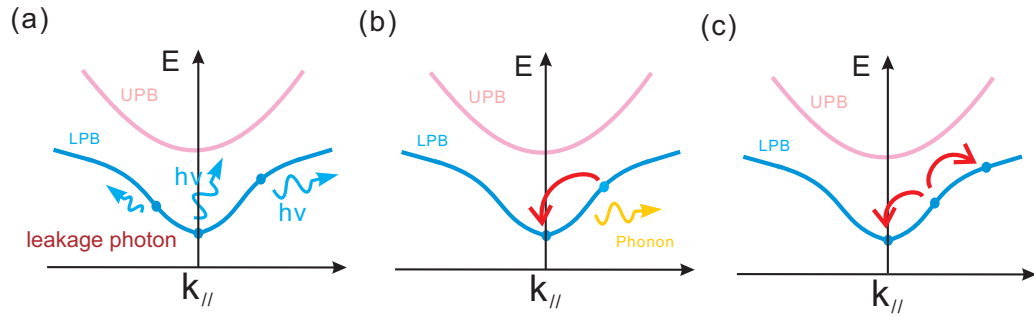
FIGURE 5.8: Schema of polariton relaxation process. (a) polaritons decay by leaking photons. (b) polaritons relax by interaction with phonons. (c) polaritons relax by polariton-polariton many-body Coulomb interactions.

The LPB has a particular dispersion law with a deep minimum at small wave vectors, a relatively flat dispersion at larger wave vectors, and a very steep curvature around anticrossing position. In order to relax to lower state, the polaritons need to transfer a large energy with small wave vector to the media. As it is not the nature of acoustic phonons who possess large wave vector and small energy of several meV, the inelastic scattering rates are weak and the energy relaxation process are therefore slow. In low pumping regime, the relaxation time in this region is much longer (a few 100 *ps*) than the radiative lifetime. The photoluminescence dynamics is governed by the balance between energy relaxation and spontaneous emission rates. As the relaxation rates are much slower than the polariton radiative emission rates, the excited polaritons can not reach the ground state at $k_{//} = 0$, but remain mainly near the inflexion point of LPB and form an incoherent reservoir of exciton-polaritons, as shown in Figure 5.9. In this case, the emissions from the higher energy states are quite broad both in energy and angle, a relaxation bottleneck thus occurs. Deveaud (2007)

5.1.3.4 Polariton laser and BEC

The Bose-Einstein Condensation (BEC) of microcavity polaritons was suggested by Imamoglu et al. in 1996, Imamoglu and Ram (1996) four years after the realization of the first microcavity working in the strong coupling regime. This idea was rather interesting as this peculiar BEC would result in coherent single mode emission without population inversion because the polaritons are mixed states of photons and excitons and they obey boson statistics. In strong coupling regime, as soon as the occupation per mode of the LPB states exceeds unity, a large population of polaritons at the bottom state $k_{//} = 0$ will be accumulated and a final-state stimulation will then be built up. Meanwhile if the thermalization processes are fast enough, the polaritons can undergo a phase transition to a BEC. It is expected this stimulated effect is very effective and large quantity of coherent polaritons are formed continually under pumping and leak out of the cavity via imperfect mirrors,La Rocca (2010) see Figure 5.10.
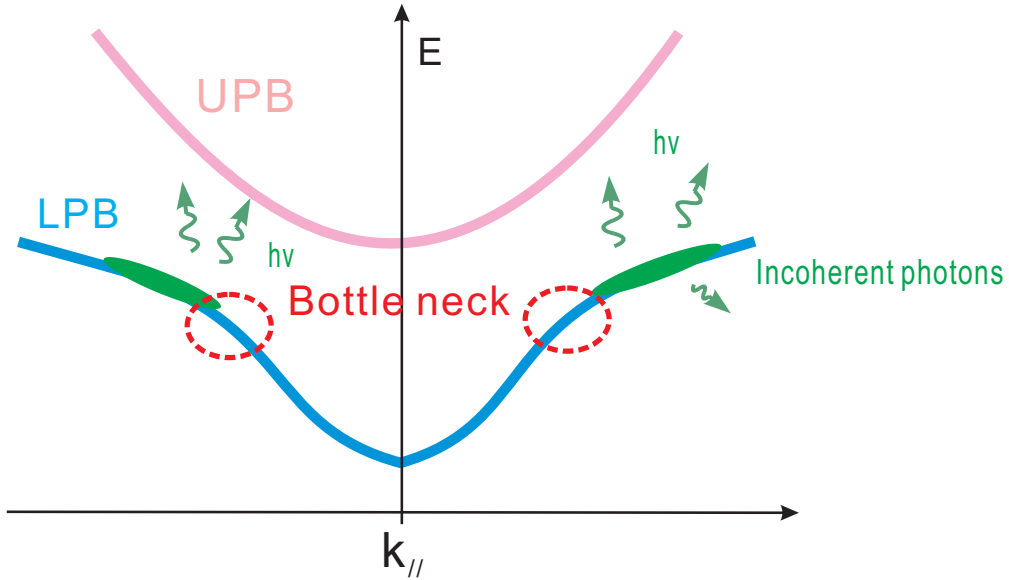
FIGURE 5.9: Schema of polariton relaxation bottleneck.
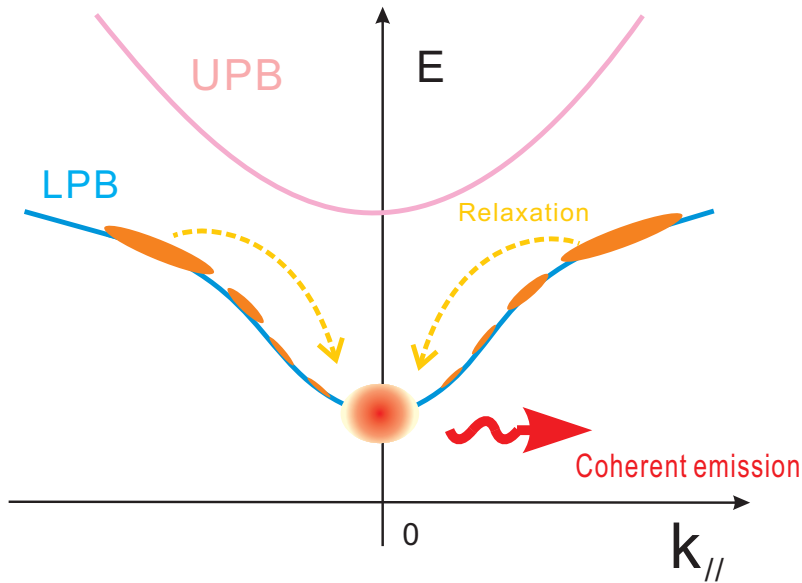
FIGURE 5.10: Schema of polariton lasing.

Compared with an atomic BEC, one striking virtue of microcavity polariton condensation is that it can occur at relatively high temperature (room temperature). We define the critical temperature as T_c, in the thermodynamic limit below which BEC occurs. For an ideal noninteracting Bose gas, the critical temperature T_c is given by Deveaud (2007)

$$k_B T_c = \frac{2\pi\hbar^2}{m}\left(\frac{n_d}{2.162}\right)^{2/3}. \tag{5.46}$$

Where the k_B is Bolzmann constant, n_d is the particles density, m is the mass of the boson. For $\delta_{p-ex} = 0$, the polaritons are partially photon-like (50 %) and exciton-like

(50 %) at $k_{//} = 0$, a polariton has an effective mass m_{pol} which is twice the photon mass. m_{pol} is four orders of magnitude lighter than the exciton mass, and seven orders of magnitude lighter than the hydrogen atom mass. Additionally, the density of polaritons is generally much higher than that of atoms. As a consequence, the critical temperature for polaritons condensation is generally eight orders of magnitude higher than that needed for atomic BECs. Deng et al. (2003)

As the temperature needed for atomic BEC is around 100 nK, it is seen that BEC can be expected at several 10 K, or even at room temperature, with semiconductor based polaritons. The problem to see BEC at room temperature is that the excitons, from which polaritons are composed, have to be stable. In GaAs structure, the exciton binding energy is around 10 meV, which is inferior to $k_BT = 26$ meV (T = 300K), so that the BEC experiments have to be performed at cryogenic temperature (several K). In II-VI semiconductors, exciton binding energy is higher, and as a matter of fact, the BEC has been seen for the first time in CdTe-based microcavities recently Dang et al. (1998). BEC is now attempted in GaN or ZnO cavities, because exciton binding energies are of the order of 30 meV in GaN, 60 meV in ZnO. The perovskite 2D layered semiconductors, with an exciton binding energy of several 100 meV, are thus good candidates for the study of stimulated effects and BEC at room temperature.

5.2   Microcavities containing perovskites

From the two recent decades of study of strong-coupling in vertical microcavities, many kinds of materials have been introduced as the excitonic active centers. For instance the inorganic semiconductor GaAs-GaAlAs Weisbuch et al. (1992), GaAs Gibbs et al. (2011), CdZnTe/ZnTe Becker et al. (1992). These inorganic semiconductors form Wannier-Mott type excitons which generally have a disadvantage: weak exciton binding energy at room temperature. This characteristic limit obstructs the study of strong light-matter interaction regime to low temperature environment and special cooling systems are required. In molecular materials, the strong coupling regime has been demonstrated recently with zinc porphyrin Lidzey et al. (1998), J-aggregates Lidzey et al. (1999), sigma-conjugated polysilane Takada et al. (2003), anthracene Kéna-Cohen et al. (2008). and in our group, many perovskites based microcavities have been successfully realized with molecules such as $(C_6H_5C_2H_4NH_3)_2PbI_4$, $(C_6H_5C_2H_4NH_3)_2PbCl_4$ Bréhier et al. (2006); Lanty et al. (2008b) and $(C_6H_9C_2H_4NH_3)_2PbI_4$ Pradeesh et al. (2009b). Strong couplings with large Rabi splittings are observed at room temperature. In these molecular materials, large exciton binding energies, of several hundreds meV, are observed, much larger than $k_BT = 26$ meV at 300 K. As a consequence, strong coupling regime exists at room temperature and due to the large oscillator strengths, large Rabi splittings are observed.

5.2.1   Experimental characterization

5.2.1.1   Fabrication of the microcavities

The microcavities we use in this thesis are constituted by a DBR mirror as the bottom mirror and a silver mirror as the upper mirror; a spin-coated perovskite layer is placed inside the cavity. PMMA can be used as a phase layer to adjust the length of cavity. The structure of DBR fabricated by Layertec company is presented in paragraph 5.1.2, See Figure 5.3(a). It consists of 6.5 pairs of two different layers with $n_H = 2.36$ and $n_L = 1.46$ alternating with each other, and a 10 nm silica deposition on the top. Before deposition, the dielectric mirrors are washed three times with solvents acetone, ethanol and isopropanol, in this order, in ultrasonic bath. These mirrors are then immersed in KOH in ethanol solution for surface treatment in order to facilitate the deposition of perovskites layers in the next step. Thicknesses of perovskites and PMMA layers are generally controlled by solution concentration and parameters of deposition (spin-coating speed and duration of rotation). The silver mirror is deposited by thermal evaporation method. The evaporator equipped in LPQM is a Auto 306 type of $Edwards^{TM}$ company. The pressure in chamber is lowered under 2.0×10^{-5} mba during deposition, the speed of deposition is controlled to be about 0.1 nm/s, a silver layer of about 30 nm thick is formed in about several minutes.

5.2.1.2   Angle resolved reflectivity experiment

Angle resolved reflectivity measurement is frequently used as a tool to examine the light-matter interaction regime inside the cavity. The reflectivity is defined as the ratio between the amplitudes of incident light and the outgoing light reflected from the surface of the cavity. For our microcavity samples whose cavity mirrors are a DBR at one side and a silver mirror at the other side, we generally measure reflectivity from the semi-transparent silver side because very few photons can enter into the cavity from the DBR side (too weak signal is then obtained). The experiment setup is shown in Figure 5.11.

The light source is a Xenon lamp with broad white light emission from 280 nm to 780 nm. Its output light is filtered by a monochromator and is collimated by a f = 50.2 mm focusing lens. Similarly to the experimental principle of OA measurement introduced in chapter 2.2.4.1, the PMT2 is firstly placed to acquire the intensity of the incident light $I_{s0}(\lambda)$ without placing sample and the reference signal is recorded as $I_{r0}(\lambda)$ by PMT1. Then, the cavity sample is fixed in the center of a rotating plate with the silver mirror side facing to incident light and the PMT2 is moved to the corresponding 2θ direction to collect the reflected beam from cavity sample. The signal of the two PMTs are recorded in this configuration as $I_{r1}(\lambda)$ and $I_{s1}(\lambda)$. A polarizer can be introduced on the incident light path for polarization dependent reflectivity measurement. The incident angle is
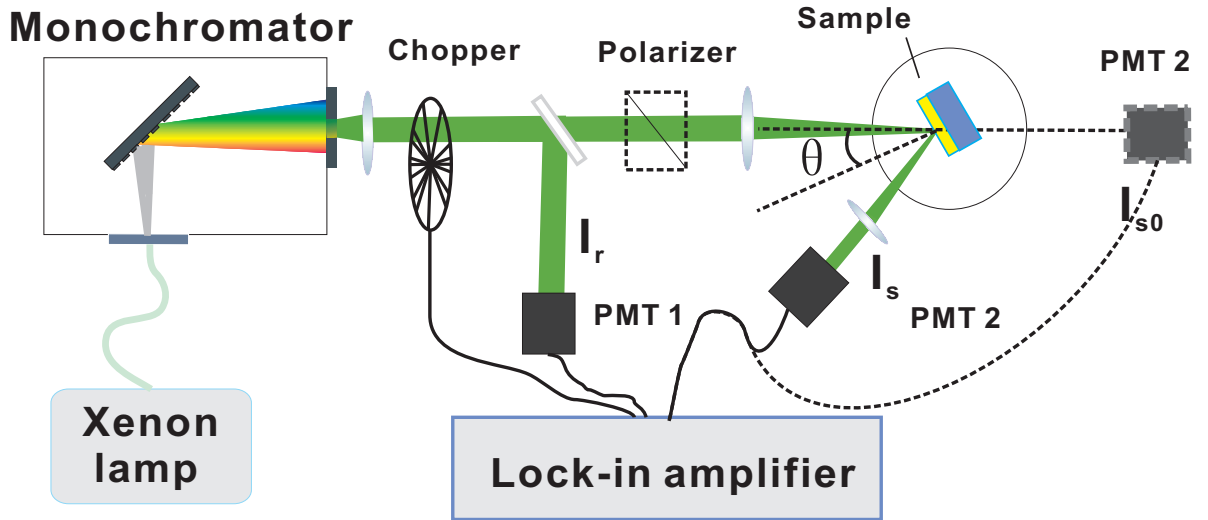
FIGURE 5.11: Schema of the angle resolved reflectivity experimental set-up.

varied by rotating the plate, and positions of PMT2 are accordingly adjusted to collect the reflection signal. The reflectivity signal R is then given by:

$$R(\lambda) = \frac{I_{s1}}{I_{s0}} \frac{I_{r0}}{I_{r1}}. \tag{5.47}$$

In the strong coupling regime, two dips appear in reflectivity curves at each detection angle, these dips correspond to the lower polariton and the higher polariton. To interpret these data, energy positions of dips are extracted and reported on a dispersion graph as a function of detection angle. A fitting of the experimental dispersion curves using the two-levels model is then realized. Effective index, length of cavity, Rabi splitting, and exciton energy are the fit parameters. This method will be used to interpret the experimental results obtained on PEPI and 4FPEPI based cavities in the following paragraphs.

5.2.1.3 Angle resolved photoluminescence experiment

Strong coupling regime in a microcavity can also be characterized by angle-resolved photoluminescence experiment. It is because the emission of a photon preserves the same energy and in-plane wave vector as a polariton. This one to one correspondence relationship enables us to study polaritons indirectly by detecting the information carried by photons leaked out of cavity. Besides, the intensity of photon emission is proportional to the instantaneous polariton population. Equally the quantum statistical properties of the emission replicate those of the polaritons, which will allow us to study the bottleneck effect concerning the population distribution of polaritons along their dispersion curve.

The experimental configuration of angle-resolved photoluminescence experiment is shown in Figure 5.12. Light beam from a continuous wave laser (usually the 405 nm
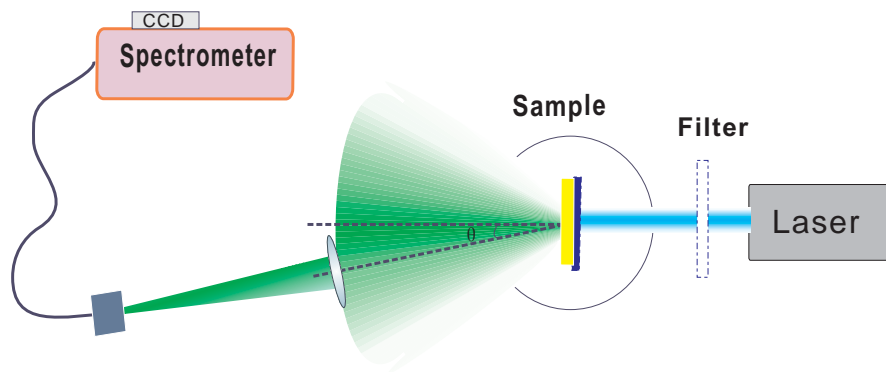
FIGURE 5.12: Schema of angle resolved photoluminescence experimental set-up.

resonance line of a diode laser or the 325 nm line of a HeCd laser) is collimated and arrives perpendicularly to the surface of cavity mirror, incident light enters from the DBR side. An optical intensity filter is placed before cavity sample to vary the intensity of incident light. Photoluminescence signal emitted from cavity sample through the silver mirror is then collected at different detection angles θ and analyzed with a spectrometer followed by a CCD camera.

5.2.2   PEPI based microcavity

a) Design and preparation

The PEPI $\lambda/2$ cavity is the most basic cavity we fabricate. It was firstly made by Antoine Bréhier in 2005 and we call it "standard cavity". It consists of two layers between a silver mirror and a DBR mirror: a PEPI 50 nm layer and a PMMA layer. Its structure is sketched in Figure 5.13.
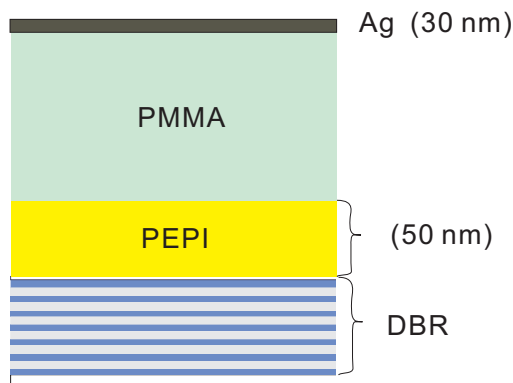
FIGURE 5.13: Schema of structure of a "standard cavity" PEPI microcavity.

The PMMA layer, which works as a transparent spacer in cavity, is used to tune the length of the cavity and thus the energy of the photon mode existing in cavity. The

behavior of the fundamental photon mode as a function of detection angle is simulated by transfer matrix method: Figure 5.14. Thickness of the PEPI layer is 50 nm, the thickness the silver mirror is about 30 nm, a normal incidence is considered. The PEPI
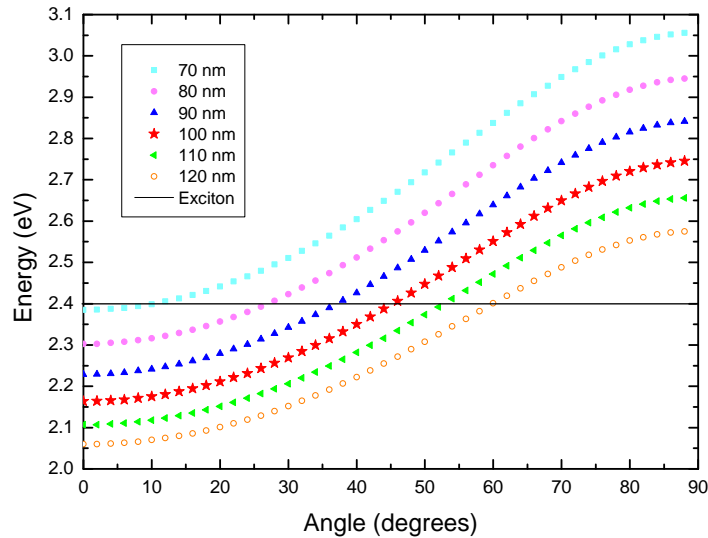
FIGURE 5.14: Simulation of the fundamental photon mode in a PEPI microcavity. PEPI layer is fixed to be 50 nm and the silver mirror is 30 nm. The curves in different colors correspond to different thicknesses of PMMA layer.

active material absorbs at 516 nm thus the exciton energy is fixed to be 2.4 eV as the black solid line. We see that, to obtain a resonance $E_p = E_{ex}$ at a detection angle of 45°, a suitable thickness for the PMMA layer is about 100 nm. The PEPI layer of 50 nm is deposited from a 10 wt% PEPI in DMF solution and the spin-coating parameters are set to be 3000 rmp for 60 s which is a little bit different from those used on quartz substrate. A 100 nm PMMA layer, which is deposited from a 4wt% PMMA in toluene solution, is then applied upon PEPI layer: the PMMA parameters of spin-coating are 2200 rmp for 40 s with gyset and the annealing condition is 95°C for 20 min. Here we use toluene as solvent because perovskites are not soluble in it, so that the PEPI layer will not be destroyed by deposition of PMMA.

The figure 5.15 presents the distribution of electric field in a standard microcavity where the thickness of PMMA layer is 100 nm. We see that the electric field node is located in the PEPI layer. Therefore this microcavity will not satisfy an optimal coupling between the excitons of PEPI and the cavity mode. This drawback can be remedied by introducing a PMMA spacer between the PEPI layer and the DBR mirror in order to displace the PEPI layer to the right position, where there is the maximal amplitude of electric field. Lanty et al. (2008a)
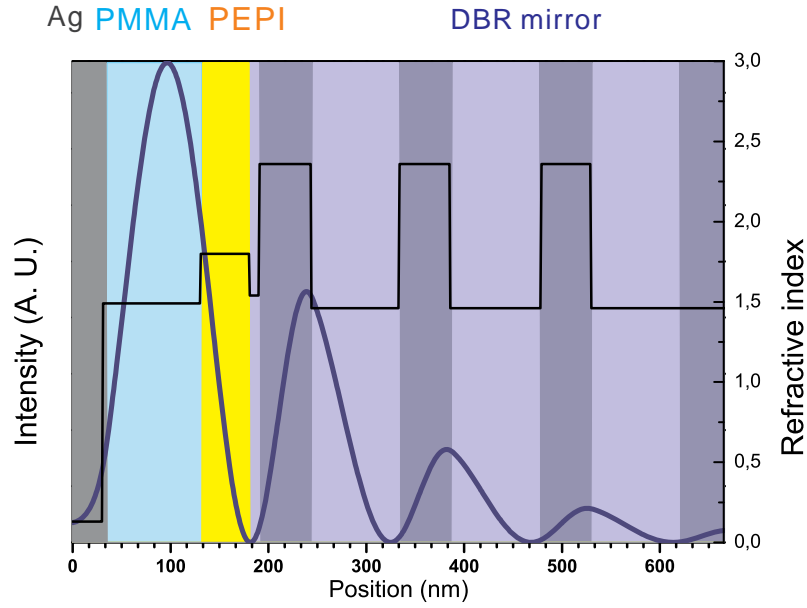
FIGURE 5.15: Profile of the electric field for the cavity mode energy 2.4 eV (blue line). The black curve presents the refractive index of the layers.

b) Optical characterization

Angle resolved reflectivity spectra for the cavity are measured at room temperature for detection angles ranging from 10º to 70º. Varying the angle of detection θ relative to the surface normal axis allows to tune the relative energy separation between the active layer exciton energy (considered as dispersionless and so angle-independant) and the cavity photon mode energy, which is related to θ by Formula 5.17: $E_p(\theta) = \frac{E_0}{\sqrt{1-(\frac{\sin\theta}{n_{eff}})^2}}$ where E_0 is the photon mode at normal incidence ($\theta = 0$) and n_{eff} is the effective refractive index of the entire cavity. As shown in Figure 5.16(a) two dips appear in each curve and their depths and positions change with angle. A clear anticrossing between the two transitions is observed. For low incidence angles, the lower energy minimum is the stronger one. As the angle increases, the intensity of the low energy dip progressively decreases whereas the intensity of the high energy one increases. Around 30 º, both transitions have the same intensity with an energy separation of 170 meV. For angles superior to 30º, the upper energy dip becomes the stronger one, while the lower energy dip intensity decreases. We extract the dip energy positions from figure 5.16(a) and report them in Figure 5.16(b) as a function of $k_{//}$, ($k_{//} = (E/hc)sin\theta$, Formula 5.16). A two level model (Formula 5.41 and 5.40) is used to fit these experimental results. We get the following fitting parameters: $n_{eff} = 1.97$ [1], $E_{ex} = 2.4\ eV$, $L = 139.66\ nm$, and Rabi splitting $\hbar\Omega = 172\ meV$. The obtained value of E_{ex} corresponds well with

---

[1] n_{eff} is a fitting value which represents the average effective refractive index of the microcavity.

the absorption energy of the PEPI exciton. n_{eff} is found to be superior to the PMMA index, due to the presence of the PEPI active layer which has a larger refractive index than that of PMMA and L has a convenient order of magnitude regarding the deposition parameters. We conclude that the strong coupling regime occurs in this microcavity and that the two dips result from the lower and upper polaritons.
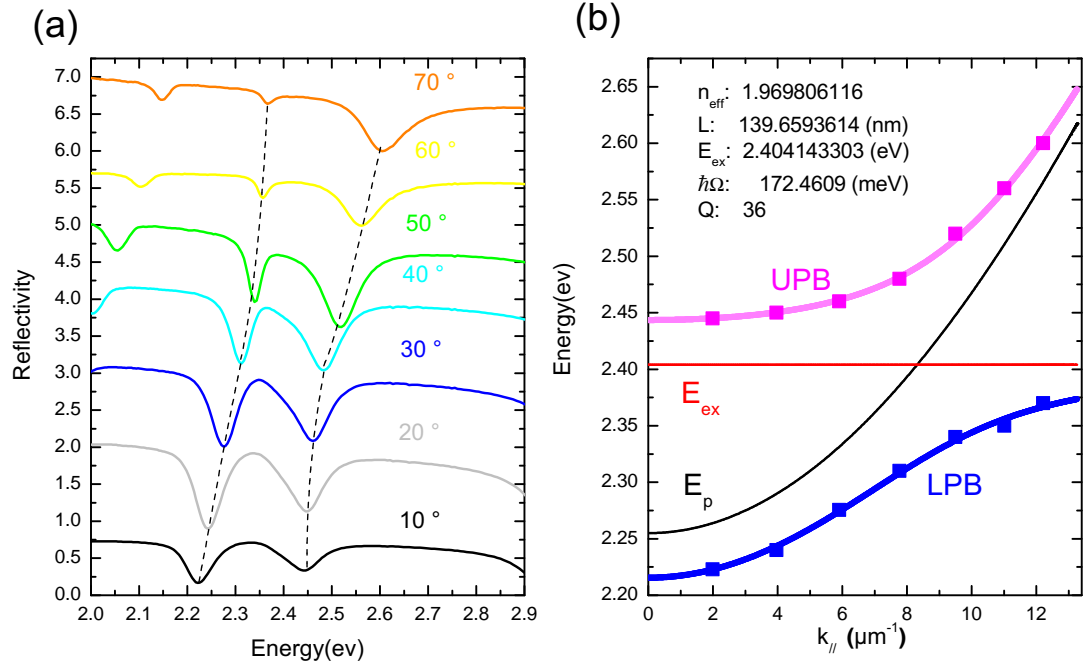
FIGURE 5.16: (a) Reflectivity spectra and (b) dispersion curve of a PEPI cavity with anticrossing around $k_{//}$= 8.3 μm^{-1} (detuning δ_{p-ex} = -147 meV). The dashed line across dips in (a) are guides for the eyes and the reflectivity curves are displaced along y axis for clarity

By changing the thickness of the PMMA layer, variation of detuning factor δ_{p-ex} can be achieved in these PEPI microcavities. Figure 5.17 and 5.18 show two cavities with anticrossing at $k_{//}$= 0 μm^{-1} (δ_{p-ex} = 0 meV) and $k_{//}$= 10.7 μ m^{-1} (δ_{p-ex} = -298 meV). Their PMMA layers are around 68 nm and 120 nm, they have been deposited with 3.5 wt% and 4.2 wt% PMMA in toluene solution respectively.

The quality factor Q of the cavities can be roughly estimated from the LPB dip in reflectivity spectra of negative detuning cavities since the LPBs are more photon-like at low angles: Q = 36 for the cavity of Figure 5.16, Q = 32 for the cavity of Figure 5.18.

Angle resolved PL spectra are measured at room temperature excited by the 325 nm line of a HeCd laser of 0.5 mW: see Figure 5.19. The energy position peaks of the lower energy PL peaks correspond well to the fitting dispersion curve of LPB in Figure 5.18(b) where the PL peak positions are signified with blue star symbols. The peak located at 2.37 eV is independent of detection angle and it is regarded to be photoluminescence of the non-coupled exciton of PEPI layer. This luminescence leaks out from the microcavity as a

(a)

(b)
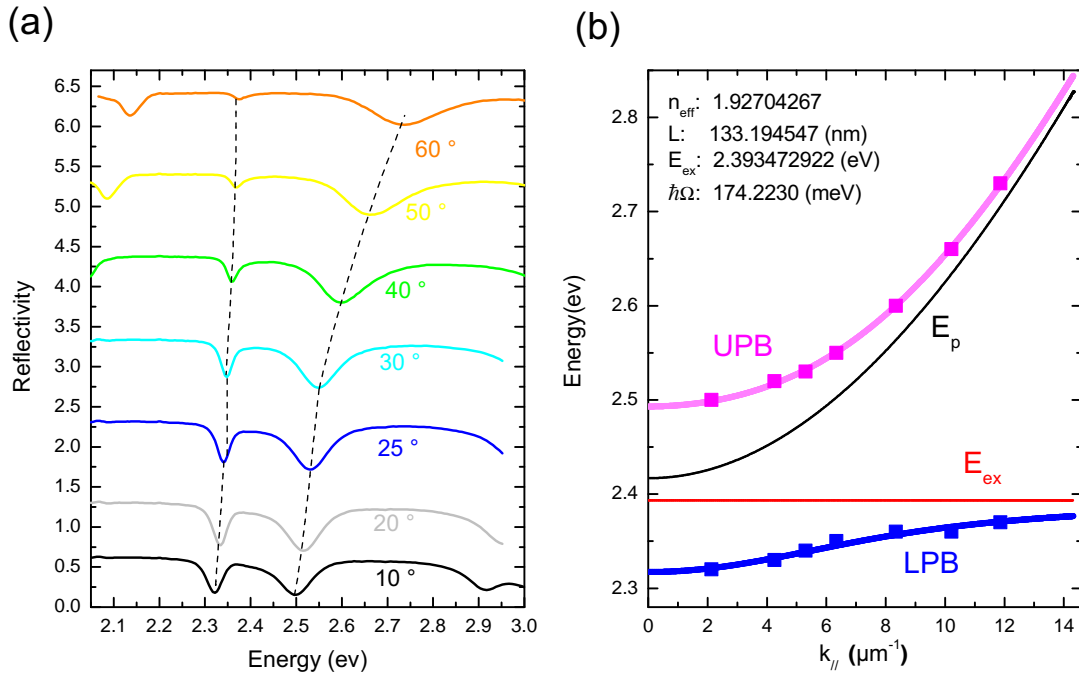
FIGURE 5.17: (a) Reflectivity and (b) dispersion curve of a PEPI cavity with anticrossing around $k_{//} = 0$ μm^{-1} (detuning $\delta_{p-ex} = 0$ meV). The dashed line across dips in (a) are guides of eyes and the reflectivity curves are displaced along y axis for clarity

(a)

(b)
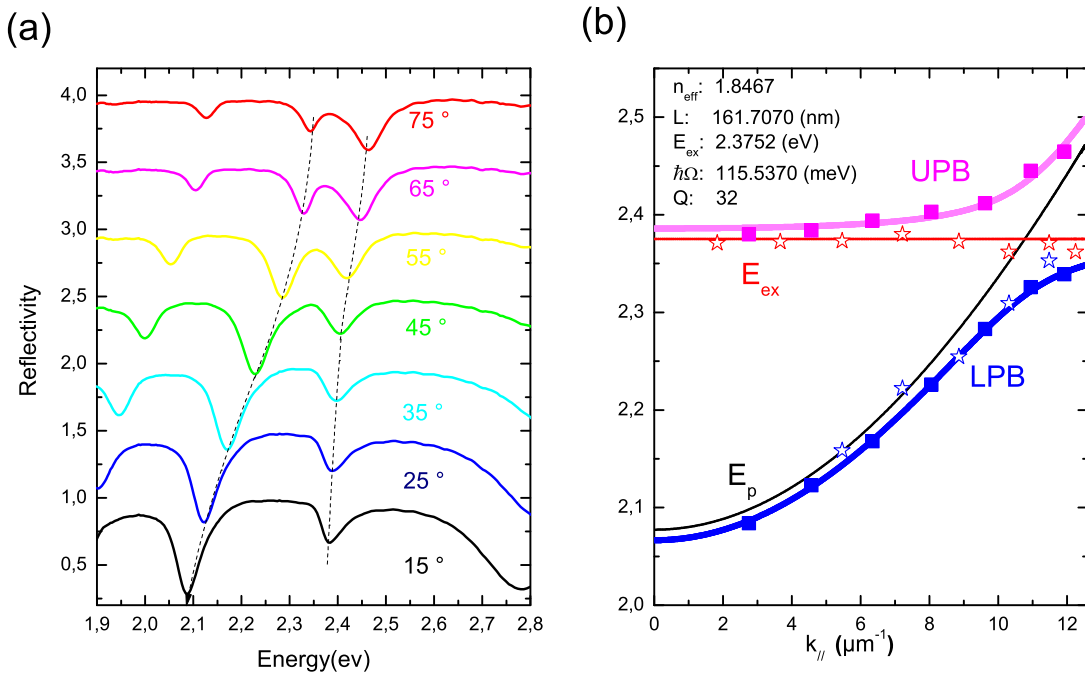
FIGURE 5.18: (a) Reflectivity and (b) dispersion curve of a PEPI cavity with anticrossing around $k_{//} = 10.7$ μm^{-1} (detuning $\delta_{p-ex} = $ - 298 meV). The dashed line across dips in (a) are guides of eyes and the reflectivity curves are displaced along y axis for clarity. The stars correspond to PL peak positions from angle resolved PL measurements of Figure 5.19.

result of imperfect cavity mirror and bad quality factor. The absence of the UPB emission has been suggested to be due to the quick relaxation towards uncoupled excitonic states. Agranovich et al. (2003)
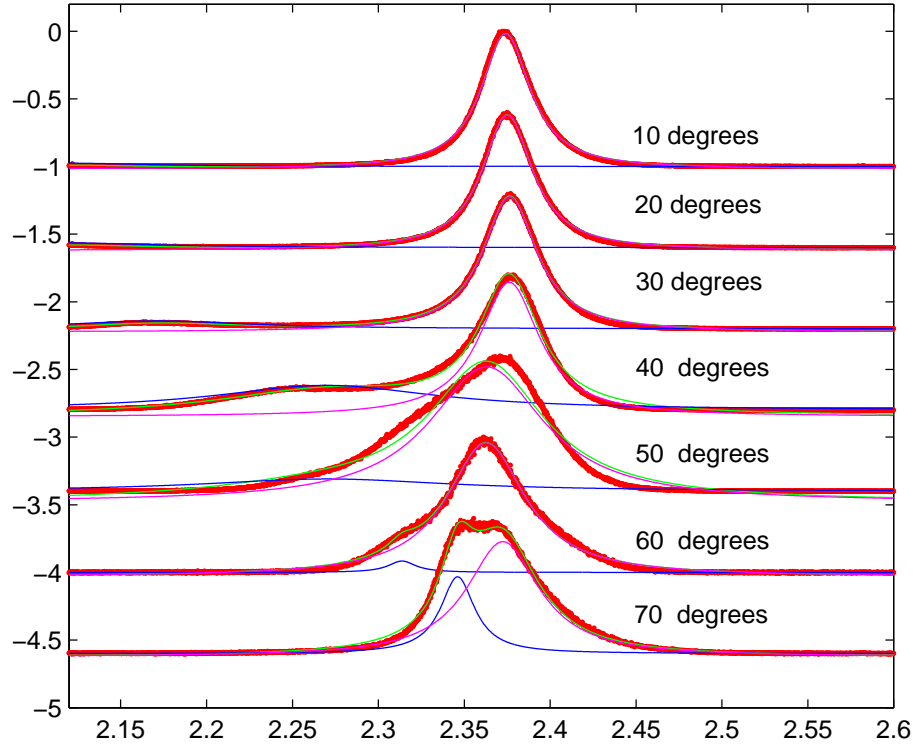
FIGURE 5.19: Angle resolved PL spectra of the PEPI standard cavity of Figure 5.18. The excitation source is the 325 nm line of a HeCd laser at 0.5 mW. PL intensities are normalized to 1, each PL curve is fitted by two lorentzian peaks (in magenta and blue); and the green curve is the sum of the two lorentzian peaks.

From angle resolved PL measurements, we can study the degree of thermalization of the polaritonic states in $k_{//}$ space. Müller et al. (2000) The intensity of the lower polaritonPL peak $I_{pl}(\theta)$ that we capture in experiment is an integration of the number of photons emitted under the angle θ during exposure time, it is therefore a value proportional to the time-averaged polariton population $n_{k_{//}}$: Tartakovskii et al. (2000)

$$n_{k_{//}} = I_{pl}(\theta) \cdot \tau_{rad}.$$

(5.48)

where $1/\tau_{rad}$ is the radiative rate. $1/\tau_{rad}$ depends on τ_{esc}, the time that photons escape through the mirrors (typically 1 ps, for our quality factor) and on photonic weight $|P_k|^2$:

$$\frac{1}{\tau_{rad}} = \frac{|P_k|^2}{\tau_{esc}}.$$

(5.49)

Then we have polariton population:

$$n_{k_{//}} = \tau_{esc}\frac{I_{pl}(\theta)}{|P_k|^2}. \tag{5.50}$$

To determine $I_{pl}(\theta)$, the intensity of the lower energy polariton emission, we need to deconvoluate the PL spectra, as we have seen that the emission of the uncoupled perovskite is close to the lower energy polariton emission. The process of this deconvolution is shown in Figure 5.19. From the fit of the dispersion curve which provides the fitting parameters to calculate $|P_k|^2$ and from the values of $I_{pl}(\theta)$ determined from deconvolution of the PL spectra, we are able to calculate the values of $I_{pl}/|P_k|^2$ as a function of $k_{//}$.

Figure 5.20 (b) shows the polariton population calculated by G. Lanty Lanty et al. (2008a) for an optimized PEPI cavity (in which the electric field is maximum under the PEPI layer): the values of $I_{pl}(\theta)$ are obtained from Figure 5.20 (a). The maximum value of $I_{pl}/|P_k|^2$ is 5 times larger at 8.5 μm^{-1} than the value at 0 μm^{-1}. We conclude that it exists a relaxation bottleneck effect in this study.

5.2.3   4FPEPI based microcavity

In previous section, we have studied standard PEPI based microcavities. The trials on these cavities provide us a technical protocol to refer as well as an experimental experience for following studies. However, there are still two difficulties to overcome in PEPI contained microcavities. Firstly, due to the too large roughness of the spin-coated perovskite layers, see Figure 2.2, 3.10 and 2.21, the improvement of the quality factor by monolithic deposition of a dielectric mirror directly on the perovskite layer, is impossible. Secondly, although better than organic materials regarding the photo-stability, the perovskite emission decreases with time under laser illumination. In chapter 4, we have identified a new material, presenting better photostability and roughness: 4FPEPI doped PMMA. So here, we will perform some microcavities containing this new material .

a) Design and preparation

The 4FPEPI based microcavity structure is shown in Figure 5.21. The 4FPEPI doped PMMA layer embedded between the two mirrors is about 350 nm, it is prepared by spin-coating a 4FPEPI-PMMA mixed DMF solution: the weight ratio of 4FPEPI and PMMA is 1:5 and the concentration of PMMA in DMF is 10% in weight. The thin layer has been annealed at 150 ºC during 30 minutes after being deposited by spin coating at a speed of 2000 rpm for 30 s. The topological properties of this layer are shown in Figure
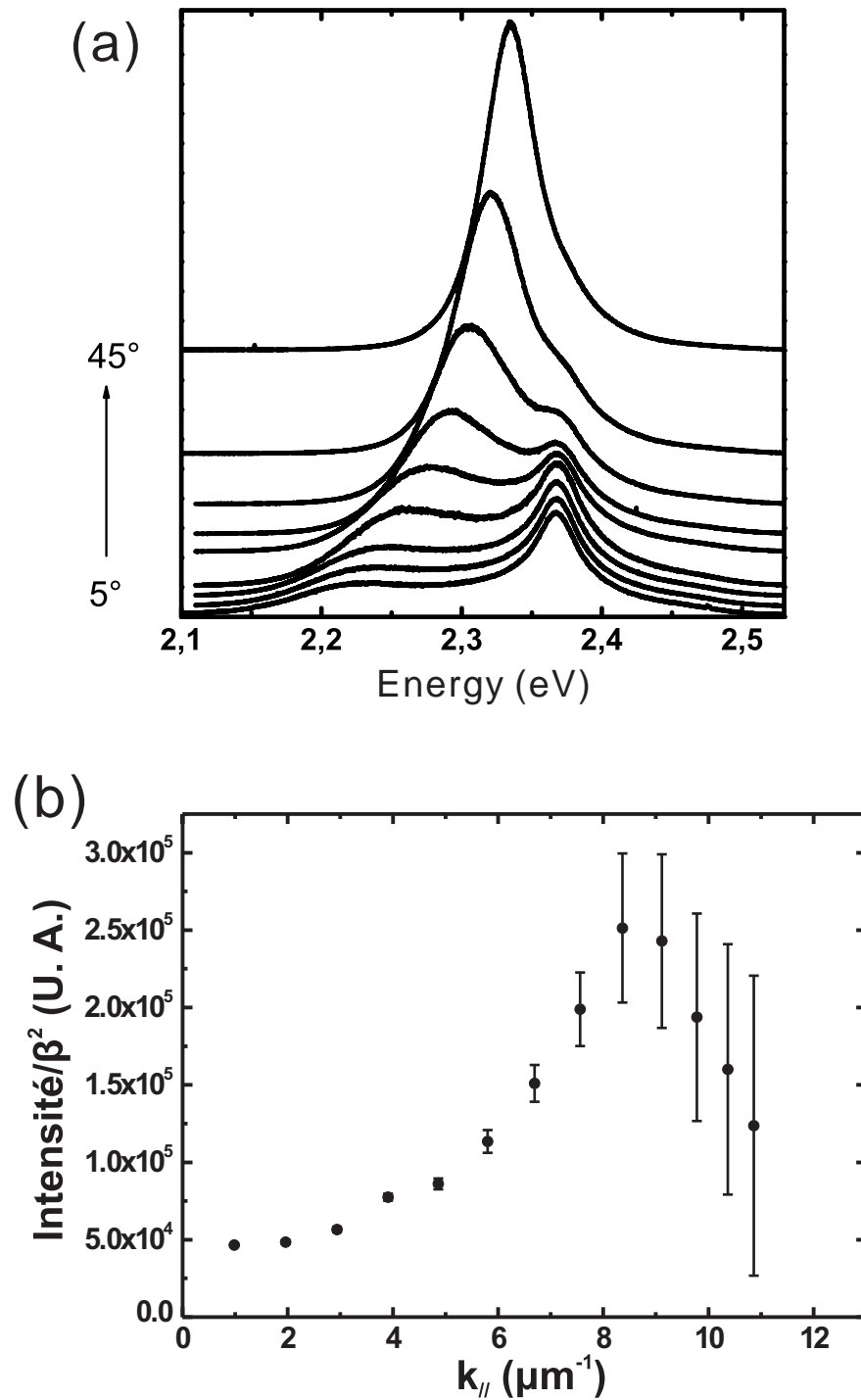
FIGURE 5.20: (a) Angle resolved PL spectra of PEPI standard cavity. The excitation source is a 405 nm diode laser. (b) Value of $I_{pl}/|P_k|^2$ as a function of $k_{//}$. The uncertainty of the PL integrated values I_{pl} have been marked as vertical errors in graph

5.22(b) where it is found that the roughness is rather small: $\Delta = 0.86$ nm compared with $\Delta = 10.55$ nm for a PEPI 50 nm layer, see Figure 5.22(a). As a consequence, we
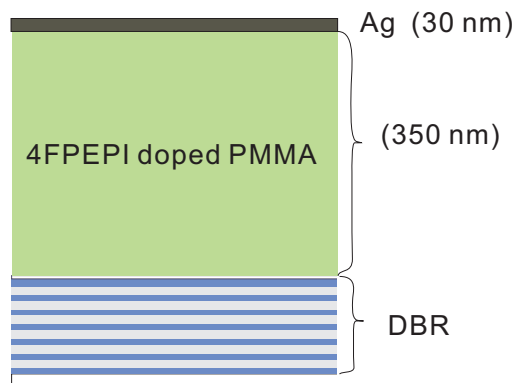
FIGURE 5.21: Schema of structure of a 4FPEPI doped PMMA microcavity.

can conclude that this method of deposition allows to improve the roughness by a factor of ten.
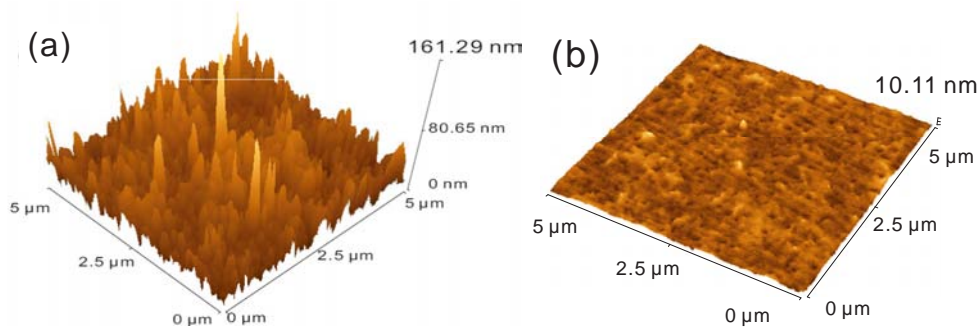
FIGURE 5.22: AFM images of (a) a 50 nm PEPI layer and (b) a 350 nm 4FPEPI doped PMMA layer.

The refractive index n of the 4FPEPI doped PMMA layer has been measured by spectroscopic ellipsometry measurement (Sopra Model GESP5): n = 1.654. With this 350 nm layer we thus realize a λ-cavity. The silver mirror is kept around 30 nm and the DBR mirror is the same as that of PEPI microcavity. The distribution of electric field is simulated by the transfer matrix method and results are presented in Figure 5.23. We see that the active 4FPEPI doped PMMA layer fully fills the cavity and that electric field experiences two maxima on this layer.

b) Optical characterization

(I) Perovskites layers

Let us remind the optical properties of PEPI spin-coated and 4FPEPI doped PMMA layers. Figures 5.24 shows the comparison of optical properties for the 4FPEPI doped PMMA layer used in microcavity and a 50 nm thin PEPI layer prepared in the same
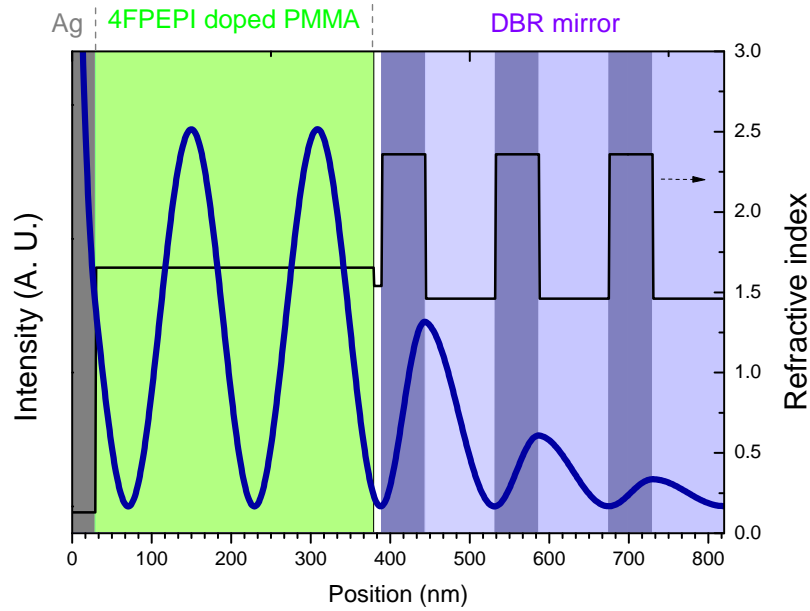
FIGURE 5.23: Profile of the electric field for the cavity mode energy 2.4 eV (blue line). The black line presents the refractive index of the layers.

conditions as in PEPI standard cavities: a 10wt% solution of PEPI dissolved in DMF is deposited by spin-coating on a quartz substrate at a speed of 2000 rpm for 30 s, and is annealed at 95 °C during 1 minute. As seen in Figure 5.24(a), this 50 nm PEPI thin layer absorbs at 2.39 eV and emits at 2.368 eV. For 4FPEPI doped PMMA layer in Figure 5.24(b), the maxima of the absorption and photoluminescence peaks of 4FPEPI doped PMMA lie at 2.386 eV and 2.357 eV respectively, that is to say practically at the same energies as PEPI spin-coated layers. The Full Width at Half Maximum of the PEPI and 4FPEPI doped PMMA peaks are quite similar. Figure 5.24(c) shows the behavior as a function of time of the integrated PL intensity of PEPI and 4FPEPI doped PMMA layer, under a HeCd laser illumination of 7.4 mW at 325 nm: it can be noticed that 99 % of the PL intensity is lost after 100 minutes for PEPI. This problem can be a critical drawback for experiments involving some non-linear effects and so requiring strong incident power. By contrast, 4FPEPI doped PMMA layer is further improved: after 100 min, 60% of the PL signal remains.

(II) Microcavity

Angle-resolved reflectivity measurements of the microcavity are performed using a xenon lamp as the excitation source, between the angles 0 ° and 65 °, at room temperature. Figure 5.25 shows a series of reflectivity spectra at room temperature. Two dips, whose energy position, intensity and linewidth are angle dependent, are observed. A clear anticrossing between the two transitions can be seen, which is the signature of
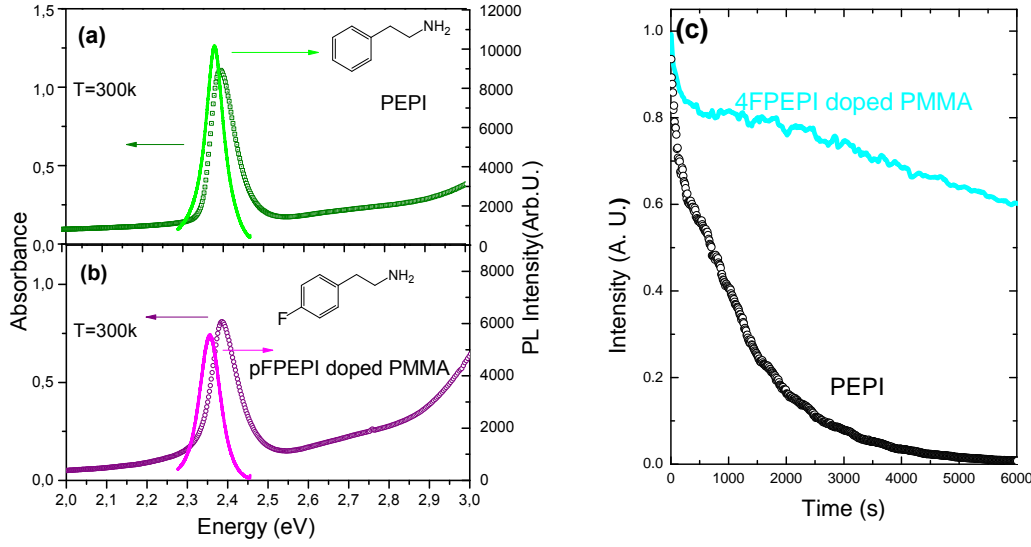
FIGURE 5.24: Optical density (scatters) and photoluminescences spectra (solid lines), at T = 300 K, of (a) a 50 nm PEPI thin layer , (b) a 1 μm 4FPEPI doped PMMA thin layer.(c) Photobleaching of 4FPEPI doped PMMA and PEPI thin layers under the laser HeCd 325nm for 6000 s.

the strong coupling between the active layer exciton and the cavity mode. The energy of the two minima observed in Figure 5.25 are reported in Figure 5.26 as a function of $k_{//}$, $k_{//} = (E/hc)sin\theta$. The experimental results are fitted using a standard two-level model (solid blue and magenta lines in Figure 5.26) with formula 5.40 and 5.41.

A good agreement between the experimental results and the two level model is obtained for E_{ex}=2.38 eV, $n_{eff} = 1.624$, $\hbar\Omega = 89.6$ meV, $L = 350.3$ nm and the quality factor estimated from reflectivity measurement is about 36. The value of n_{eff} obtained from the fit is quite coherent with the value of the refractive index of 4FPEPI doped PMMA obtained from spectroscopic ellipsometry measurements. This Rabi splitting is slightly smaller than that the Rabi splitting obtained with the spin-coated PEPI layer of the previous paragraph, which is coherent with the fact that in this new cavity, the perovskite nanosized inclusions are dispersed along the whole cavity.

Photoluminescence spectra have been performed for various detection angles, ranging from 0 $^\circ$to 60 $^\circ$, they are reported in Figure 5.27. The energy positions of the photoluminescence peaks have been reported as stars in Figure 5.26. For angles up to 35 $^\circ$, two peaks are present in the spectra. As for the PEPI cavity, the position of the high energy peak is independent of the detection angle, whereas the position of the lower energy peak varies as the detection angle is tuned. The dispersionless data correspond to the exciton of the non-coupled perovskite, since the energy position of this peak corresponds to the energy position of the photoluminescence of the active layer, see Figure
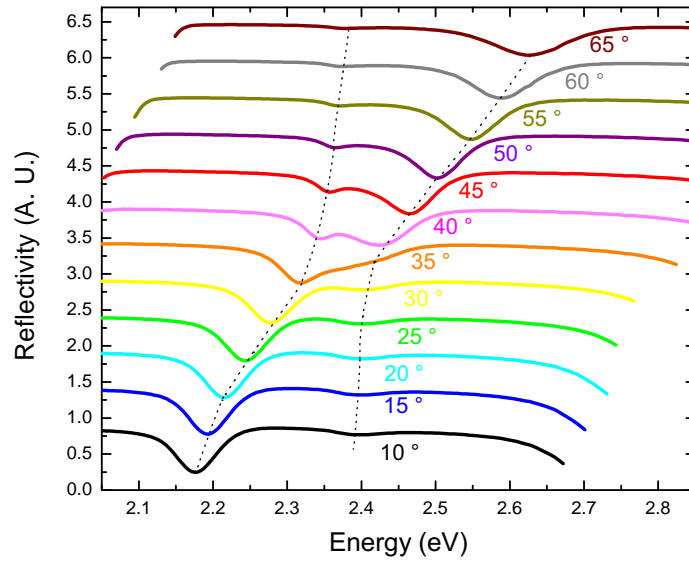
FIGURE 5.25: Reflectivity spectra of 4FPEPI doped PMMA cavity, for different angles of incidence. The dotted lines are guides to eyes. The quality factor is estimated to be about 36.
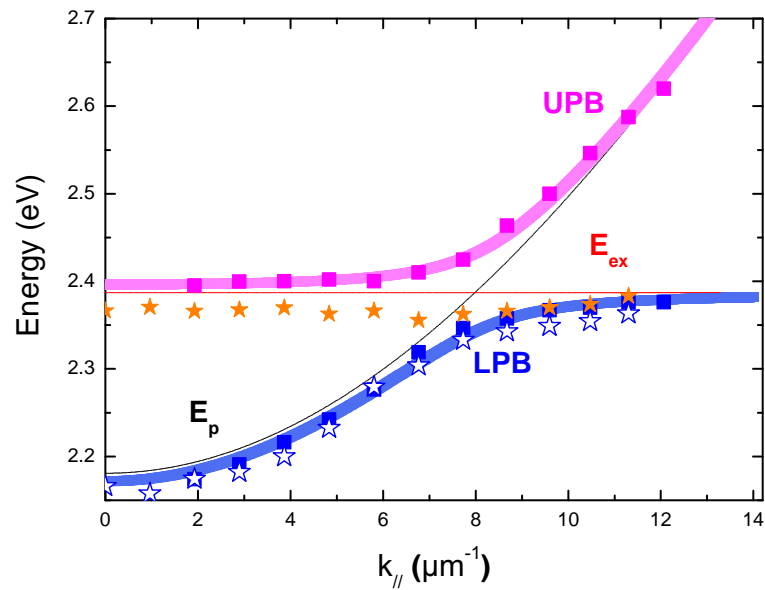
FIGURE 5.26: Polariton dispersion (LPB and UPB) measured from reflectivity spectra of Figure 5.25. Uncoupled perovskite exciton E_{ex} and cavity photon E_p are also shown. The stars represent the energy position of the PL peaks observed in Figure 5.27.

5.24(b). The variation of the position of the low energy PL peak as a function of $k_{//}$ coincides with the dispersion relation of the low energy polaritonic branch.
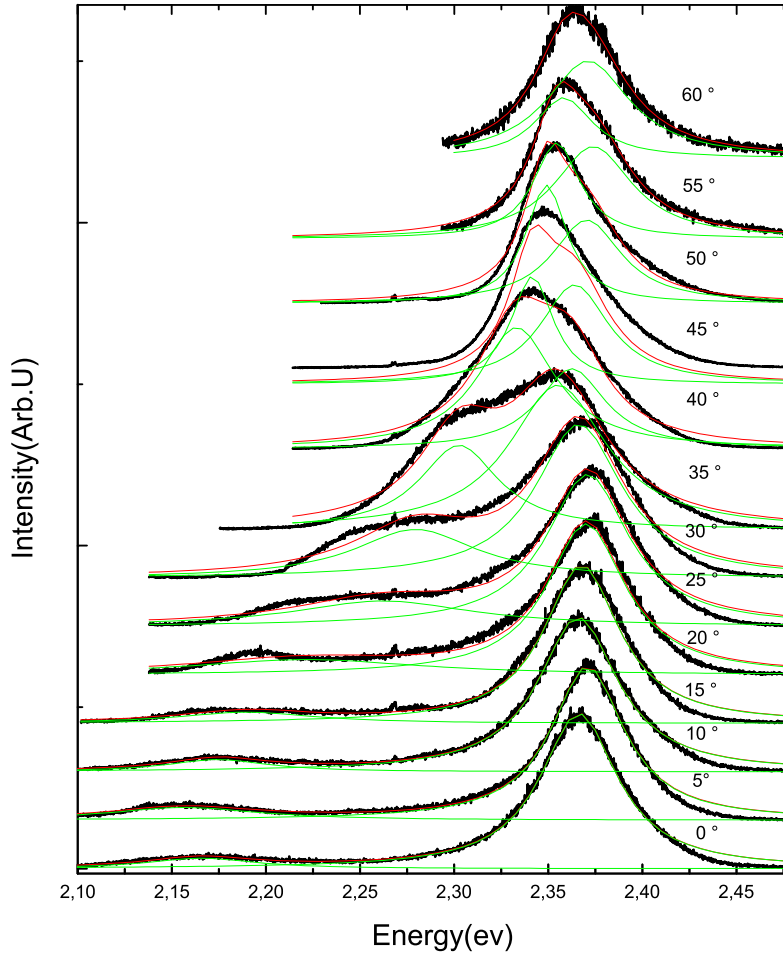
FIGURE 5.27:   PL spectra of 4FPEPI doped PMMA cavity. PL signals are detected
from 0º to 60º. Each PL curve is fitted by two lorentzian peaks(in green), and the red
curve is a sum of the two lorentzian peaks.

From the PL results, we further study the polariton population. The $|P_k|^2$ values
are obtained from formula 5.44 by using the fitting values L, n_{eff}, $\hbar\Omega$, and E_{ex}. I_{pl} is an
integration of fitted lorentzian deconvolution peak of LPB in Figure 5.27. From Figure
5.28, it is clear that largest values of polariton population along LPB don't appear at
$k_{//} = 0$. The maximum value is obtained for $k_{//} = 9.59~\mu m^{-1}$ (detection angle at 50 º),
where the polariton population is about 19 times larger than that at $k_{//} = 0~\mu m^{-1}$. In
this cavity also, a bottleneck effect is then observed.
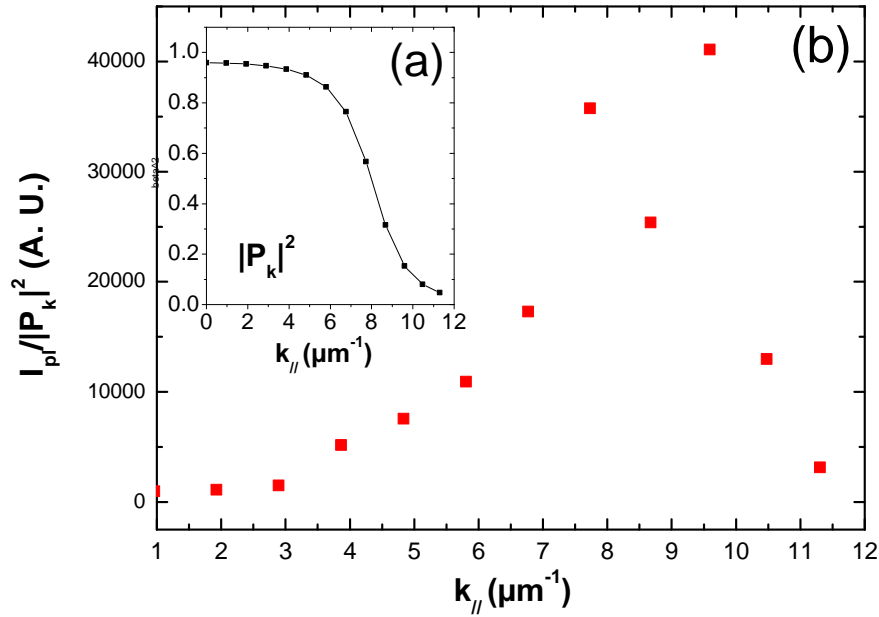
FIGURE 5.28: (a) Photonic weight $|P_k|^2$ and (b)Value of $I_{pl}/|P_k|^2$ as a function of $k_{//}$.

5.3 Conclusion

In this chapter, we have presented some basic principles and phenomena which happen in cavities presenting a photon-exciton strong coupling regime. The polaritons are quasi particles possessing a photon part and an exciton part, they have the nature of bosons and possess light effective mass. Some methods to design and characterize microcavities have been introduced. Angle resolved reflectivity and PL measurements are very useful tools to probe polariton states inside cavity, as the photon which we detect carries information about the polariton. Two microcavities have been realized: a PEPI $\lambda/2$-cavity and a 4FPEPI doped PMMA λ-cavity. Both cavities exhibit the strong-coupling regime at room temperature, and a bottleneck effect has been observed on the lower polariton branch of the two cavities.

Conclusions

The electronic industry has been developed constantly since 1950s, from the initial inorganic materials to the organic materials. The exigence of new functional materials with easy processing and less expensive manufacture cost has always been pursued and call for efforts of researchers. Organic-inorganic hybrid perovskites which combine the properties of organic and inorganic semiconductors, are hopeful candidates for future opto-electronic devices. The exciton binding energies and oscillator strengths are very large in these systems making the applications at room temperature possible. Whereas, as a relatively new material, the perovskites still have many behaviors that are not well understood and a lot of research work is necessary. In this thesis, the main aim of this research work concerns the study of the optical properties of perovskites and their use as active material in microcavities working in the strong coupling regime.

We have synthesized plenty of perovskites with conventional and new organic cations. We have investigated the molecular structure related factors that may influence the optical properties. Meanwhile, we have exploited another preparation approach by mixing different kinds of perovskites, in order to extend their photoluminescence range, improve the photoluminescent efficiency and photo-stability. Structural and optical characterizations have allowed to understand more deeply the characteristic features of perovskites and find some trends to fabricate perovskites with improved properties. At the same time, it feeds back and helps to develop the synthesis methods.
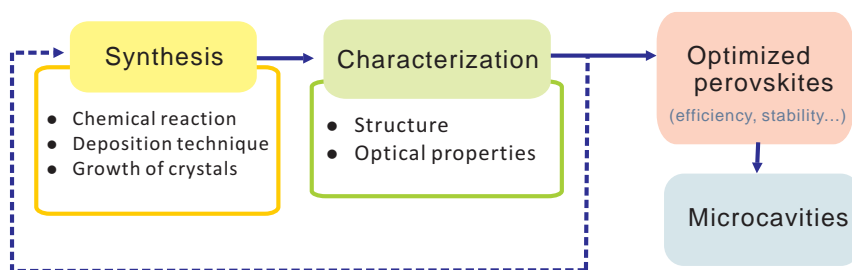
To support the substance of the thesis, we first reviewed some knowledge and results from former works on the organic-inorganic perovskites in Chapter 1. The unique organic-inorganic perovskites structure can be adapted by lots of organic cations and various inorganic atoms which provide large potential to tailor their properties. Thanks

to the self-assembling ability of these molecules, the perovskite crystals can be formed conveniently by diverse deposition techniques. Here in our work, we choose to use the simple spin-coating method for film samples and focus our attention on the PbX_4^{2-} (X = I, Br and Cl) based 2D layered perovskites group.

In the synthesis work as detailed in Chapter 2, we adopt soft chemistry methods to synthesize organic ammoniums and perovskites. In addition, we explore several other methods to fabricate nanoparticles and large crystal bulks of perovskites. Two methods have been developed to fabricate the nanoparticles: the solution method and the spray drying method, which is the most efficient method to generate nanoparticles with good optical quality and identical sizes. For the growth of crystal bulks, we mainly tried the room temperature evaporation method and worked on several different solvents. By slow solution exchange method with acetone and ether solvent, we obtained a 7 mm $\times$ 5 mm $\times$ 3 mm PMPI crystal bulk, and a 8 mm $\times$ 4 mm $\times$15 mm PEPI crystal bulk has been grown from mixed solution nitromethane/acetone, which shows bright green photoluminescence at room temperature.

In order to characterize the properties of perovskites, we have built up our home-made experiment setups at room temperature and at low temperature. By substituting different organic cations in $(R-(CH_2)_nNH_3)_2PbX_4$ and $(NH_3-R-NH_3)PbX_4$ perovskites, various interesting modifications in properties are observed. The 2D phenyl-based perovskites self-assemble via "π" - "π" stacking and have more smooth surfaces than other perovskites assembled via Van der Waals force. From the OA and PL experimental results, we find that the photoluminescence of 2D layered organic-inorganic perovskites is strongly influenced by the steric encumbrance of R group, as well as the according length of -CH_2 chain. For example, the 2-phenylethanamine and cyclohexylmethanamine are found to be optimal organic structures to accommodate in the space between the inorganic sheets provided by the PbX_6^{4-} octahedra.

The high flexibility of perovskites allows us to successfully create new groups of mixed crystals such as $(R-NH_3)PbY_xZ_{4-x}$ (mixing in the inorganic part) and $AB-(NH_3)_2PbX_4$ (mixing in the organic part). These mixed perovskites, which present averaged properties of their precursors, further enlarge the possibilities to tune the optical properties as we want: the energy gaps can be continuously tuned by changing the molar ratio among the different precursors. In the group of $CMPC_4B_{4-x}$ for example, the emission wavelength can be continuously tuned from 332 nm to 403 nm.

Photo-stability is an important feature in the study of perovskites: although more photo-resistant than the traditional organic materials, the photobleaching is still a problem for most perovskites, which limits their applications under long-term intense illumination. The Chapter 4 intensively explored the important factors which influence photo-stability. We carried on some experiments to study and summarized the possible

reasons which cause the degradation phenomena of perovskites. We found that photo-chemical process is a predominant problem in the degradation. It may cause oxidation and elimination of halogen species in inorganic parts, followed by a decomposition of the organic cations. Following the trends we discovered, we synthesized some photo-stabilized perovskites: 5FPEPI, 4FPEPI and 4FPEPI crystals embedded in a polymer (PMMA) matrix . After the continuous illumination with a 7 mW HeCd laser (325 nm) during 1h, the remaining PL intensities of the 4FPEPI based photo-stabilized perovskites are around 50% of their initial PL intensities. Compared with the 0% value for PEPI, significant improvements are obtained.

Finally, the optimized stable smooth layer 4FPEPI doped PMMA is embedded in a λ-microcavity. The strong coupling regime with a large Rabi splitting of 90 meV is demonstrated from angle-resolved reflectivity and photoluminescence experiments at room temperature.

A great asset of perovskites, regarding the applications in opto-electronic devices, is the possibility of modifying, as desired, their optical properties by molecular engineering. As a further example of moleculer engineering, we present in appendix B a new system we have performed very recently, the study of which being still in progress: perovskite-based nanoantenna.

In a more global context, the organic-inorganic perovskites compounds have been applied to many fields such as energy transfer systems, strong coupling with cavity photons or surface plasma, and many electronic devices such as OILEDs, TFTs, solar cells. The primary success is quite encouraging. Especially the perovskites-sensitized solar cells, who exhibit a high conversion efficient up to 6.54%, which is so far the highest efficiency among the reported inorganic QD sensitizers. Looking forwards, the prospect of organic-inorganic hybrid perovskites is very promising. There is still a large space to improve the performances of applications containing perovskites and substantial potential to exploit their new functions in technology and industry. Just like it is remarked in article Oulton et al. (2003): "In the future, the combination of both materials systems will allow the rules that apply to matter and light to be further stretched, potentially seeding a new paradigm in optoelectronic devices."

Appendix A

Synthesis of 2-pentafluorophenylethyamine

Since the 2-pentafluorophenylethyamine is not commercial available, we perform the synthesis in order to obtain the organic basis of perfluorophenyl perovskites. The reagents pentafluorophenylacetonitrile ($C_6F_5CH_2CN$, assay 99%), lithium aluminum hydride ($LiAlH_4$, assay 95%) and anhydrous aluminum chloride ($AlCl_3$, assay 99.9%) are purchased from Sigma-Aldrich company. The reaction process is described as in formulas. 5.29
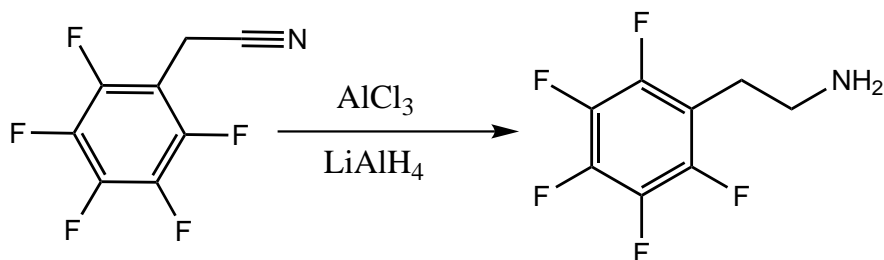
FIGURE 5.29: Proposed reaction for preparation of 2-pentafluorophenylethyamine.

Referring to the method used in reference Könemann et al. (PCT/EP2009/053201, 2009), we dissolve 1.24g $AlCl_3$ in 10 ml dry THF (tetrahydrofuran) solvent and add this solution to another reaction flask where 370 mg $LiAlH_4$ are dissolved in 10 ml dry THF. After several minutes, 2g $C_6F_5CH_2CN$ is then added slowly and dropwise (This process is very violent). After stirring at room temperature for about 1 hour, the remaining $LiAlH_4$ is quenched with water, the 16 ml of 6N sulfuric acid and 8 ml water are added. In a separating funnel, the ether phase is removed and the aqueous phase is then extracted three times with 30 ml ether at each time. The aqueous phase is brought to PH≈14 with NaOH powder. Finally, the aqueous phase is again extracted by shaking three times with 30 ml of ether each time. The organic phases are then combined and dried by evaporator. The concentrated liquid at the bottom of flask becomes solid after several days in air, it is then proved to be the 2-pentafluorophenylethyamine by NMR (Nuclear Magnetic Resonance) measurement, as shown in Figure 5.30.
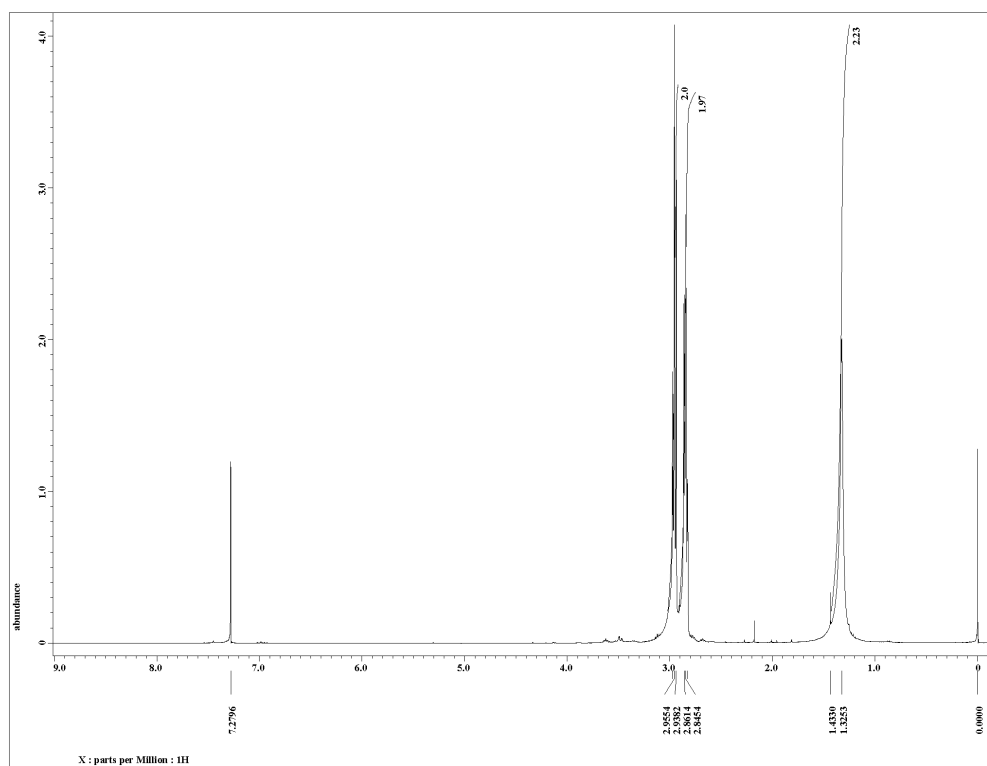
FIGURE 5.30: H^1 NMR spectrum of 2-pentafluorophenylethyamine

Appendix B

Synthesis of naphthalimide based perovskites and energy transfer between excitons

In the recent years, photo-induced energy transfer occurring at molecular scale is one of the most interesting issues which has attracted much attention from chemists and physicists in particular to exploit the potential applications of this kind of molecules, such as optical nano-antenna. It is thought that the perovskites systems, having an organic-inorganic hybrid structure may have the ability to couple two different types of excitons (Wannier excitons and Frenkel excitons) in a single molecule, and some energy transfer at the molecular scale is expected.

Take the PbX_4^{2-} based perovskites for example, as shown in Figure 5.31, if the organic cation can accumulate energy by absorbing a mount of photons, it is expected that the energy can be transferred to the inorganic part PbX_4^{2-} which is the optical center of the photoluminescent system. Therefore, the absorption ability of organic moiety is very important.
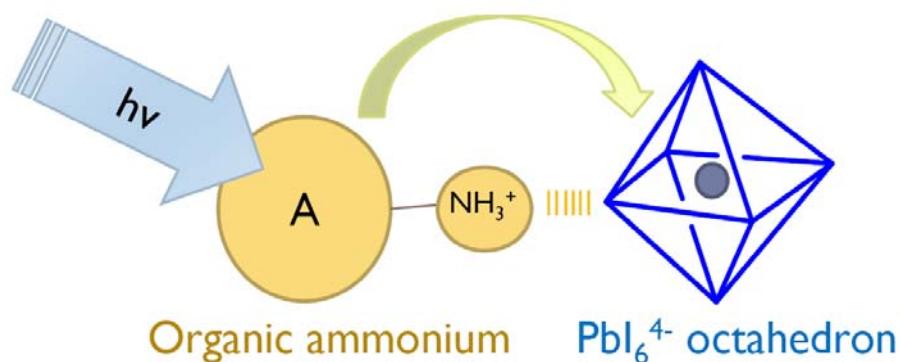
FIGURE 5.31: Schematic illustration of energy transfer from organic part to inorganic part inside a perovskite molecule

Naphthalimide compounds, who have highly unsaturated structure, are an attractive class of electron-deficient organic materials for OLEDs. They have high electron affinities, Cacialli et al. (1998) wide energy gaps Swensen et al. (2011); Koech et al. (2010); Cosimbescu et al. (2011); Liu et al. (2010) and low reduction potentials, Ozdemir et al. (2010) making them good candidates for use as n-type materials in OLEDs. Additionally, the naphthalimide counpounds are a very good optical absorbers. It is reported that the naphthalimide structure possesses large absorption coefficient about 8000 L·mol^{-1}cm^{-1}. Compared to the absorption coefficient 200 L·mol^{-1}cm^{-1} of phenyl structure, it absorbs at least 40 times stronger than the general organic structures. P.Audebert

Synthesis of naphthalimide

The reagent anhydrous 1,8-naphthalic ($C_{12}H_6O_3$, assay 97%) is purchased from ACROS company, the ethylenediamine ($NH_2CH_2CH_2NH_2$, assay 99%)is purchased from Sigma-Aldrich company and the N-Boc-ethylenediamine ((CH_3)$_3$COCONHCH$_2$CH$_2$NH$_2$, assay 98%) is purchased from Alfa Aesar company. The synthesis method is described in Formulas 5.32 and 5.34. To be clear, we define the abbreviations as shown in Table 5.1.

TABLE 5.1: Chemical structure and abbreviation of "APH" based products

Chemical structure	Abbreviation
	APH
	APH-BOC
	APHPX
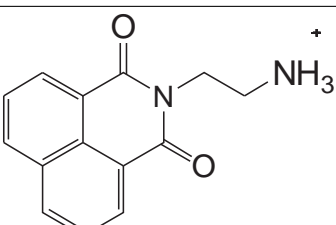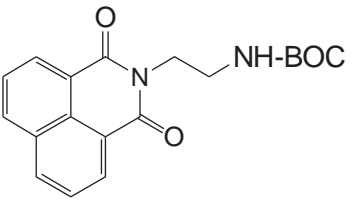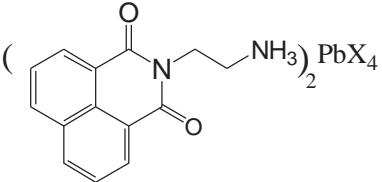
The first step is to synthesize "APH-BOC", we take 2.69 g 1,8-naphthalic, 2.42 g (3.33 ml) ethylenediamine and 2.40 g (2.4 ml) N-Boc-ethylenediamine and dissolve them in about 30 ml dichloromethane (CH_2Cl_2). After being stirring for 4 h, the reaction

mixture is quenched with an aqueous 1N HCl solution, and the organic material is extracted with acetate ethyl ($CH_3COOCH_2CH_3$). The extracts are then dried over $MgSO_4$ filtered, and concentrated in vacuum evaporator. At last some colorless sticky solid is left at the bottom of flask, which is proved to be "APH-BOC" product with high purity by NMR measurement (400 MHz, $CDCl_3$) . The resonant peaks are very coherent with the predicted spectrum.
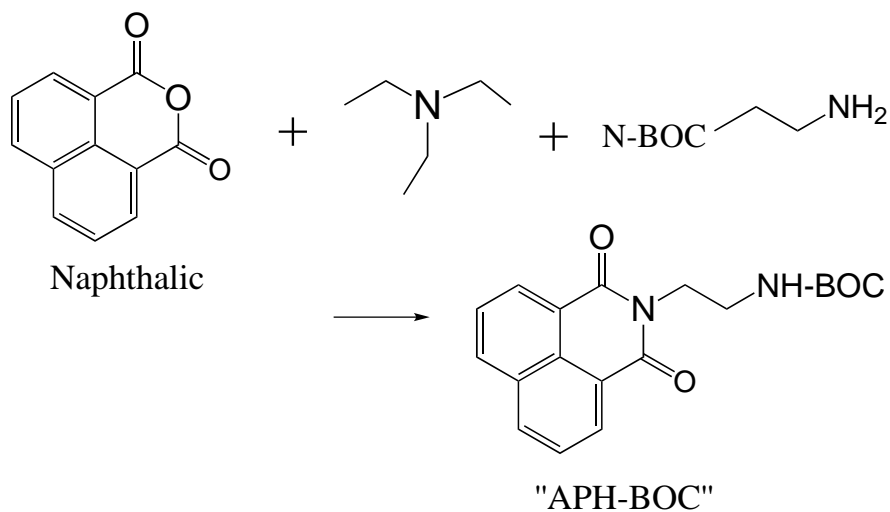
FIGURE 5.32: Proposed synthetic route for preparation of "APH-BOC".
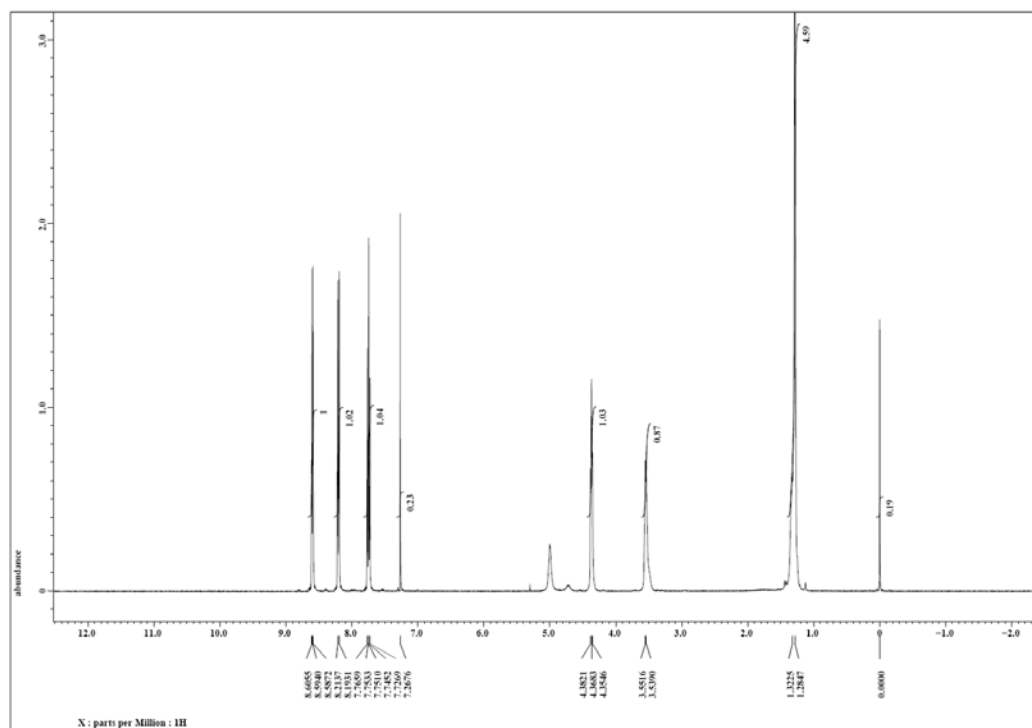
FIGURE 5.33: H^1 NMR spectrum of "APH-BOC"

After being dried for several days, the "APH-BOC" product is then passed to the second step to fabricate ammonium salts as described in Formulas 5.34. For that, APH-BOC is firstly dissolved in dichloromethane solvent since the "APH-BOC" is not soluble in ether which we always used for amines. Then, slightly over dosed HX (X = I and Br) aqueous solution is added. The ammonium salts thus generated are then filtered, wash with n-pentane and dried in vacuum. At last, this salts are mixed with inorganic PbX$_2$ to prepare the perovskites "APHPX", as seen in Formulas 5.35.
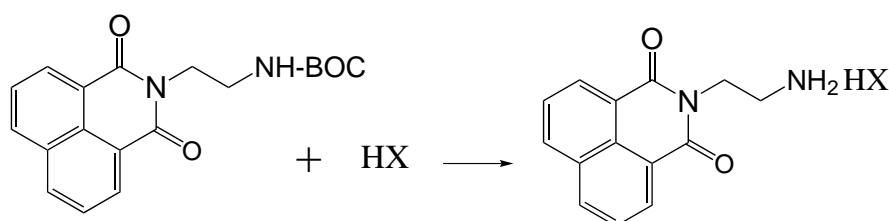
FIGURE 5.34: Proposed reaction for preparation of "APH" based ammonium salts.
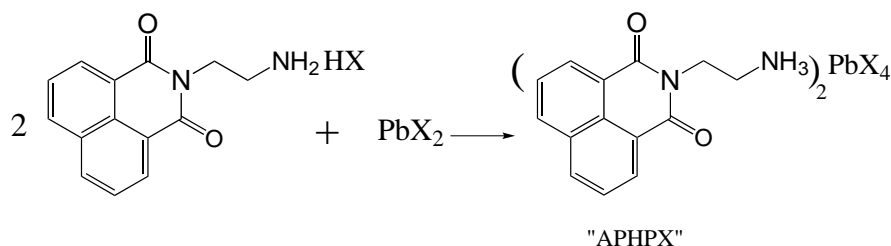
FIGURE 5.35: Proposed reaction for preparation of "APHPX" (X = I, Br and Cl) perovskites.

Optical properties

The optical measurements are carried on for the APH-BOC organic product, as well as APH based perovskites APHPX. Figure 5.36(a) shows the absorption spectra of two solution samples: APH-BOC and APHPB samples, the solvent is DMF. A large absorption band at about 335 nm is observed in both curves, which exhibit the strong absorption of organic cation. The abrupt absorption below 270 nm is due to the apsorption of DMF solvent. In Figure 5.36(b), we see the absorption spectra of APHPX (X = I, Br and Cl) thin films samples. The large peak around 335 nm appears in the curves of all these three samples, besides, anther peak at 380.5 nm is also observed for APHPI. PL spectra of APH-BOC and APHPB films are measured at room temperature, as presented in Figure 5.37. These samples are deposited by spin-coating, and annealed at 95 °C for 1 min. The intensity of APH-BOC PL is normalized to 1, this sample exhibits strong PL under an exitation of HeCd laser (325 nm). The emission centered at 461.5 nm is thought to be due to singlet state of organic "APH" structure, thus called fluorescence. The PL of APHPB and APHPC which are situated 505.4 nm and 495 nm respectively possess large FWHM, nearly 100 nm. They are not like the sharp resonance which arise
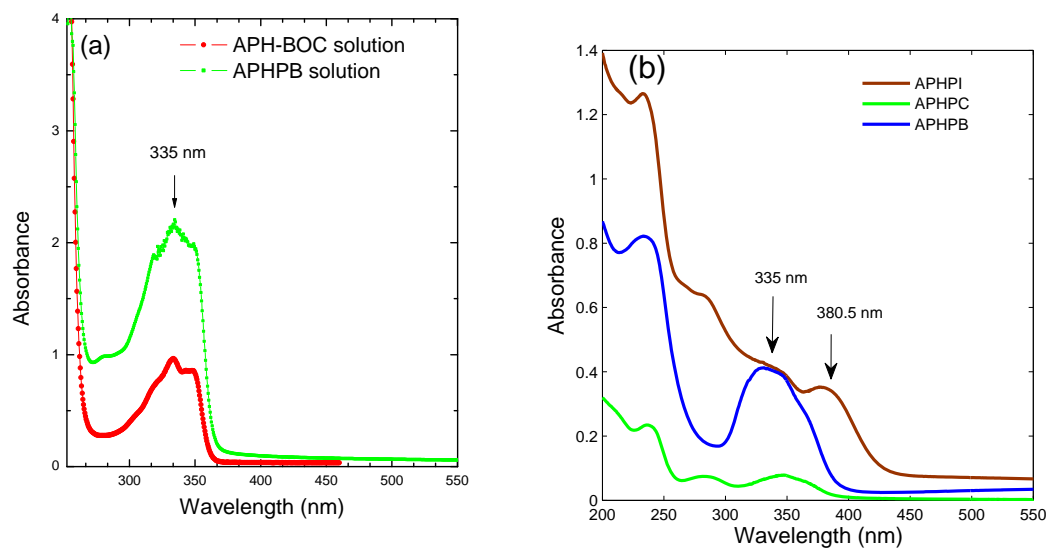
FIGURE 5.36: Absorbtion spectra of (a) two solution samples: APH-BOC and APHPB in DMF samples. (b) APHPX (X = Cl, Br and I) thin films
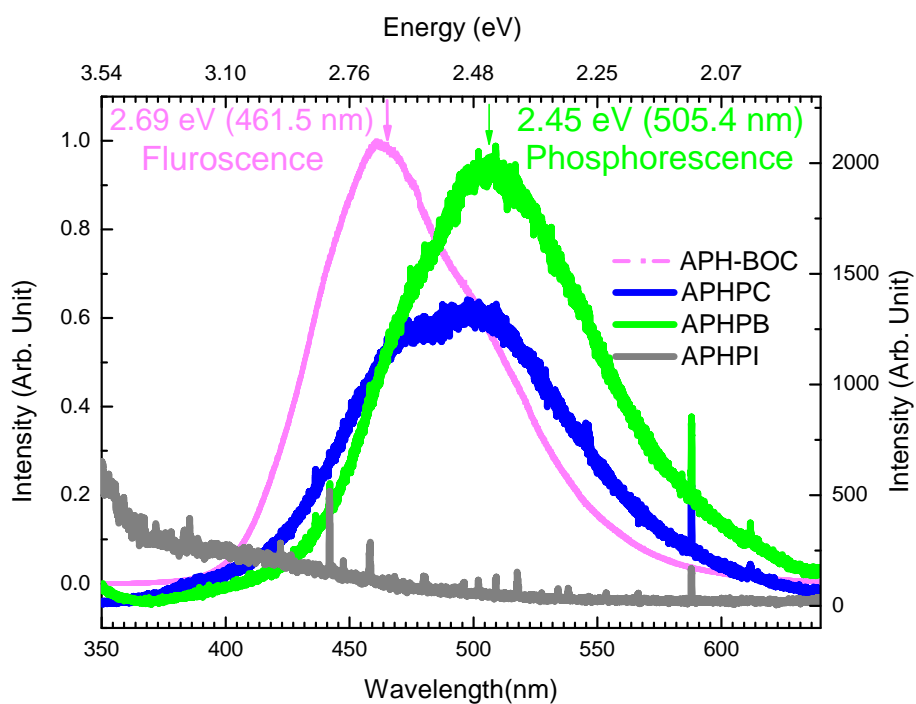
FIGURE 5.37: PL spectra of APH-BOC and APHPX (X = Cl, Br and I) film samples.

from inorganic sheets, but very similar to the large FWHM peak of APH-BOC, 79.6 nm. Therefore, it is very possible these emission of APHPB and APHPC are from the triplet states of their organic "APH" part. This assumption is likely because of the presence of the heavy atom "Pb", because of which spin-orbit coupling occurs and mixes the singlet and triplet states, which triggers the interband transition from the singlet state to triplet state. This results still need further study to prove.

Publications

- Review: Preparations and characterizations of luminescent two dimensional organic-inorganic perovskite semiconductors

  S. Zhang, P. Audebert, Y. Wei, A. Al Choueiry, G. Lanty, A. Bréhier, L. Galmiche, G. Clavier, C. Boissière, J.S. Lauret and E. Deleporte. *Materials*, **3**(5), 3385-3406, 2010.

- Synthesis and optical properties of novel organic-inorganic hybrid UV $(R-NH_3)_2PbCl_4$ semiconductors

  S. Zhang, P. Audebert, Y. Wei, J.S. Lauret, L. Galmiche and E. Deleporte. *Journal of Materials Chemistry*, **21**, 466, 2011.

- Strong exciton-photon coupling in microcavities containing new fluorophenethylamine based perovskite compounds

  Y. Wei, J.S. Lauret, L. Galmiche, P. Audebert and E. Deleporte. *Optics Express*, **20**, 10402, 2012.

- Synthesis, optical properties and photostabilities of novel fluorinated organic-inorganic hybrid $(R-NH_3)_2PbX_4$ semiconductors

  Y. Wei, P. Audebert, L. Galmiche, J.S. Lauret and E. Deleporte. *Journal of Physics D: Applied Physics*, **46**, 135105.

- Stability of 2D organic-inorganic hybrid perovskites

  Y. Wei, P. Audebert, L. Galmiche, J.S. Lauret and E. Deleporte. Submitted to *Journal of Materials Chemistry*.

- High-Q planar organic-inorganic Perovskite-based microcavity

  Z. Han, H.S Nguyen, F. Boitier, Y. Wei, K. Abdel-Baki, J.S. Lauret, J. Bloch, S. Bouchoule, and E. Deleporte. *Optics Express*, **37**(24), 5061-5063, 2012.

- Vibrational properties of $2H-PbI_2$ semiconductors studied via Density Functional Theory calculations

  L. Pedesseau, J. Even, C. Katan, F. Raoufi, Y. Wei, E. Deleporte, J-M Jancu. *Thin Solid Films*, **541**, 9-11, 2013.

Bibliography

V. Agranovich, H. Benisty, and C. Weisbuch. Organic and inorganic quantum wells in a microcavity: Frenkel-wannier-mott excitons hybridization and energy transformation. *Solid State Commun.*, 102(8):631–636, July 1997.

V. M. Agranovich. Hybrid resonant organic-inorganic nanostructures for optoelectronic applications, 2011.

V. M. Agranovich, M. Litinskaia, and D. G. Lidzey. Cavity polaritons in microcavities containing disordered organic semiconductors. *Phys. Rev. B*, 67(8):085311, Feb 2003.

N. Antoine-Vincent, F. Natali, D. Byrne, A. Vasson, P. Disseix, J. Leymarie, M. Leroux, F. Semond, and J. Massies. Observation of Rabi splitting in a bulk GaN microcavity grown on silicon. *Phys. Rev. B*, 68:153313, Oct 2003.

P. Audebert, G. Clavier, V. Alain-Rizzo, E. Deleporte, S. Zhang, J. S. Lauret, G. Lanty, and C. Boissiére. Synthesis of new perovskite luminescent nanoparticles in the visible range. *Chem. Mater.*, 21 (2):210–214, 2009.

P. C. Becker, D. Lee, A. M. Johnson, A. G. Prosser, R. D. Feldman, R. F. Austin, and R. E. Behringer. Femtosecond dynamics of resonantly excited room-temperature excitons in II-VI CdZnTe/ZnTe quantum wells. *Phys. Rev. Lett.*, 68(12):1876–1879, Mar 1992.

J.-P. Bégué and D. Bonnet-Delpon. *Chime organique et biomédicale du fluor*. EDP science and Editions du CNRS, 2005.

A. Bréhier. *Puits quantiques hybrides organique-inorganique de pérovskites pour le couplage fort à température ambiante.* PhD thesis, École Normale Supérieure de Cachan, 2007.

A. Bréhier, R. Parashkov, J. S. Lauret, and E. Deleporte. Strong exciton-photon coupling in a microcavity containing layered perovskite semiconductors. *Appl. Phys. Lett.*, 89: 171110, September 2006.

T. Böttcher, S. Figge, S. Einfeldt, R. Chierchia, R. Kröger, Ch. Petter, Ch. Zellweger, H.-J. Bühlmann, M. DieSSelberg, D. Rudloff, J. Christen, H. Heinke, P. L. Ryder,

M. Ilegems, and D. Hommel. GaN based laser diodes-epitaxial growth and device fabrication. *physica status solidi (c)*, 0(6):1846–1859, 2003. ISSN 1610-1642.

F. Cacialli, R. H. Friend, C.-M. Bouché, P. Le Barny, H. Facoetti, F. Soyer, and P. Robin. Naphthalimide side-chain polymers for organic light-emitting diodes: Band-offset engineering and role of polymer thickness. *Journal of Applied Physics*, 83(4):2343–2356, 1998.

J. Calabrese, N. L. Jones, R. L. Harlow, N. Herron, D. L. Thorn, and Y. Wang. Preparation and characterization of layered lead halide compounds. *J. Am. Chem. Soc.*, 113: 2328–2330, 1991.

J. A. Chang, J. H. Rhee, S. H. Im, Y. H. Lee, H. Kim, S. I. Seok, M. K. Nazeeruddin, and M. Gratzel. High-performance nanostructured inorganic-inorganic heterojunction solar cells. *Nano Letters*, 10(7):2609–2612, 2010.

K. Chondroudis and D. B. Mitzi. Electroluminescence from an organic-inorganic perovskite incorporating a quaterthiophene dye within lead halide perovskite layers. *Chemistry of Materials*, 11(11):3028–3030, 1999.

S. Christopoulos, G. Baldassarri Höger von Högersthal, A. J. D. Grundy, P. G. Lagoudakis, A. V. Kavokin, J. J. Baumberg, G. Christmann, R. Butté, E. Feltin, J.-F. Carlin, and N. Grandjean. Room-temperature polariton lasing in semiconductor microcavities. *Phys. Rev. Lett.*, 98:126405, Mar 2007.

L. Cosimbescu, E. Polikarpov, J. S. Swensen, J. T. Darsell, and A. B. Padmaperuma. Hole-rich host materials for blue-phosphorescent oleds. *Journal of the Society for Information Display*, 19(4):353–359, 2011.

T. Dammak, M. Koubaa, K. Boukheddaden, H. Bougzhala, A. Mlayah, and Y. Abid. Two-dimensional excitons and photoluminescence properties of the organic/inorganic $(4-FC_6H_4C_2H_4NH_3)_2[PbI_4]$ nanomaterial. *The Journal of Physical Chemistry C*, 113 (44):19305–19309, 2009.

Le Si Dang, D. Heger, R. André, F. Bœuf, and R. Romestain. Stimulation of polariton photoluminescence in semiconductor microcavity. *Phys. Rev. Lett.*, 81(18):3920–3923, Nov 1998.

A. Das, J. Heo, M. Jankowski, W. Guo, L. Zhang, H. Deng, and P. Bhattacharya. Room temperature ultralow threshold GaN nanowire polariton laser. *Phys. Rev. Lett.*, 107: 066405, Aug 2011.

H. Deng, G. Weihs, D. Snoke, J. Bloch, and Y. Yamamoto. Polariton lasing vs. photon lasing in a semiconductor microcavity. *Natl. Acad. Sci.*, 100(23):15318–15323, 2003.

B. Deveaud. *The Physics of Semiconductor Microcavities*. John Wiley & Sons, 2007. ISBN 9783527610167.

K. Ema, M. Inomata, Y. Kato, H. Kunugita, and M. Era. Nearly perfect triplet-triplet energy transfer from wannier excitons to naphthalene in organic-inorganic hybrid quantum-well materials. *Phys. Rev. Lett.*, 100:257401, Jun 2008.

M. Era, T. Hattori, T. Taira, and T. Tsutsui. Self-organized growth of PbI-based layered perovskite quantum well by dual-source vapor deposition. *Chem. Mater.*, 9(1):8–10, JAN 1997. ISSN 0897-4756.

M. Era, S. Morimoto, T. Tsutsui, and S. Saito. Organic-inorganic heterostructure electroluminescent device using a layered perovskite semiconductor $(C_6H_5C_2H_4NH_3)_2PbI_4$. *Appl. Phys. Lett.*, 65(6):676–8, 8 August 1994. ISSN 0003-6951.

M. Fox. *Optical Properties of solids.* Oxford University Press (New York), 2001.

J. Fujisawa and T. Ishihara. Excitons and biexcitons bound to a positive ion in a bismuth-doped inorganic-organic layered lead iodide semiconductor. *Physical Review B*, 70(20): 1–6, 2004.

T. Fujita, Y. Sato, T. Kuitani, and T. Ishihara. Tunable polariton absorption of distributed feedback microcavitites at room temperature. *Phys. Rev. B*, 57(19):12428, May 1998.

K. Gauthron, J. S. Lauret, L. Doyennette, G. Lanty, A. Al Choueiry, S.J. Zhang, A. Bréhier, L. Largeau, O. Mauguin, J. Bloch, and E. Deleporte. Optical spectroscopy of two-dimensional layered $(C_6H_5C_2H_4 - NH_3)_2 - PbI_4$ perovskite. *Opt. Express*, 18: 5912–5919, 2010.

H. M. Gibbs, G. Khitrova, and S .W. Koch. Exciton-polariton light-semiconductor coupling effects. *Nature Photon.*, 5:275, November 2011.

B. Gil, O. Briot, and R-. L-. Aulombard. Valence-band physics and the optical properties of gan epilayers grown onto sapphire with wurtzite symmetry. *Phys. Rev. B*, 52: R17028–R17031, Dec 1995.

T. Hattori, T. Taira, M. Era, T. Tsutsui, and S. Saito. Highly efficient electroluminescence from a heterostructure device combined with emissive layered-perovskite and an electron-transporting organic compound. *Chem. Phys. Lett.*, 254(1-2):103 – 108, 1996. ISSN 0009-2614.

G. Hodes. Comparison of dye- and semiconductor-sensitized porous nanocrystalline liquid junction solar cells. *The Journal of Physical Chemistry C*, 112(46):17778–17787, 2008.

X. Hong, T. Ishihara, and A. V. Nurmikko. Dielectric confinement effect on excitons in PbI$_4$-based layered semiconductors. *Phys. Rev. B*, 45(12):6961–6964, March 1992.

R. Houdré. Early stages of continous wave experiments on cavity-polaritons. *Phys. Stat. Sol. b*, 242(11):2167–2196, July 2005.

J. Im, C. Lee, J. Lee, S. Park, and N. Park. 6.5% efficient perovskite quantum-dot-sensitized solar cell. *Nanoscale*, 3:4088–4093, 2011.

A. Imamoglu and R. J. Ram. Quantum dynamics of exciton lasers. *Phys. Lett. A*, 214: 193–198, 1996.

T. Ishihara. *Optical Properties of Low Dimensional Materials, Vol. 2, (Eds: T. Ogawa and Y. Kanemitsu. World Scientific, Singapore, 1998, Ch. 6)*.

T. Ishihara. Optical properties of PbI-based perovskite structures. *J. Lumin.*, 60-61:269 – 274, 1994. ISSN 0022-2313. International Conference on Luminescence.

T. Ishihara. *Optical Properties of Low Dimensional Materials*, chapter 6, page 288. World Scientific (Singapore), 1995.

T. Ishihara, X. Hong, J. Ding, and A. V. Nurmikko. Dielectric confinement effect for exciton and biexciton states in PbI_4-based two-dimensional semiconductor structures. *Surface Science*, 267:323–326, 1992.

T. Ishihara, J. Takahashi, and T. Goto. Exciton state in two-dimensional perovskite semiconductor $(C_{10}H_{21}NH_3)_2PbI_4$. *Solid State Comm.*, 69(9):933 – 936, 1989. ISSN 0038-1098.

T. Ishihara, J. Takahashi, and T. Goto. Optical properties due to electronic transitions in two-dimensional semiconductors $(C_nH_{2n+1}NH_3)_2PbI_4$. *Phys. Rev. B*, 42(17):11099–11107, Dec 1990.

C. R. Kagan, D. B. Mitzi, and C. D. Dimitrakopoulos. Organic-inorganic hybrid materials as semiconducting channels in thin-film field-effect transistors. *Science*, 286:945–947, October 1999.

J. Kasprzak. *Condensation of exciton polaritons*. 2006.

J. Kasprzak, M. Richard, S. Kundermann, A. Baas, P. Jeambrun, J. M. J. Keeling, F. M. Marchetti, M. H. Szymańska, R. André, J. L. Staehli, V. Savona, P. B. Littlewood, B. Deveaud, and Le Si Dang. Bose-einstein condensation of exciton polaritons. *Nature*, 443(28):409–414, Sep 2006.

A. V. Kavokin, J. J. Baumberg, G. Malpuech, and F. P. Laussy. *Microcavities*, chapter 8. edited by Oxford University Press (New York, United States, 2007).

P. Kelkar, V. Kozlov, H. Jeon, A. V. Nurmikko, C.-C. Chu, D. C. Grillo, J. Han, C. G. Hua, and R. L. Gunshor. Excitons in a II-VI semiconductor microcavity in the strong-coupling regime. *Phys. Rev. B*, 52(8):R5491–R5494, Aug 1995.

S. Kéna-Cohen, M. Davanço, and S. R. Forrest. Strong exciton-photon coupling in an organic single crystal microcavity. *Phys. Rev. Lett.*, 101(11):116401, Sep 2008.

S. Kéna-Cohen and S. R. Forrest. Room-temperature polariton lasing in an organic single-crystal microcavity. *Nature Photon.*, 4:371–375, Apr 2010.

K Kikuchi, Y Takeoka, M Rikukawa, and K Sanui. Structure and optical properties of lead iodide based two-dimensional perovskite compounds containing fluorophenethylamines. *Curr. Appl Phys.*, 4(6):599–602, NOV 2004. ISSN 1567-1739.

K. Kikuchi, Y. Takeoka, M. Rikukawa, and K. Sanui. Structure and optical properties of lead iodide based two-dimensional perovskite compounds containing fluorophenethylamines. *Current Applied Physics*, 4(6):599 – 602, 2004. ISSN 1567-1739.

N. Kitawawa, T. Yamamoto, Y. Watanabe, and Y. Nakamura. Stability of self-assembled organic-inorganic layered perovskite. *Mat. Res. Soc. Symp. Proc*, 576:165–170, 1999.

N. Kitazawa. Excitons in two-dimensional layered perovskite compounds: $(C_6H_5C_2H_4NH_3)_2Pb(Br,I)_4$ and $(C_6H_5C_2H_4NH_3)_2Pb(Cl,Br)_4$. *Mater. Sci. Eng., B*, 49:233–238, 1997a.

N. Kitazawa. Optical absorption and photoluminescence properties of Pb(I,Br)-based two-dimensional layered perovskite. *Jpn. J. Appl. Phys.*, 36(4A):2272–2276, April 1997b.

N. Kitazawa. Preparation and optical properties of nanocrystalline $(C_6H_5C_2H_4NH_3)_2PbI_4$-doped PMMA films. *Journal of Materials Science*, 33:1441–1444, 1998.

N. Kitazawa and Y. Watanabe. Preparation and stability of nanocrystalline $(C_6H_5C_2H_4NH_3)_2PbI_4$ -doped PMMA films. *J. Mater. Sci.*, 37:4845–4848, 2002. ISSN 0022-2461. 10.1023/A:1020897710384.

N. Kitazawa, Y. Watanabe, and Y. Nakamura. Optical properties of $CH_3NH_3PbX_3$ (x = halogen) and their mixed-halide crystals. *Journal of Materials Science*, 37:3585–3587, 2002. ISSN 0022-2461. 10.1023/A:1016584519829.

O. Knop, R. E. Wasylishen, M. A. White, T. S. Cameron, and M. J. M. V. Oort. Alkylammonium lead halides. Part 2. $CH_3NH_3PbI_3$ (X = Cl, Br, I) perovskites: cuboctahedral halide cages with isotropic cation reorientation. *Canadian Journal of Chemistry*, 68 (3):412–422, 1990.

P. K. Koech, E. Polikarpov, J. E. Rainbolt, L. Cosimbescu, J. S. Swensen, A. L. Von Ruden, and A. B. Padmaperuma. Synthesis and application of pyridine-based ambipolar hosts: Control of charge balance in organic light-emitting devices by chemical structure modification. *Organic Letters*, 12(23):5534–5537, 2010.

A. Kojima, K. Teshima, Y. Shirai, and T. Miyasaka. Organometal halide perovskites as visible-light sensitizers for photovoltaic cells. *Journal of the American Chemical Society*, 131(17):6050–6051, 2009.

M. Könemann, R. Schmidt, F. Würthner, Z. Bao, and J. Oh. N,n'-bis(fluorophenylalkyl)-substituted perylene-3,4:9,10-tetracarboximides, and the preparation and use thereof, PCT/EP2009/053201, 2009.

I. Koutselas, P. Bampoulis, E. Maratou, T. Evagelinou, G. Pagona, and G. C. Papavassiliou. Some unconventional organic-inorganic hybrid low-dimensional semiconductors and related light-emitting devices. *The Journal of Physical Chemistry C*, 115(17): 8475–8483, 2011.

F. C. Krebs. Fabrication and processing of polymer solar cells: A review of printing and coating techniques. *Sol. Energy Mater. Sol. Cells*, 93(4):394 – 412, 2009. ISSN 0927-0248.

G. C. La Rocca. Organic Photonics: Polariton lasing. *Nature Photon.*, 4(6):343–345, JUN 2010. ISSN 1749-4885.

G. Lanty, A. Bréhier, R. Parashkov, J.S. Lauret, and E. Deleporte. Strong exciton-photon coupling at room temperature in microcavities containing two-dimensional layered perovskite compounds. *New J. Phys.*, 10, JUN 30 2008a. ISSN 1367-2630.

G. Lanty, J. S. Lauret, E. Deleporte, S. Bouchoule, and X. Lafosse. UV polaritonic emission from a perovskite-based microcavity. *Appl. Phys. Lett.*, 93(8), AUG 25 2008b. ISSN 0003-6951.

G. Lanty, J.S. Lauret, E. Deleporte, S. Bouchoule, and X. Lafosse. Strong-coupling regime at room temperature in one-dimensional microcavities containing ultraviolet-emitting perovskites. *Superlattices Microstruct.*, 47:10, 2010.

Le Chi Thanh, C. Depeursinge, F. Levy, and E. Mooser. The band gap excitons in PbI$_2$. *Journal of the Physics and Chemistry of Solids*, 36:699–702, 1975. ISSN 0022-3697.

H. Lee, J. H. Yum, H. C. Leventis, S. M. Zakeeruddin, S. A. Haque, P. Chen, S. Seok, M. Grätzel, and M. K. Nazeeruddin.

C. R. Li, H. T. Deng, J. Wan, Y. Y. Zheng, and W. J. Dong. Photoconductive properties of organic-inorganic hybrid perovskite (C$_6$H$_{13}$NH$_3$)$_2$(CH$_3$NH$_3$)$_{m-1}$Pb$_m$I$_{3m+1}$:TiO$_2$ nanocomposites device structure. *Materials Letters*, 64(24):2735 – 2737, 2010. ISSN 0167-577X.

K. Liang, D. B. Mitzi, and M. T. Prikas. Synthesis and characterization of organic-inorganic perovskite thin films prepared using a versatile two-step dipping technique. *Chem. Mater.*, 10(1):403–411, 1998.

D. G. Lidzey, D. D. C. Bradley, M. S. Skolnick, T. Virgili, S. Walker, and D. M. Whittaker. Strong exciton-photon coupling in an organic semiconductor microcavity. *Nature*, 395(6697):53–55, 1998.

D. G. Lidzey, D. D. C. Bradley, T. Virgili, A. Armitage, M. S. Skolnick, and S. Walker. Room temperature polariton emission from strongly coupled organic semiconductor microcavities. *Phys. Rev. Lett.*, 82:3316–3319, April 1999.

Z. Liu, M. G. Helander, Z. Wang, and Z. Lu. Band alignment at anode/organic interfaces for highly efficient simplified blue-emitting organic light-emitting diodes. *The Journal of Physical Chemistry C*, 114(39):16746–16749, 2010.

L. Meyer, A. Baig, F. Bylicki, and W. Demtröder. Enhanced efficiency and extended wavelength range of dye lasers operated with DCM. *Applied Physics B: Lasers and Optics*, 70:527–527, 2000. ISSN 0946-2171. 10.1007/s003400050856.

D. Meyerhofer. Characteristics of resist films produced by spinning. *Journal of Applied Physics*, 49(7):3993–3997, 1978.

D. B. Mitzi. Sunthesis, crystal structure, and optical and thermal properties of $(C_4H_9NH_3)_2MI_4$ (M=Ge, Sn, Pb). *Chem. Mater.*, 8(3):791–800, March 1996.

D. B. Mitzi. A layered solution crystal growth technique and the crystal structure of $(c_6h_5c_2h_4nh_3)_2pbcl_4$. *J. Solid State Chem.*, 145:694–704, 1999a.

D. B. Mitzi. *Synthesis, Structure, and Properties of Organic-Inorganic Perovskites and Related Materials*, volume 48 of *Progress In Inorganic Chemistry*, chapter 1, pages 1–122. JOHN WILEY & SONS, INC., 1999b.

D. B. Mitzi. Organic-inorganic perovskites containing trivalent metal halide layers: The templating influence of the organic cation layer. *Inorg. Chem.*, 39:6107, 2000.

D. B. Mitzi. Templating and structural engineering in organic-inorganic perovskites. *J. Chem. Soc., Dalton Trans.*, pages 1–12, 2001a.

D. B. Mitzi. Thin-film deposition of organic-inorganic hybrid materials. *Chem. Mater.*, 13(10):3283–3298, OCT 2001b. ISSN 0897-4756.

D. B. Mitzi, K. Chondroudis, and C. R. Kagan. Organic-inorganic electronics. *IBM J.Res. & Dev.*, 45(1):29–45, January 2001a.

D. B. Mitzi, K. Chondroudis, and C.R. Kagan. Design, structure, and optical properties of organic-inorganic perovskites containing an oligothiophene chromophore. *Inorg. Chem.*, 38:6246, 1999.

D. B. Mitzi, K. Chondroudis, and C.R. Kagan. Organic-inorganic electronics. *IBM J. Res. Dev.*, 45:29, 2001b.

D. B. Mitzi, C. D. Dimitrakopoulos, and L. L. Kosbar. Structurally tailored organic-inorganic perovskites: Optical properties and solution-processed channel materials for thin-film transistors. *Chem. Mater.*, 13(10):3728–3740, OCT 2001. ISSN 0897-4756.

D. B. Mitzi and K. Liang. Synthesis, resistivity, and thermal properties of the cubic perovskite $NH_2CH=NH_2SnI_3$ and related systems. *Journal of Solid State Chemistry*, 134(2):376 – 381, 1997. ISSN 0022-4596.

D. B. Mitzi, D. R. Medeiros, and P. R. L. Malenfant. Intercalated organic-inorganic perovskites stabilized by fluoroaryl-aryl interactions. *Inorg. Chem.*, 41(8):2134–2145, APR 22 2002. ISSN 0020-1669.

D. B. Mitzi, M. T. Prikas, and K. Chondroudis. Thin film deposition of organic-inorganic hybrid materials using a single source thermal ablation technique. *Chem. Mater.*, 11 (3):542–544, MAR 1999. ISSN 0897-4756.

M. Müller, J. Bleuse, and R. André. Dynamics of the cavity polariton in cdte-based semiconductor microcavities: Evidence for a relaxation edge. *Phys. Rev. B*, 62(24): 16886–16892, Dec 2000.

M. Müller, J. Bleuse, R. R. André, and H. Ulmer-Tuffigo. Observation of bottleneck effects on the photoluminescence from polaritons in II-VI microcavities. *Physica B*, 272:476–479, 1999.

A. Naumov, H. Stanzl, K. Wolf, S. Lankes, and W. Gebhardt. Exciton recombination in Te-rich $ZnSe_xTe_{1-x}$ epilayers. *Journal of Applied Physics*, 74(10):6178–6185, 1993.

K. Norrman, A. Ghanbari-Siahkali, and N. B. Larsen. Studies of spin-coated polymer films. *Annu. Rep. Prog. Chem., Sect. C: Phys. Chem.*, 101:174–201, 2005.

R. F. Oulton, N. Takada, J. Koe, P. N. Stavrinou, and D. D. C. Bradley. Strong coupling in organic semiconductor microcavities. *Semiconductor Science and Technology*, 18 (10):S419, 2003.

S. Ozdemir, C. Varlikli, I. Oner, K. Ocakoglu, and S. Icli. The synthesis of 1,8-naphthalimide groups containing imidazolium salts/ionic liquids using I^-, PF_6^-, $TFSI^-$ a anions and their photophysical, electrochemical and thermal properties. *Dyes and Pigments*, 86(3):206–216, 2010. ISSN 0143-7208.

G. C. Papavassiliou. Three- and low-dimensional inorganic semiconductors. *Prog. Solid St. Chem.*, 25:125–270, 1997.

G. C. Papavassiliou and I. B. Koutselas. Structural, optical and related properties of some natural three- and lower-dimensional semiconductor systems. *Synth. Metals*, 71: 1713–1714, 1995.

G. C. Papavassiliou, G. A. Mousdis, and I. B. Koutselas. Some new organic-inorganic hybrid semiconductors based on metal halide units: Structural, optical and related properties. *Adv. Mater. Opt. Electron.*, 9(6):265–271, NOV-DEC 1999. ISSN 1057-9257.

R. Parashkov, A. Bréhier, A. Georgiev, S. Bouchoule, X. Lafosse, J.S. Lauret, C.T. Nguyen, M. Leroux, and E. Deleporte. *Progress in Advanced Materials Research. (Editor : Nicolas H. Voler. Nova Science Publishers, 2007, Ch. 4).*

W. Patterson, G. H. David Piston. Photobleaching in two-photon excitation microscopy. *Biophys. J .*, 78:2159–2162, 2000.

P.Audebert.

A. Poglitsch and D. Weber. Dynamic disorder in methylammoniumtrihalogenoplumbates (II) observed by millimeter-wave spectroscopy. *The Journal of Chemical Physics*, 87 (11):6373–6378, 1987.

K. Pradeesh, J. J. Baumberg, and G. Vijaya Prakash. In situ intercalation strategies for device-quality hybrid inorganic-organic self-assembled quantum wells. *Appl. Phys. Lett.*, 95(3):033309, 2009a.

K. Pradeesh, J. J. Baumberg, and G. Vijaya Prakash. Strong exciton-photon coupling in inorganic-organic multiple quantum wells embedded low-q microcavity. *Opt. Express*, 17(24):22171–22178, Nov 2009b.

E. M. Purcell, H. C. Torrey, and R. V. Pound. Resonance absorption by nuclear magnetic moments in a solid. *Phys. Rev.*, 69:37–38, Jan 1946.

M. Saba, C. Ciuti, J. Bloch, V. Thierry-Mieg, R. Andre, Le Si Dang, S. Kundermann, A. Mura, G. Bongiovanni, J. L. Staehli, and B. Deveaud. High-temperature ultrafast polariton parametric amplification in semiconductor microcavities. *Nature*, 414:731–735, December 2001.

V. Savona, L.C. Andreani, P. Schwendimann, and A. Quattropani. Quantum well excitons in semiconductor microcavities: Unified treatment of weak and strong coupling regimes. *Solid State Communications*, 93(9):733 – 739, 1995. ISSN 0038-1098.

F. Semond, I.R. Sellers, F. Natali, D. Byrne, M. Leroux, J. Massies, N. Ollier, J. Leymarie, P. Disseix, and A. Vasson. Strong light-matter coupling at room temperature in simple geometry gan microcavities grown on silicon. *Appl. Phys. Lett.*, 87(2):021102, June 2005.

B. Sermage and G. Fishman. Excitons and polaritons in ZnSe. *Phys. Rev. B*, 23:5107–5118, May 1981.

M. Shinada and S. Sugano. Interband optical transitions in extremely anisotropic semiconductors. i. bound and unbound exciton absorption. *J. Phys. Soc. Jpn.*, 21:1936–1946., 1966.

M. S. Skolnick, T. A. Fisher, and D. M. Whittaker. Strong coupling phenomena in quantum microcavity structures. *Semicond. Sci. Technol.*, 13:645–669, March 1998.

J. S. Swensen, J. E. Rainbolt, L. Wang, P. K. Koech, E. Polikarpov, A. B. Padmaperuma, and D. J. Gaspar. Blue phosphorescent organic light-emitting devices utilizing cesium–carbonate-doped 2,4,6-tris(2',4'-difluoro-[1,1'-biphenyl]-4-yl)-1,3,5-triazine. *Journal of Photonics for Energy*, 1(1):011008, 2011.

C. Symonds, J. Bellessa, J. C. Plenet, A. Bréhier, R. Parashkov, J. S. Lauret, and E. Deleporte. Emission of hybrid organic-inorganic exciton/plasmon mixed states. *Appl. Phys. Lett.*, 90(9), FEB 26 2007. ISSN 0003-6951.

C. Symonds, C. Bonnand, J. C. Plenet, A. Bréhier, R. Parashkov, J. S. Lauret, E. Deleporte, and J. Bellessa. Particularities of surface plasmon-exciton strong coupling with large Rabi splitting. *New J. Phys.*, 10, JUN 30 2008. ISSN 1367-2630.

J. Takada, H. Awaji, M. Koshioka, A. Nakajima, and W. A. Nevin. Organic–inorganic multilayers: A new concept of optoelectronic material. *Applied Physics Letters*, 61 (18):2184–2186, 1992.

N. Takada, T. Kamata, and D.D.C. Bradley. Polariton emission from polysilane-based organic microcavities. *Appl. Phys. Lett.*, 82(12):1812–1814, March 2003.

K. Tanaka, F. Sano, T. Takahashi, T. Kondo, R. Ito, and K. Ema. Two-dimensional wannier excitons in a layered-perovskite-type crystal $(C_6H_{13}NH_3)_2PbI_4$. *Solid State Comm.*, 122:249–252, March 2002.

A. I. Tartakovskii, M. Emam-Ismail, R. M. Stevenson, M. S. Skolnick, V. N. Astratov, D. M. Whittaker, J. J. Baumberg, and J. S. Roberts. Relaxation bottleneck and its suppression in semiconductor microcavities. *Phys. Rev. B*, 62(4):R2283–R2286, Jul 2000.

F. Tassone, C. Piermarocchi, V. Savona, A. Quattropani, and P. Schwendimann. Bottleneck effects in the relaxation and photoluminescence of microcavity polaritons. *Phys. Rev. B*, 56:7554–7563, Sep 1997.

F. Tassone and Y. Yamamoto. Exciton-exciton scattering dynamics in a semiconductor microcavity and stimulated scattering into polaritons. *Phys. Rev. B*, 59:10830–10842, Apr 1999.

L. K. van Vugt, Sven Rühle, Prasanth Ravindran, Hans C. Gerritsen, Laurens Kuipers, and Daniël Vanmaekelbergh. Exciton polaritons confined in a ZnO nanowire cavity. *Phys. Rev. Lett.*, 97:147401, Oct 2006.

Y. Wei, J. S. Lauret, L. Galmiche, P. Audebert, and E. Deleporte. Strong exciton-photon coupling in microcavities containing new fluorophenethylamine based perovskite compounds. *Opt. Express*, 20(9):10399–10405, Apr 2012.

C. Weisbuch, M. Nishioka, A. Ashikawa, and Y. Arakawa. Observation of the coupled exciton-photon mode splitting in a semiconductor quantum microcavity. *Phys. Rev. Lett.*, 69:3314–3317, December 1992.

J. Wenus, R. Parashkov, S. Ceccarelli, A. Bréhier, J.S. Lauret, M.S. Skolnick, E. Dele-
porte, and D.G. Lidzey. Hybrid organic-inorganic exciton-polaritons in a strongly
coupled microcavity. *Phys. Rev. B*, 74:235212, December 2006.

C. Yang, M. Kuo, Y. Lai, K. Chiu, J. Shen, J. Lee, W. Chou, S. Jeng, and W. Lan. Quan-
tum confinement of Te bound exciton in $ZnSe/ZnSe_{1-x}Te_x$ and $ZnSe/Zn_{1-y}Cd_ySe$
quantum wells. *Materials Chemistry and Physics*, 81(1):1 – 7, 2003. ISSN 0254-0584.

X. Yu, B. Lei, D. Kuang, and C. Su. Highly efficient CdTe/CdS quantum dot sensitized
solar cells fabricated by a one-step linker assisted chemical bath deposition. *Chem.
Sci.*, 2:1396–1400, 2011.

S. Zhang, P. Audebert, Y. Wei, A. Al Choueiry, G. Lanty, A. Bréhier, L. Galmiche,
G. Clavier, C. Boissière, J-.S. Lauret, and E. Deleporte. Preparations and character-
izations of luminescent two dimensional organic-inorganic perovskite semiconductors.
Materials, 3(5):3385–3406, 2010.

S. Zhang, P. Audebert, Y. Wei, J.-S. Lauret, L. Galmiche, and E. Deleporte. Synthesis
and optical properties of novel organic-inorganic hybrid UV $(RNH_3)_2PbCl_4$ semicon-
ductors. *J. Mater. Chem.*, pages 466–474, 2011.